Design and Development of Acoustofluidic Platforms for On-Chip Manipulation of Bioparticles and Fluids

REZA RASOULI, M.SC.

DEPARTMENT OF BIOMEDICAL ENGINEERING
MCGILL UNIVERSITY
MONTREAL,
QC, CANADA

A THESIS SUBMITTED TO McGILL UNIVERSITY
IN PARTIAL FULFILLMENT OF THE REQUIREMENTS OF THE DEGREE OF DOCTOR OF PHILOSOPHY

Abstract

The precise, rapid, and controlled manipulation of biospecimens such as cells and bio-liquids is the central requirement in numerous biomedical processes and assays. In recent years, a great amount of research in the manipulation of bio-species has been directed toward “Lab-on-a-Chip” (LoC) technology, where the miniaturized systems offer high-precision, excellent spatial control, minimal sample and reagent consumption, parallelization, and myriads of application-specific advantages. However, the scaling laws and the dominance of surface and friction forces in micro-realm necessitate the integration of enabling physical actuation mechanisms with LoC systems in order to fully realize their tremendous potential in bioanalytical applications.

Particularly, acoustic actuation mechanisms have gained considerable attention owing to their high biocompatibility, versatility, and long well-characterized history in the biomedical field. For more than 70 years, conventional sound-powered devices have been used to screen, diagnose, and treat patients in hundreds of medical devices. The advancement of microfabrication technologies allowed easy integration of acoustic actuation with LoC systems and introduced the field of acoustofluidics. In recent years, acoustofluidics has reignited the application of acoustic methods in the biomedical field, particularly for the development of novel bioanalytical tools and protocols that benefit from distinctive microscale phenomena, remarkable resolution, and high controllability.

Hence, the overarching goal of this thesis is to both exploit the miniaturization advantages of acoustofluidics, and to explore its unique physics to introduce new on-chip tools for the manipulation of bio-samples with a focus on their application in the emerging fields of nanotherapeutics and regenerative medicine. The multifaceted nature of nanotherapeutics and regenerative medicine requires acoustofluidics to perform various tasks. To provide tools and methods for fulfilling these tasks, we designed and developed state-of-the-art acoustofluidic platforms for i) synthesizing nanoparticles as therapeutic carriers, ii) rapid formation of multicellular spheroids as building blocks for tissue engineering and 3D cellular models, and finally, iii) delivering the nanotherapeutics to the 3D spheroids by acoustic forces.

To this end, we first developed a boundary-driven acoustic mixer by the combination of oscillatory sharp edges and bubbles, to induce controllable microstreams and ultra-rapid mixing. In doing so, we aimed to introduce a new method for synthesizing nanoparticles with therapeutic capacity and address some of the challenges in microfluidic nanoparticle generation systems such as batch to batch variation, dilution of output, and clogging of channels during nanoprecipitation.

Additionally, the boundary-driven device was employed for the formation of 3D cellular spheroids. The acoustically induced hydrodynamic forces were used for the physical agglomeration of cells into compact clusters in a span of seconds. The incorporation of atelocollagen I as a bio-adhesive transformed the clusters into stable spheroids, readily retrievable for further manipulations. This novel method allows for continuous and rapid formation of spheroids while enabling real-time monitoring and controlling the spheroid size.

Finally, we developed a high-frequency acoustic platform based on surface acoustic wave technology to deliver nanotherapeutics to the spheroids as 3D cellular models. Applying biocompatible surface acoustic waves allowed sonoprinting nanoparticles onto the spheroids and enhanced their penetration in the deeper layers of the spheroids, hence promoting the therapeutic efficacy of the drug-loaded nanoparticles.

Résumé

La manipulation précise, rapide et contrôlée d'échantillons biologiques tels que des cellules ou des bioliquides est essentielle pour de nombreux processus et analyses en génie biomédical. Ces dernières années, la technologie "Lab-on-a-Chip" (LoC) a attiré beaucoup d'attention pour la manipulation d'échantillons biologiques, leur caractère miniature leur conférant une haute précision, un excellent contrôle spatial, une consommation minime de réactifs et d'échantillons, un haut potentiel de parallélisation, en plus d'avantages spécifiques à chaque application. Cependant, les lois d'échelle et la dominance des forces de surface et de friction aux micro-échelles nécessitent l'intégration d'actionneurs physiques aux systèmes LoC pour exploiter pleinement leur potentiel pour les applications bioanalytiques.

En particulier, les mécanismes d'actionnement acoustiques se sont démarqués en raison de leur excellente biocompatibilité, de leur polyvalence et de leur usage déjà courant dans le domaine biomédical. Depuis plus de 70 ans, les dispositifs acoustiques ont été intégrés à des centaines d'appareils médicaux pour le dépistage, le diagnostic et le traitement des patients, et ont été courronnés d'un succès clinique massif. L'avancement des technologies de microfabrication a facilité l'intégration de l'actionnement acoustique dans les systèmes LoC et a ainsi permis l'apparition du domaine de l'acoustofluidique. Ces dernières années, l'acoustofluidique a relancé l'usage de méthodes acoustiques dans le domaine biomédical avec le développement de nouvelles méthodes bioanalytiques bénéficiant de phénomènes microscopiques distinctifs, d'une résolution remarquable et d'une grande contrôlabilité.

Par conséquent, l'objectif principal de cette thèse consiste à exploiter les avantages de la miniaturisation et explorer la physique unique de l'acoustofluidique pour introduire de nouveaux outils pour la manipulation d'échantillons biologiques sur puce dans les secteurs des nanothérapies et de la médecine régénérative. Les multiples facettes de ces domaines et de la médecine régénérative exigent que les dispositifs acoustofluidiques puissent effectuer divers tâches. Pour ce faire, nous avons développé des plateformes acoustofluidiques de pointe pour i) synthétiser des nanoparticules comme vecteurs thérapeutiques, ii) former rapidement des sphéroïdes multicellulaires

comme blocs de construction pour l'ingénierie tissulaire et les modèles cellulaires 3D, et iii) administrer la nanothérapie aux sphéroïdes 3D par des forces acoustiques.
Premièrement, nous avons développé un mélangeur acoustique contrôlé par conditions aux limites par la combinaison d'arêtes oscillatoires et de bulles pour induire des microflux contrôlables et un mélange ultra-rapide. Ce faisant, nous visons à introduire une nouvelle méthode de synthèse de nanoparticules à capacité thérapeutique et à relever certains des défis auxquels les systèmes microfluidiques de génération de nanoparticules font face tels que la variation d'un lot à un autre, la dilution à la sortie et le blocage de canaux pendant la nanoprécipitation.

De plus, le dispositif contrôlé par conditions aux limites a été utilisé pour la formation de sphéroïdes cellulaires 3D. Les forces hydrodynamiques acoustiquement induites ont été utilisées pour agglomérer des cellules en grappes compactes en seulement quelques secondes. L'incorporation d'atélocollagène I comme bio-adhésif a transformé les grappes en agrégats stables prêts pour collecte. Cette nouvelle méthode permet de surveiller et de contrôler en temps réel la taille du sphéroïde.

Enfin, nous avons développé une plateforme acoustique à haute fréquence basée sur la technologie des ondes acoustiques de surface pour administrer des nanothérapies aux sphéroïdes en tant que modèles cellulaires 3D. L'application d'ondes acoustiques de haute fréquence permet de sono-imprimer des nanoparticules chargées de médicament sur les sphéroïdes et leur pénétration dans les couches plus profondes des sphéroïdes, améliorant ainsi l'efficacité thérapeutique du médicament chargé.

Acknowledgment

I would like to first express my deepest gratitude to my advisor, Dr. Maryam Tabrizian for her guidance, support, and confidence in me to explore new ideas throughout my Ph.D. Dr. Tabrizian was always present, encouraging, and willing to offer her wisdom and vision for discussing and troubleshooting the ideas, which not only my project greatly benefited from, but also inspired me to grow as a researcher and critical thinker. I would also like to thank my Ph.D. advisory committee, Dr. Christopher Moraes and Dr. David Juncker for their invaluable insights, detailed discussions, and helpful advices during my Ph.D. meetings.

I would also like to thank the staff of the Biomedical Engineering department, especially Pina Sorrini and Sabrina Teoli for always being available and helpful. I am also very grateful to be able to work with the staff of McGill Nanotools Microfab and McGill advanced bioimaging facility and I appreciate their constant guidance during the course of my Ph.D. I would also like to acknowledge the funding resources that made this project possible, particularly the NSERC-CREATE Continuous Flow Science (CFS) program, McGill faculty of medicine excellence award, and FRQNT doctoral fellowship.

I was fortunate to be surrounded by brilliant lab mates who made my Ph.D. journey more enjoyable. I'll start the appreciation with Rafael Castiello who welcomed me to the lab and was always eager to go out of his way to help, my fellow acoustic teammate and friend Karina Martinez Villegas, and Oscar Boyadjian, for helping with the French translation of the abstract. Thanks should also go to Nick DiStasio, Hugo Salmon, Michael Yitayew, Mariam Saad, Alex Paun, Paresa Modarres, and Shiva Naseri whom I had the privilege of collaborating and learning from and other lab members who I enjoyed working with during my Ph.D., including Kaushar Jahan, Saadia Shoaib, James Porter, Selya Amrani, Antoine Karoichan, Celine Agnes, Timothee Baudequin, Laila Benameur, Christian Moya Garcia, Ibukunoluwa Naiyeju, Nicholas Van Der Sanden, and John Nguyen. Thank you all for making the lab a fun place and to create so many beautiful memories inside and outside the lab.

I would like to express my dearest appreciation to my family. To my dad who always believed in me, even and especially when I had reservations, and my sisters, Roxana, Parisa, and Samira who accompanied me on the first day of school and remained supportive ever since! I also want to extend my dearest thanks and love to Shahrzad, I cannot imagine how this Ph.D. could have worked without your love and support. To my mom, my true hero, my savior! You are the best of us, the kindest and warmest person I know, with an ocean of love where I bask in every day. You would always cheer me up before my exams and tell me, you are almost there, well, I think I am really almost there mom and I hope this puts a smile on your face!

Table of Contents

Abstract ii

Résumé iv

Acknowledgment vi

Table of Contents viii

List of Figures xi

List of Tables xvii

List of Abbreviations xviii

Contributions of Authors xix

1 Introduction 1

1.1 Rationale and Objectives 1

1.2 Thesis Outline 5

2 Background knowledge 8

2.1 Lab on a Chip 8

2.2 Actuation Mechanisms for On-chip Manipulation of Bio-species 9

2.2.1 Passive methods of actuation 10

2.2.2 Active methods of actuation 13

3 Acoustofluidic Concepts & Phenomena 18

3.1 Introduction 18

3.2 Physics and Methods of Acoustic Excitation 20

3.3 Bulk Acoustic Waves 21

3.4 Surface Acoustic Waves 22

3.5 Acoustic Phenomena 23

3.5.1 Acoustic phenomena in fluids 24

3.5.2 Acoustic phenomena in particles, droplets, and bubbles 26

4 Recent Advances in Acoustically Driven Biomicrofluidic Devices 31

4.1 Acoustofluidics for Particle Separation and Enrichment 31

4.2 Acoustic Cell Patterning for Tissue Engineering 38

4.2.1 Single pressure node patterning 39

4.2.2 Multiple pressure nodes 40

4.2.3 Acoustofluidics for spheroids formation 42

4.3 Acoustofluidics for Therapeutic Applications 44

4.3.1 Drug development and nanoparticle synthesis 44

4.3.2 Drug delivery 47

4.3.3 Sonoporation 50

4.4 Acoustofluidics as a Functional Force for Investigating Phenotypes in Biological Organisms 55

4.5 Acoustic Biosensing 61
4.5.1 Acoustic biosensing for cells detection and quantification 62
4.5.2 DNA detection 64
4.5.3 Protein detection and quantification 64
4.5.4 Exosomes and virus detection 65
4.5.5 Acoustic waves for enhancing sensitivity limitations 67
5 An Ultra-Rapid Acoustic Micromixer for Synthesis of Organic Nanoparticles 71
5.1 Abstract 72
5.2 Introduction 73
5.3 Mixing Concept and Mechanism 75
5.4 Results and Discussion 77
5.4.1 Comparing the microstream patterns of sharp edges, bubbles, and the combined unit 78
5.4.2 Mixing assessment 81
5.4.3 Effect of frequency on mixing performance 81
5.4.4 Effect of voltage on mixing performance 82
5.4.5 Effect of flow rate on mixing performance 83
5.4.6 Nanoparticle synthesis 85
5.5 Conclusion 90
5.6 Material and Methods 91
5.6.1 Materials 91
5.6.2 Device fabrication 92
5.6.3 Experiment setup 92
5.6.4 Nanoparticle synthesis and characterization 93
5.7 Supporting Information 94
5.7.1 Bubble trapping 94
5.7.2 Impedance analysis 94
5.7.3 Mixing analysis 95
5.7.4 Mixing index 96
5.7.5 Variation in voltage 98
5.7.6 Variation in flow rate 98
5.7.7 Nanoparticle size distribution 99
6 Rapid Formation of Multicellular Spheroids in Boundary-Driven Acoustic Microstreams 101
6.1 Abstract 102
6.2 Introduction 103
6.3 Results and Discussion 106
6.3.1 Working mechanism of acoustic cell trapping 106
6.3.2 Cell-cell adhesion-promoting materials for acoustic spheroid formation 110
6.3.3 Acoustic assembly using collagen I matrix 112
6.3.4 Retrieving the spheroids 116
6.3.5 Spheroid culture and analysis of cell survival/functionality 117
6.3.6 Features of spheroid formation in acoustic microstreams 120
6.4 Conclusion 123
6.5 Material and Method 124
6.5.1 Materials: 124
6.5.2 Device fabrication and setup 125
6.5.3 Impedance Measurement 125

6.5.4 Cell culture....125
6.5.5 Collagen-MC mixture preparation....126
6.5.6 Acoustic spheroid formation....126
6.5.7 Low surface adhesion coating....127
6.5.8 Live/Dead Cell Evaluation....127
6.5.9 Immunostaining. 127
6.5.10 Cell tracking and counting....128
6.6 Supporting Information 129
6.6.1 Over crosslinked collagen solution not showing formability:....129
6.6.2 Impedance analysis of collagen at different concentrations over time: 130
6.6.3 Spheroid culture in Media vs Media+ 1% Methylcellulose 131
6.6.4 MDA-MB-231 spheroids formation in shaking plate....131
7 Sonoprinting Nanoparticles on Cellular Spheroids via Surface Acoustic Waves for Enhanced Nanotherapeutics Delivery 133
7.1 Abstract 134
7.2 Introduction....135
7.3 Results and Discussion 138
7.3.1 Working mechanism of the acoustic platform 138
7.3.2 Optimization of operating parameters for the SAW platform....140
7.3.3 Cell spheroids' exposure to SAW does not affect the cell viability....143
7.3.4 SAW increases the delivery of NPs into the core of cell spheroids....146
7.3.5 SAW increases the efficacy of anticancer drug nanoliposome delivery into spheroids 150
7.4 Conclusion....154
7.5 Materials and Methods....155
7.5.1 Materials 155
7.5.2 Device fabrication and setup 155
7.5.3 Cell culture....156
7.5.4 Spheroid formation....156
7.5.5 NP transport assay in spheroids 156
7.5.6 Live/Dead Cell evaluation....157
7.5.7 Sample preparations for imaging 158
7.5.8 Image analysis 158
7.5.9 Liposomal CuET synthesis 158
7.5.10 RNA isolation and RT-qPCR 159
7.5.11 Statistical analysis....159
7.6 Supporting Information 160
7.6.1 Characterization of liposomal CuET nanoparticles:....160
7.6.2 Delta Ct values of RT-qPCR experiments of different treatment groups in YUMM 1.7 spheroids normalized to GAPDH....161
7.6.3 Toxicity analysis of LP-CuET for both cell types 162
8 Contributions to Original Knowledge....164
9 General Discussion & Conclusion....168
10 Limitations & Future Perspective....174
10.1 Limitations and Proposed Mitigations....174
10.2 Future Research Trends....175

List of Figures

Figure 2.1. A) Structure of staggered herringbone ridges to manipulate the flow field for better mixing and [16] the flow pattern after passing upon multiple herringbone cycles.[17] **B)** An array of bumper posts embedded in the microchannel as a passive way of particle separation based on size and deformability.[26] **C)** Inertial microfluidic platforms using spiral microchannel and combination of inertia and micro-obstacles for particle separations[36]. **D)** Droplet microfluidic settings shwing flow focusing droplet generation mechanism [44] ii) Droplet microfluidics for production of Cell-laden hydrogel microcapsules [41]and iii) multicomponent emulsions with three levels of emulsification to encapsulate controlled number of droplets within droplets. [42] 12
Figure 2.2. Illustrations of active actuation mechanisms **A)** The use of magnetic fields for levitations of cells into 3D cellular blocks, and particle and cell separation by bead labelling and negative magnetophoresis respectively. [51] **B)** The concepts of electric actuation methods including dielectrophoresis for particle manipulation, AC electroosmosis flow motion, and AC electrothermal flow respectivley.[58] **C)** The schematic of an optical tweezer where a highly focused light can manipulate small particles by balance of radiation pressure and gradient forces. [444] **D)** An acoustofluidic platform for the manipulation of particles and fluids. The interplay of various acoustic forces and phenomena can be used to control both particles and flow trajectory. [70] .. 17
Figure 3.1. Schematic and classification of frequently used acoustofluidic technologies for bio-applications. BAWs and SAWs can both be used as tweezers for manipulation of bio-samples and also as biosensors. Transversal and layered BAW settings are commonly used in acoustic tweezers while shear thickness has wide application in sensors such as Quartz crystal microbalance. SAW waves types includes Rayleigh (Leaky) wave which are preferred as tweezers, as well as SH-SAW and Love SAW which are exploited as sensitive biosensors. 21
Figure 3.2. Acoustic principles for manipulation of fluids and particles. For particle manipulation, acoustic radiation forces, secondary Bjerknes force, and drag forces are frequently exploited. For fluid manipulation boundary-layer streams, Eckart streams, fluid switch and nebulization are the common approaches. 25
Figure 4.1: Acoustic cell acoustophoresis mechanisms. **A)** bigger particles experience stronger ARF in standing waves and can move faster to the pressure node **B)** tilted standing waves to increase the separation path of bigger particles. **C)** Separation by acoustic phase contrast. Particles with positive acoustic contrast move to pressure node while particles with negative acoustic contrast move to pressure antinodes. **D)** Traveling acoustic wave separate bigger particles to the direction of wave propagation. **E)** acoustic streams trap or deflect the path of bigger particles closer to the vortex source while smaller particle can pass with less deflection. 32
Figure 4.2. Acoustophoresis mechanisms for separation, isolation, and enrichment of particles. **A)** double stage acoustic system using SSAW for alignment and TSAW for separation, [129] **B)** E) particle separation by microstreams from oscillatory bubbles, [132] **C)** Particle separation by microstreams from focused TSAW.[130] **D)** Exosome enrichment by Bjerknes forces.[143] Reprinted with permission. 36

Figure 4.3. Acoustic cell patterning for tissue engineering. **A)** Myoblasts patterning using BAWs with controlled gelation showing pattern preservation over time (Scale bar =200μm).[156] **B)** Microvessels in hindlimb muscle via SSAW patterning of HUVECs and hADSCs at different HUVEC/hADSC ratios (1:0, 5:1, 2:1) (Scale bar =100 μm).[157] **C)** SSAW-patterned fibroblasts in fibrin gels with multiple 3D microscale cellular structures forming network (left), cages (center), and unidirectional bundles (right) after 30 hours.[176] 42
Figure 4.4. Cell spheroid formation methods using acoustofluidics. **A)** Ultrasound trapping platform for spheroid formation after 48 h using a protein repellent coating (Microwell is 350 μm wide).[183] **B)** Acoustic assembly showing multicellular aggregates encapsulated in the ECM mimic hydrogel pillars (left, top right) and convection-diffusion based gradient drug fluid generating microfluidic system at different drug environments (bottom right).[189] **C)** SSAW-based spheroid formation platform consisting of a polyethylene tube coupled to a parallel IDT setup with a water-coupling layer (left), where cells seeded in a cross-linkable hydrogel are patterned and UV crosslinked (right).[166] **D)** Acoustic streaming-based cell agglomeration platform consisting of a fluid coupling layer (left) to transmit acoustic waves to a 24-well plate (right) (Scale bar=30 mm).[193] 43
Figure 4.5. Mechanism of nanoparticle synthesis using acoustic waves **A)** acoustic microstreams induced by multiple edges system used for synthesis of Budesonide nanodrugs and DNA nanoparticles.[197] **B)** SAW nebulization device for synthesis of multilayer nanocarriers with encapsulated plasmid DNA.[200] **C)** SAW nebulization device with a gas control unit which introduces reactive gases to atomized airborne drops for synthesis of amorphous $CaCO_3$ nanoparticles.[209] Reprinted with permission. 46
Figure 4.6. Acoustic devices for drug delivery. **A)** Acoustic nebulization for pulmonary drug delivery of aeorosols.[212] **B)** Acoustic nebulization for pulmonary plasmid delivery.[204] **C)** Stem cell delivery by acoustic nebulization. [213] **D)** Acoustic waves for permeabilization of tissue and inducing localized immune response.[214] 49
Figure 4.7. Acoustic platfroms for sonoporation and gene delivery to cells and tissue. **A)** Sonoporation by acoustic steams from an array of oscillatory bubbles.[223] **B)** combination of acoustic microstreams by bubbles and electroporation for gene delivery.[224] **C)** BAW-based microfluidic device for high-throughput shear stress-sonoporation by combination of microstreaming and acoustic radiation forces that push cells towards opposite capillary walls.[226] **D)** high frequency bulk-based nano-electromechanical device for delivery of eGFP plasmid DNA and doxorubicin through hypersonic membrane poration and acoustic streaming.[228] **E)**Focused TSAW for delivering siRNA into nonadherent cells.[231] 52
Figure 4.8. Acoustic settings to investigate the effect of the wave as functional mechanical stimuli on **A)** Cell's viability, morphology, metabolic activity and proliferation,[235] **B)** cell migration pattern and wound-healing properties,[239] **C)** neuromodulation and stimulation of neurons,[246,249] and finally **D)** the effect of acoustic waves on sensory neurons of C. elegans which induced short-term memory loss and brain injury.[81] 59
Figure 4.9: Acoustic waves as biosensors for **A)** ssDNA detection, **B)** cell detection and quantification, **C)** cell morphology characterization, **D)** bacteria detection, **D)** protein detection, and **E)** virus or exosome detection..... 62

Figure 4.10. Acoustic settings for various biosensing strategies. **A)** Embedded microcavities on a SAW platform to characterize the single-cell stiffness,[260] **B)** a conformable SAW immunosensor for the detection of E. coli bacteria,[261] **C)** Integrated LoC device that can capture, lyse, and detect bacteria in separate modules for rapid detection of foodborne pathogens,[264] **D)** a SAW sensor with three-fold pathline for sensitive detection of cardiac disease biomarker,[266]and **E)** Protein detection platform using imprinted polymer as synthetic probe.[267] Reprinted with permission..... 66
Figure 4.11. Acoustic waves for improving sensitivity and removing biofouling A)[275] and **B)** [276] integration of SAW mixers with SPR sensing systems to enhance the binding kinetics **C)** The hydrodynamic forces from acoustic microvortices used to wash off the loosely surface-bound non-specific proteins.[278] **D)** SAW used for both enhancing the mixing and removing NSB protein bindings, showing significantly better performance over chemical rinsing.[279] 69
Figure 5.1 A) Conceptual illustration of the acoustic streaming and the resultant mixing used for self-assembly of nanoparticles. **B)** Rendered picture of the acoustic platform. The piezoelectric transducer is embedded next to the PDMS part, emitting acoustic pressure waves. **C)** Schematic drawing of the combined unit. Slanted sharp-edges allow the bubble to be trapped. **D)** Fluorescent polystyrene particles (2-micron diameter) behavior in the presence of acoustic field. The closed-circular pathline of microparticles shows complete coverage of channel width. 77
Figure 5.2. A) Microstreaming comparison with and without bubble. The left structure is filled with the particle solution and shows limited streaming of sharp edge structure while the combined unit on the right of the picture with bubble ($r_e \approx 98$ μm) induces strong microstreams which span through the channel width. **B)** The microstreaming pattern of the bubbles of different sizes ($r_e \approx 65$-100 μm) which are trapped between PDMS bars in the absence of sharp-edges. The microstream intensity is comparable to those of the sharp-edges without bubble and considerably weaker than the combined unit. **C)** Characterization of mixing performance in each of the design at the excitation voltage of 15 V_{PP}. 80
Figure 5.3. Sonogram of three Piezoelectric transducers **A)** Radioshack, **B)** Thorlabs and **C)** STEMiNC and mixing index (MI) for their corresponding platforms. For each piezoelectric system, the highest mixing index appears at the proximity of its resonance frequency, confirming the dominant effect of electro-mechanical resonance (the mixing index is average of two repetitions)..... 82
Figure 5.4. A) The mixing performance in the presence of acoustic mixing at the input voltage of 14 V_{PP} and flow rate of 18 μL/min. **B)** The minimum length required to reach mixing threshold (normalized concentration of 0.6, i.e. MI = 0.8). **C)** The relation between input voltage and flow rate to reach the adequate mixing threshold in the designated mixing length (25.2 μm) 84
Figure 5.5 A) Schematic of PLGA-PEG nanoparticle synthesis. **B)** Schematic of liposome synthesis. Size variation of **C)** PLGA-PEG nanoparticle and **D)** Liposomes synthesized in the acoustic platform by changing the mixing time through total flow rate and comparison with hydrodynamic flow focusing method for three different concentration of precursors. **E)** I. TEM image of PLGA-PEG nanoparticles. II. Size and size distribution as measured by DLS. **F)** I. TEM image of nanoliposomes by negative staining. II. Size and size distribution as measured by DLS. 88

Figure 5.6. **A)** Nanoliposomes concentration synthesized in the acoustic and HFF platforms for three different concentration of precursors. **B)** NTA video frame of liposomes produced in HFF method with Average 4.6 $\pm$ 0.4 particles per frame with a dilution factor of 200. **C)** NTA video frame of liposomes produced in acoustic micromixer with Average 23.3 $\pm$ 2.1 particles per frame with a dilution factor of 200. 90
Figure S 5.1. The channels are initially empty which means there is only air in them. When an aqueous liquid gets infused to the channel, it fills all the channel except for the sequestered volume between the slanted sharp-edges due to the surface tension, leaving a trapped bubble. 94
Figure S 5.2. Sonogram of impedance and phase for piezoelectric transducer model no. 273-073, Radioshack. The resonance frequency is in line with reported optimum frequency for mixing index. 95
Figure S 5.3. The concentration distribution of fluorescein and DI water in the A) absence and B) presence of acoustic mixing. 96
Figure S 5.4. Concentration profile across the channel width before and after mixing by acoustic microstreams. 97
Figure S 5.5. Mixing performance by changing the input voltage at the flow rate of 18 μL/m. 98
Figure S 5.6. Mixing performance by changing the flow rate at the input voltage of 10 V_{PP}. 98
Figure S 5.7. Size distribution of PLGA-PEG nanoparticles with precursor concentration of **A)** 1.25 mg/ml, B) 2.5 mg/ml and **C)** 5 mg/ml measured by DLS. Size distribution of Liposomes with precursor concentration of **D)** 0.5 mg/ml, **E)** 1 mg/ml and **F)** 2 mg/ml measured by DLS. 99
Figure 6.1. A) Rendered image of the acoustic platform. Upon activation by a function generator, the acoustic waves generated by the piezoelectric transducer creates boundary-driven microstreams in the microfluidic channel which can trap cells. **B)** Depicts the correlation of input voltage and flow rate for tapping cells. **C)** and **D)** Show the viability of cells after exposure to the acoustic field with different input voltages. Scale bar: 200 μm. 109
Figure 6.2. **A)** Conceptual illustration of acoustic spheroid formation mechanism by collagen assembly. Cells encompassed by collagen fibrils are infused in the microfluidic channel toward the boundary-driven acoustic streams, whereby they are trapped and reshaped into spheroids. **B)** Window of operation at different collagen concentrations showing the period the cell-collagen solution maintains its homogenous fluidity and adhesivity for acoustic assembly. **C)** Acoustic spheroid formation process in the device over time. Scale bar: 500 μm. **D)** Close up of a spheroid after acoustic assembly, showing the cells are enveloped by collagen, scale bar: 100 μm. 115
Figure 6.3. Long-term culture of **A)** MDA-MB 231 and MCF-7 cell spheroids. Pictures acquired by bright field microscopy showing the evolution of the morphology and size of spheroids from 1h after acoustic formation to day 5. The individual cell profiles become less discernible as spheroids develop and secret their ECM proteins. The diameter development of **B)** MDA-MB-231 and MCF-7 over 5 days showing an initial decrease in size during the first day, followed by gradual growth ($n \geq 15$). **C)** 3D reconstruction of a spheroid. **D)** The cross-sections of spheroids acquired by confocal

microscopy and stained with Hoechst (blue), Alexa Fluor 594 phalloidin (yellow), and E-cadherin (green) for MDA-MB-231 and MCF-7. Scale bar: 100 μm. 118
Figure 6.4. Cell Viability in acoustically formed spheroids. **A)** MDA-MB-231 and **B)** MCF-7 spheroids were stained with green Calcein AM for live cells, red ethidium homodimer III for dead cells, and Hoechst 33342 for nuclei. **C)** and **D)** show the cell number and the percentages of viable cells in the spheroids in 12 hrs., Day 3 and Day 7. Scale bar: 100 μm. The bar shows mean+SD. 120
Figure 6.5. **A)** The multicellular spheroids of MCF-7 cells stained with Green CellTracker™ CMFDA and MDA-MB-231 cells stained with Deep Red Fluorescence – Cytopainter. Nuclei of both cell types were stained with Hoechst 33342. **B)** Hybrid Cell particle spheroids. MDA-MB-231 (blue) and green fluorescent PS particles (5 um) were mixed in collagen solution and assembled in acoustic microstreams to form cell-particle spheroids. **C)** spheroids of MCF-7 cells (Green) and MDA-MB-231 (red) merged after 24 hrs. Scale bar: 150 μm. 122
Figure S 6.1. Collagen solution after reaching the time window shows stiffer cell-collagen fiber network that is not formable by acoustic streams. 129
Figure S 6.2. A) Collagen concentration: 2.5mg/ml. **B)** 1.25mg/ml. **C)** 0.75mg/ml. **D)** 0.5mg/ml. **E)** 0.42mg/ml. 130
Figure S 6.3. Acoustically formed Spheroids incubated in **A)** Media and **B)** Media +1% MC. The spheroids in media alone tend to merge to each other while addition of MC could help to maintain them as individual spheroids. 131
Figure S 6.4. MDA-MB-231 spheroids formed by shaking plate method after 7 days. In this method, in contrast to acoustic methods, the formed aggregates were more fragile and surrounded by numerous floating singles cells. 131
Figure 7.1. A) Rendered image of the SAW platform including a piezoelectric substrate with focused interdigitated transducers (FIDT) and a glass-bottom Petri-dish. Upon activation by the function generator, the surface acoustic waves generated by IDTs travel on the substrate surface and leak into the Petri-dish through the coupling layer (water). **B)** Inside the Petri-dish, acoustic waves propel the media and create acoustic streams which bring the nanoparticles and spheroids in the center of the microstreams to increase the NP uptake. **C)** Comparison of acoustic microstream intensity produced by straight and focused IDTs. **D)** Demonstration of Eckart microstreams' formation in the presence of SAW by using fluorescent polystyrene microparticles. **E)** Suspension of cellular spheroids and microparticles. Upon activation of SAW, spheroids attract the microparticles and increase their concentration in their vicinity. The scale bars are 500 μm. Data is plotted as mean + SD. 141
Figure 7.2. A) The morphological characterization of MCF 7 and YUMM 1.7 spheroids, including the diameter, roundness, and optical intensity. The cell viability in the **B)** YUMM 1.7 spheroids and **C)** MCF 7 spheroids after different exposure times to 10 V_{PP} SAW. Spheroids were stained with green Calcein AM for live cells, orange ethidium homodimer III for dead cells, and Hoechst 33342 for nuclei. The figures show the maximum projection of the planes at a Z distance of 10 μm, acquired by high-resolution confocal microscopy. Scale bar is 200 μm. The quantification of cell viability is performed using the Harmony 4.9 software for **D)** YUMM 1.7 and **E)** MCF 7. Data is plotted as mean + SD. 144
Figure 7.3. A) Overview of the SAW-mediated sonoprinting experiments and analysis. Accumulation of the 100 nm polystyrene nanoparticles (orange) on spheroids of **B)**

YUMM 1.7 and **C)** MCF 7 cells in the presence (SAW) and absence (NSAW) of acoustic waves with different exposure times. The cells' nuclei were stained with blue Hoechst 33342. The figures show the maximum projection of the planes acquired by water-immersed, high-resolution confocal microscopy. Scale bar is 200 μm. The fluorescent intensity of the nanoparticles was measured and quantified in graph **D)** for YUMM 1.7 and **E)** for MCF 7. Data is plotted as mean + SD. 147
Figure 7.4. A) The experiment sketch for the nanoparticle transport assay, deep confocal microscopy, and zone analysis of spheroids. After the transport assay, the spheroids are fixed and cleared. The mid cross-section of spheroids are imaged and divided into two zones of total and core zones delineated by white boundaries. The distribution of the 100 nm polystyrene nanoparticles (red) after different chase times, in the spheroids of **B)** YUMM 1.7 and **C)** MCF 7 spheroids with (SAW) and without (NSAW) acoustic waves. The figures show the mid cross-section of the spheroids in red channel for nanoparticles (top) and cyan channel for cells' nuclei stained with Hoechst 33342 (bottom) acquired by water-immersed confocal microscopy. In the Cyan channel, the outer line shows the boundary of the spheroids defined by the nuclei, and the inner line (the same line in red channel) shows the core zone of the spheroids with a 30 μm margin from the spheroid's boundary. Scale bar is 200 μm. **D)** and **E)** show the intensity of the nanoparticles penetrated to the core region for YUMM 1.7 and MCF 7 cells respectively, quantified by image analysis of spheroids' cross-sections. Data plotted as mean + SD. 150
Figure 7.5. A) The anticancer activity of liposomal CuET nanoparticles with different concentrations, with and without acoustic waves. The dead cells are stained by orange ethidium homodimer III, while blue Hoechst 33342 shows the nuclei of total cells. More dissociated cells and less compact structure are observable with the exposure of SAW, especially at higher concentration. The figures are the maximum projection of confocal planes, and the scale bar is 200 μm. **B)** and **C)** show the percentage of dead cells over total number of cells for YUMM 1.7 and MCF 7 spheroids, respectively. Data is plotted as mean + SD. **D)** and **E)** RT-qPCR results of CD90 and HSP70 genes with YUMM 1.7 cell spheroids exposed to 10 min SAW alone (SAW), 10 μM of LP-CuET NPs, and the combination of SAW and LP-CuET NPs for 10 min. The results are normalized to NSAW, and the data is plotted as mean ± SD, and the statistical analysis is performed using ΔCt values (Figures S7.3). 153
Figure S 7.1. Nanoparticle tracking analysis of LP-CuET, Showing the size and size distribution **A)** averaged concentration / size for experiments, **B)** intensity / size graph. 160
Figure S 7.2. Delta Ct values of RT-qPCR experiments of different treatment groups in YUMM 1.7 spheroids normalized to GAPDH **A)** CD90 **B)** HSP70. 161
Figure S 7.3. A) Representative IC50 curve of an individual experiment for MCF7 treated with LP-CuET. **B)** Representative IC50 curve of an individual experiment for YUMM 1.7 treated with LP-CuET **C).** IC50 difference between MCF 7 and YUMM 1.7 showing increased sensitivity of MCF 7 cells to LP-CuET. Student's t-test with Welch's correction of 3 individual experiments (n=3) derived from the previous curves in **A)** and **B)**..... 162

List of Tables

Table 4-1 Acoustophoresis for particle manipulation 37
Table 4-2 Acoustically mediated therapeutics delivery 54
Table 4-3 Acoustic waves as functional stimuli 60
Table 4-4 Biosensing modes using surface acoustic waves 67
Table 6-1 Media and materials tested for acoustic spheroid assembly and their performance in three criteria of adhesion: rapid and robust adhesion of cells together, retrievability: no attachment to the channel, and formability of cell aggregates into spherical structures. 111

List of Abbreviations

2D	Two dimensional
3D	Three dimensional
AC	Alternating current
ARF	Acoustic radiation force
ASF	Acoustic streaming force
BAW	Bulk acoustic wave
DLS	Dynamic light scattering
DNA	Deoxyribonucleic acid
ECM	Extracellular matrix
EV	Extracellular vesicle
ELISA	Enzyme-linked immunosorbent assay
FIDT	Focused Interdigitated transducer
FRR	Flow rate ratio
GFP	Green fluorescent protein
IDT	Interdigitated transducer
LoC	Lab on a Chip
MC	Methylcellulose
MEMS	micro-electromechanical system
mRNA	Messenger RNA
NP	Nanoparticle
NTA	Nanoparticle tracking analysis
PLGA	Poly (lactic-co-glycolic acid)
PEG	Poly (ethylene glycol)
PLL	Poly(L-lysine)
PCR	Polymerase chain reaction
PoC	Point of care
RF	Radio Frequency
RBC	Red blood cell
RNA	Ribonucleic acid
RT-PCR	Reverse transcription polymerase chain reaction
SAW	Surface acoustic wave
SBAW	Standing Bulk acoustic wave
SPR	Surface plasmon resonance
SSAW	Standing Surface acoustic wave
TEM	Transmission electron microscopy
TFR	Total flow rate
TSAW	Traveling Surface acoustic wave

Contributions of Authors

This thesis is presented as a collection of three original manuscripts and a review paper written by the candidate, with the assistance and guidance of the supervisor and co-authors. The candidate conceptualized the acoustic platforms, developed the methodologies, conducted the experiments and characterizations, and performed data collection and analysis. Maryam Tabrizian appears in the publications for her guidance and supervisory role throughout the project and for her input in developing workflow and her contribution to the manuscripts' preparation. Ms. Karina Martinez Villegas contributed to the writing, organizing, and preparation of the tables in the review publication presented in Chapters 3 and 4. Mr. Radu Alexandru Paun appears as a co-author in the third original research publication (Chapter 7) for conducting the PCR experiments and analysis, synthesizing the liposomal CuET nanoparticles, and contributing to the manuscript preparation.

1 Introduction

1.1 Rationale and Objectives

Acoustofluidics, the merging science of acoustics, fluid mechanics, and micro/nanotechnology, has proven to be a powerful tool for on-chip handling of particles and fluids, owing to its ability to integrate with other microfluidic modules, easy controllability of acoustic forces, and high precision.[1–3] In the biomedical field, the non-contact, non-invasive, and label-free nature of acoustofluidic platforms is employed in an extended range of applications from separation and trapping of bioparticles to therapeutics development and tissue engineering.[3–5]

The acoustofluidics' ability in generating controllable forces for manipulating biofluids and particles, to our hypothesis, can offer unique venues to address some of the fundamental challenges in nanotherapeutics and regenerative medicine. Hence, in this thesis we aim to employ and expand these capacities by introducing acoustofluidic systems as novel means for i) synthesizing organic nanoparticles as therapeutics carriers, ii) rapid formation of spheroids as 3D cellular models and tissue engineering building blocks, and iii) delivering nanotherapeutics to the 3D spheroids as pseudo-tumor models. The rationale, hypotheses, and steps of each objective are discussed subsequently.

Objective 1: Design & fabrication of a rapid acoustic micromixer for the synthesis of organic nanoparticles.

In the first part of the project, we aimed to develop an acoustic platform with rapid mixing capacity and employ the platform as a nanoparticle synthesis unit. Organic nanoparticles have been widely explored as a revolutionary mechanism of drug delivery to reduce the off-target toxicity and immune response by protecting the cargo while transporting high payloads of the active agents and inducing controlled release.[6] Advances in microfluidics have shown the potential to accelerate nanoparticle transition to clinical application by improving the nanoparticle synthesis process in a confined and controlled domain.[7] One of the key steps in nanoparticle synthesis is the mixing, where the quality and time of mixing directly determine the ultimate size and polydispersity of the nanoparticles, as two of the most influential parameters in determining their fate in the body after administration.[8] Therefore, micromixers are widely exploited in microfluidic set-ups for nanoparticle production, for instance, Tesla micromixer [9] and herringbone micromixer.[10] However, these microfluidic nanoparticle generation systems still face issues such as dilution of output[7] and the clogging of channels during nanoprecipitation.[8] We intended to address some of these challenges in nanoparticle synthesis by designing and manufacturing an ultra-rapid acoustic mixer to generate strong boundary-driven acoustic microstreams. We hypothesized that these strong acoustic microstreams can rapidly disrupt the laminar flow in the microfluidic chamber and enable us to control the nanoparticle synthesis process and nanoparticle size while addressing the output dilution and clogging. To verify this hypothesis, a set of sub-objectives were defined including:

- Design and development of a novel acoustic-based microfluidic platform with rapid mixing capacity through the combination of oscillatory sharp edges and bubbles.
- Characterization of the microstream intensity with different designs and analysis of the optimum frequency.

- Validation of the platform's functionality through the synthesis of polymeric NPs and liposomes.
- Controlling the nanoparticle size and size distribution via tuning the mixing time and enhancing the nanoparticle output concentration.

Objective 2: Rapid formation of cellular spheroids in boundary-driven acoustic microstreams.

Three-dimensional spheroids are the focus of many studies as faithful models for recapitulating the cells' growth environment and native architecture of tissues, both for drug screening applications and as building blocks in regenerative medicine.[11] Many of the spheroid generation methods primarily focus on the physical arrangement of cells, as the first stage of spheroid formation to promote cell-cell contact by applying different forces. U-traps and microwells are some of the most widely employed methods to aggregate cells and form clusters by gravity or hydrodynamic forces. Recently, other methods such as magnetic forces,[12] surface acoustic wave (SAW),[13] and dielectrophoresis are used to produce cell clusters. However, these methods rely on cells and their capacity to gradually secrete adhesive and matrix proteins for transforming loose cell clusters into coherent spheroids. Therefore, these spheroid formation processes can become very time-consuming, while their success in forming mechanically stable spheroids is often cell-type dependent.[14] We, therefore, aimed to develop a continuous flow and on-chip method for rapid spheroid formation to address some of the aforementioned challenges. We speculated that the locally controllable acoustic microstreams not only can trap and aggregate cells as the first step in the spheroid formation, but also allow for the incorporation of bioadhesives to accelerate the formation of coherent spheroids and reduce cell-type dependency. Therefore, the sub-objectives for the second part of the thesis include:

- Exploring the ability of the localized acoustic boundary-driven microstreams to accelerate the physical aggregation of cells in the acoustic microstreams as the first step in spheroid formation.

- Investigating the compatibility of a small library of materials with the acoustic technique to ensure rapid attachment of cells under acoustic waves and the formation of mechanically stable spheroids.
- Validating the functionality of the acoustic platform for the rapid and continuous formation of spheroids without off-chip processes.
- Testing the versatility of the acoustic platform through the formation of multicellular spheroids, cell-particle composite spheroids, and spheroids as building blocks for tissue engineering.

Objective 3: Sonoprinting nanoparticles on cellular spheroids via surface acoustic waves for enhanced nanotherapeutics delivery.

In the first two objectives, acoustic waves are employed for the synthesize of drug nanocarriers and to form 3D spheroids. To fully explore the capacity of the acoustic waves in nanotherapeutics development, in the third part we aimed to use acoustic waves as means for delivery of drug-loaded nanoparticles to 3D spheroids as pseudo-tumor models.

Drug delivery to 3D spheroids and solid tumors is often hindered by physicochemical barriers that limit the penetration of nanocarriers into deeper layers of tissue, preventing the efficient delivery of drug cargo. Hence, it is one of the main challenges in nano-based drug development.[15] To address this challenge, different mechanisms are proposed which include the strategies focusing on the characteristic of the nanoparticle themselves to facilitate the diffusion into tumors, or the strategies for controlling the target tissue microenvironment.[16] We sought to propose a method for the active delivery of nanoparticles into spheroids and pseudo-tumors via developing a high-frequency surface acoustic wave (SAW) platform as a biocompatible external force. Our hypothesis was that by inducing acoustic phenomena such as Eckart microstreams and interparticle Bjerknes forces, the delivery efficiency of nanoparticle and nanotherapeutics to 3D spheroids can be boosted, leading to enhanced therapeutic efficacy. Therefore, five sub-objectives were defined including:

- Developing a SAW platform with the capacity to emanate and efficiently transport focused traveling surface acoustic waves to the spheroids-nanoparticle mixture.
- Optimizing the acoustic setting and design to generate vigorous acoustic microstreams and Bjerknes forces for delivering nanoparticles and nanotherapeutics to 3D spheroids.
- Investigating the capacity of the SAW platform in sonoprinting NPs onto the spheroids.
- Characterizing the effect of SAW on the spatiotemporal distribution of nanoparticles inside the spheroids.
- Assessing the efficiency of the acoustic-mediated nanotherapeutic delivery method by analyzing the cytotoxic performance of anti-cancer drug-loaded nanoparticles in cell spheroids used as pseudo-tumor models.

1.2 Thesis Outline

This thesis is composed of three main sections including 1) The background knowledge, physical concepts, and literature review of the recent advances in acoustofluidic systems for biomedical applications, 2) the original contributions to developing acoustic devices for nanoparticle synthesis, spheroids formation, and acoustically mediated nanoparticle delivery to the spheroids, and 3) general discussions and conclusion along with outlining the limitations and future perspectives of the studies presented in this thesis and acoustofluidics technology on a broader scope to develop protocols and tools for applications in biomedical sciences. Each section embeds chapters to form this dissertation as outlined below:

Chapter 1 is the current chapter that includes the general introduction, the rationales, hypotheses, and objectives along with the thesis outline.

Chapter 2 begins with a brief introduction to the lab on a chip technology, the scaling-down effects of miniaturization, and the functionalities that it offers, particularly for the

manipulation of bio-particles and bio-fluids. An overview of the LoC operation mechanisms pertinent to the manipulation of bio-species is presented, including the passive and active methods.

Chapter 3 highlights the fundamental concepts and main working mechanisms of acoustofluidic devices for the formation of waves, the wave transfer methods to the region of interest, and the manifestation of the acoustic waves in the target region. Two categories of acoustic devices, based on bulk acoustic waves and surface acoustic waves as well as acoustic phenomena generated by each category such as primary and secondary acoustic radiation forces, and acoustic streaming are then described.

Chapter 4 is a state-of-the-art literature review submitted to *Lab on Chip*. This chapter provides a comprehensive overview of the recent biomedical applications of the acoustofluidic phenomena described in chapter 3. The use of acoustic forces for bioparticle manipulation and fluid handling through various platforms and their application in cell separation and sorting, nanoparticle enrichment, cell analyses, therapeutics development, tissue engineering, and biosensing are discussed.

Chapter 5 is the first original contribution, published in the *Lab on Chip*. In this study, we introduced the application of the boundary-driven acoustic platform for the fabrication of organic nanoparticles through controlling the mixing process. The chapter describes the rationale behind the design of the platform followed by the characterization of the boundary-driven microstreams for rapid mixing. The performance of the device was then validated for the synthesis of PLGA-PEG nanoparticles and liposomes with high yield and control over the NPs size.

Chapter 6 reports on the second original contribution towards the application of the boundary-driven acoustic platform for the rapid formation of spheroids, published in *Small* in 2021. In this chapter, we covered the methods of spheroid formation, with an emphasis on the state-of-the-art microfluidic platforms, their potential, and shortcomings. The mechanism of the acoustic platform for spheroid formation is then introduced for addressing some of the current challenges in spheroid formation. We

then demonstrated the capacity of the platform in producing multicellular spheroids, composites spheroids, and spheroids as tissue engineering building blocks.

In **Chapter 7**, a high-frequency SAW device is introduced for enhancing nanoparticle accumulation and penetration in spheroids, as the third original contribution of this thesis, under review in the journal of *Lab on chip*. The chapter describes the design and fabrication of the surface acoustic wave platform and the induction of acoustic phenomena such as acoustic microstreaming and Bjerknes forces for sonoprinting nanoparticles onto the spheroids. The performance of the SAW platform as means for nanotherapeutic delivery was further analyzed by delivering anti-cancer drug-loaded nanoliposomes to Pseudo tumor models.

Chapter 8 summarizes the contributions of this project to the original knowledge and its outcomes.

Chapter 9 presents the general discussion wherein the main findings of each objective are discussed along with the concluding remarks.

Chapter 10 discusses the limitations of the present study followed by opportunities and future perspectives that would expand the potential of this project as well as acoustofluidic technology beyond this project as a new paradigm for biomedical sciences.

2 Background knowledge

2.1 Lab on a Chip

The rapid development of micro-electromechanical systems (MEMS) in the past few decades sparked the idea of miniaturizing laboratory sets onto small chips, leading to the promising field of Lab on a Chip. The two prominent goals of LoC technology are to recreate the conventional laboratory procedures in compact platforms and to employ the distinct physics that are dominant in the micro realm for introducing novel bioanalytical methods and tools.

Through miniaturization, the lab modules can be compacted into one portable platform, with significantly lower volumes of samples and reagents consumption. Moreover, the parallelization and automation capacities of the LoC devices allow multiplexing the experiments to reduce both the time and cost of assays. Additionally, the inherent confined and controllable experimental domains of LoC devices lend themselves to high precision and high sensitivity methods, particularly for the detection and diagnosis applications. This precision and controllability coupled with the abovementioned advantages of miniaturization have rendered LoC the focused technology for the accurate manipulation of bioparticles and fluids.

When translating to the miniatured systems and designing new LoC devices, the shifts in the balance of physical forces become particularly noticeable. For instance, when the characteristic length (L) of an object shrinks by 10-fold, the surface forces on

that object will diminish by 100 times (L^2) while the body forces are proportional to the volume change (L^3), and thus will be reduced by 1000-fold. This square-cube scaling leads to the dominance of the surface forces such as friction while the body forces such as gravity become less significant. One of the major implications of the scaling effect is the laminar flow pattern in microchannels which proved instrumental for guiding and aliquoting minute fluid volumes as well as predictable spatial control of particles. Other unique physics introduced in microscale includes i) the pronounced significance of boundary effects and boundary layers, ii) near-field application of electrical, optical, and acoustic forces which become sufficient for particle manipulation in micro dimensions, and iii) the high surface to volume ratio and efficient heat transfer.

To fully realize the potential of LoC devices and to introduce mechanisms that are not feasible at the macroscale, these physical phenomena should be astutely exploited, tailored, and fine-tuned based on the application-specific requirements. For instance, the laminar flow, which is a tool for aliquoting the fluids, is contrastingly a limitation for mixing applications that can be addressed by using external forces. Hence, it is essential to identify and integrate enabling physical actuation mechanisms with LoC systems to devise functional and clinically successful platforms. Various physical actuation techniques have been developed in recent years for on-chip handling of particles and fluidics, which are discussed subsequently.

2.2 Actuation Mechanisms for On-chip Manipulation of Bio-species

Accurate and gentle manipulation of biological specimens is a fundamental requirement in numerous biomedical assays and procedures. Transporting, aliquoting, and mixing fluids are the common steps in almost any bioassay. In a similar vein, manipulating, trapping, enrichment, or patterning bioparticles such as cells, bacteria, nanoparticles, and vesicles are crucial in various research areas, namely point of care diagnosis, tissue engineering, and therapeutics development. Therefore, an arsenal of enabling actuation mechanisms is required to equip LoC devices for these diverse bio-tasks.

The physical actuation mechanisms in LoC devices generally are classified into passive and active methods. The collection of these methods offers a wide spectrum of

precision, throughput, and biocompatibility which allows bio-researchers to pick the best-suited techniques for their research. However, cost, integrability, fabrication difficulty, and specific limitations are other criteria that should be considered before adopting any of these methods. Here, we discuss some of the frequently employed methods and their features for on-chip handling of bio-species.

2.2.1 Passive methods of actuation

In general, passive methods focus on the design of microchannels geometry and architectures for controlling the flow field configuration. For manipulating bioparticles, either the hydrodynamic forces from these flow fields are employed or additional design features such as obstacles and bumpers are used to direct the trajectory of particles.

Passive flow handling methods are widely explored for mixing, droplet generation, stratification, and creating a gradient of concentration while passive bioparticle manipulation enables particle isolation, sorting, washing, and separation. Some widely explored passive actuation methods include:

Embedded obstacles and pillars in microchannels.

The use of obstacles or pillars is one of the well-established methods for both mixing fluids and directing particles' paths. The addition of obstacles, particularly at higher flow rates, is shown to disrupt the laminar flow pattern and induce normal advection for better mixing efficiency.[18] Moreover, the flow field can be guided by embedding grooves and ridges in the channel. For instance, the addition of a series of herringbone ridges in the channel skews the flow direction and creates oblique flow circulation for better mass transfer (Figure 2.1.A).[17,18] These baffle-embedded designs have been used for a variety of bio-applications such as mixing,[19,20] synthesis of organic nanocarriers,[21] nanotherapeutics development,[10,22] cell separation,[23] microfiltration,[24] and biosensing.[25,26]

Inserting bumper and pillars in the channels can also direct the trajectory of particles based on their physical characteristics and separate them accordingly.[27] The combination of size and deformability of particles introduces a characteristic known as effective particle diameter. When particles with small effective diameters bump into the

array of the pillars shown in Figure 2.1.B, their path follows the trajectory of fluid flow. On the other hand, particles with bigger effective diameters follow the trend of bumper posts and therefore can be separated in the outlet. This method has been used for isolation of various biological particles including separation of blood components,[28,29] detection of cancer cells from blood,[30] isolation of parasites,[31] fractionation of extracellular vesicles,[32] and analyzing the deformability of cells.[33]

Inertial microfluidics.

Inertial microfluidic systems are another category of passive devices which use the inertia of the flow and particles to produce effects such as secondary flow and inertial migration.

The introduction of curvature to the channel design can produce secondary rotational flows such as Dean vortex. These vortices are induced because of the mismatch between fluid momentum in the center and outer walls and can enhance mixing by introducing an advection component normal to the channel. The equilibrium of inertial lift force and drag forces by the secondary flow on particles also determines their position in the channel for size-dependent separation (Figure 2.1.C).[34,35,36] Inertial microfluidics has been employed as a bioparticle manipulating tool for a range of bioapplications such as cell separation,[36,37] isolation of circulating tumor cells,[38] removal of bacteria,[39] exosome detection,[40] and cell mechanical phenotyping.[41]

Droplet microfluidics.

One of the powerful microfluidic tools for liquid and bioparticles handling, with tremendous potential to fulfill the LoC goals, is the droplet-based technique. In droplet microfluidics, the fluids break into minuscule droplets by using two immiscible phases such as oil and aqueous solutions (Figure 2.1.D).[42,43,44] The size of these droplets can be predicted by controlling the channel geometry, fluid properties such as surface tension and viscosity, and flow rate ratio of the two phases.[44,45]

Fragmenting bulk flow into minute droplets enables high-throughput and parallel processing of discrete samples to achieve large data sets with high precision.[46] Moreover, the volume reduction in droplet methods also offers better control over the reactions, rapid temperature regulation, and higher sensitivity. Hence, a great body of literature has used droplet-based platforms for PCR analysis,[46] enzyme discovery,[47]

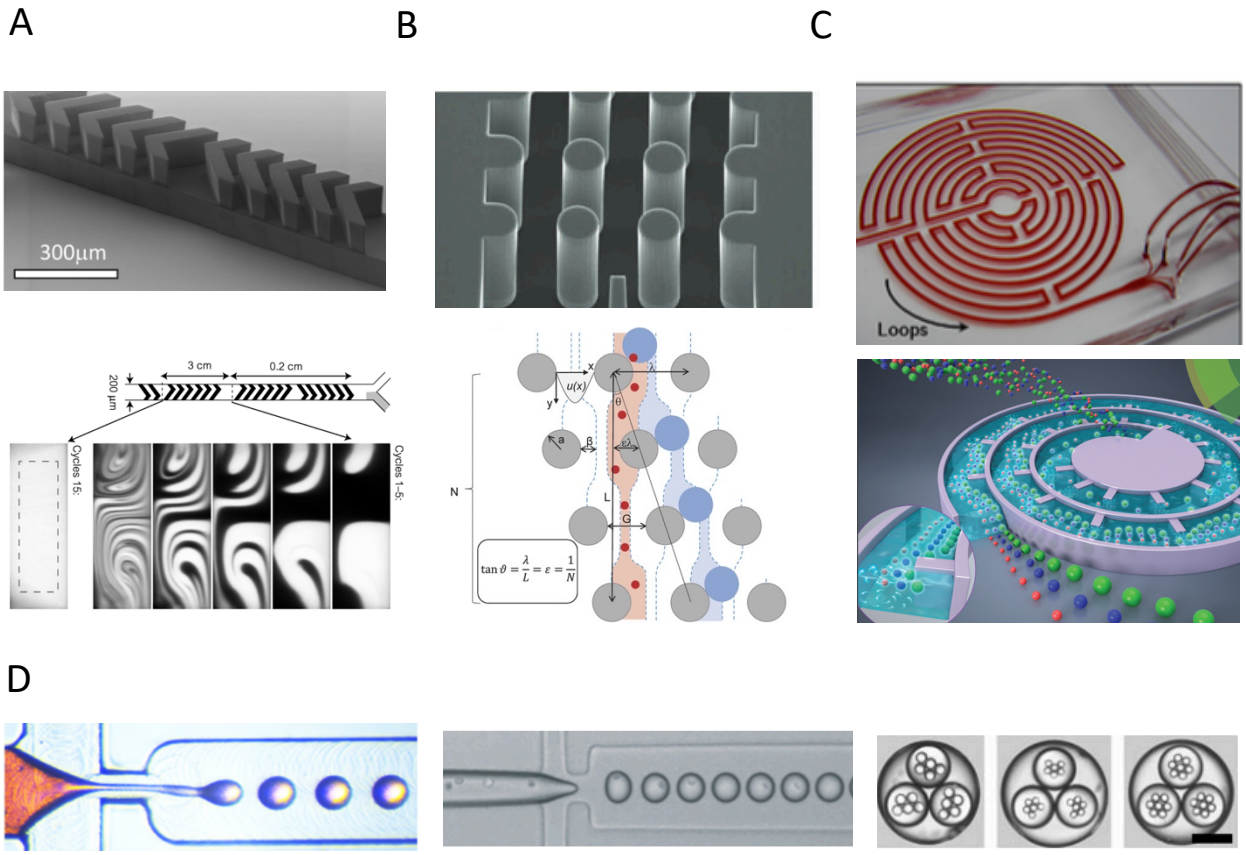

Figure 2.1. A) Structure of staggered herringbone ridges to manipulate the flow field for better mixing[17], and the flow pattern after passing upon multiple herringbone cycles.[18] **B)** An array of bumper posts embedded in the microchannel as a passive way of particle separation based on size and deformability.[27] **C)** Inertial microfluidic platforms using spiral microchannel and a combination of inertia and micro-obstacles for particle separations.[37] **D)** From left to right: droplet microfluidic settings showing flow-focusing droplet generation mechanism,[44] droplet microfluidics for production of cell-laden hydrogel microcapsules,[42] and multicomponent emulsions with three levels of emulsification to encapsulate a controlled number of droplets within droplets.[43]

early cancer diagnoses by cell sorting and single-cell analysis,[48,49] nanoparticle synthesis,[50] and 3D spheroid formation.[51]

2.2.2 Active methods of actuation

In contrast to passive devices, active methods employ externally activated force fields in the microchannels for the manipulation of particles or fluids. Active methods generally offer higher tunability, precisions, and efficiency while they can also introduce new physics and mechanisms for bio-species manipulation. Magnetic, electrical, and acoustic forces are some of these active methods that not only are easy to integrate into microchips, but also their microscale application can enhance their magnitude, controllability, and functionality.

Magnetic Methods.

On-chip magnetic manipulation, in general, requires a strong magnetic field with a significant field gradient, and a magnetic susceptibility mismatch between the two fluids or particles and their surrounding media (Figure 2.2.A).[52] Magnetic field, is usually generated by simply embedding a permanent magnet in the vicinity of the channel, making the fabrication of the device straightforward and cheap. However, there are limited examples of bio-species with inherent magnetic properties and the majority of the bio-species need to be extrinsically tagged for magnetic manipulation.[53] The labeling step is usually carried out by exploiting magnetic beads, particularly magnetic nanoparticles which offer selective binding and a large surface to volume ratio.[52] Nevertheless, the labeling requirements add to the experimental steps, costs, and time while it can cause adverse biointerference. To alleviate the labeling complexities, a negative magnetophoretic method is recently proposed where a media with magnetic properties is used to induce a magnetic mismatch with cells and particles.[54]

For fluid handling, one interesting method is the miniaturization of magnetic stirring bars into micro stirrers which spin in response to a rotating magnetic field and induce mixing in the microchannels.[55] All in all, the magnetic methods can offer a sensitive and high-throughput method for fluid mixing[56], cell separation,[57] and droplet

handling[58], albeit the bio implications and the preparation steps of the magnetic manipulation should be assessed before adopting the method.

Electrical Methods.

Owing to the advancement of microfabrication techniques, strong electric fields can be generated in the microdevices by embedding interdigitated electrodes (IDE) inside or in the vicinity of the channel. The presence of an electrical field offers promising actuation techniques for both particles and fluids, due to their high controllability and various physical phenomena.

One of these phenomena that has been widely used for particle maneuvering is dielectrophoresis (DEP). When non-charged particles are exposed to a non-uniform electric field, they get polarized and experience dielectrophoretic force. This force directs the particles that are more polarizable than the surrounding media (Figure 2.2.B) to the strongest regions of the field (positive DEP) while the less polarizable particles are guided to the regions with the lowest field intensities (negative DEP).[59] The amplitude of DEP is dependent on the particle properties such as volume and relative permittivity. Hence, DEP devices are powerful and sensitive tools for bioparticle separation, trapping, concentration, and characterization.[59–61]

Electric-based microdevices also offer other interesting mechanisms as flow actuation methods such as electrothermal effect and electroosmosis. Electrothermal mixing occurs when the embedded electrodes in the microchannel are activated by AC signals; IDEs experience Joule heating and initiate the AC electrothermal (ACET) effect (Figure 2.2.B).[59] The local heating in the electrodes creates a gradient of temperature in the surrounding fluid which subsequently, leads to fluid motion in the vicinity of the electrodes. As for AC electroosmosis (ACEO), it is associated with the adsorption of ions from electrolyte fluids at the interface of electrodes that forms an electrical double layer on the interface. When a non-uniform electric field is applied to the setting, an electrostatic force occurs on the double layer which creates fluid flow (Figure 2.2.B).[59,62] These electrical methods have been reported for numerous bio-applications such as fluid mixing,[63] pumping,[64] nanoparticle synthesis,[65] and particle assembly.[66]

However, electrical systems also face compatibility restrictions with bio-samples which should be taken into account before employing them. One major limitation is that DEP devices are functional only in low conductivity media which are not suitable for cell viability. The same restriction holds true for ACEO mechanisms which are ineffective for fluids with high ionic conductivities, a feature that is common in most biological buffers. ACET devices are operational in biological fluids; nevertheless, bubble generation, electrode deterioration, and the local high temperatures are common phenomena in these devices that should be considered in the design of experiments.[59,62]

Optical Methods.

Arthur Ashkin introduced the use of focused light beams as optical particle tweezers, a fundamental work that gained him the 2018 Nobel prize in physics.[67] In this method, highly focused light beams are used to exert attractive or repulsive forces on objects and trap them for further analysis. These forces are comprised of scattering component and gradient component which are dependent on the particle radius, wavelength, and power of the beam (Figure 2.2.C).[67,68]

Optical tweezers offer high controllability and remarkable resolution for manipulating small biological species such as cells, bacteria, viruses, and biomolecules, which render them valuable tools in many biological studies.[67,69,70] This high resolution, however, comes at the expense of costly and complex settings which defeats the purpose of portable LoC devices. Moreover, the application and manipulation of high-power lasers very often require a designated environment, can damage living organisms, and could lead to photobleaching.[71]

Acoustic Methods.

Among numerous actuation methods, acoustic forces have gained considerable attention as versatile, tunable, and powerful tools for on-chip handling of bioparticles and fluids. Various acoustic wave types and configurations offer a unique spectrum of precision, throughput, and sensitivity, which are adaptable for a plethora of biomedical applications and therefore, are the method of interest in this dissertation.

For manipulating particles, passive methods use hydrodynamic forces that are proportional to particle radius (R), the magnetic and DEP forces scale with particle volume ($F \propto R^3$), and optical tweezers have either third power or six power relation with radius ($F \propto R^3$ or $F \propto R^6$) depending on the traveling or standing field configurations. Acoustofluidics, on the other hand, offers various force relations by producing hydrodynamic acoustic streaming ($F \propto R$), standing fields ($F \propto R^3$), traveling fields ($F \propto R^6$), or even the combination of these forces on a single particle (Figure 2.2.D).[72] As such, the sensitivity of the acoustic tweezers can be considerably tailored based on the requirement of the applications.

One other remarkable advantage of the acoustic methods in biofield is their high biocompatibility. Unlike the electric-based methods where electrodes need to be inside the channel to induce a strong electric field, the acoustic waves can propagate from a source outside the channel and create strong fields by standing waves. Thereby, this non-contact operation combined with the non-invasive nature of the acoustic waves result in a more biocompatible mechanism compared to their optical and electric counterparts. Moreover, acoustic manipulation does not require specific working media and labeling. In contrast to optical and electrical working conditions which restrict the choice of media, acoustic methods are operational even in complex biological cocktails. Also, since the acoustic tweezers can distinguish particles based on their inherent mechanical properties such as size and density, no pre-labeling steps are required as opposed to magnetic techniques.

These advantages coupled with the variety of the acoustic handing mechanisms to choose from and tailor, render the acoustofluidic an exceptionally powerful tool, and therefore the method of choice to build on this thesis. As such, the next chapter reviews in detail the acoustofluidics concepts, working principles, and various biomedical applications arising from its distinct features in manipulating bio-sample.

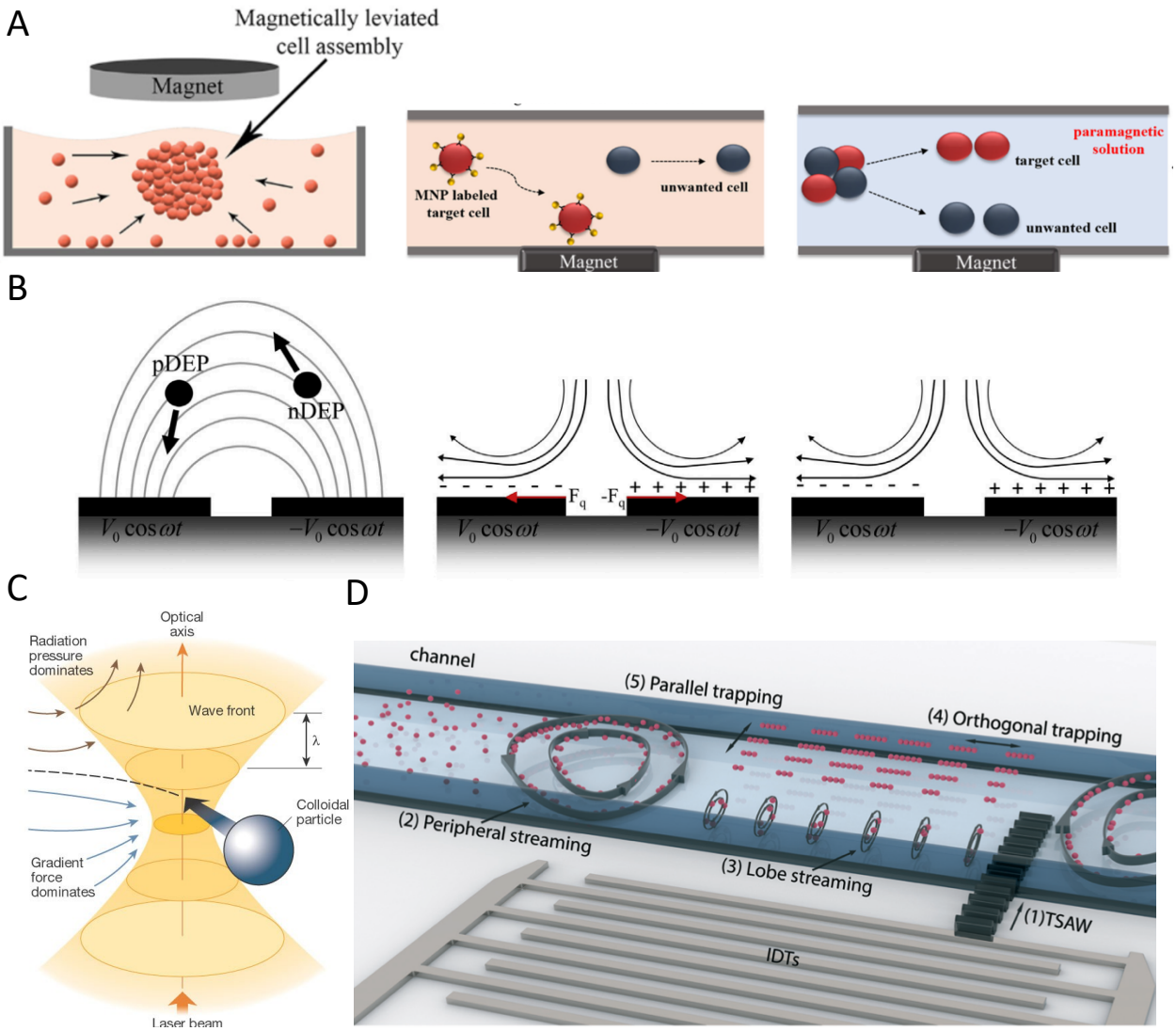

Figure 2.2. Illustrations of active actuation mechanisms **A)** The use of magnetic fields for levitations of cells into 3D cellular blocks, and particle and cell separation by bead labeling and negative magnetophoresis respectively.[52] **B)** The concepts of electric actuation methods, from left to right: dielectrophoresis for particle manipulation, AC electroosmosis flow motion, and AC electrothermal flow.[59] **C)** The schematic of an optical tweezer where a highly focused light can manipulate small particles by the balance of radiation pressure and gradient forces.[68] **D)** An acoustofluidic platform for the manipulation of particles and fluids. The interplay of various acoustic forces and phenomena can be used to control both particles and flow trajectories.[72]

3

Acoustofluidic Concepts & Phenomena

In this chapter, we discuss the physics and working mechanisms of acoustofluidic devices, as well as the acoustic phenomena that are frequently used for the manipulation of biospecies. This chapter and the following chapter constitute a review article titled:
Acoustofluidics–Changing Paradigm in Tissue Engineering, Therapeutics Development, and Biosensing", submitted to *Lab on Chip.*

3.1 Introduction

Acoustic waves have a long history in biomedical sciences with a wide range of applications from diagnostics and imaging techniques to shock wave lithotripsy, using high-energy sound waves. The development of microelectromechanical systems and miniaturized technologies enabled the integration of acoustics with minuscule, confined, and well-controlled microfluidic domains and introduced acoustofluidics. The miniaturization of acoustic platforms not only allows for the precise manipulation and analysis of cells, particles, and biomolecules from nanometers to millimeters length scales, but also introduces numerous phenomena unique to the micro realm.[4,73] The wide range of working frequencies (from kilohertz to gigahertz), efficient delivery

and localized energy, and various acoustic phenomena that can be independently chosen and tuned, make this technology suitable for a diverse gamut of applications.

In the biomedical field, acoustofluidics has attracted high interest due to its contactless and label-free nature, its capability to easily modify the energy and frequency of waves for high biocompatibility, and its flexibility with working media as it does not require specialized media, as in electrophoresis or optical tweezers.[5,74–76]

Moreover, miniaturized acoustic platforms allow for the generation of uniform and well-controlled acoustic pressure profiles, exertion of gentle and precise acoustic forces on sensitive bio-samples, and minimizing heating and mechanical stresses.[5] One distinctive feature of acoustic systems is their ability to function as both actuators, for particle and fluid manipulation, and sensors to detect bioparticles including viruses or bacteria. This versatility emerges from the capability of piezoelectrics to convert energy between mechanical vibrations and electric signals in both directions, through direct and inverse piezoelectric effects.[77]

To move and manipulate objects using acoustic energy, known as acoustophoresis, acoustic waves exert energy on the objects mainly in the form of acoustic radiation forces (ARFs), and/or Stokes' drag forces initiated from the acoustic streaming. One advantage of acoustic methods for particle manipulation is that every dispersed object that shows a mismatch in density and/or compressibility with its surrounding medium is acoustically visible to the system, without labeling. This acoustic contrast, together with the particle size, determines the magnitude of the acoustic force exerted on the particles and is subsequently used for accurate and sensitive separation, label-free sorting, enrichment, and patterning of cells, bacteria, and nanoparticles. In addition, these accurate and controllable acoustic forces on submicron to millimeter-scale particles, combined with their compatibility with complex biofluids such as sputum and blood, make acoustic manipulation a versatile and powerful tool for handling clinical specimens. The non-invasive nature of acoustic tweezers can also be employed to gently move and pattern single particles and arrays of cells and particles with a micro-scale precision to study cell communications and to assemble complex cell architectures for tissue engineering.

The interaction of acoustic waves with objects reciprocally impacts the characteristics of the waves and causes shifts in their amplitude, phase, and propagation velocity. These shifts in the waves' features can be measured and employed as a sensing strategy to detect pathogenic species, such as viruses and bacteria, quantify proteins and DNA, or divulge information about the change in physical properties of cells such as viscoelasticity. Surface acoustic wave (SAW)-based sensors could detect Ebola, Influenza A, and HIV with higher accuracy than standard polymerase chain reaction (PCR).[78,271] Another advantage of these acoustic sensors is their ability to be integrated with smartphones since the radiofrequency input and output of SAW-sensing facilitates the electronic readout.[79] These unique features coupled with the fast detection time establish acoustics as one of the most promising and powerful sensing technologies for point of care testing.[80]

Apart from acoustophoresis and biosensing, acoustofluidics can be further exploited as a functional mechanical trigger to induce biological responses in samples in unique ways: from enhancing wound healing to inducing concussions to worms for brain injury research! [81,82,83]

In this chapter, we briefly introduce the physics behind the acoustic phenomena to fathom the mechanism of operation and in the following chapter we put the spotlight on the exciting developments of acoustics in recent years with an application-based perspective.

3.2 Physics and Methods of Acoustic Excitation

The generation of acoustic waves in on-chip platforms generally starts by introducing an alternating electric current (AC) to a piezoelectric material. The electrical field modifies the polarization of the dielectric material, in a process known as the converse piezoelectric effect. The electrical field is transduced into mechanical oscillations, and subsequently, into acoustic waves which carry the mechanical energy and momentum by compression and rarefication through the medium.[84] The path of propagation in the medium within a piezoelectric slab classifies acoustic waves. Here, we focus on the two most frequently used acoustic waves in acoustofluidics including surface acoustic waves (SAWs), which as the name suggests, propagate on the surface plane of the

material, and bulk acoustic waves (BAWs), which travel throughout the bulk of the material. Although this general classification is based on the wave direction, BAWs and SAWs show more fundamental differences including the selection of the piezoelectric material, the fabrication process, the operating conditions, and the nature of waves interacting with objects.

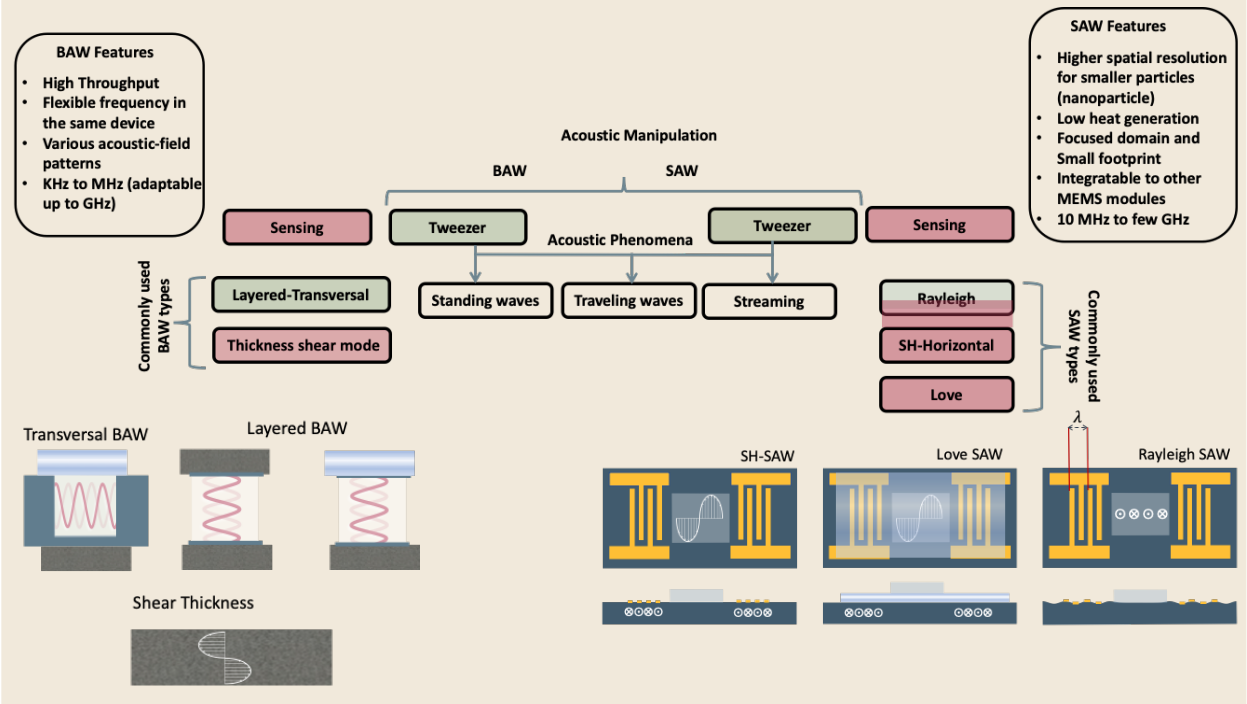

Figure 3.1. Schematic and classification of frequently used acoustofluidic technologies for bio-applications. BAWs and SAWs can both be used as tweezers for the manipulation of bio-samples and also as biosensors. Transversal and layered BAW settings are commonly used in acoustic tweezers while shear thickness has wide application in sensors such as quartz crystal microbalance. SAW wave types, including Rayleigh wave which are preferred as tweezers, as well as SH-SAW and Love SAW which are exploited as sensitive biosensors.

3.3 Bulk Acoustic Waves

Bulk Acoustic Waves are well-developed technology with decades of history in numerous biomedical applications, many of which are currently commercialized, such as the Quartz Crystal Microbalance (QCM) biosensor. BAWs in microfluidic devices are typically produced by thickness or transverse vibrations of the piezoelectric transducers

adhered in the vicinity of the fluid channel (Figure 3.1.left). The piezoelectric material in BAWs is usually piezoceramics, for example, lead zirconate titanate (PZT). When activated by an electrical signal, the piezo element resonates through the device and the acoustic waves travel via the bulk of an intermediate medium. By tailoring the position, configuration, the number of piezo elements, and their interaction with intermediate layers, one can induce various acoustic phenomena, including standing acoustic waves, traveling acoustic waves, and different types of microstreaming. Generally, the operational frequency of these devices is lower than 10-Megahertz (MHz), corresponding to wavelengths ($\lambda \geq 100$ μm) that are significantly larger than many biological particles, *e.g.* cells, biomolecules, and cellular vesicles. Therefore, the direct manipulation precision of individual particles can be generally lower in BAW, however, they can handle bigger clusters of particles and work with high flow rates, making BAW suitable for scale-up applications.

3.4 Surface Acoustic Waves

SAW-based devices are fabricated by patterning interdigitated electrodes on highly efficient piezoelectric substrates, for example, quartz crystals or lithium niobate ($LibNO_3$). Upon activation, each interdigitated transducer (IDT) conducts an electrical signal to generate mechanical oscillations on its fingerprint, which subsequently propagates as surface acoustic waves.[85] When the wave from one IDT finger reaches the wave from an adjacent IDT finger, it experiences a constructive interference, and the amplitude of the wave increases (Figure 3.1.right). In SAW systems, most of the acoustic energy is confined between the surface of the substrate to one wavelength (λ) below the surface.[86] To ensure a pure SAW regimen, the substrate thickness (h) should be $h/\lambda > 1$, otherwise other wave types such as lamb waves ($h/\lambda < 1$) or even the reflection of the surface wave onto the other side ($h/\lambda \approx 1$) can happen.[87]

This localization of the acoustic energy at the substrate surface leads to a confined active region in SAW devices and minimizes the power consumption compared to that of BAWs.[3,76] SAW devices typically operate at megahertz (MHz) to lower-end gigahertz (GHz) frequencies which corresponds to micron-order wavelengths. Hence, SAW devices are usually equipped with a high spatial resolution for the manipulation of

single cells and micron-to-nano-sized bioparticles. Since these piezoelectric substrates are biologically inert, the microchannel can be placed in direct contact with the substrate; however, the heat generation should be monitored.[3]

The most explored surface acoustic wave type is Rayleigh SAW. This wave type can efficiently leak into the liquids in contact with the propagation path, therefore they are also referred to as leaky waves. Due to this strong liquid coupling, leaky waves are almost ubiquitously used for the manipulation of biofluids and suspended particles. However, this leaky nature can limit the sensing sensitivity of these wave types in liquids due to attenuation.[80,88] Typically, the standard piezoelectric substrate to create leaky waves is a 127.86° Y-rotated, X-propagating lithium niobate, although the use of zinc oxide, aluminum nitride, and quartz is also reported. [85]

For its part, shear horizontal surface acoustic waves (SH-SAW) are the gold standard waves for sensing applications. The horizontal direction of vibration (Figure 3.1.right) in this wave type reduces the leakage of acoustic energy into the media and preserves the signal strength. Hence, SH-SAW offers a higher signal-to-noise ratio compared to Rayleigh waves and is more commonly used for sensing in liquid environments. The most frequently used piezoelectric substrates for SH-SAW include 36° YX, 41°YX, 64° YX $LiNbO_3$, lithium tantalite, and ST-cut quartz.[80,88]

Love mode is another SAW wave type for biosensing which is similar to SH-SAW with a waveguide layer on the propagation path (Figure 3.1). The waveguides, typically SiO_2 layers, have a smaller shear rate compared to that of the substrate and can further inhibit leakage into the media. This leads to the concentration of the acoustic energy at the surface, rendering Love-based devices highly sensitive to physical changes such as mass and viscosity for better sensing in both gas and liquid environments.[80,89]

3.5 Acoustic Phenomena

When objects are exposed to acoustic waves, they show distinctive absorption, reflection, and scattering behaviors that lead to unique phenomena. In fluids, acoustic forces can create different types of microstreams such as boundary-driven and Eckart streams. On the other hand, for particles, bubbles, and droplets the main acoustic forces are acoustic radiation forces (ARF), Bjerknes forces, and drag forces induced by

acoustic streams. These acoustic phenomena are introduced and briefly discussed in the following sections with a focus on functional concepts and mechanisms, while for readers interested in the theory of acoustics, we recommend the insightful articles by Friend's and Bruus' group.[90-91]

3.5.1 Acoustic phenomena in fluids

Acoustic streaming is the formation of steady microvortices by the viscous dissipation of the acoustic energy or vibratory motions within the fluid medium. In an environment with no energy dissipation, the movement of fluids in response to a time-harmonic acoustic excitation is also a harmonic motion. Hence, the fluid volume elements return to their exact starting point after a full wave cycle. However, in real life, energy dissipates and distorts this harmony by adding a relativity small time-independent component to the fluid movement; *i.e.,* the fluid component does not return to its exact starting point after each wave passes. As the fluid component faces more wave cycles, this minuscule time-independent displacement accumulates to form a time-averaged momentum flux, leading to acoustic streaming.[92,93] The conversion of acoustic energy to steady convective momentum-flux forms various flow patterns which are determined by their respective mechanism of energy dissipation. Two of the most notable acoustic streams in microfluidic systems are the *Boundary-driven streaming* and the *Eckart streaming.*

Boundary-driven Streaming.

This streaming, also known as boundary-layer-driven streaming, is the result of the acoustic energy dissipation in a thin boundary layer around oscillatory solid-liquid or gas-liquid interfaces.[94,95] The steep change of velocity from zero (on a no-slip interface) to a free-field value within a thin domain, known as the boundary layer, creates a strong velocity gradient that dissipates the acoustic energy on a markedly larger scale compared to the bulk dissipation.[93] The acoustic energy transforms into a strong streaming flow, referred to as 'Schlichting streaming', in the confined boundary layer.

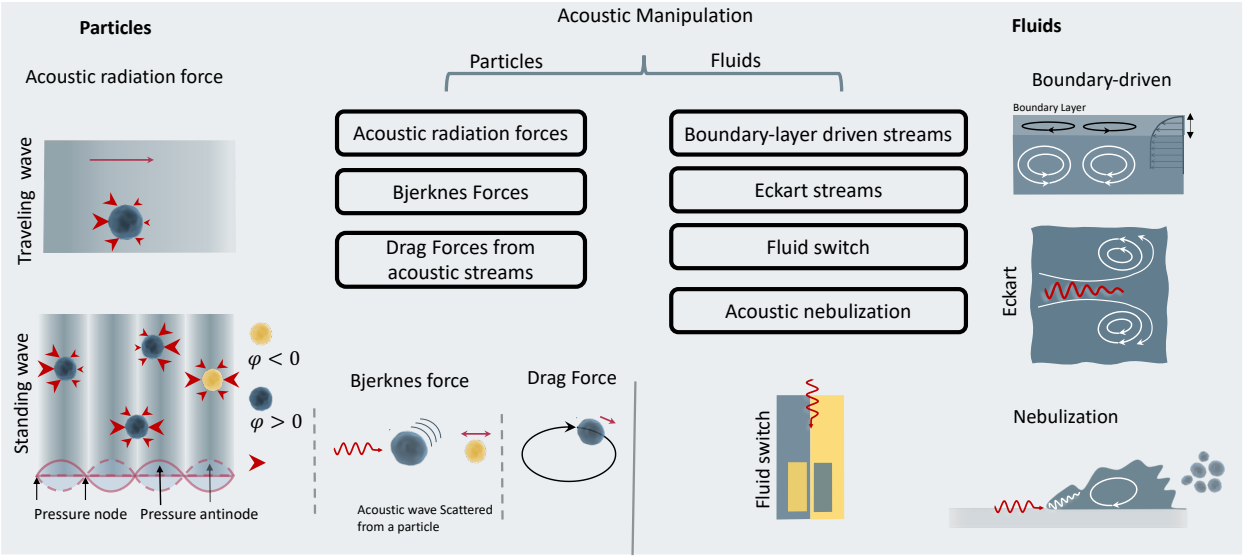

Figure 3.2. Acoustic principles for the manipulation of fluids and particles. For particle manipulation, acoustic radiation forces, secondary Bjerknes force, and hydrodynamic forces are frequently exploited. For fluid manipulation boundary-driven streams, Eckart streams, fluid switch, and nebulization are the common approaches.

This primary stream generates an outer counter-rotating vortex. As a result, the energy is transmitted to the bulk of the fluid, in a similar fashion as gear trains (Figure 3.2.right). This method is commonly employed in microfluidic platforms by embedding oscillatory sharp edges,[96] bubbles,[97] the combination of both,[98] and even channel walls.[92]

Eckart Streaming.

The origin of the Eckart phenomenon is the viscous attenuation of the acoustic energy during the propagation of the waves in the bulk of a fluid.[99] As the acoustic beam travels away from the source, the energy of the waves dissipates at a rate proportional to the square of their frequency, thus generating an acoustic pressure gradient along the direction of propagation (Figure 3.2.right). A steady momentum flux arises from this gradient, which in turn pushes the fluid towards a lower pressure level. In microfluidic channels, this phenomenon usually leads to circulatory streams. For noticeable Eckart streaming to happen, the length of the bulk fluid medium must be in the order of the acoustic attenuation length, which usually occurs in high-frequency SAW devices.[93,99]

Acoustic Relocation of Fluids.

Acoustic relocation of fluids (fluid switch) is another interesting phenomenon that differs from the former acoustic streams, as it does not stem from acoustic attenuation, but from the acoustic mismatch between two fluids. Hertz and Mende[100] showed that when two or more fluids with different acoustic contrasts are subjected to acoustic waves, they experience a net acoustic radiation force (ARF) at their interface. This ARF, which is independent of the wave direction, can subsequently cause a fluid switch (Figure 3.2). Deshmukh *et al.* further investigated the nature of the radiation forces and showed that its amplitude is proportional to the acoustic impedance's mismatch between fluids. This acoustic radiation force was also shown to relocate the fluid with higher acoustic impedance to the acoustic pressure node in an impedance mismatch of as little as 0.1%.[101–103] Considering that the flow regimes in microfluidics are generally laminar and there are distinct interfaces between fluids, this phenomenon can be very instrumental for applications such as mixing.

3.5.2 Acoustic phenomena in particles, droplets, and bubbles

Particles, droplets, and bubbles experience three main types of forces in an acoustic field: primary acoustic radiation force, secondary acoustic radiation force, and the drag forces induced by acoustic streaming. The first force occurs due to direct radiation of acoustic waves, while the latter two are indirectly induced by the acoustic field from wave scattering in other objects.

Primary Acoustic Radiation Force.

When acoustic waves face a change in the acoustic properties of their path, such as encountering particles or interfaces of different media, they experience absorption, refraction, and scattering. The change in acoustic momentum creates a net body force on the particles or fluid interface, known as the acoustic radiation force (ARF).

In general, the acoustic radiation force is comprised of two components: acoustic gradient forces and scattering forces.[104,105]

Eq 3.1:

$$\boldsymbol{F}_{ARF} = \underbrace{\boldsymbol{F}_{grad}}_{\propto (kR^3)} + \underbrace{\boldsymbol{F}_{scat}}_{\propto (kR^6)}$$

The gradient forces, as the name suggests, stem from the gradient of the acoustic pressure and can be formulated as a gradient of acoustic potential (U).

Eq 3.2:

$$\boldsymbol{F}_{grad} = -\nabla U$$

$$U = \frac{4\pi}{3} R^3 \left[f_1 \frac{1}{2} \beta_0 \langle |p_1|^2 \rangle - f_2 \frac{3}{4} \rho_0 \langle |\mathbf{v}_1|^2 \rangle \right]$$

$$f_1 = 1 - \frac{\beta_p}{\beta_0} \text{ and } f_2 = \frac{2(\rho_p/\rho_0 - 1)}{2\rho_p/\rho_0 + 1}$$

Where $\langle |p_1|^2 \rangle$ and $\langle |\mathbf{v}_1|^2 \rangle$ show the mean squared pressure and velocity at the object, R is the radius, while ρ and β are density and compressibility of 'p' particles or '0' surrounding. For fluids, $\beta = 1/\rho c^2$. The gradient component of acoustic radiation force is proportional to R^3 while the scattering component is proportional to R^6. In small particles, the scattering force becomes negligible compared to the gradient pressure force, except when the terms $\langle |p_1|^2 \rangle$ and $\langle |\mathbf{v}_1|^2 \rangle$ are almost uniform in space, such as in traveling plane waves. In this scenario, the terms in (Eq 3. 2) balance each other out to equal a zero gradient force and as a result, the scattering component becomes the only governing term in Eq 3.1. Hence, depending on whether the waves are standing or traveling, one of these terms (gradient or scattering forces) becomes dominant and determines the acoustic radiation force.

Standing acoustic waves create a strong ARF on particles by increasing the gradient force factor in Eq 3.1, and therefore are very efficient for manipulating particles. This increase in the gradient pressure force is due to standing waves periodically dividing the acoustic domain into regions of low and high pressure that push particles and droplets to either pressure nodes or antinodes (Figure 3.2).

Standing acoustic waves in BAWs can be generated through the interference of waves from two facing acoustic sources with the same frequency or through an incident

wave from a single source and its reflection by an acoustic reflector. On the other hand, standing surface acoustic waves (SSAW) are generated by two or more even pairs of counter-facing IDTs. Two IDTs with an orthogonal configuration can also induce standing waves. In BAW devices, the number and position of pressure nodes and antinodes can be tailored by altering the actuation frequency, while in SAW devices, the operating frequency is restricted to the unique frequency dictated by the IDT design. The acoustic contrast of particles (Φ) determines whether the particles reside in the pressure nodes (particles with positive contrast) or antinodes (particles with negative contrast), which can help separate particles with significant differences in density (Figure 3.2).

Traveling acoustic waves can be generated in either BAW devices, by adhering to a single piezoceramic, or SAW devices, by depositing one set of IDTs that propagate waves to the microchannel. Generally, particles experience a negligible acoustic pressure gradient in planar traveling waves. By neglecting the gradient component in Eq 3.1, the ARF reduces to a scattering force with a magnitude that scales with R^6. The scattering forces continuously push particles in the direction of the beam propagation, causing particles to migrate away from the acoustic source. This continuous unidirectional translation, coupled with the high size sensitivity of traveling waves (due to the R^6 relation), make them a high-resolution approach for particle manipulation. However, it also results in a much smaller ARF in particles compared to standing waves.

In SAW devices, ARF can be simply increased by changing the configuration of IDTs to confine the acoustic region, and by increasing the frequency of operation. Hence, the majority of the traveling wave platforms are based on SAWs and use a focused field to generate stronger ARFs. In doing so, they introduce a pressure gradient factor.[3] Another approach to generate traveling wave forces comparable to that of standing waves is by increasing their frequency. It has been shown in high frequency traveling SAW (TSAW), where $R < \lambda$, the scattering terms are significant, leading to a high ARF.[104,106,107]

Secondary Acoustic Radiation Forces.

The scattering of primary acoustic waves from particles or bubbles creates a net force on their adjacent particles. This force is known as secondary acoustic radiation force or Bjerknes force and can create mutual particle-particle attraction or repulsion depending on the nature of the particles. The intensity of the secondary acoustic radiation force decays by the square of the distance of particles and is also frequency-dependent, with forces usually peaking when the particle diameter approaches half to one wavelength ($d/\lambda \approx 0.5 - 1$).[108,109]

Acoustic Streaming-induced Hydrodynamic Forces.

Acoustic streaming force (ASF) is another indirect force of acoustic waves on particles that comes from vortices in their surrounding fluid. The ASF and their resultant drag forces can manipulate the trajectory of suspended cells or droplets. When a suspended particle with initial velocity $\mathbf{V}_p$ becomes exposed to a streaming velocity field $\mathbf{V}_S$, it experiences a Stokes' drag force, which realigns its direction of motion to the streamline of the vortices. The force is described in the Stokes drag equation as:

Eq 3.3: $$\mathbf{F}_{drag} = 6\pi\eta R(\mathbf{V}_s - \mathbf{V}_p)$$

where η is the fluid viscosity and R indicates the radius of the particle. This equation assumes that the particles have a homogenous density.

Acoustic manipulation of particles for separation, arrangement, or enrichment in microfluidics can be performed by the combination of the aforementioned acoustic phenomena. Often, multiple acoustic forces are present in each system, however, their effect might not be synergetic. For instance, in both standing waves and traveling waves, some forms of acoustic streaming are usually accompanying the primary acoustic radiation force. Therefore, there is often a competition between the ARF and streaming drag forces to determine the trajectory of the particles. Depending on the application, acoustic streaming might serve as the principal operating mechanism, while in other situations it might appear as an undesirable artifact or noise. For scenarios where streaming is unwanted, the strategies to mitigate the streaming noise

include increasing the operating frequency and altering the physical characteristics of the medium (η, ρ, β).[103,110,111]

4 Recent Advances in Acoustically Driven Biomicrofluidic Devices

In this chapter, the recent advances in acoustofluidics for the manipulation of bioparticles and biofluids are overviewed. Particularly, we explored the mechanisms and design features of state-of-the-art acoustofluidic technologies for their use in particle separation and enrichment, cell patterning for tissue engineering, therapeutic development and delivery, cell functionality analysis, and biosensing.

4.1 Acoustofluidics for Particle Separation and Enrichment

The interplay of primary, secondary, and acoustic streaming forces creates various acoustic phenomena that can be used in applications such as the separation, enrichment, pattering, and rotation of particles. Acoustic waves can manipulate cells and bioparticles without disrupting the surrounding fluid via ARFs while maintaining the flow path. Conversely, when disruption is desirable, *e.g.,* to promote mixing, acoustic streaming can be introduced into the system.

ARF in standing waves stands out due to their high controllability, relatively large magnitude, and its third power relationship with the particle's radius (R^3), in which a small increase in the particle size leads to significantly stronger ARFs. Stronger ARFs in larger particles can overcome the fluid resistance due to drag force. Therefore, bigger

particles can travel faster and longer distances towards low acoustic pressure nodes, while the movement of smaller particles is dominated by drag forces of background streamlines. This difference in the reposing site of particles, based on their size, has been extensively used in both BAW and SAW modes for particle separation (Figure 4.1).[3]

The use of standing BAWs (SBAWs) have been reported for separating MCF-7 cancer cells from red blood cells (RBC),[112] prostate cancer cells from white blood cells with flow rates up to 100 µl min^{-1},[113] and platelets from undiluted whole blood with over 85% platelet recovery, and flow rates of 10 mL min^{-1}.[114] SBAW were also used to separate different sized polystyrene particles (2, 5, 8, 10 µm) by increasing the source input power from ~0.5 to ~2.0 W.[115] In a similar manner, standing SAWs (SSAWs) can separate particles by creating a single pressure node in the channel center, and relocate particles

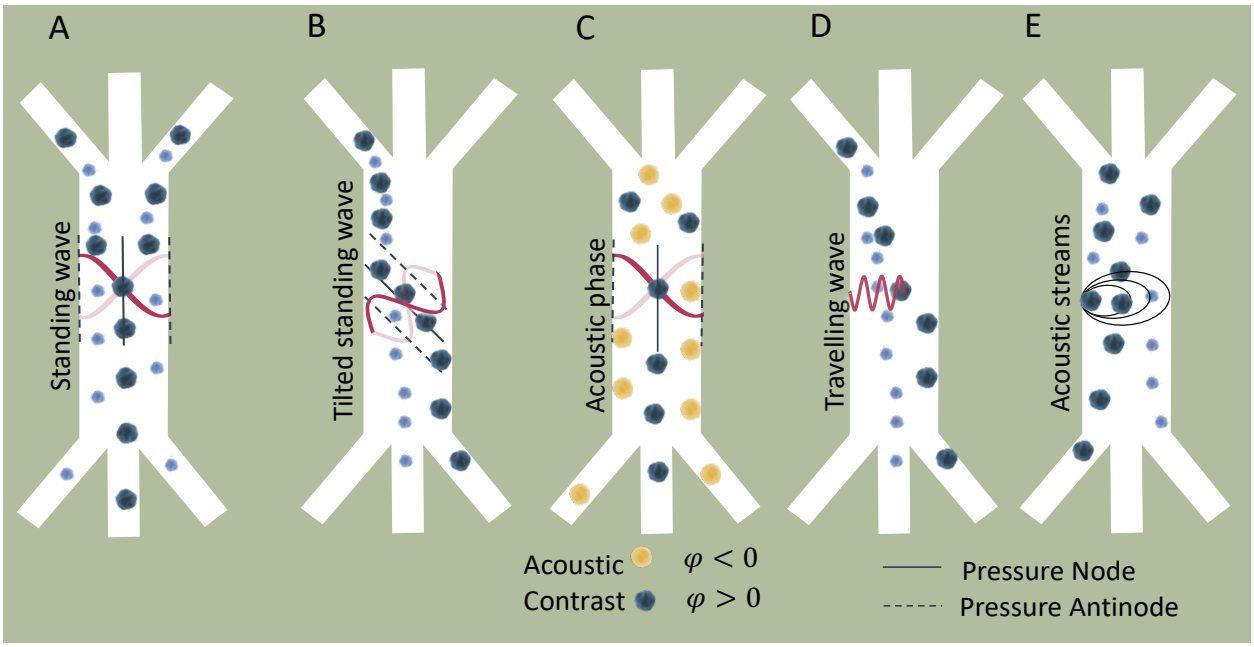

Figure 4.1: Acoustophoretic mechanisms for particle separation. **A)** bigger particles experience stronger ARF in standing waves and can move faster to the pressure nodes. **B)** Tilted standing waves increase the separation path of bigger particles. **C)** Separation by acoustic phase contrast. Particles with positive acoustic contrast move to pressure nodes while particles with negative acoustic contrast move to pressure antinodes. **D)** Traveling acoustic waves separate bigger particles in the direction of wave propagation. **E)** Acoustic streams trap or deflect the path of bigger particles closer to the vortex source while smaller particle can pass with less deflection.

based on their size (Figure 4.1.A).[116] This approach was used for the separation of platelets from whole blood with a purity of 98%,[117] water in oil droplets with a sorting rate of 222 droplets per second,[118] and extracellular microvesicles and 200 nm nanoparticles.[119]

Despite the great potential in applications, the isolation and enrichment of target nanosized organisms with this method is challenging. The difference in scaling order in the nanoparticles (ARF$\propto R^3, F_d \propto R$) results in the dominance of Drag forces in the nano realm. Therefore, for the ARFs to dominate the manipulation of particles, the frequency of acoustic waves should be in the high MHz-to-GHz range, a feature typically exclusive to SAWs. SSAWs were successfully used to separate 500 nm from 100 nm particles,[120] and exosomes (<300 nm) from a mixture of extracellular vesicles with >90% separation yields.[119,121]

The maximum travel distance of particles in standing waves is the spatial distance between pressure nodes and antinodes ($\lambda/4$). This distance in SAW devices which usually have a high frequency of operation can be very short, limiting their sensitivity and efficiency of separation.[122] Hence, by tilting the SSAW direction, such that the pressure nodal lines stand at an angle to the flow direction (optimally 15°), the normal displacement of the particles can be increased by ~10 times, while the trajectory of smaller particles is still dominated by the flow field (Figure 4.1.B).[123] This mechanism was adopted by various groups to separate breast cancer cells from leukocytes with a purity of 84% and throughput of 2 µL min^{-1},[123] and for the isolation of low concentrations of cancer cells (~100 cells/mL) from white blood cells with an 83% recovery.[124]

In addition to the size, the acoustic contrast factor (Φ), associated with the compressibility and density of a particle and its contrast to the surrounding medium, can also be used to separate particles by standing acoustic waves.[125] A particle with a higher density mismatch has a larger Φ value, calculatable by:

Eq 4.1: $$\Phi = \frac{5\rho_p - 2\rho_0}{2\rho_p + \rho_0} - \frac{\beta_p}{\beta_0}$$

and thus experiences a larger ARF. This concept can be particularly used when mixed particles are indistinguishable by their size. Furthermore, the acoustic contrast factor

can have a negative value when the density of the particle is below that of the medium. As such, the density of the medium can be modulated, such that it divides the relative contrast factor of particles into negative (−Φ) and positive (+Φ), where in the presence of ARFs, two particles can move in opposite directions from one another, *i.e.,* antinodes (−Φ) and nodes (+Φ) (Figure 4.1.C). To exploit this method, cesium chloride was added to the working media to reach a density of 1.16 g/cm^3 and separate 3 µm polystyrene particles (1.05 g/cm^3) from PMMA particles (1.22 g/cm^3) of the same size.[115] Similarly, a high acoustic impedance-to-viscosity ratio medium (OptiPrep™ Density Gradient Medium) was used to increase the acoustic impedance of the medium. Cells were injected in normal media near the sidewalls where the pressure antinode was located, and high-contrast media was infused in the central channel where the pressure node sits. This allowed to effectively quantify the acoustic impedance of various cell types, including monocytes, lymphocytes, neutrophils, and cancer cells.[102] In another study, RBCs were sorted in a BAW device by guiding RBCs (+Φ) towards the pressure nodes while lipid microemboli (−Φ)were located at the anti-pressure nodes, with a 100% efficiency.[126]

The other acoustophoretic method is traveling surface acoustic waves (TSAW), which can be a double-edged sword for particle separation. On one hand, its R^6 relation results in smaller magnitudes of ARF compared to that of SSAW, on the other hand, the R^6 relation renders it more sensitive to the size of particles. Another interesting feature of TSAW is the migration distance of particles, which unlike SSAWs, is not limited to the node-antinode distance. Instead, TSAW applies a unidirectional force on particles, continuously pushing them away from the source (IDT). Therefore, particles travel longer lateral distances allowing them to be sorted more efficiently (Figure 4.1.D). Straight TSAWs have been used to guide the direction of water droplets in oil and polyacrylamide particles,[127] and slanted TSAW were used to sort human keratinocytes, mice fibroblasts, and melanoma cells.[128] TSAW has also been used in combination with functionalized microparticles to separate target-protein complexes which have bigger diameter unbound particles.[129] To compensate for the lower force magnitude, the acoustic field in TSAW is usually limited to a small, focused domain by using focused-IDTs (FIDT), used for the continuous separation of 3 µm and 10 µm particles with a

100% efficiency.[130] SSAW and TSAW can also be combined in a multi-module platform to enhance separation (Figure 4.2.A).[131]

Another efficient separation method is the use of acoustic streaming. Acoustically-induced microvortices are advantageous due to their high controllability, rapid formation, facile tuning, precise location, and the ability to scale up for high-throughput applications.[132] When particles approach the acoustic field, microstreaming can deflect the trajectory of the particles based on their size. Larger particles move to the center of rotation, being trapped in closed streamlines, while smaller particles can pass through the vortex (Figure 4.1.E). By using oscillating microbubbles, the selective capturing and release of different sized particles was attained with a high resolution of 1 μm.[133] Bubbles can be used at the neck of bifurcated channels to deflect the trajectory of particles from the streamline and thus be collected at the outlets (Figure 4.2.B).[134,135] Lateral Cavity Acoustic Transducers (LCATs) with oscillatory bubbles at the sides of a channel, could efficiently separate platelets, red, and white blood cells from undiluted whole blood,[136,137] with high throughput (50×10^6 cells/min).[138] Moreover, acoustic streaming can be coupled to ARFs in SAW platforms to create both traveling and standing waves. As an example, an acoustic beam was employed as a virtual filter membrane to separate 8 μm from 5 μm particles,[139] 2 μm from 1 μm particles, and MDA-MB-231cancer cell lines from a mixture with red blood cells (Figure 4.2C).[132]

The dominance of drag forces in sub-micron particles encourages the use of acoustic streaming-induced drag forces to separate and enrich nanoparticles. Using SAW-based acoustic streams, the enrichment of particles with sizes of 300 nm,[140] 87 nm,[141] and even 80 nm were shown.[142] Another interesting nanoparticle enrichment approach is using Bjerknes forces. In the presence of acoustic waves, microparticles scatter acoustic energy and emanate secondary ARF (or Bjerknes force), which can attract nanoscale particles and vesicles near the microparticles for filtration and enrichment.

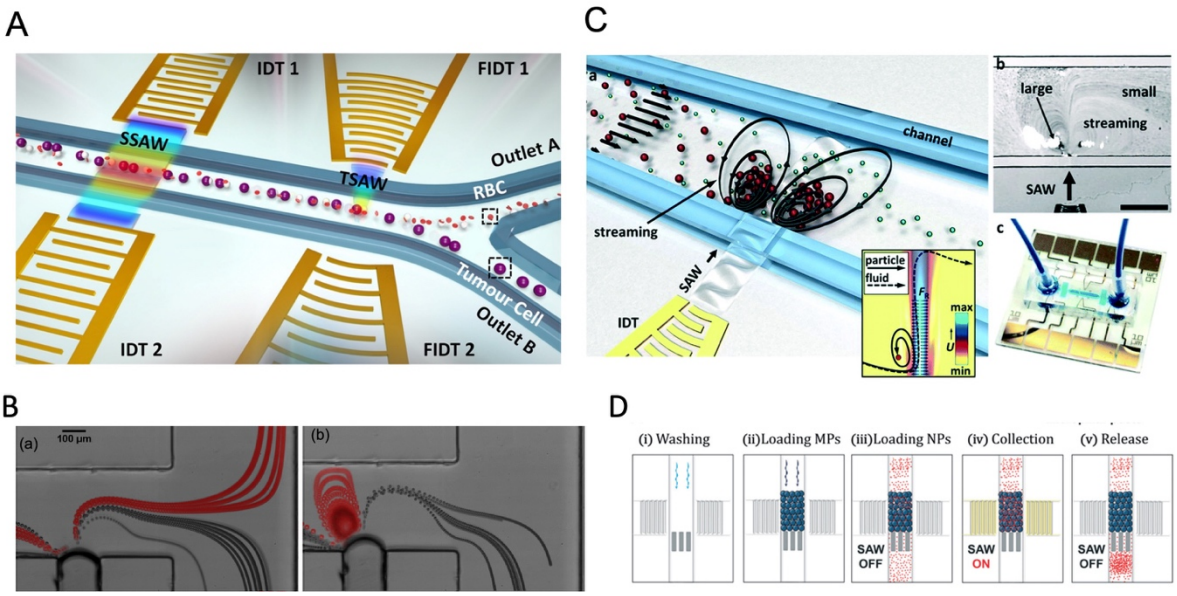

Figure 4.2. Acoustophoresis mechanisms for separation, isolation, and enrichment of particles. **A)** double stage acoustic system using SSAW for alignment and TSAW for separation, [131] **B)** particle separation by microstreams from oscillatory bubbles, [134] **C)** Particle separation by microstreams from focused TSAW.[132] **D)** Exosome enrichment by Bjerknes forces.[145] Reprinted with permission.

This technique was explored in both SAW and BAW devices for trapping E. coli bacteria and 110 nm diameter polymeric nanoparticles with a 95% efficiency,[143] enriching extracellular vesicles (EVs) from cell culture media, urine, and blood plasma,[144] and the enrichment of 100 nm particles by increasing the input power (Figure 4.2.D).[145]

The overview of acoustic modes, parameters, and throughput/efficiency of recent acoustophoretic systems for particle and cell manipulation is presented in Table 4.1.

Table 4-1. Acoustophoresis for particle manipulation

Application	Acoustic mode	Acoustic parameters	Particles/cells	Throughput/ Efficiency
Particle Separation	Standing Wave (SBAW)	2 MHz, 0.5-2.0 W; 0.36, 0.13, 0.04 mL/min flow rate from center inlet, outlet, and sample suspension	PS particles (2, 5, 8, 10 µm), RBC[115]	~96% PS recovery, ~92% RBC recovery
		4.91 MHz and 10 V (pre-alignment); 1.99MHz and 0-12V (actuation); 100µL/min	PS particles (5, 7 µm), MCF-7, RBC, DU-145, WBC[112]	99.3 ± 0.3% PS, 91.8±1.0% MCF-7, 84.1±2.1% DU145 recovery
		1.805 MHz, 20.1 Vpp (2W), 30-60µl/min (HeLa/PBMC) and 20-40 µl/min (MDA-MB-231/PBMC)	HeLa, MDA-MB-231, PBMCs[146]	89±8% with 49.2 ±15.2 fold enrichment (HeLa cells/PBMC) 86±11% with 56.5 ±17 fold enrichment (MDA-MB-231/PBMC cells)
		10 Vpp, 0.3ml/min	Lipid particles (5µm), RBC[126]	100% separation efficiency, 70% recover (RBC) >80% of lipid particles removed
		1.9-2.1MHz (1ms), 3.5-6.0Vpp	BA-F3 murine pro B, MCF-7, monocytes, lymphocytes, neutrophils[102]	12 sequential samples within 3 hours
		2.96 MHz, 31 V, 200µL/min	Elastomeric particles, KG-1a[147]	N.I.
	SSAW (Primary ARF)	12.6MHz (λ=300µm), 15-22dBm (30-160mW), 2µl/min	Fluorescent PS beads (4.17µm and 0.87 µm)[116]	90% recovery (4.17µm) and 80% (0.87µm)
		13.0168 MHz (λ= 300µm), 23.8-26.7dBm, 0.8µl/min (particles), 0.5 µl/min (cells)	Fluorescent PS particles (2µm and 5.86µm); E. Coli, PBMCs[148]	95.65% purity (E. coli/PBMCs)
		410-463mW, 0.25-5.0 µL/min	RBC, platelets, whole blood[117]	99% RBC clearance ratio, 98% purity of platelets, 2.7 x 10^4 cells/s
		10.02, 10.20, 10.35, 10.46, 10.60 MHz, 48 Vpp, 0.2-8.0 µL/min	Picoliter water-in-oil droplets[118]	222 droplets/s
		38.5 MHz, 0.5W, 2.8mm/s (particles), 1.5W, 2mm/s (eMVs)	PS beads (190 nm and 1000nm), Microvesicles (<200nm)[119]	>90% recovery rate particles, >80% for exosomes, >90% for larger MVs
	taSSAW (Tilted Angle)	19.40 to 19.60 MHz (15°-tilted), 20-40 Vpp, 1-5 µl/min	PS beads (9.77 µm and 0.87 µm), MCF-7, WBC[123]	>98% recovery (9.77/0.87µm) >97% purity (WBC/MCF-7)
		19.573 MHz (5°-tilted), 35-38 dBm, 75 µL/min-1.2 mL/h	PS beads (10 µm), MCF-7, WBCs, HeLa cells, UACC903M-GFP, LNCaP[124]	>87% recovery (MCF-7 and HeLa cells), >90% removal (WBCs), >83% recovery (UACC903M-GFP and LNCaP), 90.4 ± 4.7% cell viability
	Acoustic Streaming	381 MHz (λ=10µm), 68-200 mW, 0.5-8 µl/min	Particles (1µm and 2µm), MDA-MB-231, RBC[132]	>98% capture efficiency at v*=112 2 um particles
		10-50 kHz, 40-60 V	PS particles (1-5µm)[149]	1µm separation efficiency
		32 kHz (3.1ms, 100 cycles), 20-27 Vpp, 3 µL/min	K562, PS beads (10µm)[135]	800 cells/s, 99% sorted cells, 94.5 ±4.7 cell viability
		15-50 kHz, 70 Vrms, 1.33 mm/s	PS particles (radius, 1,2.5,5µm)[133]	1µm resolution
		20 kHz	PS particles (2.5, 5, 10µm)[134]	>80% sorting, 1400 particles/s (8 enrichment ratio)
		50.3 kHz, 3-5 Vpp, 83 ± 2 µL	PS beads (5, 10µm), RBC (7.5 ± 0.8µm) K562 (16.3±2.0µm)[137]	100% trapping (5 and 10µm) at 3Vpp, 94-100% cell viability
		49.8 KHz, 2.75-6.5 Vpp, 27.5µL/min	PS particles (7.32, 25µm), DU-145, WBCs, RBCs, Monocytes[138]	>50 x 10^6/min, 90% efficiency, 77x enrichment (DU-145 cells), 91.7% purity (DU-145)
		2.5-5.0 Vpp, 25 µL/min	Platelets, RBCs and WBCs, MCF-7, SKBR-3[136]	100 % trapping efficiency at 10/mL MCF7, 200x enrichment ratio

		129.5-258 MHz (λ=20 µm), 43.4-49 mW, 0.2µm/min	PS particles (5.0, 8.0, 7.0, 10.36 µm)[139]	95 ± 5% capture efficiency (10µm PS particles)
Particle Enrichment	SAW (Secondary Radiation Forces)	48.8 MHz (λ=80 µm), 18.3V (0.12 W/mm²), 12.2µL/min	PS particles (100, 300 nm)[150]	86.3% separation efficiency
		663 MHz, 251mW, 0.45 µL/min	PS particles (300, 500 and 100nm)[140]	84 ± 9% capture of 300nm
		55-85 MHz, 12 dBm power, 1uL/h flow rate	Particles (100 nm, 190 nm, 500nm)[145]	97% collection efficiency (500nm)
	BAW (Secondary Radiation Forces)	4 MHz, 17 Vpp, 10 µL/min	PS particles (110 nm, 490nm), E. coli[143]	95±3% capture efficiency
		4 MHz, 10 Vpp, 15 µL/min	PS particles (0.1-1µm), EVs (30-500 nm)[151]	81.7% trapping efficiency (1µm), 9.3% CV
	(ta)-SSAW (Primary Radiation Forces)	39.4 MHz, 45 Vpp, 4-8 µL/min	PS particles (110nm, 5µm), Exosomes, MV (50-600 nm) from whole blood[121]	99% recovery rate (110nm from 5µm) 98.4% purity (EVs) with 99.999% blood cell removal rate
	TSAW	3.3- 7.138 MHz, 5V	Silica and polystyrene particles (80-500nm)[142]	80 nm resolution

4.2 Acoustic Cell Patterning for Tissue Engineering

The label-free, precise, and gentle spatial control of particles using acoustic tweezers allow for a flexible and versatile patterning of cells, while its non-contact and biocompatible nature can preserve cell viability and functionality, rendering it a suitable tool for tissue engineering.[152–154] Reconstructing the physical architecture of native tissues is one of the key aspects in tissue engineering.[155] Patterning cells is instrumental for analyzing cell-cell interactions and collective cell behavior such as network formations and neurite guidance, angiogenesis, cardiomyocyte beating, and myofibrillogenesis.[156–159] Acoustic radiation forces are more commonly used to pattern cells into 2D or 3D constructs wherein suspended cells can be actively guided and accurately organized in pressure nodes or antinodes, based on their compressibility and density. These reposing sites can be designed to create various spatial patterns, which can remain fixed over time or dynamically reconfigured by changing the frequency or by shifting the phase.[160]

The two main steps in tissue engineering are often divided into the initial organization of the cells into the pattern guided by acoustic forces, followed by a step to preserve the cell pattern to establish cell-cell connections to mature into tissues.[160] The preserving step, *i.e.,* maintaining the patterned architecture over the tissue development period, is highly dependent on the cell type, cell-cell affinity, and cell-

environment interactions. Cells with higher affinity rapidly form a strong arrangement shaped by the acoustic pressure node design, while low-affinity cells can easily migrate from their initial position.[161] To overcome this issue, hydrogels are often used to better maintain the cell patterns over time.

4.2.1 Single pressure node patterning

The linear organizations of cells are commonly seen in native tissues. For instance, cardiac, endothelial, and fibroblast cells tend to spontaneously organize in linear arrangements of elongated cell structures to induce cell-cell interconnections and enhance their capability to withstand contractile and tensile loads in tissues.[162,163] ARFs in standing waves have been widely reported to effectively guide cells and particles in parallel lines and nodes within seconds by activating one or two pairs of IDTs.[164] For instance, SSAWs were used to pattern HEK293T, endothelial (HMVEC), and glioma (U87) cells into pressure nodes and lines to study the gap junctional dye transfer dynamics.[165] This method allowed to successfully quantify the average dye transfer rates for all three cell types, showing an increase in intensity signal over time as an indicator of stronger cell-cell connection. Taking a step further, epithelial cancer cells (HeLa) and endothelial cells (HMVEC-d) were linearly patterned using SSAWs to study the cell migration of cancer cells with a preserved cell viability (>99%) after 24h.[166]

Despite the straightforward and rapid acoustic linear cell patterning, one of the main challenges of tissue engineering is the preservation of the cell pattern over time for tissue maturation. One approach for maintaining the cell pattern is to transform the free-moving cells to an adherent state. Under the presence of SSAWs, cells can form linear patterns levitated above the substrate, avoiding surface contact. Upon the removal of acoustic waves, cells were shown to be gently gravity-deposited on a collagen-treated surface, allowing for the pattern to be maintained.[165] However, this scaffold-free approach to preserve cell patterns can be time-consuming (>1h) and the patterns can easily be deformed. As a solution, scaffolds have been proposed to maintain the cell pattern over time. The formation of functional collateral cylindroid for ischemia therapy was performed by acoustically patterning endothelial cells (HUVECs) and human adipose-derived stem cells (hASC) in hyaluronic acid hydrogel (Figure 4.3.B).[158] SSAW-patterned structures exhibited higher secretion of angiogenic growth

factors (VEGF) and anti-inflammatory cytokines (IL-10) for up to 7 days prior to transplantation into a mouse model. Many studies are focused to retain acoustically defined patterns by polymerizing the surrounding hydrogel after the SAW exposure. Photocurable polymers, including poly(ethylene glycol) diacrylate (PEGDA) and gelatin methacryloyl (GelMA), were used to create patterns of HeLa, MC3T3-E1, and P12 Adh cells in capillary tubes using one mirrored IDT pair,[167] and slanted-finger interdigital transducers (SFITs) for the nodal alignment of cardiomyocytes in GelMA (<10 sec).[159] Acoustically patterned cardiac cells demonstrated beating activity after 5-7 days with high cell viability (90%).

Linear patterning via BAWs has also been vastly used, for instance, to study angiogenesis. ARFs in the form of standing waves were shown to induce cell banding patterns for HUVECs in a 3D collagen-based hydrogel for up to 10 days.[168] Acoustically patterned HUVECs resulted in lumen-containing networks throughout the hydrogel on day 10. Linear patterning has also been reported to recreate muscle fibers and enhance the ability of cells to withstand tensile loads.[157] C2C12 myoblasts cells were suspended and acoustically patterned in GelMA, where cells showed enhanced myofibrillogenesis with aligned bundles of myotubes after 7 days (Figure 4.3A).[157] Acoustic patterning and high-frequency ultrasound imaging tools have been integrated to study the vascularization of constructs with defined microvessel size and orientation.[169] One particular prospect of acoustic manipulation of cells is their combination with 3D bioprinting. ARFs were generated in a bioprinter nozzle to align C2C12 cells and HUVECs in the center of GelMA fibrin hydrogel, narrowing the cell distribution to 5% of the bioink width and thus enhancing the orientation control and the elongation of the cells in the printing direction.[170] In a similar manner, but using human osteosarcoma cells (MG63) and hASCs, linear cell patterns were successfully produced in an alginate-$CaCl_2$ solution as a bioink for acoustic printing with high cell viability (>80%).[171]

4.2.2 Multiple pressure nodes patterning

In addition to linear patterns, complex geometries of cellular arrangements can be attained using acoustic waves. BAW-based devices have been more often reported for patterning cells and particles into various geometries due to their wider acoustic

domain compared to SAWs. For instance, a heptagonal acoustic chamber with 7 transducers could dynamically pattern particles, MDCK cells, and microbubbles in linear and hexagonal geometries by controlling the number, position, and phase-shifting of activated transducers.[172,173] In a similar heptagonal platform, C2C12 and Schwann cells were patterned to form neural network interconnections, and study the outgrowth of neurites, which was largely governed by the orientation of the initial pattern.[174,175] ARFs in BAWs also allowed studying the forces for cell adhesion and cell organization, which influence cell functionality. Rat C6 cells were patterned in a hexagonal arrangement, showing an increased concentration of the adhesion molecules NCAM and N-cadherin at the cell-cell interfaces after 8 minutes of BAW induction.[176] Despite the advantages and applications of BAWs to induce cell-cell contacts, some considerations should be taken into account when choosing this platform, including the heat generated by the piezoceramics, spatial control limitations, time of exposure, and the avoidance of the direct cell contacts to cytotoxic piezoceramics.

As discussed in the previous section, cell patterns can be preserved over time by suspending cells in a hydrogel. NIH 3T3 fibroblasts were embedded in fibrin gels and SSAW patterned in nodes, where a cage-like structure was formed due to cell migration and growth (Figure 4.3.C).[177] Moreover, acoustic radiation forces can levitate cells in multiple parallel horizontal planes to form 3D constructs. Examples have been shown for the development of multilayer brain-like architectures with human embryonic stem cell-derived neuro-progenitors using fibrin hydrogels,[178] and sheet-like assemblies of epithelial and fibroblasts for up to 14 days.[179]

One limitation that should be considered with SAW devices compared to BAWs, is that usually their optimum operating frequency is fixed by the IDT geometry. As a solution, a dynamic cell patterning mechanism can be performed using slanted-finger IDT (SFITs).[180] SFITs allow changing the distance between pressure nodal lines, and hence the dynamic adjustment of cell alignments. Circular slanted-finger interdigital transducers (CSFITs) were also reported to dynamically manipulate particles.[181]

Another approach to create complex geometries is using waveguides, consisting of structures mounted on top of the piezoelectric element. Circular, rectangular and

triangular acoustic waveguides were studied for guiding particles to the reference waveguide shape.[182] Similarly, but using a Petri dish as the waveguide coupled to a PZT piezo, PC12 cells were successfully patterned in concentric circles.[183]

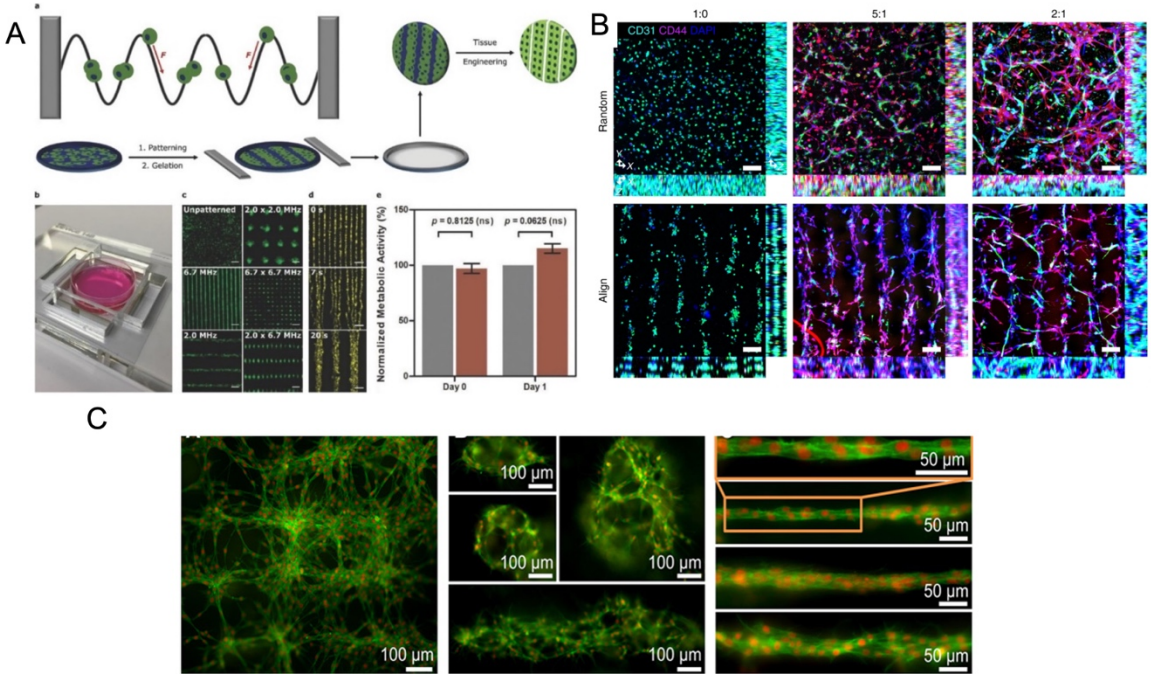

Figure 4.3. Acoustic cell patterning for tissue engineering. **A)** Myoblasts patterning using BAWs with controlled gelation showing pattern preservation over time (Scale bar =200 µm).[157] **B)** Microvessels in hindlimb muscle via SSAW patterning of HUVECs and hADSCs at different cell ratios (1:0, 5:1, 2:1) (Scale bar =100 µm).[158] **C)** SSAW-patterned fibroblasts in fibrin gels with multiple 3D microscale cellular structures forming network (left), cages (center), and unidirectional bundles (right) after 30 hours.[177]

4.2.3 Acoustofluidics for spheroids formation

In addition to linear and multiple nodal cell patterning, significant work on spheroid formation via acoustophoresis has been conducted. SBAWs have been effectively used to aggregate cells into spheroids (Figure 4.4.A),[161] including embryonic mouse brain cells using photocurable GelMA to model Alzheimer's disease,[184] $HepG_2$ showing high viability for up to 10 days[185], and 3 weeks,[186] RBCs and $HepG_2$ using different transducer geometries,[187] and core-shell ovarian cancer (OVCAR-8) cells for therapeutic studies and tumor interactions.[188]

SAWs have also been exploited to form spheroids by modulating pressure nodes for controlled cellular aggregation. In an SSAW platform, size controllable $HepG_2$ and HEK293 aggregates were formed with a smooth spheroid surface after 24 h and high proliferation and viability for up to 7 days.[13] Similarly, 3D multicellular human mononuclear leukemia spheroids (THP-1) were acoustically formed within pressure nodes using GelMA hydrogel (Figure 4.4.B). These spheroids showed faithful resemblance to cancer models where the cell aggregate activity was inversely proportional to the drug concentration with a lower sensitivity to drug toxicity in

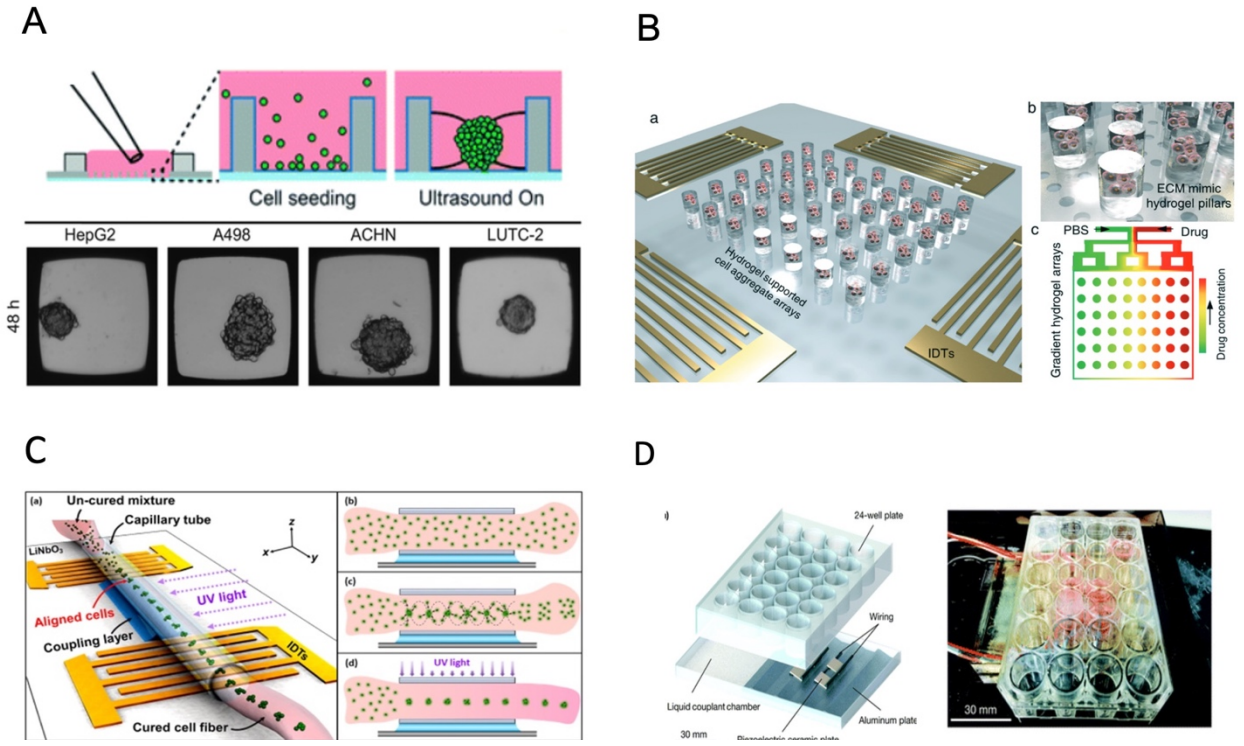

Figure 4.4. Cell spheroid formation methods using acoustofluidics. **A)** Acoustic trapping platform for spheroid formation after 48 h using a protein repellent coating (Microwell is 350 μm wide).[161] **B)** Acoustic assembly showing multicellular aggregates formed in acoustic pressure nodes and photocrosslinked in the hydrogel pillars (left, top right) and convection-diffusion based drug gradient system (bottom right).[189] **C)** SSAW-based spheroid formation platform consisting of a polyethylene tube coupled to a parallel IDT setup with a water-coupling layer (left), where cells seeded in a cross-linkable hydrogel are patterned and UV crosslinked (right).[167] **D)** Acoustic streaming-based cell agglomeration platform consisting of a fluid coupling layer (left) to transmit acoustic waves to a 24-well plate (right) (Scale bar=30 mm).[193]

comparison to monolayers.[189,190] Single SSAW fields have also been shown to generate mono-sized spheroids by coupling capillary tubes to the piezoelectric substrate along the wave propagation direction.[167,191,192] In this method, cells are first guided by acoustic pressure nodal arrays and then self-assembled to form spheroids. This mechanism was tested for HeLa cells in polymerized hydrogels (PEGDA and GelMA) to create spheroid embedded fibers (Figure 4.4.C).[167]

Although less explored, acoustic streaming can be also used for spheroid formation. The hydrodynamic drag forces induced by acoustic microstreaming via a piezo element coupled to a microwell channel could agglomerate cells in the center bottom of the wells, forming spherical and compact spheroids (Figure 4.4.D).[193] A similar approach, albeit in a SAW setting, used 30 MHz focused surface acoustic waves to create microstreaming for BT-474 cell aggregation in well plates.[194]

4.3 Acoustofluidics for Therapeutic Applications

The acoustically formed tissue structure, such as pseudo tumors are valuable drug screening models to investigate the response to chemotherapeutics such as Gemcitabine on pancreatic cancer cells (Panc02) and 5-fluorouracil (5-FU) on HepG2 spheroids.[190,13] However, the role of acoustofluidics in drug development is not limited to the drug model's fabrication. Various phenomena caused by acoustofluidics, such as acoustic streaming and mixing, sonoporation, nebulization, and other acoustic forces are shown to be powerful tools in therapeutics development from the drug synthesis and nanocarrier fabrication to the delivery of active agents into the target tissue using acoustic energy.

4.3.1 Drug development and nanoparticle synthesis

One of the recent applications of acoustics in drug development is the synthesis of nanoparticles as drug nanocarriers. Nanoparticles have been increasingly employed for delivering therapeutic agents such as chemotherapeutics and vaccines. These nanocarriers can reduce the off-target toxicity and immune response by protecting the cargo from opsonization and subsequent sequestration by the phagocyte system. This protective mechanism, combined with targeted delivery and controlled release, can

help the nanocarriers to release their cargo more effectively at the target site of interest and reduce their overall toxicity.[6]

In the self-assembly of nanoparticles, the mixing time and quality are critical and generally govern the nucleation rate and the size of the nanoparticles. Therefore, controlling the mixing time allows to tune the size of the nanoparticles which is the key physical characteristic for their transportation in the body and the target delivery efficiency. Huang *et al.*[195] used microstreams to synthesize various types of organic and inorganic nanoparticles, such as DNA/lipid complexes, polymeric, and chitosan nanoparticles. In another approach, a resonating membrane was embedded in a microfluidic platform with multiple edges to induce acoustic microstreams. The microstreams were used to facilitate and accelerate the mixing time for the synthesis of budesonide nanodrugs, a poorly soluble asthma medication.[196] Among various proposed designs, the 8-point star shape system showed the highest throughput of 8 ml/min for the production of Budesonide nanodrugs, DNA, and protein nanoparticles (Figure 4.5.A).[197,198]

In addition to microstreams, SAWs can be exploited for nanoparticle synthesis, albeit through a unique mechanism known as acoustic nebulization. SAW atomizers, first introduced by Kurosawa,[199] generally consist of a set of IDTs and a nozzle, channel, or paper wicking for the controlled dispensing of liquid at the propagation path of waves. When Rayleigh waves reach the liquid, the waves leak into the medium and deliver the acoustic energy to the fluid (33% approximately). The high-energy leaky SAW can cause destabilizing capillary waves at the interface of liquid and air, creating fine aerosols (Figure 4.5.B).[200–202]

The size of the aerosols can be tuned within the range of 0.1 and 30 μm by tailoring the acoustic frequency, fluid flow rate, and liquid characteristics, such as the surface tension and viscosity.[111,202,203] The lower power requirements and higher operating frequencies in SAW devices lead to higher biocompatibility of these systems, as opposed to the mechanical and cavitation-based aerosolization methods, which tend to cause damage to the structure and functionality of biomolecules during aerosolization. The preserved biocompatibility along with the control on the particle's size, higher delivery percentage,[204] and the miniaturization of the system, render SAW

as a potential platform not only for the generation of micro/nano-sized drugs but also as a delivery method, particularly for the pulmonary system.[205,206]

Friend's and Yeo's groups have extensively investigated the use of high-frequency SAWs for nanoparticle generation and drug delivery purposes. They studied the effects of SAW nebulization on the integrity and functionality of various shear-sensitive bioagents.[207,208] Upon atomization, the solvent content of the aerosols evaporates in flight and leaves behind the polymeric or protein nanoparticles to solidify. Friend *et al.*[201] used this mechanism to synthesize nanoparticles of poly-ε-caprolactone (PCL), a biocompatible and biodegradable polymer used for controlled release drug delivery. They further used this evaporative technique to produce solid protein nanoparticles of

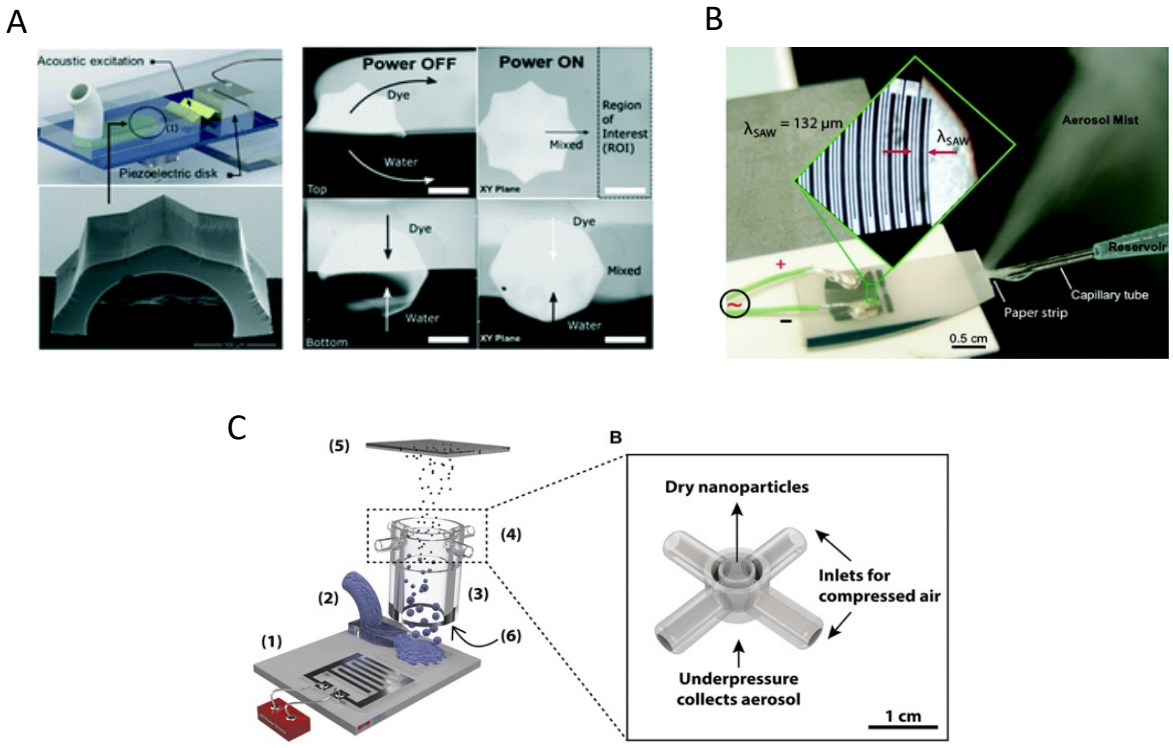

Figure 4.5. Mechanism of nanoparticle synthesis using acoustic waves **A)** acoustic microstreams induced by multiple edges system used for the synthesis of Budesonide nanodrugs and DNA nanoparticles.[197] **B)** SAW nebulization device for the synthesis of multilayer nanocarriers with encapsulated plasmid DNA.[200] **C)** SAW nebulization device with a gas control unit which introduces reactive gases to atomized airborne drops for the synthesis of amorphous $CaCO_3$ nanoparticles.[209]

bovine serum albumin (BSA) and insulin and showed the compatibility of the SAW atomization with proteins, in addition to the ability of nebulization to control the size of nanoparticles by tuning the initial protein concentration in the solvent.[201] In another work, a SAW atomizer was coupled with a drying unit to control the kinetics of crystallization through the rate of drying, where reactive gases were introduced for chemical modification of drops while in flight. As a proof of concept, CO_2-enriched air was introduced to initiate the reaction with airborne drops of $Ca(OH)_2$ and synthesized amorphous $CaCO_3$ nanoparticles (Figure 4.5.C).[209]

One unique capacity of this nanoparticle generation method is in fabricating multilayer polyelectrolyte nanocarriers. Qi *et al.* synthesized layer-by-layer coated nanoparticles of positively charged chitosan or polyethyleneimine and negatively charged carboxymethyl cellulose. In their method, they collected the condensed nanoparticles of the first layer in an oppositely charged polymer solution to form the second layer. Through the repetition of this atomizing-suspension cycle, nanoparticles with up to 8 alternating layers were produced, with a controlled drug release profile. The nanoparticles were used to encapsulate plasmid DNA and showed the capacity for transfection (gene delivery) of human mesenchymal progenitor cells and COS-7 cells.[200]

4.3.2 Drug delivery

Acoustic nebulization not only could be used for synthesizing therapeutics, but also has been explored as means for therapeutic delivery, including RNA, proteins, and even cells. The facile, low-energy, and biocompatible aerosol formation method via acoustic atomization has vast potential for the delivery of drugs to the pulmonary system. In this non-invasive approach, aerosols between 1 and 5 μm diameters can penetrate and be deposited in the lower pulmonary tract and alveoli where the large surface area and network of blood vessels facilitate the drug uptake.[210] Moreover, the high frequency and lower power requirement of SAW atomization methods significantly minimizes the large shear stress and cavitational damages of bigger molecules, being ideal for the manipulation of shear-sensitive bioagents, proteins, and DNA.[206,208]

SAW atomization was shown to be an efficient inhalation therapy method, which can directly deposit 70 to 80% of the short-acting b2 agonist salbutamol (asthmatic steroid) in the lungs, used for the treatment of asthma.[205] Furthermore, this technique

was used to synthesize peptide-laden aerosols of anti-mycobacterial peptides for pulmonary delivery.[211] Interestingly, 70% of the aerosols were in a favorable size range for deep lung penetration with a 90% recovery rate, while retaining their integrity and anti-mycobacterial activity.[211] This method was also used for the pulmonary delivery of antibiotic alternatives, phage K, and lysostaphin with minimal losses in antimicrobial activity (Figure 4.6.A).[212] Rajapaksa *et al.*[204] proved the ability of the SAW nebulization method to address some of the challenges in pulmonary gene therapy and vaccination (Figure 4.6.B). The plasmid DNA, encoding virus surface protein (influenza A, human hemagglutinin H1N1), was delivered through intratracheal instillation to successfully immunize rats and sheep. The results showed that atomization did not harm the integrity of the plasmids nor hindered the vaccine to promote protective antibodies.

A very novel application of biocompatible SAW nebulizers could be in the promising field of inhaled stem cell therapy. Cell therapy can be an alternative to chemotherapy for progressive respiratory system diseases. However, the susceptibility of stem cells to mechanical stresses during nebulization such as shear, cavitation, and heat hinders their direct delivery to the lungs. Alhasan and coworkers studied the cell viability and functionality under acoustic nebulization with an optimal 1.5 W driving power with the viability of up to 86.0%. They reported that the metabolic rate, proliferation, gene expression, and protein expression after SAW nebulization did not show significant differences compared to untreated cells, confirming the feasibility of this approach for pulmonary stem cell therapy (Figure 4.6.C).[213]

The ability of acoustics as a drug-delivering method is not restricted to nebulization and the pulmonary system. Ramesan *et al.*[214] used SAW to permeabilize the mucosal layer to enhance the delivery of small and large molecular therapeutic agents as an efficient route for local vaccine administration. The low penetration depth of SAW waves proved to be useful in inducing a local immune response, allowing to transport the cargo through the mucus lining and epithelial barriers into immunocyte-rich regions. This method avoids the cargo passing into the deeper vascularized submucosal regions in which the agent would be taken up by the circulatory system and thus diminishing the immunity (Figure 4.6.D).[214]

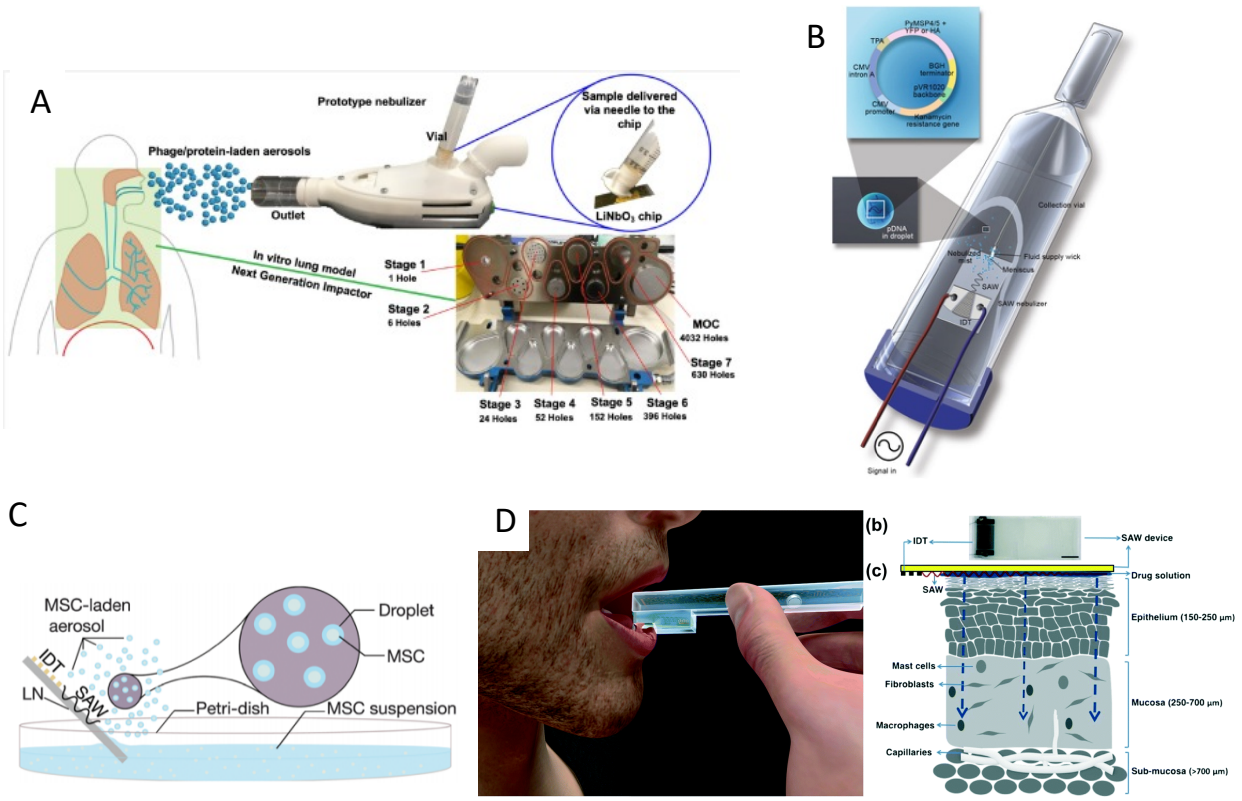

Figure 4.6. Acoustic devices for drug delivery. **A)** Acoustic nebulization system for pulmonary drug delivery of aerosols.[212] **B)** Acoustic nebulization for pulmonary plasmid delivery.[204] **C)** Stem cell delivery by biocompatible acoustic nebulization.[213] **D)** Acoustic waves for permeabilization of tissue and inducing localized immune response.[214]

Despite this clever use of lower penetration depth in high-frequency acoustic waves, the limited penetration often renders this mechanism more applicable for *in vitro* or *ex vivo* applications rather than *in vivo*. One of the growing *ex vivo* applications of acoustic waves, especially with high-frequency SAW is to acoustically mediate the transport of biomolecules, siRNA, nanoparticles, DNA, and membrane-impermeable dyes or nanoparticles inside the cell with methods such as sonoporation.

4.3.3 Sonoporation

The principal mechanism of acoustic-mediated cargo delivery into cells is sonoporation, which is the disruption of the cells' phospholipid membrane under acoustic energy. When acoustic pressure waves encounter cells or tissues, they promote both the opening at the cellular junctions, as well as the poration of the cell membrane.[215] Sonoporation has particularly been of interest as a nonviral transfection method to lower the toxicity and immunogenicity of viral transfection.[216]

Microbubbles are the focus of many ultrasound sonoporation methods, as the expansion and contraction of microbubbles under acoustic waves are shown to induce cell permeability and facilitate the entry of therapeutics into the cells.[217] If the variation in acoustic pressure is strong enough, it can lead to the collapse of the bubble, known as inertial cavitation, which creates a shock wave and high shear stresses. Qiu showed that acoustic cavitation could induce pores with diameters from 100 nm to 1.25 μm in cells. The higher acoustic pressure or longer treatment, the larger the pore size, leading to also a higher permeability and better transfection efficiency; nonetheless, at the expense of cell viability.[216,218,219]

Working with the uncontrolled and unpredictable nature of inertial cavitation is challenging as it leads to excessive cell and DNA damage, as well as the production of free radicals and reactive oxygen species (ROS), generating oxidative stresses.[215,220] Various proven alternatives have been introduced to avoid the micro-jetting forces of inertial cavitation, such as stable cavitation. In stable cavitation, the acoustic pressure is controlled to ensure that the expansion and contraction do not lead to the collapse of the bubble. This oscillation can be used directly for infiltrating the cell membrane by pulling and pushing the plasma,[221] or indirectly by generating acoustic microstreams. Although the flow field induced in steadily oscillating bubbles has a generally lower velocity than that of micro-jetting, the continuous shear stress and Stokes' drag force on cells can be sufficient to reduce the micro-viscosity of the lipid bilayer and effectively disrupt the membrane, while remaining controllable and safe for cells.[93,222]

Meng *et al.*[223] used an array of monosized bubbles, sequestered in the sidewalls of their microfluidic channel to induce sonoporation (Figure 4.7.A). The microbubbles oscillate stably with similar amplitude and resonance frequency and each one

independently created a pair of counter-rotating microstreams. The infused cells were trapped by the drag force from the acoustic microstreaming vortices and the secondary acoustic radiation force at the bubble surface, where the shear stress permeabilized MDA-MB-231 cells to allow propidium iodide (PI) to pass through the membrane. Recently, a versatile and high throughput intracellular delivery method was proposed by integrating hundreds of oscillating lateral cavities with an interdigitated electrodes array in a platform named Acoustic-Electric Shear Orbiting Poration (AESOP).[224] In this two-step strategy, cells initially were trapped in the acoustic microstreams where the mechanical shear stress induces nanopores in cell membranes while the electric field from electrodes expands the nanopores (Figure 4.7.B). AESOP system showed the delivery of molecules from <1 kDa to 2 MDa into both adherent and suspension cells, with over 90% delivery efficiency, >80% cell viability, and remarkable throughput of 1 million cells/min per chip.

In addition to the bubble-based mechanism, direct interaction of acoustic waves with cells can also induce sonoporation, especially at high frequencies.[216,222] For instance, standing waves were shown to permeabilize the cell membrane in the absence of bubbles. The viability of cells with and without cavitation was compared and the cavitation-free method showed higher viability rates. This method was further used to enhance the intracellular delivery of drugs such as doxorubicin, apigenin, and luteolin to cardiac myoblast cells.[225] Belling *et al.*[226] introduced another BAW-based microfluidic device for high throughput sonoporation. Their platform consisted of a square glass microcapillary attached to a piezoelectric operating at 3.3 MHz. Under this acoustic field, cells experienced acoustic microstreaming and acoustic radiation forces that thrust cells towards opposite capillary walls, inducing shear stress-sonoporation (Figure 4.7.C). The platform showed an efficient gene delivery with a nuclear membrane rupture at a clinically-relevant rate of 200,000 cells min^{-1}, thus promising a non-viral transfection method for gene-modification treatments.[226]

One concurring challenge is that the frequency in these bulk platforms is not high enough to completely obviate the possibility of cavitation. Belling *et al.* mentioned their

system may not categorically suppress cavitation.[226,227] As a solution to avoid the risk of cavitation, Zhang *et al.* used a bulk-based nano-electromechanical device for achieving a hypersound (≈GHz) regimen (Figure 4.7.D). They proved that they can deliver both eGFP plasmid DNA and doxorubicin through transient nanopores created in the cell membrane by the combination of hypersonic poration and acoustic streaming, with high viability and internalization efficiency.[228]

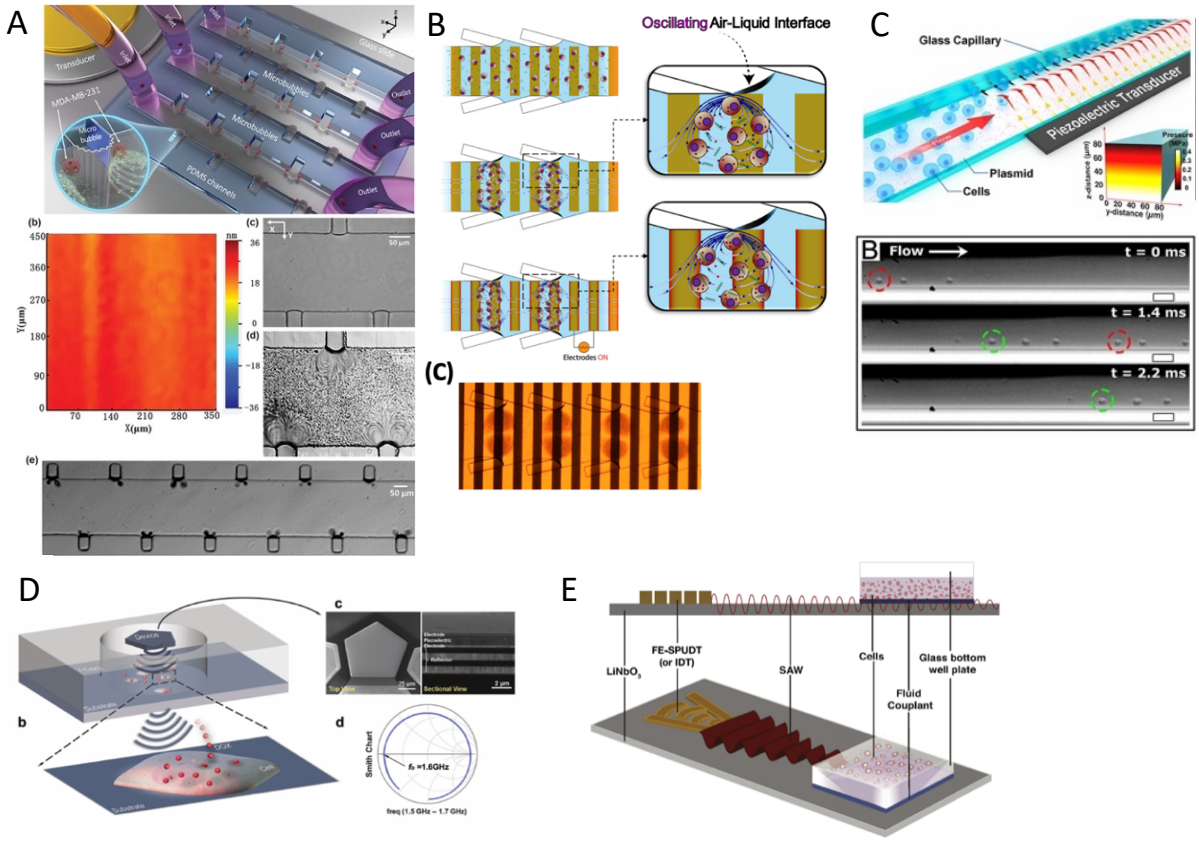

Figure 4.7. Acoustic platforms for sonoporation and therapeutics delivery to cells and tissue. **A)** Sonoporation by acoustic steams from an array of oscillatory bubbles.[223] **B)** combination of acoustic microstreams by bubbles and electroporation for gene delivery.[224] **C)** BAW-based microfluidic device for high-throughput shear stress-sonoporation by the combination of microstreaming and acoustic radiation forces that push cells towards opposite capillary walls.[226] **D)** high-frequency bulk-based nano-electromechanical device for delivery of eGFP plasmid DNA and doxorubicin through hypersonic membrane poration and acoustic streaming.[228] **E)** Focused TSAW for delivering siRNA into nonadherent cells.[231]

A plausible reason for the high viability of high-frequency molecular delivery devices may lie in the mechanism of cell permeabilization. In high-frequency platforms, unlike cavitational sonoporation, the disruption of the lipid membrane is a temporal and rapidly healing mechanism.[206,229] Hence, SAW platforms that generally operate in high frequencies can be pertinent technologies for efficient sonoporation. Under SAWs, the openings in the membrane facilitate intracellular delivery through the cytosol in the absence of endocytosis. This lower power method allows the exogenous biomolecules to be uniformly distributed in the cytosol, escape endosomal recycling, and it also increases their chance of reaching the nuclei while retaining the integrity of both cells and cargo during the exposure.[206,230] One of the reasons for the maintained integrity is the nature of exposure, which involves continuous and low-amplitude waves with higher frequencies compared to short and fierce pulses.[231]When the transmembrane delivery is achieved and upon the removal of the acoustic excitation, the lipid membrane instantaneously reorganizes into its native structure to keep cells healthy. The high biocompatibility and delivery efficiency can be used for applications such as cell transfection in the emerging field of chimeric antigen receptor (CAR) T-cell therapy.[206,230]

The short exposure of cells to SAW with frequencies over 10 MHz was also shown to facilitate homogenous internalization of gold nanoparticles by two- and six-fold increments after 30 sec and 10 min exposure times, respectively. Successful cellular uptake of the fluorescently labeled Dextran and small interfering RNA (siRNA) was reported with cell viability of over 97%. The acoustically-transfected HeLa cells, with GAPDH silencing RNA, showed a two-fold knockdown in the gene expression and protein levels of the target enzyme.[230]

In a follow-up study, the same group exploited the use of focused TSAW to deliver siRNA into nonadherent Jurkat and HuT 78 cells which are particularly challenging to transfect (Figure 4.7.E). The efficiency of this acoustofection technique was comparable to that of the standard nucleofection in achieving a 2-fold gene knockdown, however, with superior cell viability of over 91%, as opposed to 76% in nucleofection.[231]

Table 4-2 Acoustically-mediated therapeutic delivery

Application	Delivery Mechanism/ Acoustic parameters	Nanoparticle and Drug Agents (target)/Cell type (cargo)	**Delivery route**	Uptake/Results Advantages/Shortcomings
	SAW Nebulization (20-30 MHz, 1W, 110 uL/min)	pVR1020-PyMSP4/5, pVR1020-YFP; H1N1 (pDNA encoding influenza virus protein) in droplets[204]	Intratracheal instillation (in vivo, mice) and pulmonary inhalation (in vivo, sheep)	>90% of pDNA integrity preserved, serum hemagglutination inhibition (HAI) titers of 95-122, YFP expression after 24 hr
	SAW Nebulization (30MHz, λ=132μm)	Plasmid DNA encapsulated in PE/CMC, Chi/CMC bilayer and Chi/CMC/Chi trilayer NP; pVR1020-YFP encapsulated in PEI/CMC[200]	In vitro hMPCs and COS-7 cells	Release up to 19 days for trilayer nanocarrier
Drug Delivery	SAW Nebulization (20 MHz, 1-1.5W, λ=200μm, 110 uL/min)	B2 agonist salbutamol-octanol (for asthma) in droplets (2.84 ± 0.14μm)[205]	In vitro pulmonary model (60 L/min airflow)	70-80% delivery to lung model
	SAW permeabilization (17-55 MHz, λ=243-72μm, 100mV)	Molecular therapeutic agents (fluorescein, FITC-dextran, FITC-albumin) [214]	Mucosa of a porcine buccal model	>95% penetration rate in mucosal layer
	SAW Nebulization (29.78MHz, 2.93W)	Peptide-laden aerosols (1-5μm)[211]	In vitro pulmonary model 'Next Generation Cascade Impactor' (15 L/min respiratory flow rate)	> 90% recovery rate
	SAW (HYDRA) Nebulization (10MHz, λ=400μm, 30 Vrms, 1.3 mL/min)	Myoviridae (phage K) and a lytic enzyme (lysostaphin) (for Staphylococcus aureus) (1-5μm aerosols)[212]	In vitro pulmonary model 'Next Generation Cascade Impactor'	>90% recovery rate
Stem Cell Therapy	SAW Nebulization (30 MHz, 1.5-3W, 350uL/min)	MSCs encapsulated in droplets (13.5 ± 0.5μm)[213]	Lung delivery	86±4.2% cell viability
Transfection	BAW inertial cavitation (microstreaming) (1MHz, 0.05-0.3 MPa, 50 dB (gain), 5-60s (sonication))	MCF-7 (PEI, DNA complex, pIRES2-eGFP)[218]	Sonoporation	32.0±3.9% DNA transfection efficiency, 95.2 ± 3.2% cell viability
	BAW inertial cavitation (bubble bursting) (0.5-100 Hz, 1.0 W/cm^2, 15-30s (sonication))	HeLa (plasmid pGL3-Luc, 4KD FITC-dextran)[219]	Sonoporation	6.0±1.9% necrotic cells, 8-fold increase of gene expression at 5Hz
	BAW inertial cavitation (microstreaming, shear induced) (10-30kHz, 12.5-35Vmax, 10ms)	HeLa, K562, Jurkat (plasmid DNA encoding Cas9 protein and sgRNA)[224]	Sonoporation	>80% delivery efficiency >20% gene knockout >80% cell viability
	BAW inertial cavitation (acoustic force microstreaming, shear stress) (3.3 MHz, 0.48 ±0.04MPa, 40Vpp)	Jurkat, PBMCs, CD34+ HSPCs (Cy3-DNA, eGFP-expressing plasmid)[226]	Sonoporation	200,000 cells/min delivery throughput >80% cell viability
	BAW (acoustic streaming) (1.6GHz, 300 mW, 1-10min (exposition))	HeLa (plasmid DNA pEGFP-N3, doxorubicin DOX)[228]	Sonoporation	50% cell apoptosis due to uptake of DOX (10 min exposition)
	TSAW (Rayleigh wave) (10-30 MHz, (λ=390-133μm), 10Vpp, 10min (sonoporation))	Jurkat and HuT78 (siRNA)[231]	Sonoporation	2-fold gene knockdown >91% viability

Membrane Permeability and Drug Delivery	SAW-phase shifting inertial cavitation (microbubble bursting) (22-24MHz, 100Vpp (bursting))	MCF-7 (PI)[232]	Sonoporation	82.4±6.5% sonoporation efficiency, 90±8.7% cell viability
	BAW cavitation (microstreaming, sharp edges) (4.6kHz, 5-40Vpp (switch))	DU-145 (PI)[233]	Sonoporation	>90% sonoporation efficiency >90% cell viability
	BAW (cavitational and non-cavitational) (1-3 MHz, 2.2 W/cm^2, 0.25 MPa, 360s (sonoporation))	Live-cell goldfish epidermis (in vivo)[227]	Sonoporation	Cavities within intracellular membranes
	SAW stable cavitation (microbubbles cavitation) (50Hz (cyclic, 5s), 0.4MPa, 60dB, 50 Hz (cyclic))	Bovine endothelial cells (PI)[221]	Sonoporation	No ROS, controllable shear stresses, no cell lysis
	BAW stable cavitation (microstreaming microbubbles) (107kHz, 41.7kPa, 7.4 and 41.7 kPa, 30-90s (actuation))	MDA-MB-231 (PI)[223]	Sonoporation	96.6 ± 1.74% sonoporation efficiency, 97.9 ± 1.26% cell viability
	SBAW (acoustic pressure, contrast agent-free) (2.27 MHz, 3.2-40 Vpp, 0.11-1.39MPa)	H9c2 (doxorubicin, apigenin, luteolin)[225]	Sonoporation	CA-free showed higher cell viability at 40Vpp Cytotoxicity >40% (doxorubicin) >50% (apigenin) >90% (luteolin)
	TSAW (Rayleigh wave) (10MHz (λ=398μm), 2W, 0.5-10 min (sonoporation))	HEK293T and HeLa (Au NP-FITC tagged, Dextran, Cy3-labeled siRNA, GAPDH)[230]	Sonoporation	>6-fold increase of NP concentration 2-fold knockdown in gene expression and protein levels >97% cell viability

4.4 Acoustofluidics as a Functional Force for Investigating Phenotypes in Biological Organisms

Acoustic waves can have a complex functional influence on cells and tissues which requires extensive investigation. Sonoporation, as discussed in the previous section, is one of these functional effects of acoustics that leads to the disruption of the cell's membrane. However, the interaction of acoustic waves is not limited to membrane rupture. Although many of these effects have been studied in conventional US systems, the MEMS-specific wave modes and operating frequencies can introduce unique and interesting effects on cell behavior, structure, and phenotypes. Moreover, miniaturization allows to focus or amplify the acoustic effects without drawbacks in large-scale systems such as uninhibited heating and cavitation, by offering a well-controlled domain.[234]

Devendran *et al.*[235] scrutinized the phenotypes of four distinct human and mouse cell lines after exposure to 48.5 MHz SAW. The viability, nuclear morphology, and proliferation rates after exposure remained unaffected, however, they noted less cell attachment and spreading for mesenchymal stromal cells and mouse osteosarcoma. More interestingly, SAWs increased the metabolic activity in human keratinocytes and mouse fibroblasts. They hypothesized that the increased metabolic activity might be due to the acoustophoretic force pushing cells to the sides of channels, which could protect them from shear stresses from background flow. However, their further results confirmed that the acoustic excitation directly increased the cell's metabolic activity (Figure 4.8.A).[235] As suggested by this study, the SAW effect on cells can be very cell-type dependent. Moreover, since the acoustic radiation forces are often accompanied by other acoustic effects such as acoustic microstreaming, one of these acoustic phenomena might be the dominant effect depending on the experimental conditions. For instance, the change in proliferation rate that was not observed in the previous study, was seen in another study using a similar frequency of 48.8 MHz, but in a streaming-dominant system.[236] The circulation of the culture media by SAW-driven acoustic streaming on a Petri-dish, coupled to a lithium niobate substrate by a layer of PDMS, showed a 36% increase in the rate of cell proliferation. This indicates that apart from frequency, other acoustic parameters such as the wave mode, time of exposure, the amplitude of the driving voltage, and the amplitude of vibration, can influence the dominant acoustic phenomenon and should be carefully considered.

Returning to the effects of acoustic waves on cells, one other interesting effect was reported by Brugger *et al.*[237] who patterned primary neuron cells in an SSAW platform and investigated the cell growth and cell adhesion direction after acoustic exposure. They observed that the neurite outgrowth was preferentially aligned to the axis of the SSAW pressure nodal lines,[237] which suggests the possibility of the cytoskeleton or the ECM realignment by acoustic waves.[234]

The mechanical stimulation of cells by conventional ultrasound waves has already been proved to cause various effects such as the increase in production of ECM and enhanced proliferation rate of fibroblasts and osteoblasts.[238] Stamp *et al.*[81] stipulated that these mechanical stimulations might be also present in SAW platforms. They used

a SAW platform to promote cell growth and to direct the migration of Saos-2 cells along an acoustic path for tissue stimulation, showing a 17% increase in the healing rate of an *in vitro* artificial wound.[81] The same group, in a more in-depth study, explored the effects of different acoustic parameters such as frequency, power, and wave modes on the proliferation rate and ROS levels for various cell types. Cells were exposed to SAWs and electrode-generated electrical fields, activated by similar radiofrequency signals, to distinguish the biological response to mechanical and electrical stimulation (Figure 4.8.B). Cells exposed to piezo mechanical SAWs exhibited a marked increase in growth rate and a 135 ± 85% surge in wound-healing speed, while the electrical-only stimulation did not show a significant effect. By excluding electrical effects, vibration and its mechanical stimulation on cells were pinpointed as the root cause for enhanced wound-healing and overall proliferation. Moreover, no SAW-induced ROS was observed in low power levels. [239] SAW has been also reported as an effective stimulus for wound healing by promoting tissue oxygenation in ischemic feet. Human patients treated with a commercial SAW Patch device (NanoVibronix), experienced an increase in oxygen saturation and an overall reduction in pain.[82]

In a similar vein, acoustic waves are an interesting topic for mechanical cues in stem cell studies.[215] Low-intensity acoustic waves were also associated with enhanced differentiation and production of growth factors in neural stem/progenitor cells,[240] while acoustic biophysical stimuli were employed by Lee *et al.*[241] to reprogram human dermal fibroblasts into multipotent cells.

One recent finding concerning the functional effects of acoustic waves on cells is the enhancement of exosome generation. Ambattu *et al.*[242] evidenced that after 10 min of low-intensity acoustic waves exposure to cancer cell lines, the exosome generation was increased by 1.7-fold. The high exosome production was attributed to increased calcium ion (Ca^{2+}) levels after acoustic exposure, which subsequently triggered a pathway that regulates exosome production.

The change in ion profile by acoustic waves is reported in other studies too. Membrane proteins, including ion channels under acoustic waves, experience mechanical vibrations that can alter the conformation of their active state. Some of these mechanosensitive proteins are calcium, potassium, and sodium ion channel

families which can translate mechanical stimuli into biochemical signals, in a process known as mechanotransduction.[243] These ion channels therefore can act as acoustically activated nano-valves which have been particularly a subject of interest in neuromodulation where an altered ion profile in neurons is the hallmark of neurological disorders.[244] The activation of ion channels and evoking action potentials are fundamental in the study of neuronal circuits and their functioning.[234] Ye *et al.*[245] transfected rat hippocampal neurons to express a mechanosensitive channel of large conductance (MscL), and used a 30 MHz SAW system to activate the channel. The MscL in the membrane sensitized the cells to an ultrasound stimulus of 0.25 MPa. While acoustically activated, the open MscL gate allows dyes to pass into the cytoplasm which can be a pathway for drug delivery. Moreover, the MscL-expressing cells showed faithful spike trains in response to acoustic pulses up to 5 Hz with millisecond accuracy. Lin *et al.* also reported on SSAW acoustic neurostimulation to modulate the kinetics of native mechanosensitive ion channels such as sodium and potassium in rat hippocampal slices.[246,247] In doing so, they could control the ion efflux, activate and regulate the shape and rate of spikes, and could study the effects of acoustic waves on neurons' excitability and firing thresholds, which are the minimum current neurons needed to produce an action potential (Figure 4.8.C).

The characteristics of acoustic signals such as intensity, duration, continuous or pulsed nature, and frequency of pulses are also influential in promoting or suppressing neuronal activities.[247,248] Zhou *et al.*[249] used a TSAW to trigger the neuronal behavior of C. elegans under a single-shot and short acoustic pulse. They observed that the mechanical stimulation of acoustic waves can reverse the locomotion behavior in C. elegans, as 85.29% ± 6.17% of them started to move backward after a 6.4ms pulse. The analysis of the calcium profile in the worms showed an elevated concentration of Ca^{2+} after acoustic excitation in a type of sensory neuron that are triggers in the face of danger or stress.[250,251]

This results suggests that it is possible to directly activate sensory neurons by acoustic waves. In another study, Miansari *et al.*[83] exposed C. elegans to SAW for an extended duration of 10 s to induce traumatic brain Injury (Figure 4.8.D).

The continuous exposure, although with less acoustic pressure than that of the pulsed, caused temporary paralysis of the worms and reduced chemotaxis learning and short-term memory loss. The effects of SAW on C. elegans in both studies were tightly connected with the mechanical vibrations on the cell membrane by the acoustic waves.

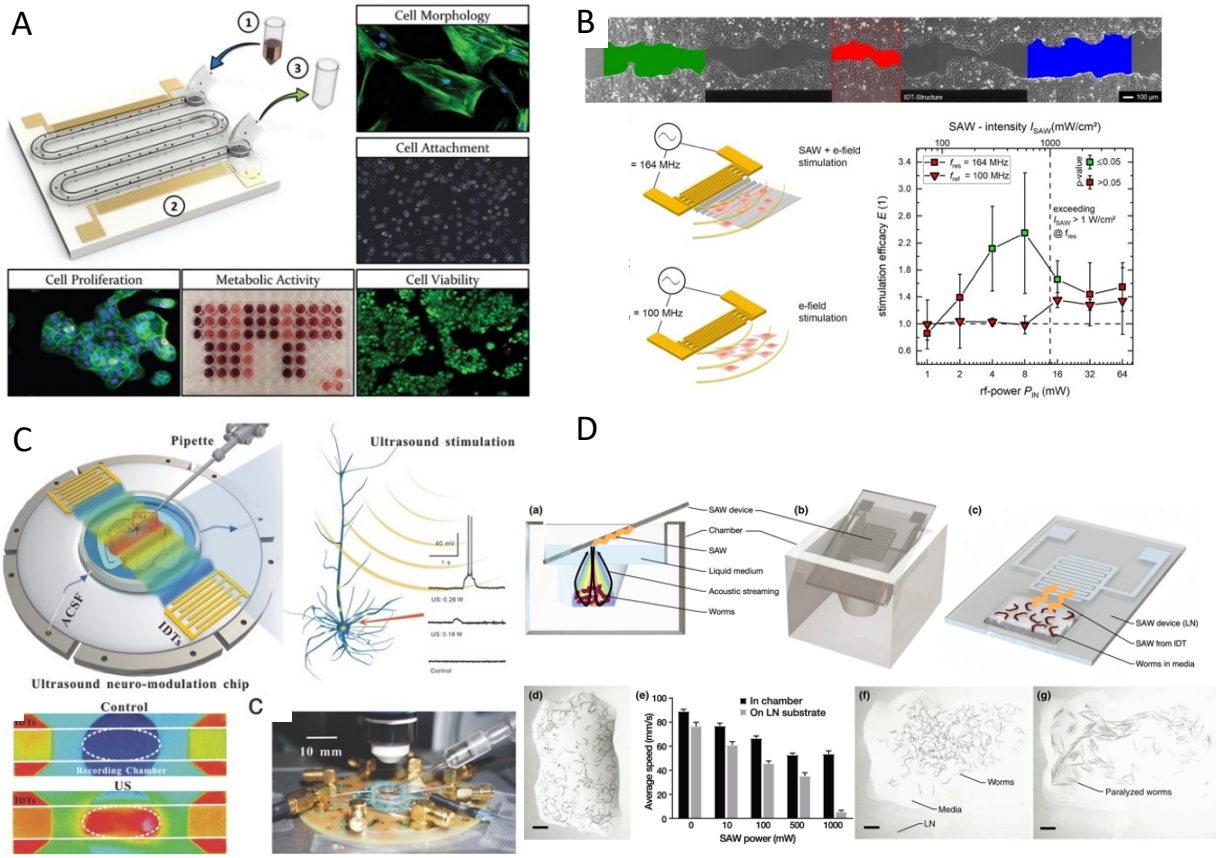

Figure 4.8. Acoustic settings to investigate the effect of the wave as functional mechanical stimuli on **A)** Cell's viability, morphology, metabolic activity and proliferation,[235] **B)** cell migration pattern and wound-healing properties,[239] **C)** neuromodulation and stimulation of neurons,[246] and **D)** the effect of acoustic waves on sensory neurons of C. elegans which induced short-term memory loss and brain injury.[83]

Table 4-3 Acoustic waves as functional stimuli.

Phenotype/ phenomena study	Target species	Wave mode	Acoustic parameters	Outcomes
Cell adhesion, cell morphology and cell metabolism	MSCs, MG63, L929 and HaCaT[235]	SAW (Leaky waves)	48.5MHz (λ=80μm), 400 or 800mV, 5 or 10 μL/min	Increased of metabolic activity in HaCaT and L929, cell adhesion was prevented, and morphology changed in MG63 and MSCs
Increase in proliferation rate	U-937[236]	SAW (Acoustic streaming)	48.8MHz (λ=80μm), 21.5 dBm	36±12% increase in cell proliferation
Cell proliferation, collagen, and non-collagenous protein (NCP) synthesis	Gingival fibroblasts, mandibular osteoblasts, monocytes[238]	BAW	1-3MHz 1:4 (pulsed), 0.1 and 0.4 W/cm^2; 45 kHz (continuous), 15 and 30 mW/cm^2	35-52% increase in cell proliferation in fibroblasts and osteoblasts, 112% increase in collagen and NCP synthesis, slight stimulation of IL-1B by all, VEGF production is stimulated by all, IL-8 and bFGF production was enhanced by osteoblasts
Cell growth and direct migration	Saos-2[81]	SAW (Leaky waves)	159MHz (λ=25μm), 300mW/cm^2, 4mW	15.2 ± 1.7% increased migration (correlated to wound healing effects)
Cell migration, proliferation rate and ROS production	MDCK-II, SaOs-2, T-Rex-293[239]	SAW	164MHz, 1 W/cm^2, 1-16mW	135 ± 85% increment in wound healing
Wound healing by tissue oxygenation	Ischemic feet patients[82]	SAW (PainShield SAW Patch)	96kHz for 30 min	Increase in oxygen saturation, pain levels dropped
Neurite outgrowth and cell differentiation	NSPCs spheroids[240]	BAW (stable cavitation)	1138kHz (single frequency mode) and (560kHz, 1138kHz (dual frequency mode), 40kPa,533mW/cm^2	Attachment and differentiation of NSPCs, Increase in calcium ion influx by dual-frequency ultrasound (stable cavitation)
Exosome generation	U87-MG, A549[242]	TSAW (sonoporation)	10MHz (λ=398μm), 10 min exposure (x7 cycles)	1.7 fold increase of exosome generation and 8-10 fold increase in exosome concentration 95% viability
Ion channel activation	CA1/CA3[246]	SSAW (Leaky waves)	30 MHz (5Hz pulses), 0.12-0.45MPa, -65mV	Large depolarizing currents up to 26 ± 2.1 pA/pF after 1s of SAW (0.45 MPa) 20% Calcein release in I92L-expressing neurons with repetitive SAW stimulation
Neuromodulation and neurostimulation of sodium (1), potassium (2) channels	CA1[247]	SSAW	27.38MHz, 0.13MPa, 2.9W/cm^2 (30s) 465mW/cm^2	Increase of neuronal excitability, change in sodium channel kinetics by 30% US stimulate the outward potassium currents by 13%
Neuromodulation for epilepsy treatment	Penicillin-induced epileptic monkeys, human epilepsy brain samples[252]	SAW (low-intensity)	28MHz, 0.13 MPa, 465 mW/cm^2	65% inhibition of epileptiform activities by increasing the local inhibitory neurons
Neuronal activation (1) Reduction of chemotaxis learning and short-term memory loss (2)	C. elegans[249]	TSAW (short-pulsed)	28.11MHz, 5W, 6.40 ms (pulsed) 20 MHz (λ=200μm), 50-1000 mW (5-10s)	85.29% ±6.17% mechanical stimulation Hindered associative learning, short-term memory and mobility

4.5 Acoustic Biosensing

Acoustic waves have a long history of application as biosensors, one well-known example is the commercialized quartz crystal microbalance (QCM) and its dissipation version (QCM-D). The QCM-D is a BAW method that can measure mass/density changes, viscosity, and elastic modulus of biological samples inside the liquid medium with pulse excitation of 5-20 MHz.[253] In recent years and with the advancements in MEMS manufacturing, the majority of the latest platforms have been shifted from QCM-D to SAW biosensors. The wide range of operating frequencies of SAWs allows for easy customization for detecting various biological samples, with higher frequencies yielding better sensitivity for smaller samples, such as biomolecules. Moreover, the confined and well-controlled detection region, low power consumption, and the capability of surface modification are some of the advantages of SAWs that render them appealing for biosensing applications.[80] The main sensing mechanism of SAW biosensors is somehow similar to that of QCM, in that the decay in frequency and the amplitude of acoustic waves are quantified for the detection of various biomolecules and biospecies (Figure 4.9).[254]

The general architecture of SAWs consists of an excitation IDT (input), a sensing region, and a readout IDT (output). The sensing region is on the propagation path of SAWs between the IDTs sets. This sensing zone can either be functionalized with probe molecules to bind to the floating target biomolecules and immobilize them for sensing, or it can be directly used for biosensing species, such as cells and tissues. As the acoustic waves emanated from the input IDT travel on the surface and reach the sensing region, they interact with the target species adsorbed on the surface, causing a change in the mass loading that is detectable by shifts in the SAW phase, resonant frequency, and amplitude.

When the output acoustic waves are received in the readout IDT, they re-transduce into electric signals for deciphering the measured changes in the acoustic waves into the concentration of target biological species or other sensing targets, such as the viscoelasticity of the species.[207]

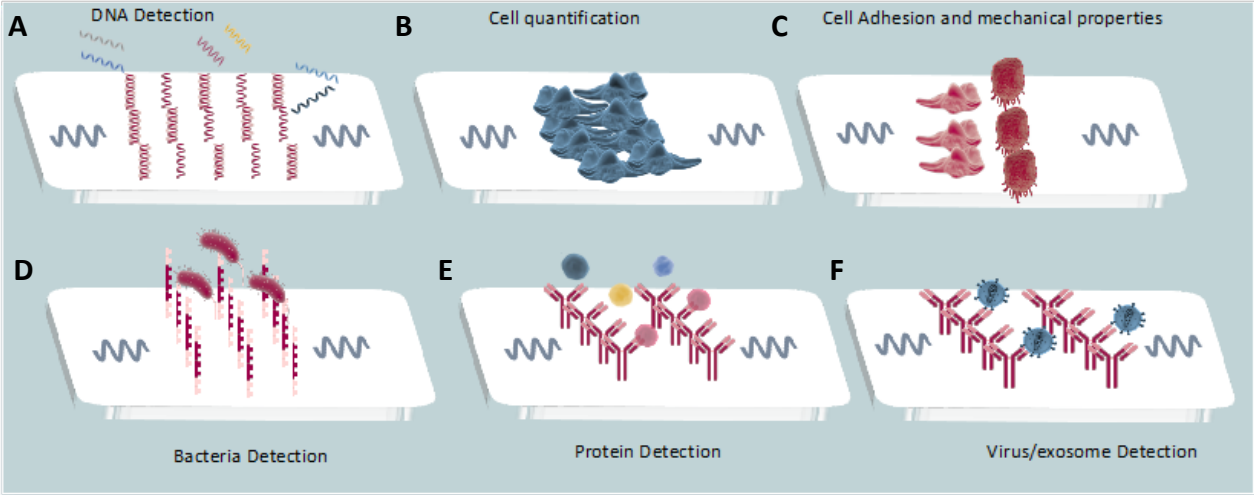

Figure 4.9: Acoustic waves as biosensors for **A)** DNA detection, **B)** cell detection and quantification, **C)** cell morphology characterization, **D)** bacteria detection, **E)** protein detection, and **F)** virus or exosome detection.

4.5.1 Acoustic biosensing for cells detection and quantification

The two major applications of acoustic biosensors for cell analysis are the quantification of cells and the characterization of their physical properties, such as viscoelastic properties. For instance, Chang *et al.*[255] devised a leaky SAW sensor for label-free quantification of MCF-7 cells. They coated gold electrodes with aptamers for specific capturing of target MCF-7 to enhance their sensitivity. The sensor showed a linear relationship between phase shift and the logarithmic concentration of MCF-7 cells from $1{\times}10^2$ to 1×10^7 cells per ml and showed that the detection limit of this method was 32 cells per ml.[255]

Wang *et al.*[256] used an SH-SAW sensor to quantify the mass loading of RAW264.7 macrophages and A549 cancer cells, by measuring the frequency shift in both 2D and 3D setups, showing no significant adverse effects on cell viability. They cultured A549 cells in a nanofiber scaffold to promote tumor formation and were able to monitor the increase in cell density and tumor growth over 8 days. In a similar way, the frequency shift could be monitored to measure the mass of the cells that sit in the delay zone. To increase the sensitivity, a high frequency of 6.4 GHz was used with a confined detection

region and was able to detect EMT6 and 3T3 cells at a single-cell level with a throughput of 10^5 cells.[257]

In addition to cell quantification, acoustic sensors can measure the mechanical properties of cells, such as stiffness and viscoelasticity. An extensive library of papers used QCM-D to measure these important physical properties of cells, which can divulge fundamental information about their physiological behavior and phenotypes.[258] More recently, SAW-based sensors have been reported for measuring the cell mechanical response with higher sensitivity. Wei *et al.*[259] used a Love-mode SAW sensor to measure the contractile properties of forces in cardiomyocytes. They seeded 10,000 HL-1 cardiomyocytes cells in the detection regions and controlled the contraction forces and stiffness by treating the cells with verapamil, which reduces the contraction forces and stiffness in the cells, and isoprenaline which acts reversely. By recording the phase and amplitude shifts, the changes in contractile properties could be correlated to the amplitude shift. Embedded microcavities on the SAW interrogation region could also be used to characterize the single-cell stiffness of MCF-7, MDA-MB-231, SKBR3, and JJ012 cell lines (Figure 4.10.A).[260]

Moreover, the high sensitivity of SAW sensors rendered them instrumental for the detection of pathogenic cells such as bacteria. Lamanna and colleagues proposed a conformable SAW immunosensor for the detection of E. coli bacteria where they grafted E. coli binding antibodies on the sensing zone and measured the change in mass loading caused by the bacterial adhesion. Their platform was based on the deposition of a thin film of piezoelectric aluminum nitride (AlN) on a recyclable polyethylene, Naphthalate, substrate. They compared the detection limit of identical IDT designs and piezoelectric (AlN) mounted on flexible PET substrate, to create Lamb wave modes and on a hard silicon wafer to create Rayleigh wave modes. A superior detection limit of 6.54×10^5 CFU (colony-forming units) mL^{-1} was attained on PET substrate compared to 1.04×10^6 CFU mL^{-1} on silicon (Figure 4.10.B).[261] This study is a showcase of direct bacteria detection, however, most studies in this area used the DNA equivalent of bacteria as the model for detection.

4.5.2 DNA detection

The common method for the detection of single-strand DNA (ssDNA), is to immobilize their matching strand as the DNA probe, introduce the sample for binding, and finally measuring the changes in the acoustic waves' characteristics. Cai *et al.*[257] immobilized DNA probes in the sensing area and upon hybridization of the target strand with the immobilized probe strand, a molecular film was formed, changing the wave velocity and the resonance frequency. Their platform showed a high detection sensitivity of 6.7 $\times 10^{-16}$ g cm^{-2} Hz^{-1}, making it capable of detecting a single DNA base.[257]

In addition, a similar mechanism has been specifically used to model bacterial detection to detect food pathogenic strain (E. coli, O157:H7).[262] A specific DNA sequence from E. coli O157:H7 was immobilized on the sensing region as the probe of ssDNA, allowing to measure the frequency shift (Δf) upon their hybridization with the complementary DNA.[262] A Love wave biosensor was also reported for the detection of Salmonella bacteria. The ratio of the wave amplitude change over phase shift (ΔA/ΔPh) was monitored during the binding of the target DNA to the Salmonella DNA template that was immobilized in the sensing zone and reported a detection limit of 100 bacteria cell equivalents per sample.[263] In a recent study, a LoC sensing platform that utilized SAW, was employed for the rapid detection of foodborne pathogens such as Bacillus cereus, Salmonella, E. coli, and Listeria (Figure 4.10.C).[264]

4.5.3 Protein detection and quantification

The mechanism of protein detection, similar to that of DNA detection, generally involves the immobilization of the capturing molecules, such as the corresponding binding antibody on the sensing area. Matatagui *et al.*[265] integrated a Love-mode SAW with a PDMS channel to measure the immunoreactions in a continuous flow condition. They immobilized a goat anti-rabbit antibody to capture rabbit immunoglobulins and compared the method with static QCM, reporting superior sensitivity for SAW.[265] Another application of SAW was proposed for detecting cardiac troponin I (cTnI), which is a standard biomarker for measuring risk stratification of acute myocardial infarction. In this platform, an anti-cTnI antibody on the delay line was anchored to capture the cTnI in human plasma and AuNP conjugated anti-troponin I was used as the detecting

antibody. Instead of traveling from input to output, these waves traveled three times due to reflections in IDTs, making their path three-fold longer. This longer path led to higher sensitivity and a better detection limit of 24.3 pg mL^{-1}, compared to 766 pg/ml for a single path (Figure 4.10.D).[266]

An alternative to the use of corresponding binding molecules as probes was proposed by Tretjakov *et al.*[267], where an imprinted polymer was used to create synthetic receptors. As Figure 4.10.E shows, after immobilizing IgG, the polymer was deposited on the substrate to form an ultrathin film via electrosynthesis. After washing out the cleavable IgG, their shape remained imprinted on the surface, and acted as a template for IgG detection for up to four regeneration cycles. The recognition efficiency of the imprinted surface for IgG was 4 times higher compared to interfering IgA, and 10 times higher compared to Human serum albumin (HSA).[267]

4.5.4 Exosomes and virus detection

Similar to protein detection, antibodies can be used as probes on the sensor surface to target membrane proteins on nanovesicles. Wang *et al.*[268] coated a SAW sensing zone with antibodies that target CD63 on the exosome surface for probing and interacting with a secondary (EpCAM) antibody and consequently measured the phase shift. The sensitivity was increased nearly two orders of magnitude by integrating an amplification method for gold nanoparticles, reaching a limit of 1.1×10^3 particles per mL of exosomes.[268]

The capacity of SAW sensors as a rapid and accurate PoC sensor for the detection of the Ebola virus, a relevant interest and necessity given the recent outbreaks, has been also demonstrated. By functionalizing the surface with an anti-Ebola virus antibody. A detection limit of 1.9×10^4 PFU (plaque-forming unit) mL^{-1} of the virus before inactivation was reported, being lower than that using standard PCR tests. Moreover, this platform was powered by batteries to make it portable, and also showed the advantage of time with a sensing time of 5-10 min.[269] Influenza A virus was also shown to be captured and detected by the immobilization of anti-H1N1 HA antibodies on the SAW platform with a detection limit of 1 ng mL^{-1}.[78]

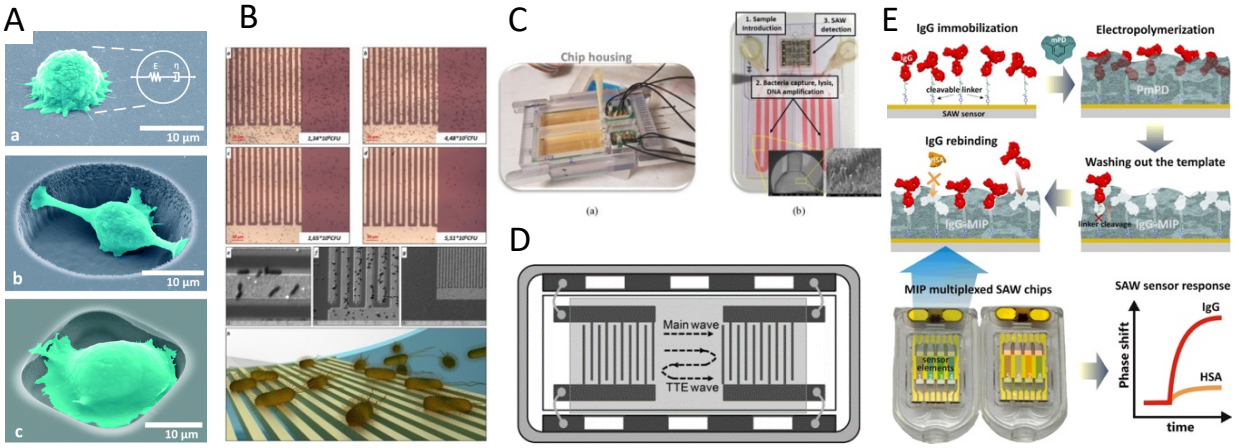

Figure 4.10. Acoustic settings for various biosensing strategies. **A)** Embedded microcavities on a SAW platform to characterize the single-cell stiffness,[260] **B)** a conformable SAW immunosensor for the detection of E. coli bacteria,[261] **C)** Integrated LoC device that can capture, lyse, and detect bacteria in separate modules for rapid detection of foodborne pathogens,[264] **D)** a SAW sensor with three-fold pathline for sensitive detection of cardiac disease biomarker,[266] and **E)** Protein detection platform using imprinted polymers as synthetic probes.[267]

Furthermore, the potential of SAW sensors as rapid detection chips for clinical applications was effectively proven by Gray *et al.* In their design, the authors functionalized detection channels using anti-HIV antibodies and they engineered the chip to require only 6 µL of blood plasma. Samples from 31 patients with HIV and 102 healthy volunteers were tested using this device, showing a remarkable 100% for both sensitivity and detection specificity. Moreover, all the positive results were read within 60 s of sample injection, paving the groundwork for their following smartphone-connected diagnostic platform.[270,271]

Table 4-4 Biosensing modes using surface acoustic waves

Detection target	Target details	Accuracy/Detection limit sensitivity	Wave mode (Substrate type)	Frequency
Cells	MCF-7 (human breast cancer cell)[255]	32 cells/mL	Leaky SAW (36 deg YX-LiTaO3)	100 MHz
	A549 (human lung adenocarcinoma tumoroids)[256]	Relative frequency shift with R^2 =0.9183 (3000-50,000 in 100 uL)	SH-SAW (36 Y-cut LiTaO3 with ZnO coating)	14.0412 MHz (λ=297μm)
	HL-1 cardiomyocytes[259]	10,000 cells/sensor missing info	SH-SAW (Quartz crystal)	(λ=28μm)
	E. coli[261]	LoD 6.54*10^5 CFU/mL	Lamb wave SAW (Polyethylene naphthalate)	500 MHz (λ=20μm)
DNA detection	DNA[257]	6.7 x 10^-16 g/cm²/Hz	SAW (LiNbO3)	6.4GHz
	E. coli O157:H7 DNA[262]	0.6439 nM/0.1kHz	SH-SAW (64 deg Y-cut LiNbO3)	386MHz
	Salmonella enterica (DNA binding)[263]	<100 Bacterial Cell Equivalents (BCE)	Love wave SAW (ST-cut quartz)	267-298kHz
	Typhimurium cells (DNA amplification)[264]	1-5 cells in 25 mL of milk	Love wave SAW (ST quartz)	155 MHz
	DNA mutation[272]	100% sensitivity and 88.6% specificity (CT & CC genotype) 98.0% sensitivity and 96.2% specificity (CT and TT genotype)	SAW (graphine oxide) sam5 system SAW instruments	N.I.
	DNA[273]	Detection limit 0.8pM	Love SAW (N.I.)	N.I.
Protein Detection	Rabbit immunoglobulin (antigen)[265]	602 ng/cm^2, and mass sensitivity of 38 m^2/kg	Love wave SH-SAW (ST-cut quartz)	163 MHz (λ=28μm)
	Cardiac troponin[266]	Detection limit of 24.3 pg/mL	Triple transit echo TTE SAW (36° YX-cut $LiTaO_3$)	200MHz
	IgA and HAS[267]	Selectivity factors of 0.3 and 0.09 for IgA and HSA	Love Wave SAW (IgG-MIP ultrathin films)	100-500 MHz
Exosomes and viruses	Exosomes (HepG2)[268]	1.1 x 10^3 particles/mL exosomes	SAW (silicon dioxide guiding layer SAW Instruments GmbH)	N.I.
	Ebola virus[269]	1.9 x 104 PFU/mL	SH-SAW (36° Y-cut $LiTaO_3$)	80 and 400 MHz
	Influenza A virus (H1N1)[78]	Detection limit of 1ng/mL	Love wave SH-SAW (41° YX $LiNbO_3$)	120 MHz
	HIV [270,271]	100% sensitivity for anti-gp41. 64.5% sensitivity for anti-p24	SH-SAW (Quartz crystal 36° Y-cut and 90° X-propagation)	251.5MHz

4.5.5 Acoustic waves for enhancing sensitivity limitations

One of the main challenges in biosensing assays which are based on the immobilization of the capture probe, such as ELISA and surface plasmon resonance (SPR), is the low signal-to-noise ratio. Two of the factors that are key in low signal-to-noise scenarios are the inefficient binding between the probe and target molecules, which causes a low signal, and non-specific adsorption of parasitic molecules, interfering with the target signal.[274] Acoustic waves have been used to address these biofouling issues by improving the target binding kinetics through acoustic mixing, and also breaking off the unwanted molecules from the surface by acoustic vibrations or streaming.

Renaudin *et al.*[275] integrated a Rayleigh-mode SAW mixer with an SPR sensing system to induce acoustic streaming and enhance the binding kinetics of an avidin-biotin assay (Figure 4.11.A). The acoustic streams led to effective mixing on a SPR prism and showed a 5-fold acceleration of binding kinetics. Despite these results, they reported interference in signal due to heat generated by the SAW platform.[275] Another SAW-enhanced SPR sensor was proposed to discern the streaming contribution from the heating effect by varying the SAW parameters and monitoring the temperature and streaming velocity (Figure 4.11.B). By doing so, the saturation time for polyethylene and avidin adsorption was accelerated by 82% and 24%, respectively.[276]

Many papers have been also dedicated to studying the ability of acoustic waves to break off non-specific bindings. The target biomolecules, especially in clinical samples, are immersed in a cocktail of other biological molecules which can induce noise signals in label-free biosensing applications. Meyer *et al.* used a thickness-shear mode resonator to clean non-target proteins from the patterned protein array, in a non-destructive manner. Upon the penetration of shear waves, the mechanical stress decreased the activation energy for the desorption of nonspecifically bound species, leading to an 85% drop in fluorescent intensity of the non-sensing area and 77% for the sensing area.[277] In another study, a high-frequency resonator was investigated to create controllable acoustic microstreams and to wash off the loosely surface-bound proteins by vortex-induced hydrodynamic forces. A human IgG antibody was immobilized on their platform showing a 58.3% drop in fluorescence intensity of the nonspecific mouse IgG antigen, while the reduction for specific human IgG was only 12.1% after hypersonic treatment (Figure 4.11.C).[278]

Furthermore, a Rayleigh SAW combined with plasmonic silver nanocubes was shown to lower the detection limit for immunofluorescence assays to <1 ng/mL of the antigen. In this platform BSA and 50 nm silver nanocubes were immobilized on the sensor surface and carcinoembryonic capture antibody was incubated above the nanocubes. After adding a carcinoembryonic antigen, the fluorescently-labeled detection antibody was introduced to complete the sandwich structure. Acoustic waves improved fluorescence signal by enhancing mixing, and prevented the adsorption of

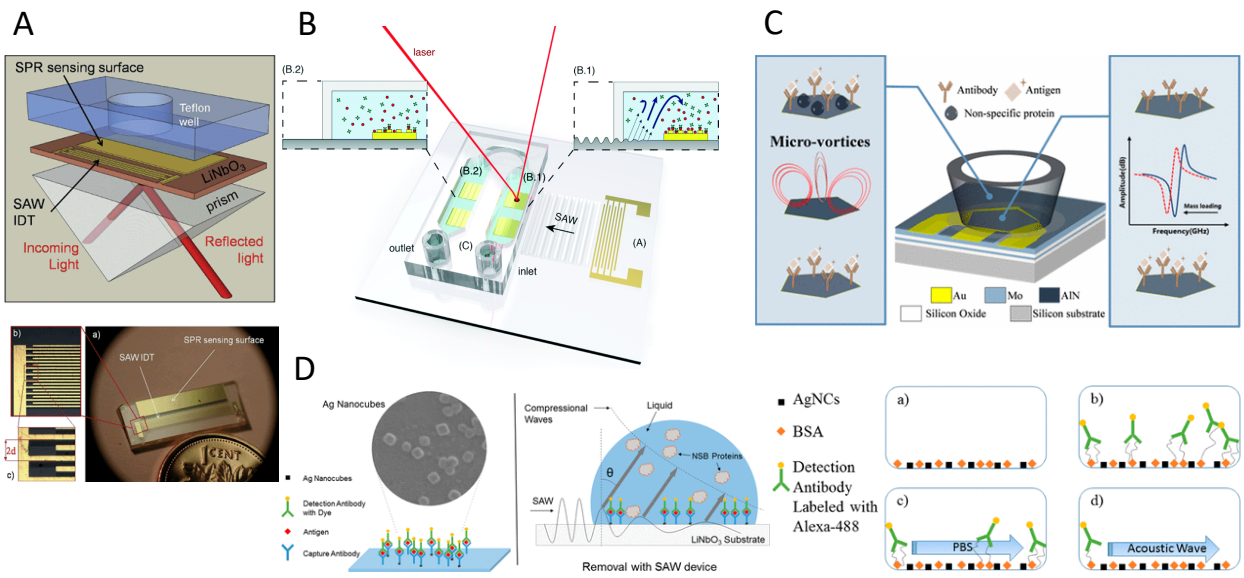

Figure 4.11. Acoustic waves for improving sensitivity and limiting biofouling **A)**[275] and **B)** [276] integration of SAW mixers with SPR sensing systems to enhance the binding kinetics. **C)** The hydrodynamic forces from acoustic microvortices used to wash off the loosely surface-bound non-specific proteins.[278] **D)** SAW is used for both enhancing the mixing and removing non-specific protein bindings, resulting in significantly better performance over chemical rinsing.[279]

nonspecific protein. The mixing induced by acoustic streaming reduced the antibody/antigen incubation time to 1/6th of the acoustic-absent setup. Moreover, removing the nonspecific protein adsorption using SAW was significantly more effective compared to the technique of chemical rinsing, leading to an overall stronger fluorescence signal (Figure 4.11.D).[279]

Merging both SAW-based sensing and biofouling alleviation mechanisms can be a very promising and efficient biosensing strategy. However, one should cautiously consider the difference in wave modes and the piezoelectric substrate used in each application. As mentioned earlier, the wave mode suitable for biosensing is SH-SAW and Love, which limits the damping of the wave in the liquid medium. However, for biofouling removal, the leakage of the waves is necessary to induce vortices, and therefore, substrates that support Rayleigh-SAWs are required. To overcome this obstacle, substrates like $LiTaO_3$ and LGS can be used to generate both wave modes by

changing the direction of the wave propagation. A set of IDTs can be embedded on these substrates in the direction in which shear vertical waves are generated to create microstreams, while the IDTs in the direction that activate shear horizontal waves can be used for the biosensing.[280,281] Given this efficient integrability, there is an increasing interest for SAW-based sensors to combine these two features to increase the biosensing specificity and detection limits.

5 An Ultra-Rapid Acoustic Micromixer for Synthesis of Organic Nanoparticles

In this chapter, we introduce an acoustic-based micromixer to synthesize organic nanoparticles as therapeutic nanocarriers. A boundary-driven system is proposed to generate vigorous microstreams for disrupting the laminar flow and accelerating the mixing time. The platform was then employed as a nanoparticle synthesis unit to produce organic nanoparticles and fine-tune their size by controlling the mixing time.

Journal Publication:

Rasouli, M. Reza, and Maryam Tabrizian. "An ultra-rapid acoustic micromixer for synthesis of organic nanoparticles". Lab on a Chip 19.19 (2019): 3316-3325.

5.1 Abstract

Mixing is a crucial step in many chemical analyses and synthesis processes, particularly in nanoparticle formation, where it determines the nucleation rate, homogeneity, and physicochemical characteristics of the products. In this study, we propose an energy-efficient acoustic platform based on boundary-driven acoustic streaming, which provides the rapid mixing required to control nanoprecipitation. The device encompasses oscillatory bubbles and sharp edges in the microchannel to transform the acoustic energy into vigorous vortical fluid motions. The combination of bubbles and sharp edges at their immediate proximity induced substantially stronger acoustic microstreams than the simple superposition of their effects. The device could effectively homogenize DI water and fluorescein within a mixing length of 25.2 μm up to a flow rate of 116 μL min^{-1} at a driving voltage of 40 V_{PP}, corresponding to a mixing time of 0.8 ms. This rapid mixing was employed to mitigate some complexities in nanoparticle synthesis, namely controlling nanoprecipitation and size, batch to batch variation, synthesis throughput, and clogging. Both polymeric nanoparticles and liposomes were synthesized in this platform and showed a smaller effective size and narrower size distribution in comparison to those obtained by a hydrodynamic flow focusing method. Through changing the mixing time, the effective size of the nanoparticles could be fine-tuned for both polymeric nanoparticles and liposomes. The rapid mixing and strong vortices prevented the aggregation of nanoparticles, leading to a substantially higher throughput of liposomes in comparison with the hydrodynamic flow focusing method. The straightforward fabrication process of the system coupled with low power consumption, high controllability, and rapid mixing time renders this mixer a practical platform for a myriad of nano and biotechnological applications.

5.2 Introduction

Nanoparticles are the focus of numerous biomedical studies for developing novel diagnostic assays, enhancing targeted drug delivery, and improving imaging capabilities.[282] The synthesis process of nanoparticles (NPs) directly determines their characteristics such as composition, size, stability, and size distribution.[283–285] To deliver the full potential of nano-constructs and regulate their behavior in biological environments such as biocompatibility, biodistribution, interaction with the immune system, and therapeutic efficiency, it is imperative to develop highly-controllable and precise methods for their synthesis.[283,284] Nanoprecipitation (also called solvent displacement method) is the most widely employed bottom-up nanoparticle synthesis method due to its rapidity, simplicity, and reproducibility.[286,287]

The confined and hence, controllable domain of microfluidic platforms lays the foundation to outperform conventional nanoparticle synthesis methods in achieving the homogenous nucleation environment, which is the key step for the nanoprecipitation of consistent and uniform nanoparticles.[284] To ensure this homogeneity, rapid mixing should be accomplished in a time span shorter than aggregation times of precursors (usually in the order of 10 milliseconds).[283,284,288] However, the common laminar flow regimes in microfluidic platforms limit the mass transfer across the channel to a slow diffusion process.[289] Various mixing strategies have been developed to address this so-called 'microfluidic mixing challenge'. In passive micromixers such as hydrodynamic flow focusing (HFF) mixers,[45,290] chaotic mixers,[18] and curved-channel mixers,[19] the channels are engineered to adjust flow field configuration with the aim of shortening diffusion length and thereby, mixing time.[291] Passive mixers, specially HFF mixers, are widely used for nanoparticle synthesis and have shown superior size control and distribution over conventional methods.[10,284,292,293] However, clogging, dilution, and limited mixing performance can restrict their functionality.[292] In contrast, active mixers use an external source of energy such as electrical, magnetic, or acoustic energy and generally present higher mixing

efficiency. Acoustic micromixers offer high mixing efficiency while remaining non-invasive and safe to operate in the proximity of biological and chemical samples. These features coupled with the obviation of requisites such as magnetic particles or conductivity requirements of fluid medium, advance acoustic mixers as a versatile device for biochemical applications.[294]

Acoustic-driven micromixers employ bulk acoustic waves (BAWs),[295] surface acoustic waves (SAWs),[296] and acoustically vibrating microstructures to transfer acoustic energy into the fluid medium and induce mixing. Among the latter, oscillatory sharp edges[96] and bubbles[97] have shown advantage in mixing due to their strong localized microstreams, low power consumption,[297] and facile and inexpensive manufacturing procedure as they do not require interdigitated electrodes deposition or expensive piezoelectric substrates. When exposed to an acoustic field, the sharp edges or bubble's interface function as a vibrating boundary in response to pressure fluctuations of acoustic waves and induce a secondary fluid motion known as acoustic microstreams.[298] Liu *et al.*[299] used acoustically excited bubbles for inducing micro vortices and accelerating mixing time to the span of seconds. To stabilize the air bubble in microchannels, Ahmed *et al.* [300] embedded a horseshoe structures that trap bubbles upon passage of fluid in the channel. The bubble-based mechanism was applied for DNA hybridization,[301] enzyme reaction analysis,[302] cell separation,[137] and bacterial aggregation.[303] Similarly, oscillatory sharp edges are shown to generate microstreams using the boundary-driven mechanism with reportedly comparable performance to that of the bubble's.[304] Huang *et al.* [305] used sharp edges to reduce mixing time to as low as 180 ms. They showed the intensity of microstreams substantially increases as the tip angle of edges becomes more acute. Leibacher *et al.*[96] employed acoustically agitated sharp edges to trap cells and particles in a microfluidic channel.

In this study, we demonstrate that the acoustic microstreaming could be considerably reinforced by integrating sharp edges and bubbles together in the design of a microfluidic platform to enhance the speed and homogeneity of the mixing. The essence of the design is to magnify the amplitude of vibration in the oscillatory

structures by exciting sharp edges and bubbles synchronously. The acoustic streaming intensity and mixing capability of oscillatory bubbles, sharp edges, and the proposed combined unit were compared by measuring their mixing efficiency. To demonstrate the functionality and versatility of the device and introduce a proof-of-concept application for acoustic micromixers, two types of organic nanoparticles, polymeric (PLGA-PEG) nanoparticles and nanoliposomes were synthesized. The high controllability of flow streams in the platform was exploited to modulate the size of both nanoparticle types by simply altering the mixing time, and to prevent clogging in the channel.

5.3 Mixing Concept and Mechanism

In boundary-driven acoustic streaming, the tangential velocity of the fluid is essentially zero on solid surfaces due to a no-slip boundary condition and rapidly reaches the free-field value within a thin domain characterized by thickness $\delta_v = \sqrt{2\nu/\omega}$ where ω represents the angular frequency of the acoustic wave.[95,306] This steep velocity gradient results in a substantial variation in the momentum of the acoustic wave which subsequently produces significant Reynolds stress forces,[90,307] leading to strong vortices.[308] For the simplified boundary layer condition, the magnitude of steady streaming velocity is proportional to the square of the oscillatory interface velocity:[137]

Eq 5.1 $$\mathbf{V_S} \propto \mathbf{V_h}^2/\omega$$

in which, $\mathbf{V_S}$ is streaming velocity and equals the time-average of the second-order velocity field and $\mathbf{V_h}$ is the velocity of the oscillatory interface which can be calculated by:

Eq 5.2 $$\mathbf{V_h} \sim d\omega$$

substituting Eq 5.2 to Eq 5.1:

Eq 5.3 $V_S \propto d^2\omega$

where *d* is the displacement amplitude of the interface. Therefore, the vibration displacement amplitude is the most influential factor in microstream strength due to its squared relationship with the speed of streaming.[309,310]

Bubble.

In response to the local pressure variation by acoustic waves, bubbles in liquid show two modes of displacement: volumetric (radial) oscillation and translational oscillation.[92,97] The compressibility of the gas in the bubble permits the interface to expand and contract by five percent of its initial radius which leads to high-amplitude volume pulsations.[297,311] This large volume pulsation enables the bubble to perform as a secondary acoustic transmitter which locally intensifies the sound field.[312] These phenomena contribute to strong microstreams in the immediate proximity of pulsatile bubbles.[92]

Sharp Edges.

Oscillatory sharp edges form large Reynolds body force and up to 100-times stronger microstreams compared to their non-sharp analogs.[313] Considering the sharp edge structure as a cantilever, it is assumed that the lower flexural rigidity at its tip yields higher displacement in each stroke and as a result, generates stronger microstreams.[305] Although, there is another explanation that also recognizes the centrifugal forces of oscillatory fluids around sharp edges.[313]

On the hypotheses that the integration of the two abovementioned mechanisms yields mutual enhancement and amplification of the acoustic effects, we developed a microfluidic device with a geometry that incorporates both features, herein referred to as 'combined unit'. Figure 5.1.A-C delineate the design of the microfluidic platform. The length, width, and depth of the channel are 1.2 cm, 600 μm, and 100 μm respectively. The height of sharp edges is set at 250 μm and the tip angle of the edges at 15° degrees, as it has been shown to be the optimum angle for microstreaming.[305] The sharp edges are slanted with a sequestered volume between every two of them where

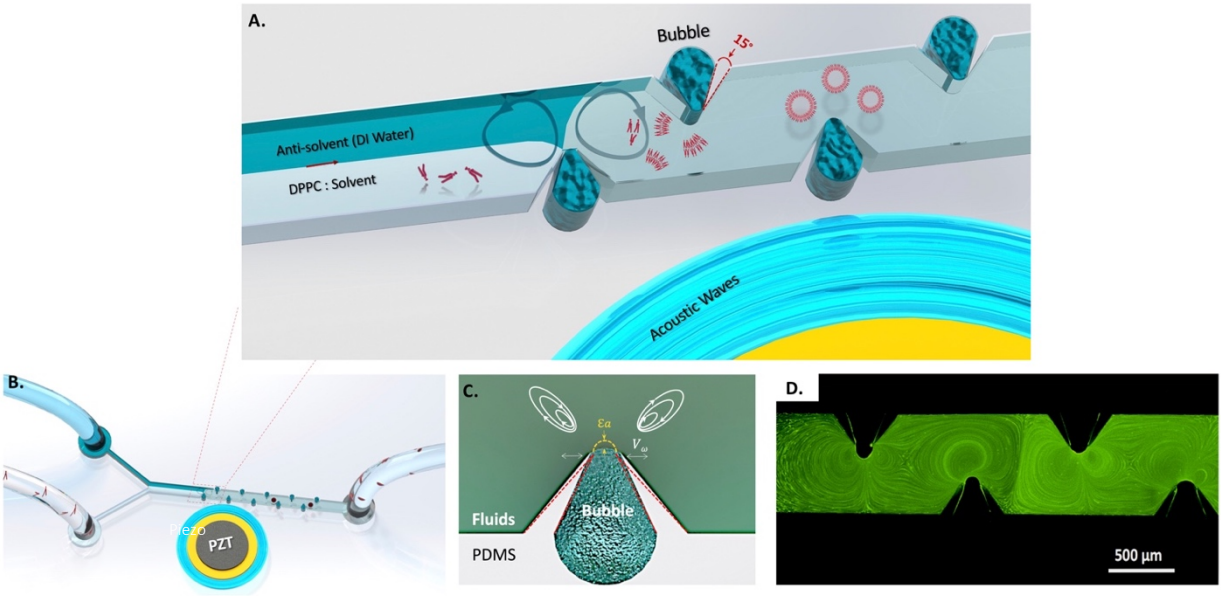

Figure 5.1 A) Conceptual illustration of the acoustic streaming and the resultant mixing used for self-assembly of nanoparticles. **B)** Rendered picture of the acoustic platform. The piezoelectric transducer is embedded next to the PDMS part, emitting acoustic pressure waves. **C)** Schematic drawing of the combined unit. Slanted sharp edges allow a bubble to be trapped. **D)** Fluorescent polystyrene particles (2-micron diameter) behavior in the presence of the acoustic field. The closed-circular pathline of microparticles shows complete coverage of channel width.

air bubbles can be confined upon the passage of fluids, due to surface tension. The combined units are positioned on the upper side and lower side asymmetrically. As such, the acoustic vortices traverse fluids interface and transport mass between two fields.

5.4 Results and Discussion

The variation of pressure and the velocity field caused by acoustic effects generates streams around the sharp edge and bubble structures. To verify this effect in our platform and picture the formed flow pattern, a solution of DI water and fluorescently labeled polystyrene beads with 2 micrometer diameters were infused into the

microchannels. Small fluorescent particles lend themselves to minimizing the acoustic radiation forces[314] and instead, pointing the spotlight on the microstreaming effect. In the absence of a background flow and acoustic streaming, the particles remain quiescent. By introducing the acoustic field upon activation of the piezoelectric transducer, microparticles start to circulate in closed trajectories which help to visualize the pattern of the vortices (Video S5.1).

To spot the most pronounced microstreams, the transducer excitation frequency was incremented in 100 Hz steps from 1 kHz to 150 kHz, while visually exploring for a distinguished prevalence of the acoustic vortices. The microstreams were observable on multiple frequencies, but the effect was prominent at the frequency of 74.2 kHz. Figure 5.1.D illustrates the pathline pattern of the acoustic microstream at this frequency through the trajectories of the fluorescent microparticles. The closed pattern of the streamlines affirms that their origin is the hydrodynamic forces of the microstreams rather than the acoustic radiation forces on the microparticles. This verifies the trajectories as a pertinent representative of the flow field.[96]

5.4.1 Comparing the microstream patterns of sharp edges, bubbles, and the combined unit

To fathom the impact of bubbles, half of the channel was treated with ethanol, which has low surface tension, to prevent the bubble trapping. Ethanol was then withdrawn and replaced by a suspension of microparticles. As a result, the bubbles could only be trapped in the unexposed half of the channel. The frequency exploration was performed to find the resonant frequency for structures without a bubble. Interestingly, their prominent microstreams were generated at 74.2 kHz, which was the same as the frequency of the structure with bubble. The intensity of the microstreams, however, showed a significant difference. Figure 5.2.A and Video S5.2 represent the difference in acoustic microstream intensity in the same device for two sharp edges, with and without a bubble in their vicinity. As it can be perceived in the left portion of the

microfluidic device (no bubble), the microstreams are substantially weaker than that of the structure with a bubble.

To investigate the contribution of sharp edges to the microstreaming, the sharp edges were replaced by non-sharp bars of the same size and with increasing distances to trap air bubbles of different sizes ($r_e \approx 65$ - 100 μm). Figure 5.2.B shows the microstreaming intensity for bubbles in the absence of sharp edges (Video S5.3 elucidates streams). The produced microstreams had a comparable intensity to that of sharp edges without bubble (Figure 5.2.A left) but were considerably weaker than the microstreams formed by the combined unit (Figure 5.2.A right). Another interesting observation is that the microstreams of both bars at the sides were stronger than the ones in the middle. This can be due to the addition of bar vibration, even though they are not sharp, to the microstreaming effect.

The capacity of mixing in each design was assessed by evaluating the mixing quality through the width of the channel. Although the definition of sufficient mixing is subjective to the specific application, a mixing index of 80% is commonly considered as an adequate mixing and therefore is designated as the lower threshold in this study (Details of MI calculation in Supporting Information). Figure 5.2.C shows the significant advantage of the combined design over bubble and sharp edge alone in the allowable throughput that can reach the adequate mixing. It can be perceived that the effect is more than the simple superposition of sharp edges and bubble microstreams. It implies that integration of sharp edges and bubbles can have a synergistic effect on each other in that the presence of a bubble can facilitate vibration of the sharp edge by (a) amplifying and focusing the acoustic field in its vicinity[312] and (b) reducing the viscous resistance to the vibrational motion due to significantly lower viscosity of air compared to liquids.[312] The vibration of sharp edges can reciprocally contribute to the bubble's volumetric pulsation by varying their intermediate space. The existence of these two features in the proximity of each other can create a positive feedback loop which exponentially boosts the produced microstreams. This obviates the need for high

voltages to reach effective mixing, thus, lowering input energy and the subsequent heating effect that can be detrimental for many biological applications.

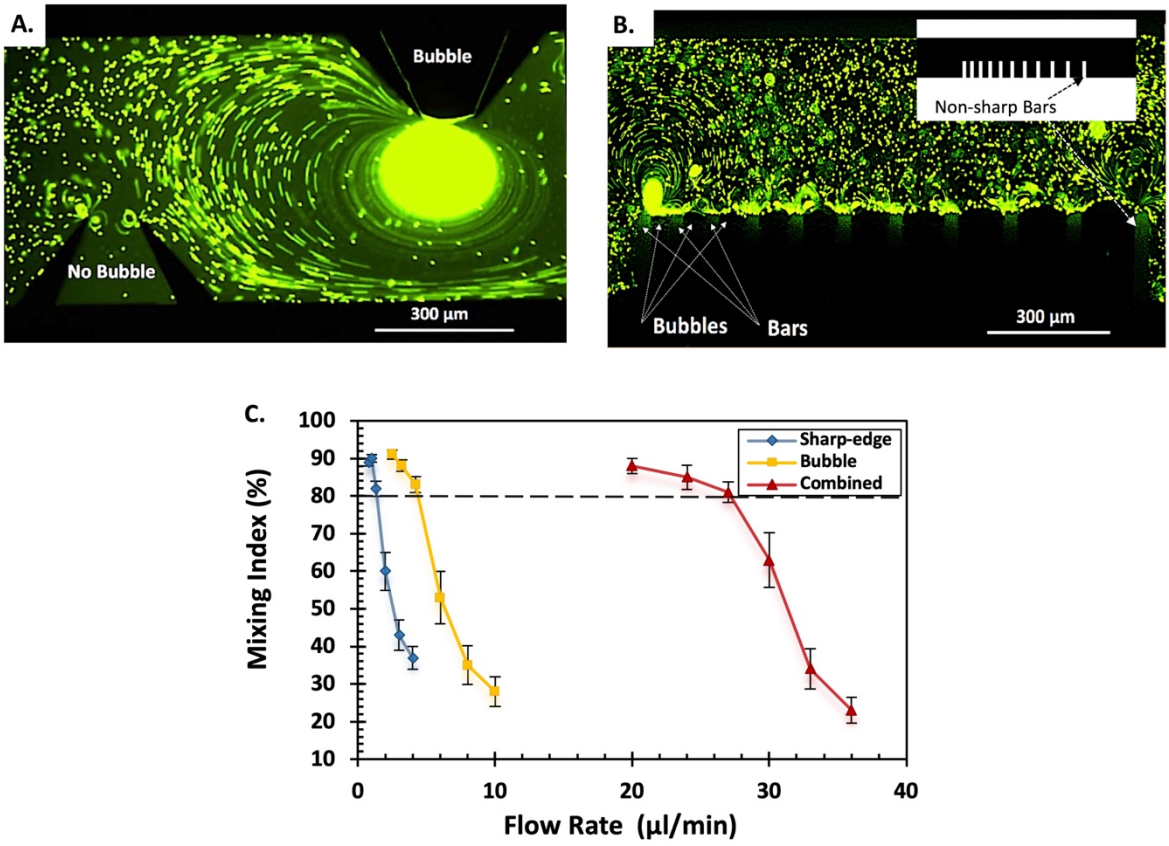

Figure 5.2. **A)** Microstreaming comparison with and without bubble. The left structure is filled with the particle solution and shows limited streaming of sharp edge structure while the combined unit on the right of the picture with bubble ($r_e \approx 98$ µm) induces strong microstreams which span through the channel width. **B)** The microstreaming pattern of the bubbles of different sizes ($r_e \approx$ 65-100 µm) which are trapped between PDMS bars in the absence of sharp edges. The microstream intensity is comparable to those of the sharp edges without bubbles and considerably weaker than the combined unit. **C)** Characterization of mixing performance and allowable throughput to reach the complete mixing threshold in each of the designs at the excitation voltage of 15 V_{PP}.

5.4.2 Mixing assessment

Uniform mixing requires the prevalence of the motion momentum of acoustic microstreams over the laminar flow to disrupt its parallel streamlines, including the interface of fluids. For zones of the channel not exposed to the microstreams, the background flow preserves its parallel streamlines, limiting mass transport to inefficient diffusion. Hence, the competition between the acoustic microstream and the background flow to conquer the flow field determines the quality of mixing. Stronger microstreams can expand through the channel and disrupt all streamlines while stronger background flow can suppress microstreams and confine their effect. Apart from the intrinsic behavior of the oscillatory structures (bubbles and edges), three factors are at play in this competition: the optimum frequency that emanates maximum driving pressure, the input voltage which controls the driving pressure, and the flow rate of the background flow which tends to suppress the microstream. These three criteria are examined for the proposed micromixer to determine the impact of each of them on the mixing performance of the system.

5.4.3 Effect of frequency on mixing performance

The resonance of bubble and piezoelectric transducer are both known to influence the intensity of acoustic streaming. However, the optimum frequency is attributed to the resonance frequency of one or another in different studies. Locating the optimum frequency is usually done by visual observation of pronounced microstreams as described earlier. To quantitatively analyze the relationship between frequency and microstreams intensity as well as to identify the nature of the dominant resonance in this platform, different types of piezo elements were used and the electrical impedances of each and their corresponding mixing indexes within the range of 40 Hz - 100 kHz were measured. Three models of piezo elements from RadioShack, STEMiNC, and Thorlabs with dissimilar natural frequencies were embedded adjacent to the identical channel geometry and were resonated with 10 V_{PP}.

Figure 5.3 shows the impedance value of each piezo element and the outcome mixing index as a function of frequency. The local extrema nodes in graphs from the impedance analyzer indicate the vibrational resonance frequency of the mounted piezo element. Given the mechanical impedance is the lowest at the resonance frequency, the vibration amplitude and the resultant acoustic pressure show the highest local amplitude at the resonance frequency node.[315,316] The mixing indexes reached their maximum value at the proximity of the resonance frequency of each piezoelectric transducer system, while at the resonance frequency of the bubble, which is calculated to be 33.7 kHz by Rayleigh-Plesset equation, MI does not show significant fluctuation. For the rest of the experiments, the frequency was set at its optimal value to gain the maximum driving pressure from the piezo elements.

5.4.4 Effect of voltage on mixing performance

As shown in equation 5.3, the velocity of the microstreams is proportional to the square of the oscillation amplitude.[137] An influential parameter in the oscillation amplitude is the input voltage of the driving signal, which has a square relation with electrical

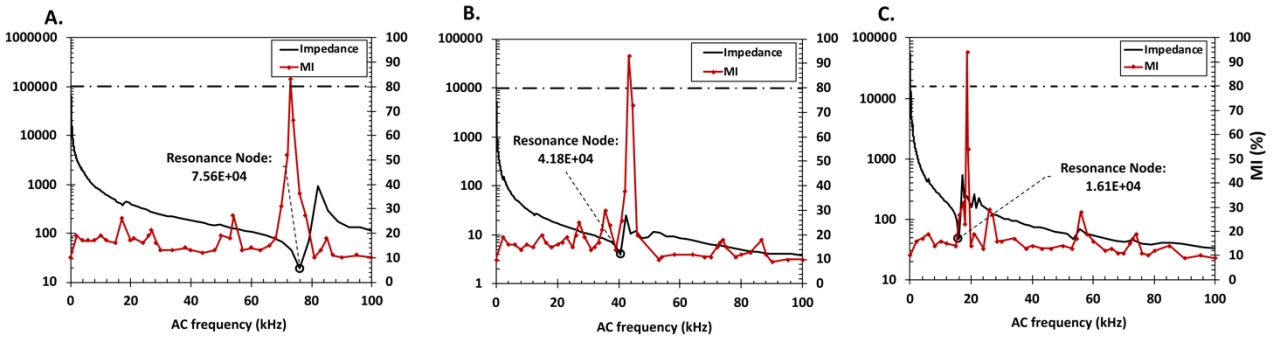

Figure 5.3. Sonogram of three Piezoelectric transducers **A)** Radioshack, **B)** Thorlabs and **C)** STEMiNC and mixing index (MI) for their corresponding platforms. For each piezoelectric system, the highest mixing index appears at the proximity of its resonance frequency, confirming the dominant effect of electro-mechanical resonance (the mixing index is an average of two repetitions).

power.[305] Figure S5.5 and Video S5.4 show the concentration distribution of fluorescein for different input voltages at the constant flow rate and frequency. At 10 V_{PP}, the mixing distance to reach the threshold of adequate mixing (MI = 80%) is approximately 2500 μm. As the input electrical power amplifies, the acoustic wave power emitted by the transducer increases. This leads to a higher vibration amplitude and stronger fluid motion as observable in Figure 5.4.A The strong microstreams are generated instantaneously and homogeneous mixing occurs at 14 V_{PP}. Increasing voltages over 14 V_{PP} does not alter the mixing pattern significantly, rendering this voltage the optimum for the flow rate of 18 μL/min. The mixing length for this condition, which is the shortest one, was measured by calculating the thickness of transition from the unmixed zone with the normalized concentration of ≈1 (dark side) to 0.6 which corresponds to 80 % mixing. The thickness was measured for ten positions on the transition line and found to be in the range of 25.2 $\pm$ 2.3 μm (Figure 5.4.B).

5.4.5 Effect of flow rate on mixing performance

To investigate the impact of flow rate on the mixing index, the signal's voltage was kept constant at 10 V_{PP} and the flow rate was altered. Figure S5.6 and Video S5.5 display the mixing performance with each flow rate of 12 μL/min to 24 μL/min. For the experiment with the flow rate of 12 μL/min, the mixing index reached its threshold within 25.2 $\pm$ 2.3 μm. As flow rate increased, the background field became stronger and started to suppress the acoustic microstream and narrowed its domain of motion. In contrast, the flow rate 24 μL/min predominantly overpowered the microstream and dropped the mixing index. The balance between the driving voltage and the flow rate is the key to both optimize energy consumption and control the mixing time. Time is an important factor in mixing and can be determined by $t_{mix} = L_{mix} /V$ where t_{mix} shows the time of mixing, L_{mix} is the distance required for fluid to reach the mixing threshold, and V is the net velocity of fluids in the channel direction. Figure 5.4.C shows the balance of input voltage and flow rate for reaching the mixing threshold at the mixing length of 25.2 μm.

The graph shows a linear relation in logarithmic scale between the flow rate and the input voltage with a slope of 1.75. This is in line with the linear relation (in logarithmic scale with a slope of 2) between electrical power and the voltage which transduces to mechanical vibration and finally, fluid streams. The difference in the slopes can be attributed to the damping effect. One can use this diagram for alternating voltage or flow rate to adjust the time of mixing while having a satisfactory mixing index. For applications requiring extremely fast mixing, such as nanoparticle synthesis, voltages should be equal or higher than the balance diagram to ensure the shortest mixing length. The fastest mixing time of 0.8 ms was obtained within this mixing length for the flow rate of 116 µL/min at the input voltage of 40 V_{PP}.

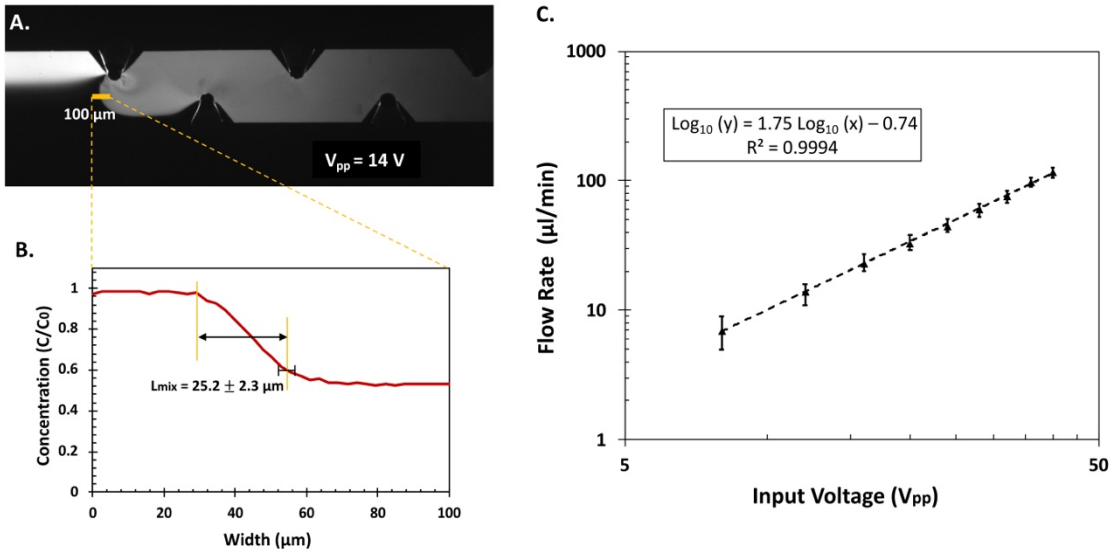

Figure 5.4. A) The mixing performance in the presence of acoustic mixing at an input voltage of 14 V_{PP} and flow rate of 18 µL/min. **B)** The minimum length required to reach the adequate mixing threshold (normalized concentration of 0.6, *i.e.* MI = 0.8). **C)** The relation between the input voltage and flow rate to reach the adequate mixing threshold in the designated mixing length (25.2 µm).

5.4.6 Nanoparticle synthesis

For the proof of concept, the micromixer platform was employed as a synthesis unit to control the nanoprecipitation process by regulating mixing time and homogenizing the nucleation environment. The entire microchannels were coated with Parylene-C dimers through chemical vapor deposition (CVD) to prevent the diffusion of uncross-linked PDMS oligomers to the synthesis unit and ensure solvent compatibility of the device. To show the versatility of our device, liposomes as hollow nanoshells and rigid PLGA-PEG nanoparticles were synthesized. These two families of organic nanoparticles are extensively employed as FDA-approved controlled release systems in pharmaceutical and biomedical fields, owing to their biocompatibility, biodegradability, and surface tunability.

Both liposome and PLGA-PEG nanoparticle generation processes started with dissolving the precursors in a water-miscible organic solvent (Figure 5.5A and B). Upon contact of these solutions with the co-flowing DI water (anti-solvent), the hydrophobic forces expulse the precursors to self-assemble into nanoparticles in a thermodynamically driven process. The hydrophilic component of the precursors (PEG in PLGA-PEG and phosphate head in phospholipids) forms a barrier on the surface of the nanoparticles to prevent further addition of precursors. When mixing is incomplete, this hydrophilic shield is not robust enough to block further aggregation, leading to the formation of larger NPs with higher polydispersity. The introduction of acoustic microstreams increases the normal advection to mix solutions with antisolvent in a millisecond order. This rapid mixing ensures the homogenous environment prior to nucleation and aggregation of amphiphilic precursors which is essential for the formation of a monodisperse population of nanoparticles.[9,317] Four important parameters, *i.e.* size, size distribution, the concentration of nanoparticles synthesized in the micromixer, and the level of aggregation were used as the measures for the performance of the acoustic platform in making nanoparticles. Hydrodynamic flow focusing (HFF), commonly reported in the literature as a standard microfluidic nanoparticle synthesis method, was opted as the comparison reference.

Nanoparticle Size Tuning.

Size is deemed to be one of the most decisive physicochemical characteristics of nanoparticles for their interactions with the reticuloendothelial system (RES), transcytosis pathways, payload release rate and cellular uptake, and renal clearance to name a few. The nanoparticle size is tightly dependent on the mixing time and nucleation homogeneity.[318,319] First, to examine the capability of the acoustic microfluidic platform to finely tune nanoparticles' size, the mixing time was varied by altering the total flow rate (TFR) at a fixed voltage of 30 V_{PP}. Figure 5.5.C, and D show the variation in the average diameter of nanoparticles, measured by Dynamic Light Scattering (DLS), for total flow rates of 10 μL/min, 20 μL/min, 40 μL/min, 60 μL/min, and HFF method. Since the most influential factor on the size of nanoparticles produced in HFF method is the flow rate ratio (FRR) of the precursor-solvent mixture and the antisolvent, it is kept constant for the HFF and acoustic experiments to be consistent in comparison. However, the mixing mechanism in the acoustic platform is not dependent on FRR which means the precursor-solvent flow rate should not be decreased to achieve adequate mixing. Therefore, the dilution of produced nanoparticles which is a common challenge in the HFF method could be addressed.

For all the flow rates, the nanoparticles were smaller in acoustic micromixer compared to the HFF method which relies merely on slow diffusion. At the slowest flow rate, *i.e.*, 10 μL/min, the size of nanoparticles was closest to that of HFF. This can also be due to the occurrence of some extent of diffusion before reaching the mixing units. As the total flow rate increases, the mixing time decreases proportionally and thereby leads to smaller nanoparticles. This trend was reproducible for three different concentrations of PLGA-PEG. For 1.25 mg/ml the nanoparticle size could be tailored from 59.1 ±11.3 nm offered by HFF to the minimum of 35.1± 6.2 nm, for 2.5 mg/mL the range was between 67.6 ± 16.1 nm to 42.4 ± 7.2 nm, and for 5 mg/ml nanoparticle size could be tuned between the range of 118.9 ± 32.1 nm for HFF to 51.9 ± 6.8 nm for TFR = 60 μL/min. The larger size for higher concentrations was in line with Johnson's[320] study which states that the time of aggregation decreases by an increase in the initial

concentration. Thus, as concentration increases, the gap between τ_{agg} and τ_{mix}, which is a window for the addition of dispersed precursors, increases resulting in larger nanoparticles. It also explains the wider distribution with the change of mixing time in higher concentrations.

Liposome synthesis was also conducted with flow rates of 10 μL/min, 20 μL/min, 40 μL/min, and 60 μL/min. For the concentration of 0.5 mg/ml, the size of nanoparticles was modulated from 101.1 ±17.4 nm with HFF method to 65 ± 4.1 nm at the fastest TFR. For the concentration of 1 mg/ml, the size range was between 144.3 ±15.6 nm to 70.9 ±4.9 nm and for the concentration of 2 mg/ml, sizes could be varied from 234.4 ± 17.1 nm to 117.5 ± 9.2 nm.

The rate of change in size in response to TFR also offers insight into analyzing the formation process. The decrease in size is steeper for the concentration of 2 mg/ml than 1 mg/ml and it is the least for 0.5 mg/ml. However, the rates of change decrease at higher TFR, which shows a tendency to converge as the mixing accelerates. This is congruous with Johnson's[320] size-mixing time diagram that shows a minimum threshold limit for the size of nanoparticles.

Size Distribution of Nanoparticles.

The polydispersity indexes of nanoparticles were 0.072 for PLGA-PEG nanoparticles and 0.127 for liposomes. Figure 5.5.E.I, and F.I show Transmission Electron Microscopy (TEM) images of PLGA-PEG nanoparticles and liposomes synthesized by the acoustic mixer. These images confirmed the low polydispersity in the size distribution of the nanoparticles and the absence of large aggregation of precursors. The actual diameter of the nanoparticles, which is usually smaller than the hydrodynamic one, was also measured by processing the TEM image via ImageJ software. An average of 57.4 ± 5.2 nm and 73.1 ± 8.1 nm was found for PLGA-PEG nanoparticles and nanoliposomes respectively.

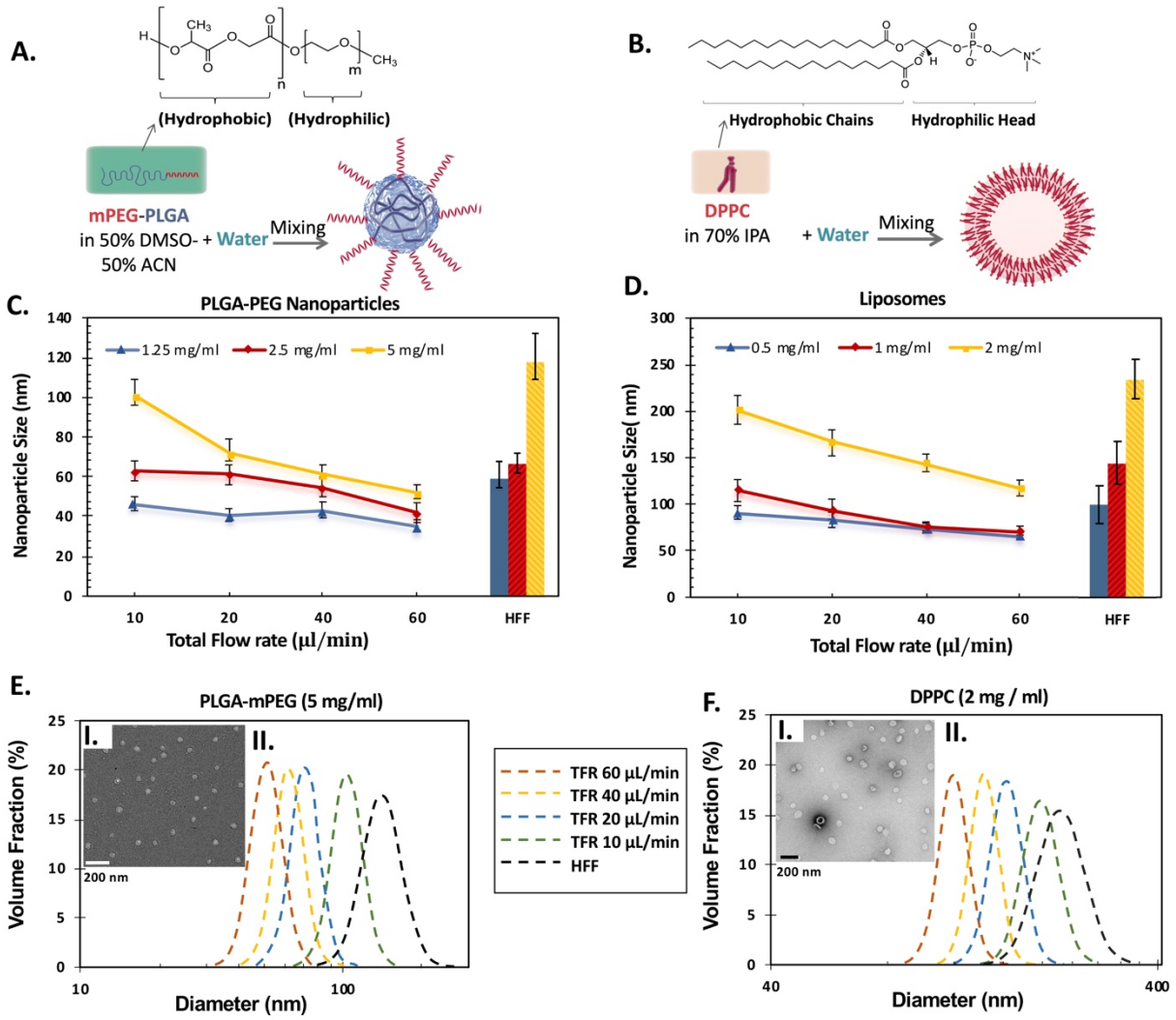

Figure 5.5 A) Schematic of PLGA-PEG nanoparticle synthesis. **B)** Schematic of liposome synthesis. Size variation of **C)** PLGA-PEG nanoparticle and **D)** Liposomes synthesized in the acoustic platform by changing the mixing time through total flow rate and comparison with hydrodynamic flow focusing method for three different concentrations of precursors. **E)** I. TEM image of PLGA-PEG nanoparticles. II. Size and size distribution as measured by DLS. **F)** I. TEM image of nanoliposomes by negative staining. II. Size and size distribution as measured by DLS.

The DLS results of the size distribution for nanoparticles synthesized with the acoustic

platform and the HFF method with the above flow rates and concentrations are delineated in Figure 5.5.E.II, F.II and S5.8. As anticipated, the size distributions of the NPs from HFF were wider due to the slower nanoprecipitation. In the acoustic platform, as mixing time decreases by an increase in the TFR, nanoparticle size distributions tend toward narrower polydispersity. This trend was more discernable in liposome experiments.

Concentration of Nanoparticles and Effect of Aggregates.

The initial concentration of the precursors is often considered as the yield of the nanoparticle generation systems in the absence of an actual direct method for nanoparticle concentration measurement. Amrani *et al.*[293] were among the first to use the nanoparticle tracking analysis (NTA) to measure the concentration of liposomes at the output of an HFF system. Interestingly, the authors showed that not only an increase in precursor concentration does not necessarily translate to an increase in the number of nanoparticles, but also it could reduce the nanoparticle concentration at the output. Apart from the size difference, this discrepancy between the initial concentration and the number of nanoparticles at the output can be attributed to the formation of a few but large aggregates, which is common in HFF methods

To understand whether the intense acoustic microstreams and rapid homogenization can alleviate the aggregation and influence the yield of nanoparticle formation, samples of liposomes synthesized with HFF and the acoustic device for three different precursor concentrations were measured with NTA. The results showed an increase in the produced liposomes in the acoustic method compared to that of the HFF method for each precursor concentration (Figure 5.6). The pervasive acoustic microstreams across the channel increase the interface of solvent-solute mixture and antisolvent where the formation starts, and by creating a homogenous environment during self-assembly, it reduces the risk of big aggregates. As a result, this method can

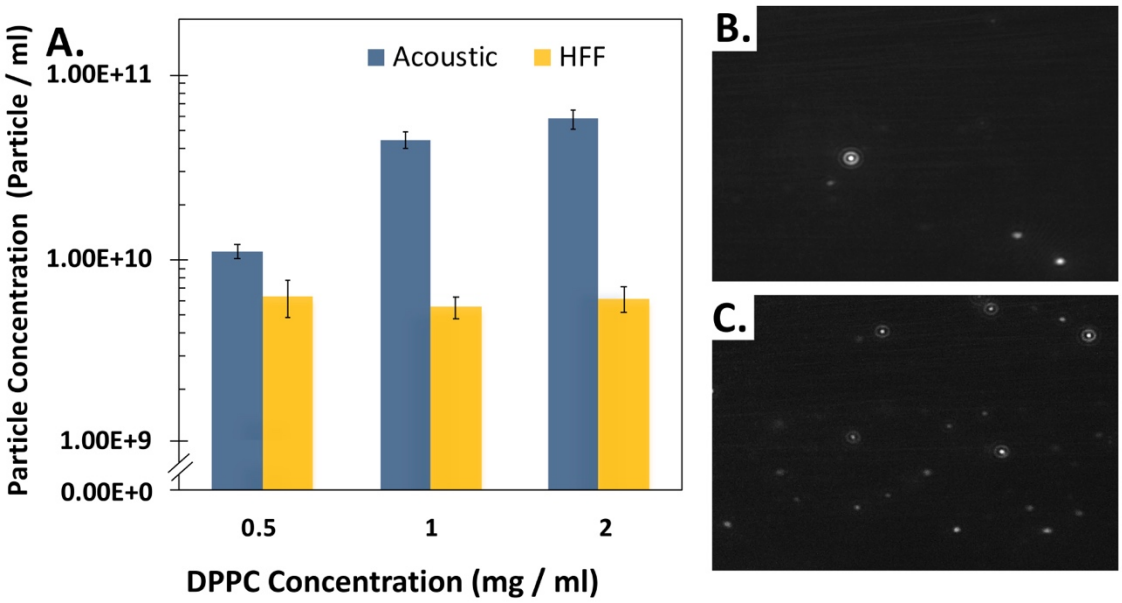

Figure 5.6. **A)** Nanoliposomes concentration synthesized in the acoustic and HFF platforms for three different concentrations of precursors. **B)** NTA video frame of liposomes produced in HFF method with an average of 4.6 ± 0.4 particles per frame with a dilution factor of 200. **C)** NTA video frame of liposomes produced in acoustic micromixer with an average of 23.3 ± 2.1 particles per frame with a dilution factor of 200.

be an efficient procedure of nanoparticle generation with higher nanoparticle output compared to HFF at the same precursor concentration.

5.5 Conclusion

We introduced an ultra-rapid, efficient, and practical acoustically-driven microfluidic micromixer through integrating bubbles and sharp edges in the device. We demonstrated that these features act synergistically to maximize the conversion of the acoustic pressure to high-amplitude vibrations and produce considerably stronger and broader microstreams compared to the designs possessing only one of these features. The bubbles increase the sharp edge vibration by local amplification of the acoustic field and by reducing the viscous resistance to the vibrational motion. The sharp edge can also contribute to the bubble volume pulsation by varying their intermediate space.

The acoustic microstreams showed the capacity of accelerating the mixing process to 0.8 ms at the flow rate of 116 μL/min, which is meaningfully faster than available acoustic micromixers in the literature. Due to the pronounced microstreaming effect, the mixing capacity of this design for the same input voltage is higher which can be an advantage in the setups with limited output voltage such as the emerging field of cell phone guided microfluidics.[321] The inherent high-controllability of the acoustic streams through governing the input electrical energy lent itself to a well-regulated mixing process necessary for uniform nanoprecipitation. This capability was used to synthesize monodispersed PLGA-PEG nanoparticles and nanoliposomes. Through the alteration of mixing time, the nucleation process of nanoparticles was manipulated to finely tune their size. This technique can be employed to reproducibly synthesize nanoparticles with the desired size for a specific application or to generate a library of organic nanoparticles with a broad range of physicochemical properties. The intense mixing allowed the production of a higher number of nanoparticles in the acoustic platform compared to that of the HFF method. Also, the intense and pervasive acoustic microstreams in this platform could prevent the formation of large nanoparticle aggregates and clogging of the channel, which is a common challenge in microfluidic platforms.

5.6 Material and Methods

5.6.1 Materials

A negative photoresist (SU-8 2050) was purchased from MicroChem Corp., USA. Polydimethylsiloxane (PDMS) was obtained from Dow Corning Corp., Canada. PTFE tubings (RK-06407-41) are from Cole-Parmer Inc., Canada. Analytical grade Acetonitrile, fluorescein, and Trichloro (1H,1H,2H,2H- perfluorooctyl) silane were ordered from Sigma-Aldrich, Canada. 1 mL Hamilton glass syringes were purchased from Fisher Scientific, Canada. Three Models of piezoelectric transducers: model 273-073 from Radioshack Corp. USA, model SMBA4510T05M from STEINER & MARTINS

INC, USA and model PB4NB2W from Thorlabs Ltd., USA were purchased. Fluorescent polystyrene particles (PSF-002UM) were purchased from Magsphere, USA. Methoxy poly (ethylene glycol)-b-poly(lactide-co-glycolide) (mPEG-PLGA) with MWs of ≈ 5,000 Da: 30,000 Da were purchased from, Poly-SciTech, USA. 1,2-Dipalmitoyl-sn-glycero-3-phosphocholine (DPPC) was ordered from Avanti Polar Lipids Inc. (Alabaster, AL, USA). Parylene-C dimers were obtained from Specialty Coating Systems, USA.

5.6.2 Device fabrication

The device was fabricated through standard photolithography, followed by single-layer soft lithography. The negative photoresist (SU-8 2050) was spin-coated on a silicon wafer, per the manufacturer protocol, to fabricate the master of 100-micron thickness. PDMS was poured on the silanized master to replicate the pattern of the channels and microstructures by soft lithography. The patterned PDMS was bonded onto a glass substrate by plasma surface treatment. A piezoelectric transducer was then mounted on the glass substrate along the side of the PDMS microchannels to complete the assembly of the chip. The devices were then treated with a step of Parylene coating. The deposition was conducted in SCS Labcoter 2 PDS 2010 (Specialty Coating Systems, USA) with 2 grams of Parylene-C dimers which corresponds to a coating thickness of 1 μm.

5.6.3 Experiment setup

Harmonic electrical signals were initiated by a function generator (AFG3011C, Tektronix, USA) which governed the signal's frequency and waveform. The function generator is then connected to an amplifier (25A250A, Amplifier Research, USA) to regulate the amplitude of the voltage and transmit the signal to the piezo transducer. The electrical impedance of the transducer system was measured with an Agilent 4294A impedance analyzer (Agilent, Palo Alto, CA). The spectra of 40 Hz–100 kHz was explored using 201 nodes. The piezo elements were mounted on the chip and connected to low and high voltage terminals with the peak to peak amplitude of 1 V_{PP}.

5.6.4 Nanoparticle synthesis and characterization

The mixtures of precursor monomers in the organic solvent were prepared by dissolving various concentrations of PLGA-PEG (Methoxy poly(ethylene glycol)-b-poly(lactide-co-glycolide) in 50% acetonitrile: 50% DMSO for polymeric nanoparticles and DPPC: cholesterol in 70% IPA for liposome generation. Ultrapure water was collected from a Barnstead Nanopure filtration system with a resistivity above 18.2 MΩ cm. The organic solution and DI water were infused with a Harvard syringe pump with a flow rate ratio of 1:4 for polymeric nanoparticles and 1:6 for liposomes. PTFE tubing was used to deliver the solutions to the channels. Hydrodynamic diameter, distribution by volume, and polydispersity index (PDI) of the PLGA-PEG nanoparticles were measured by dynamic light scattering (DLS) using a ZetaPALS Zeta Potential Analyzer (Brookhaven Instruments Corp., USA). Nanoparticle Tracking Analysis (NTA) was conducted to measure the concentration of synthesized nanoparticles by NanoSight 300 (NanoSight, Amesbury, United Kingdom) with a 640 nm laser at T = 25 °C. Measurements were performed in dynamic flow mode controlled with built in syringe pump at level 60. The TEM (transmission electron microscopy) images of the PLGA-PEG nanoparticles and liposome were acquired after negative staining by a 2% solution of uranyl acetate with a Tecnai 12 BioTwin electron microscope, FEI Technologies Inc., USA at an acceleration voltage of 120 kV.

5.7 Supporting Information

5.7.1 Bubble trapping

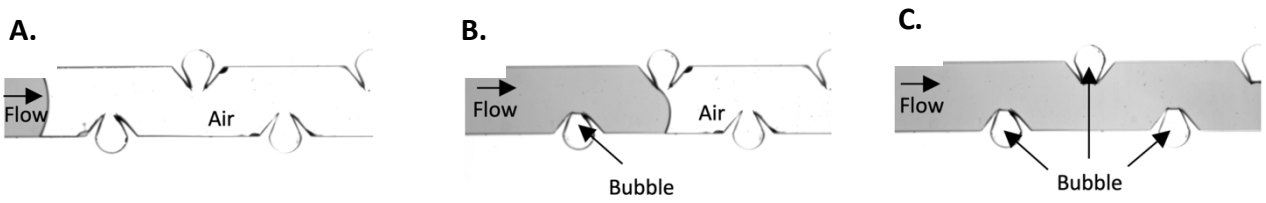

Figure S 5.1. The channels are initially empty which means there is only air in them. When an aqueous liquid gets infused to the channel, it fills all the channel except for the sequestered volume between the slanted sharp edges due to the surface tension, leaving a trapped bubble.

5.7.2 Impedance analysis

In the majority of works related to bubble-based acoustic streaming, the pronounced frequency is attributed to the natural frequency of the bubble calculable by the Rayleigh-Plesset equation. However, the independence of this frequency from the bubble's existence in Figure 5.2.A and also the identical optimum frequency of different-sized bubbles in Figure 5.2.B which by Rayleigh-Plesset equation should be different, highlight the role of the electromechanical resonance of the piezoelectric.

Figure S 5.2 shows the impedance sonogram for the transducer mounted on a 1mm thick glass substrate, adjacent to the PDMS microchannels. The spectrum has a smooth

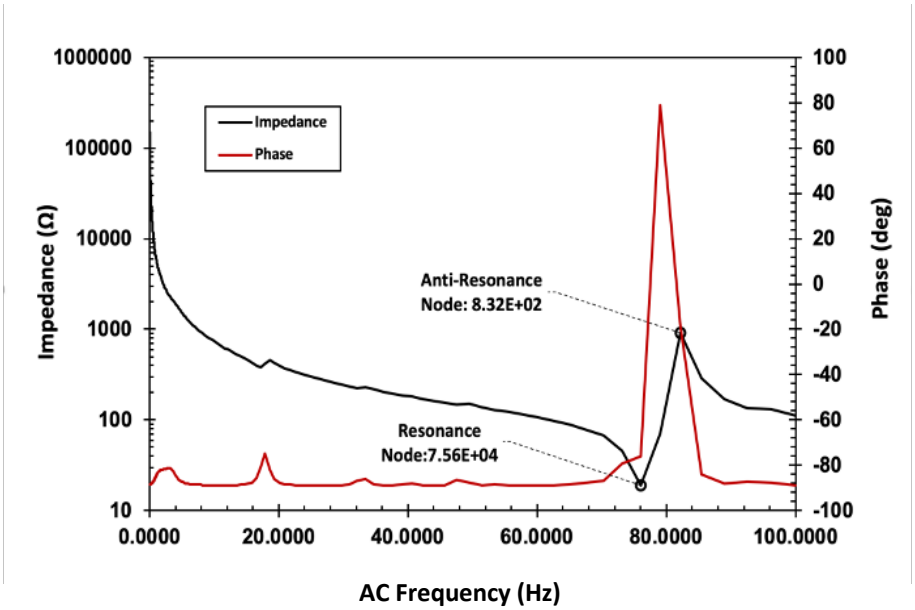

Figure S 5.2. Sonogram of impedance and phase for piezoelectric transducer model no. 273-073, Radioshack. The resonance frequency is in line with reported optimum frequency for mixing index.

behavior except at the frequency of 75.6 kHz, which is close to the optimum frequency of microstreams, where strong fluctuation in the impedance amplitude occurs.

5.7.3 Mixing analysis

To visualize and characterize the mixing process by the acoustic microstreams, DI water and fluorescein solution were infused simultaneously through two separate inlets with a flow rate of Q = 18 µL/min. Figure S 5.3.A shows the laminar flow pattern of the solutions moving side by side in the direction of the channel. In the absence of the acoustic field, the advection ensued only in the direction of the laminar flow. Thus, the mixing process is purely dependent on the diffusion process which is by nature very slow and ineffective, as witnessed by the discernible interface and unmixed fluid domains. Upon excitation with an input voltage of 14 V_{PP}, the piezoelectric transducer emanates the driving acoustic pressure required for inducing closed-circular

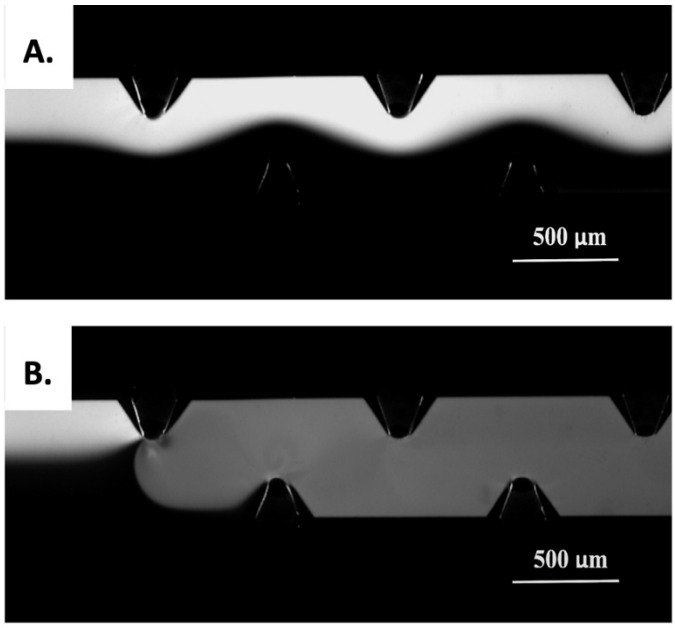

Figure S 5.3. The concentration distribution of fluorescein and DI water in the A) absence and B) presence of acoustic mixing.

microstreams and homogenous mixing of DI water and fluorescein (Figure S 5.3.B). The motion momentum of acoustic microstreams prevails over the laminar flow and disrupts its parallel streamlines, including the interface of fluids.

The rotational fluid motion exponentially increases the interface of fluids by twisting and stretching it. This microscale stirring drastically accelerates the previously sluggish mixing process by increasing the interface of fluids and hence, curtailing the diffusion distance through twisting and stretching along with reciprocal advection of mass fractions between the co-flowing fluids.

5.7.4 Mixing index

To visualize and characterize the mixing process by the acoustic microstreams, DI water and fluorescein solution were infused simultaneously through two separate inlets. Mixing index was employed as the quantitative function for evaluation of the mixing quality through the width of the channel.

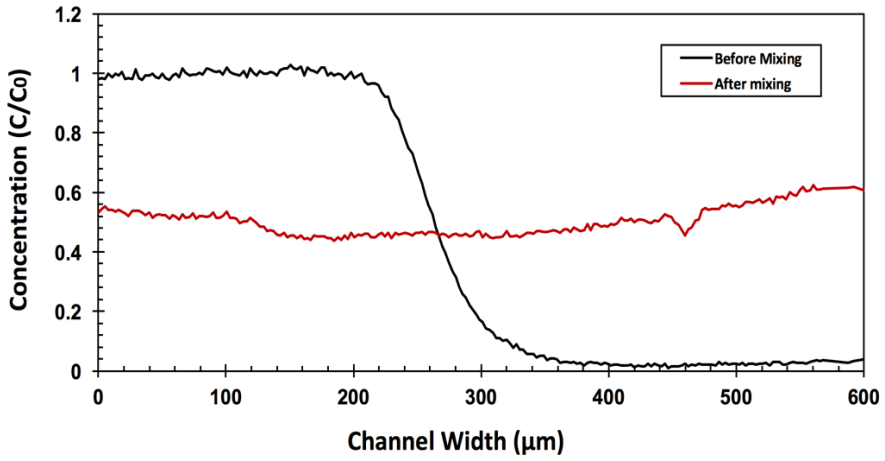

Figure S 5.4. Concentration profile across the channel width before and after mixing by acoustic microstreams.

The variance of normalized concentrations was obtained at the reference cross-section from the gray-scale images. The mathematical form of the function is:

Eq S5.1:

$$MI = 1 - \sqrt{\frac{\frac{1}{N}\sum_{i=1}^{N}(c_i - \langle c \rangle)^2}{\langle c \rangle(1 - \langle c \rangle)}}$$

where N is the number of sampling elements, c_i exhibits the concentration of each mass fraction, and $\langle c \rangle$ shows the average concentration of the cross-section. For perfectly mixed solutions, the mixing index equals one, whereas for completely segregated flows the value is zero. A mixing index of 0.8 was designated as the lower threshold for adequate mixing.

Mixing index was measured at two mixing distances of 2500 μm and the minimum distance needed to reach to normalized concentration of 0.6 was measured for 10 nodes Figure S 5.5.B and D.

5.7.5 Variation in voltage

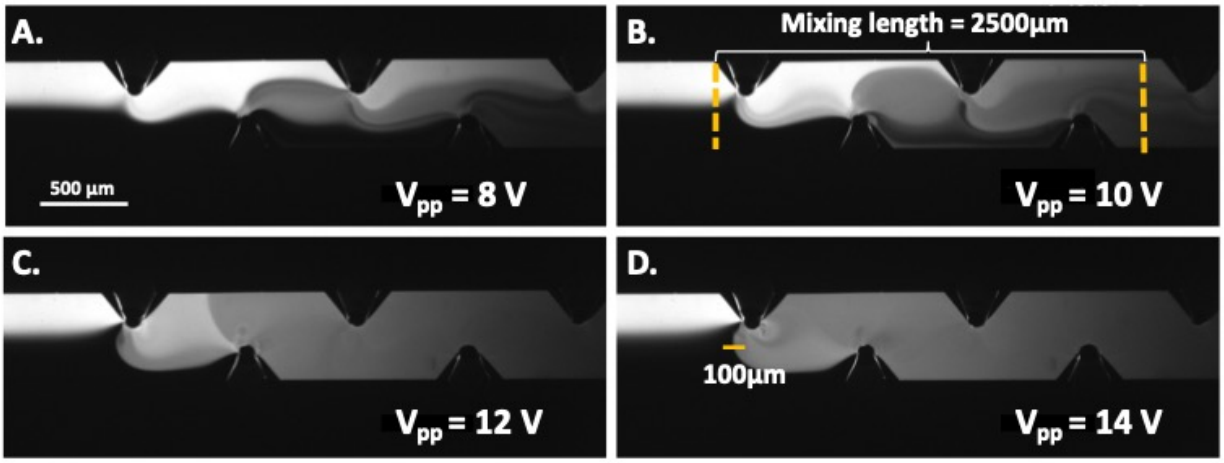

Figure S 5.5. Mixing performance by changing the input voltage at the flow rate of 18 μL/m.

5.7.6 Variation in flow rate

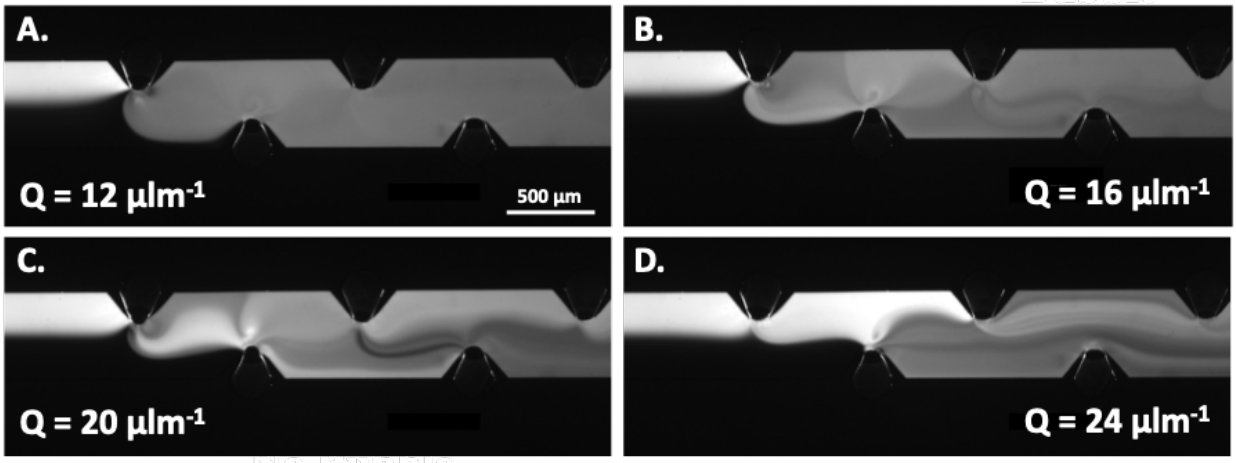

Figure S 5.6. Mixing performance by changing the flow rate at the input voltage of 10 V_{PP}.

5.7.7 Nanoparticle size distribution

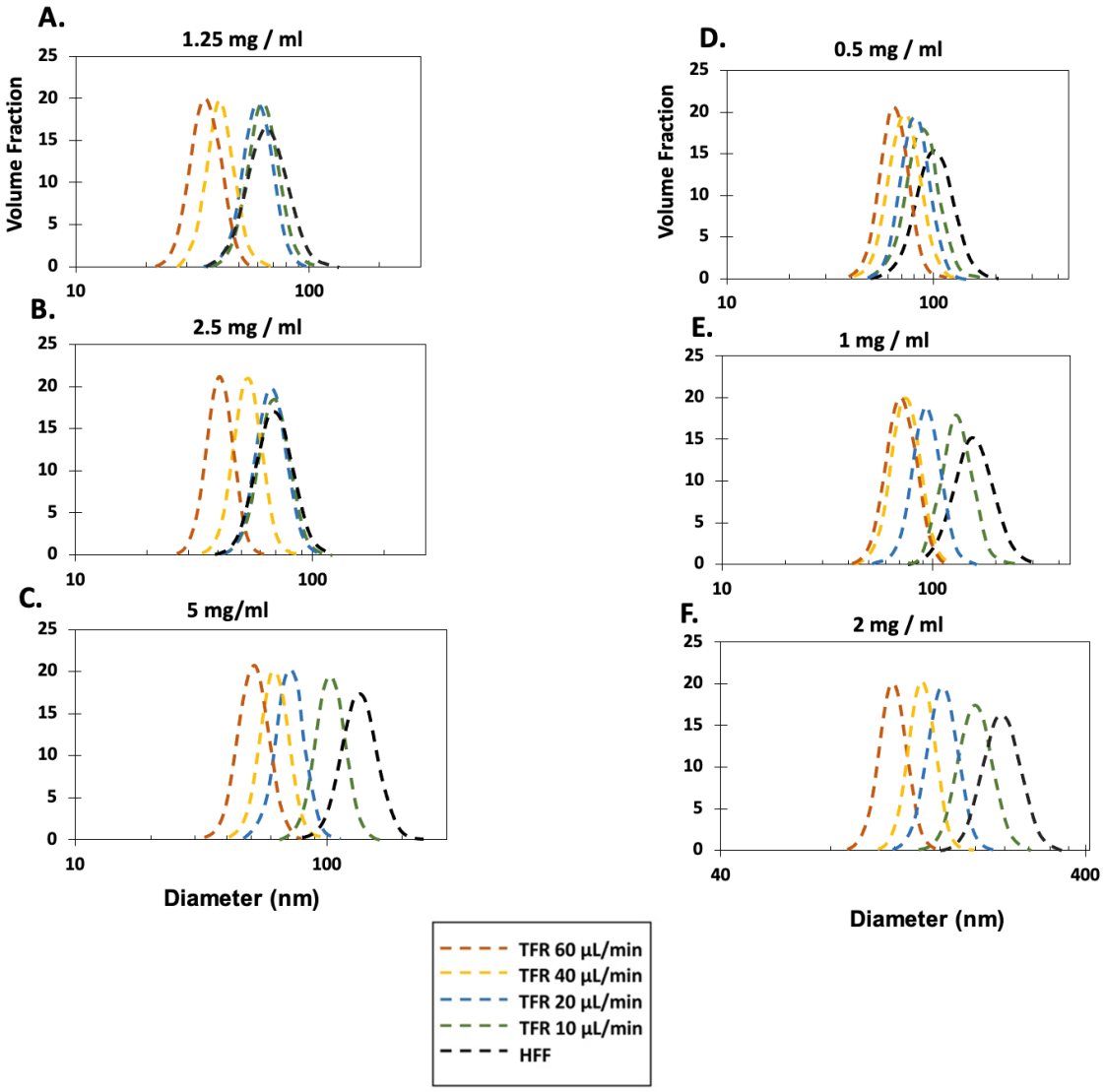

Figure S 5.7. Size distribution of PLGA-PEG nanoparticles with precursor concentration of **A)** 1.25 mg/ml, B) 2.5 mg/ml and **C)** 5 mg/ml measured by DLS. Size distribution of Liposomes with precursor concentration of **D)** 0.5 mg/ml, **E)** 1 mg/ml and **F)** 2 mg/ml measured by DLS.

Video captions.

Video S5.1: The 2-micron diameter polystyrene particles showing the pattern of microstreams in response to acoustic field.

Video S5.2: The microstream pattern shown by trajectory of 2-micron diameter polystyrene particles for a sharp-edge feature without bubble (left feature) and the integrated feature of bubble and sharp edges (right feature).

Video S5.3: The microstream pattern shown by trajectory of 2-micron diameter polystyrene particles for bubbles in the absence of sharp edges.

Video S5.4: The mixing performance of the design by variation of the input voltage at the constant flow rate of 18 μL/m.

Video S5.5: The mixing performance of the design by changing the flow rate at the constant input voltage of 10 V_{PP}.

6 Rapid Formation of Multicellular Spheroids in Boundary-Driven Acoustic Microstreams

This chapter presents a boundary-driven acoustic platform as an on-chip and continuous-flow spheroids assembly line. We aimed to use the locally controllable acoustic microstream as the first stage of spheroid formation, and to incorporate ECM as the second phase of spheroids formation to accelerate the spheroids formation in a single-step process. In doing so, we speculated that some of the challenges in spheroids formation tissue engineering and drug screening such as cell-dependency, labor-intensive steps, and the time-consuming process could be addressed.

Journal Publication:

Rasouli, Reza, and Maryam Tabrizian. "Rapid Formation of Multicellular Spheroids in Boundary-Driven Acoustic Microstreams." Small 17.39 (2021): 2101931.

6.1 Abstract

Three-dimensional cell spheroid culture has emerged as a more faithful recreation of cell growth environment compared to conventional 2D culture, as it can maintain tissue structures, physicochemical characteristics, and cell phenotypes. The majority of current spheroid formation methods are limited to a physical agglomeration of the desired cell type, and then relying on the cells capacity to secrete extracellular matrix to form coherent spheroids. Hence, apart from being time-consuming, their success in leading to functional spheroid formation is also cell-type dependent. In this study, we present a boundary-driven acoustic microstreaming tool that can simultaneously congregate cells and generate sturdy cell clusters through incorporating a bioadhesive such as collagen for the rapid production of spheroids. The optimized mixture of type I collagen (0.42 mg/ml) and methylcellulose (0.4% w/v) accelerates the coagulation of cell-matrix as fast as 10 s while avoiding their adhesion to the device, and thereby offering easy spheroid retrieval. The versatility of the platform is shown for the production of MDA-MB-231 and MCF-7 spheroids, multicellular spheroids, and composite spheroids made of cells and microparticles. The ability to produce densely packed spheroids embedded within a biomimetic extracellular matrix component, along with the rapid formation and easy collection of spheroids render the proposed device a step in technology development required to realize the potential of 3D constructs such as building blocks for the emerging field of bottom-up tissue engineering.

6.2 Introduction

Multicellular spheroids are believed to be excellent *in vitro* models to replicate the physiological functions, structural complexities of living tissues, and their native configuration. Their three-dimensional (3D) architecture and the obviation of cell-substrate interaction in such environment allow for faithful recapitulation of biochemical and biomechanical communication between cell-cell and cell-matrix. These unique characteristics render spheroids the optimal candidate for numerous fundamental studies and biomedical applications including the development of pre-clinical models for drug discovery, regenerative medicine, and tissue engineering.[11,322]

Spheroids of cancer cells, also known as tumoroids, are emerging as preferred models for the investigation of anticancer therapeutics' response, as they provide analogous spatial architecture, diffusion gradient, tumor dynamics, metabolic activity, and drug resistance behavior of solid tumors.[323–325] In a similar vein, spheroids of stem cells are also largely investigated owing to their higher cell viability, proliferation, stemness, and regenerative characteristic compared to 2D culture.[11,326] Cell spheroids have also been trending as tissue engineering building blocks to replace single-cell printing,[327] where their complex composition, prolonged survival, and fusion capacity are used to reconstruct various tissues, from branched blood vessel[328] to thyroid gland,[329] and osteochondral interface.[330]

The scalable application of spheroids in the above-mentioned studies necessitates a high-throughput production method with consistent physiological and morphological characteristics. The standard spheroid formation methods include hanging droplets, agitation-based systems, culture on non-adherent surfaces, and scaffold-based fabrication.[14,331] These methods are generally labor-intensive, low-yield, time-consuming, and show heterogeneous spheroids in shape and size due to poor control over the process which limits their scaled-up application.[49,332]

Microfluidics has shown the capacity to overcome some of the technical hurdles in spheroid formation by offering controlled physical conditions, minimized cells and

reagent consumption, high sensitivity in drug screening, precise manipulation of cells, continuous perfusion, and regulation of the nutrients and oxygen supply.[333,334,335] These advantages coupled with decreasing user-device interaction, compatibility for automation, low fabrication and operation costs make microfluidics an attractive tool for producing high throughput and uniform spheroids, desirable for clinical translation.[336,337]

Generally, spheroid formation starts with the physical agglomeration of cells. Next, cell-membrane integrins bind to long-chain extracellular matrix (ECM) fibers of adjoining cells to form loose aggregates. This step is usually followed by a delay phase of cadherins overexpression and finally the development of compact and robust cell spheroids through homophilic cadherin interactions.[331,338]

The main mechanism of spheroid generation in the majority of microfluidic platforms is based on the physical arrangement of cells and promoting direct cell-cell contact by applying different forces. U traps and microwells are relatively convenient methods to convene cells in the vicinity of each other by gravity or hydrodynamic forces. More recently, other methods such as magnetic forces,[12] surface acoustic waves (SAW),[13,190] and dielectrophoeresis[339] are reported to collect cells. These methods enable tailoring the number of cells and shape of spheroids, producing high-density cell clusters, and increasing cell to fluid ratio.[14,333,340] However, since these methods rely on the gradual secretion of adhesive proteins by cells to develop clusters into spheroids, the process usually takes hours to days, depending on cell types.[14] Moreover, during this incubation time, cells can develop adhesion to the channel walls and make the spheroids' retrieval challenging.

Droplet-based strategies, specifically with recent automation advances, hold the potential to address some of the limitations for scalable spheroid formation.[44] Droplets of egg protein components were used as biocompatible scaffolds on which cells could be seeded to form cell-coated microcarriers.[341] One particularly interesting strategy was reported as "predator-like swallowing" where thermoresponsive droplet scaffolds were added to the cell suspension to trap cells. The tunable pores size allows cells to

penetrate and then the droplets were exposed to near-infrared radiation to shrink and squeeze media out, which led to cell enrichment inside the droplet scaffold.[342] The more common droplet-based spheroid formation method, however, is to sequester cells in hydrogel or aqueous droplets during the emulsification. The cell-laden droplets will be exposed to either heat, ion solution, or UV to initiate the gelation and form cell-laden 3D scaffolds.[343,344] High frequency of droplet generation along with rapid gelation which omits reliance on slow and spontaneous adhesion of cells by cell-secreted proteins, make this technique suitable for scalable production. Moreover, the droplet-based spheroid formation has so far been the only method with the ability to embed biomaterials and various ECM components to generate cell-laden microgels,[345] which can be exploited to investigate cell-matrix attachments, ECM signaling, and their effect on cell phenotyping.[333,340,337] Despite these favorable features, since the droplet formation procedure does not preconcentrate cells prior to gelation, it leads to a low cell-fluid ratio in droplets. This scattered distribution of cells in stiff hydrogels such as alginate and agarose can result in limited cell-cell contact and communication, which hinders the proliferation of some cell types such as mesenchymal stem cells.[14] This is a major limitation of droplets for tissue engineering applications where densely cellularized units are required.[331,346] Advanced droplet formation methods such as microfluidic electrospray have been introduced to generate a soft and flexible core with a solid shell of cross-linked alginate.[347] This method has been reported for encapsulation of opal particles but upon lowering the voltage, which as it stands is 5.2 kV and high for cell use,[348] the soft-core droplets can be used to facilitate cell migration inside the capsule. The collection of droplets from the cytotoxic oleaginous phase and extraction of encapsulated cells from their surrounding microgel are other challenges that require additional steps such as magnetic separation and enzymatic or thermal degradation.[345,349,350]

In this paper, we report on a rapid spheroid formation technique based on boundary-driven acoustic streaming to produce compact cell-collagen aggregates. Our hypothesis was that acoustically induced hydrodynamic forces can agglomerate cells

into compact clusters in a span of seconds and allows real-time monitoring and controlling the size of cell aggregates. The working mechanism section describes the propagation of the acoustic wave in the platform and conversion into a strong set of counter-rotating microstreams. The hydrodynamic forces stemmed from these microstreams can trap cells and form cell clusters, as the initial step of spheroid formation. Since the cell clusters are loose at this point, strong acoustic microstreams are simultaneously used to incorporate matrix for rapid coagulation of cells, and hence, accelerate the slow stage of matrix development to seconds. We identified microfluidic spheroid formation challenges such as adhesion to channels and disintegration during retrieval, and used these criteria to test the acoustic assembly performance of various materials, including collagen type I as the foundational ECM component and a fast bioadhesive. The methods were applied to two cell types of MDA-MB-231 and MCF-7 which differ in compaction methods in reliance on cadherins.[351] Finally, the platform was used to show its ability for multicellular spheroid formation by coculturing MDA-MB-231 and MCF-7 cells, cell-particles composite spheroids of MDA-MB-231 and polystyrene microparticles, and spheroids as building blocks.

6.3 Results and Discussion

6.3.1 Working mechanism of acoustic cell trapping

Primarily, spheroid formation includes a cultivation system for the physical aggregation of the cells. The proposed platform employs boundary-driven acoustic streaming to convene cells into the compact vicinity of each other to form clusters. These acoustic vortices are the result of acoustic energy dissipation in a thin boundary layer around oscillatory solid-liquid or gas-liquid interfaces. The acoustic system for the spheroid assembly consists of an acoustic source mounted next to the microfluidic channel where systems of oscillatory sharp edges and bubbles are embedded as described in our previous study (Figure 6.1.A).[98] To introduce the acoustic field, the piezo transducer is activated by radiofrequency signals at the resonance frequency of the system.[98] Upon

activation of the transducer, acoustic waves propagate toward the microfluidic channel where they instigate vibration in the oscillatory features. The vibration leads to the formation of closed counter-rotational microstreams which cover the whole channel width.

Suspended particles such as cells, when encountering these acoustic microstreams, experience hydrodynamic forces that alter their straight pathline. When the microstreams become strong enough, these hydrodynamic forces can overcome the momentum inertia of particles and drag force of background flow to trap cells in the vortex eye. To create strong vortices, we combined oscillatory bubbles and sharp edges. The combination of the two features creates a phenomenon that is stronger than the mere superposition of their effect.[98] The bubble diminishes the viscous resistance against the sharp edges oscillation while the movement of sharp edges also contributes to the volume pulsation of the bubble. The combinatory platform showed considerably stronger microstreams compared to each feature separately, which then allows the trapping of various sizes of particles in the vortex at higher flow rates. Modifications to the design of the platform have been implemented to adapt it for spheroid formation. The depth of the channel is increased to 250 μm to allow the production of spheroids up to this size without adhesion to the channel. The height of sharp edges is increased to 300 μm for stronger microstreams. Huang *et al*.[305] used the cantilever deformation formula, $k = F/d = Ewt^3/4L^3$, to model sharp edge vibration where E represents Young's modulus, w is the width, and t is the thickness of the cantilever. Increasing the length of sharp edges (L) decreases the spring constant (k) and leads to a larger displacement amplitude (d). The velocity of streams (Vs) is proportional to the second power of this displacement according to $Vs \propto d^2\omega$, where ω is the frequency. Hence, longer sharp edges can produce stronger microstreams which is also experimentally confirmed by Zhao *et al*.[352] Also, the gap between the sharp edges is decreased for the smaller interface of bubbles and the liquid. This results in a more stable bubble and also increases the microstreaming velocity as it has the inverse relationship with the

oscillating interface of the bubble (R), following the relationship of $V_s \sim V_o^2 / \omega R$, where V_o is the velocity of the oscillating flow field.[137]

Video S6.1 shows the arrangement of the cells into aggregate as the first step in spheroid formation through applying acoustic pressure for trapping and conglomeration of cells in close vicinity of each other. The intensity of the microstream is easily tunable by controlling the driving voltage during the experiment. This allows us to analyze the relationship between the input voltage and the flow rate at which the cells can be trapped. The higher voltage leads to stronger microstreams whereas increasing the flow rate tends to suppress the microstreams domains.[98] This results in a trade-off between these two factors in which increasing the input voltage, expands the microstream domains to cover the whole channel and trap almost all cells. In contrast, increasing the flow rate leads to the suppression of the microstream domains, which allows the cells far from the oscillatory complex to escape the acoustic trap. Graph 6.1.B depicts the relationship between the voltage and its maximum corresponding flow rate, where cells remain trapped in the vortex. As it can be seen, the intercept of the curve starts from 1 V_{PP}. This is due to the fact that the microstream intensity below the intercept value is not strong enough to cover the whole channel width and overcome the momentum inertia of the cells. Thus, the speed of the acoustic spheroid assembly can be controlled by regulating these two factors, considering that applying higher voltages allows higher flow rates and therefore faster trapping, aggregating, and releasing of the spheroids.

Another factor to be considered before initiating the spheroid formation is the effect of acoustic microstreams on the viability of the cells. The main impact of acoustic streams on cells is the shear stress in the acoustic domain. High shear stress can lead to membrane rupture and cell lysis. Wang *et al.* showed acoustic cell lysis at V = 50 V_{PP} in 180 pairs of sharp-edged structures.[353] Since, the magnitude of the shear stress is proportional to acoustic streaming velocity, it can be controlled by the input voltage.[354]

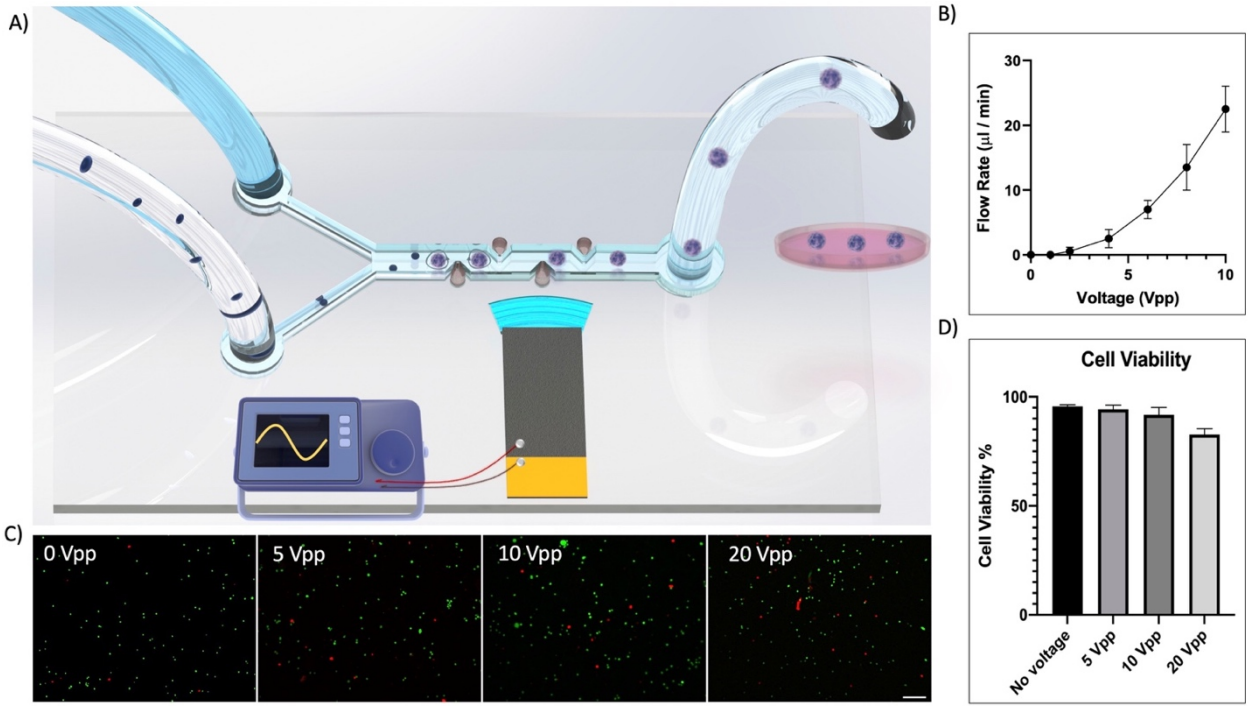

Figure 6.1. A) Rendered image of the acoustic platform. Upon activation by a function generator, the acoustic waves generated by the piezoelectric transducer create boundary-driven microstreams in the microfluidic channel which can trap cells. **B)** Depicts the correlation of input voltage and flow rate for tapping cells. **C)** and **D)** Show the viability of cells after exposure to the acoustic field with different input voltages. Scale bar: 200 µm.

To assess the impact of shear stress generated by acoustic streams on cell health, we examined the cell viability for 3 driving voltages. Figure 6.1.C shows the cells exposed to the acoustic microstreams of 5 pairs of oscillatory structures at the flow rate of 5 µl/min. Cell viability remained over 90% for voltages up to 10 V_{PP} and dropped to ≈85% for 20 V_{PP} (Figure 6.1.D). In order to ensure the minimal effect of voltage on the cells, it was set below 10 V_{PP} during the spheroid formation experiments. Noteworthy, due to the low operating voltage and noncontact nature of this acoustic platform, the heat generation is not significant.

6.3.2 Cell-cell adhesion-promoting materials for acoustic spheroid formation

To develop sturdy cell-cell binding and transform them into spheroids, the cell clusters need to tether together through the secretion of adhesion protein molecules. Otherwise, the cells will disperse and follow the flow trajectory as soon as the acoustic source stops, which we confirmed by conducting the acoustic experiments in basic fluids media such as PBS and DMEM. Relying on cells to secret the ECM to stabilize the cell-cell adhesion for the formation of spheroids can take hours and it varies among cell types. To circumvent this delay phase, a bioadhesive matrix is needed to glue cells as they convene in the acoustic trap. In searching for the compatible media for acoustic assembly, we explored a few biocompatible and frequently used bioadhesives to assess their performances with respect to: i) instantaneous adhesion and robustness for holding cells together, ii) easy spheroids' retrieval by preventing spheroids' adhesion to the PDMS channel sidewalls, and iii) formability of cell aggregates into spheroids under acoustic microstreams.

Table 6.1 shows the materials and their performance in each criterion. Cells in PBS and DMEM showed no observable cell-cell adhesion and upon removal of acoustic microstreams, the cells were dispersed. The addition of Fetal Bovine Serum (FBS) in the media helped the cell-cell adhesion but it was very weak, leading to the disintegration of clusters before retrieval. To overcome this issue, three strategies were implemented: Firstly, the spheroid formation was tested under stop-flow conditions for over an hour to provide cells with time to form clusters. Secondly, the acoustic microstreams were switched off after the initial cell trapping because acoustic streams created cells' mobility that would not allow them to attach together. Thirdly, since cells were gradually dispersing in stagnant conditions, methylcellulose (MC) was added in the stop-flow condition. Its high viscosity allowed to confine cells and helped them to attach to each other in 30 min to 1h. Our results showed that the use of MC is critical for parallel spheroid formation where multiple oscillatory structures embedded in a microfluidic device, such as the one used here, can each form a spheroid in stop-flow condition.

Table 6-1 Media and materials tested for acoustic spheroid assembly and their performance in three criteria of adhesion: rapid and robust adhesion of cells together, retrievability: no attachment to the channel, and formability of cell aggregates into spherical structures.

Material		**Criteria**		
Name	**Concentration**	**Adhesion**	**Deformability**	**Retrievability**
PBS	1x	✗	✓	✓
DMEM Media	1x	✗	✓	✓
DMEM Media + FBS	1x	$> 1hr$	✓	✓
Methylcellulose	0.3- 1% w/v	$> 30\ min$	✓	✓
TrueGel3D 6	0.25 x-1x	✗	✗	✓
GelMa+ LAP	5% +1% w/v	✓	✓	✗
Alginate + PLL	2%+ 0.05% w/v	✓	✓	✗
Atelocollagen (Bovine Type1)	0.4- 2.5 mg/ml	✓	✓	✓

Since parallel spheroid formation in stop-flow conditions requires an incubation time and thus a temperature-controlling setup to ensure cell viability, the methodology was adapted to accelerate spheroid formation in continuous flow. Under continuous flow conditions, the physical arrangement of cells under acoustic force is a matter of seconds, and therefore the rapidity with which the cells adhere together is very important, as it dictates the coagulation time. To promote cell-cell or cell-material adhesion under continuous flow with minimum time, various biomaterials with different mechanisms of adhesion were tested, namely True gel 3D, GelMA, Alginate and Poly-L- lysine solution along with Type I collagen.

True gel 3D, a customizable hydrogel that contains slo-Dextran and PEG, was used with diluted concentrations to maintain them as a fluid. Although small clusters of cells could be formed in the channel, the cell-to-cell attachment under acoustic streams was not stable. Cells suspended in a GelMA (methacrylated gelatin) + LAP photoinitiator solution, could be acoustically trapped and form aggregates when exposed to UV. However, the crosslinked aggregates attached to the sidewalls and were not easily retrievable. The retrieval of formed aggregates was also challenging with alginate and Poly-L-lysine solution (PLL), both widely used biomaterials for electrostatic layer by layer coating of cells and spheroids.[355] Coating the channels with Parylene C helped to reduce the sidewall adhesion of spheroids, attesting that both GelMA and Alginate + PLL still present good candidates for promoting the spheroid formation if further scrutiny of optimized concentration and channel coating can be conducted. Finally, type I collagen showed the potential to form rapid adhesion between cells simultaneous to cell trapping. The formed spheroids were easily retrievable, once the optimization of all parameters was achieved. Given the superior performance of collagen both for acoustic assembly of spheroids and as a natural ECM, as well as considering that it does not require additional steps such as washing between alginate and PLL or UV crosslinking for GelMA, collagen I was selected as the optimal matrix for further investigation in spheroid formation.

6.3.3 Acoustic assembly using collagen I matrix

Collagen I is the most abundant and foundational component of ECM which is frequently used for 3D culture and tissue engineering to recapitulate the native microenvironment of growth.[356] The triple helix proteins of collagen interact laterally and end to end to structure fibrils that support cells while its plethora of cell-binding ligands mediate the cell-collagen adhesion.[357] Moreover, the collagen's inherent ability to recreate the complexities of cell-ECM communication allows cells to interact with dynamic mechanical forces and chemical cues. This active cell-matrix interaction can regulate both the collagen properties through mechanisms such as metalloproteinases

(MMPs) degradation,[358] as well as cell phenotypes such as proliferation, polarization and particularly, metastasis and invasiveness in cancer cells,[335,359] and stemness and differentiation in stem cells.[360]

The cell-collagen mixture was prepared through neutralization of acid solubilized collagen and 10x media by sodium hydroxide, followed by the addition of cells in the collagen solution. In this condition, collagen fibrils self-assemble at the cell surfaces and form networks with single or multiple cells trapped in the collagen network.[361,362,363] When this cell-collagen solution is introduced into the microfluidic channel and reaches the acoustic region, the microstreams act as a spheroid assembly line where they trap and compress cells in the eye of the vortices while the collagen fibrils induce rapid adhesion between cells as they make physical contact (Figure 6.2.A). Upon reaching the spheroid size of interest, which can be monitored and controlled by trapping duration and flow rate, the acoustic force can be switched off. The assembly process was not sensitive to cell concentration and the spheroids could be assembled with a wide cell population range of 0.3 to 2 mil cells per ml. The critical factor in the process, however, is the gelation time. The neutralized collagen molecules self-organize into a network at room temperature and the kinetics of this process directly influences the fluidity of collagen solution and its adhesiveness.[364]

The operation window for the acoustic spheroid assembly is the time period that collagen solution remains liquid while the collagen fibril networks are formed around the cells. This will provide the necessary adhesiveness to allow cells to remain attached to each other after the removal of the acoustic force. Exceeding this time window, the collagen solution is converted into a two-phase solution, consist of a gelly fiber network with cells, and a liquid portion depleted of collagen fibrils. In such cases, the collagen loses its adhesive role in that the fully gelled network phase is too rigid to infuse in the channel or to be restructured by acoustic shear stress into a spheroid (Figure S5.1), whereas the liquid phase lacks collagen fibrils to prompt the cell-to-cell adhesion. This gelation window is highly dependent on the initial concentration of collagen.[364] Understandably, collagen as a natural biopolymer shows batch to batch variation, and

therefore, an ever-accurate collagen concentration for the acoustic assembly cannot readily be defined. To establish an optimized collagen concentration range, impedance spectroscopy was performed to monitor gelation time for different concentrations by measuring the rate of change in electrical impedance over time.[365] Figure 6.2.B and Figure S5.2 show the gelation window at room temperature for concentrations of 0.42 mg/ml to 2.5 mg/ml. The oscillation source of impedance spectroscopy was limited to 5 mV to avoid Joule heating on the electrodes which can influence the gelation time, since crosslinking of collagen is temperature dependent. At lower concentrations, the gel transition is slower, giving a longer window of operation for acoustic spheroid assembly. At concentrations below 0.42 mg/ml, the collagen solution could not act as an adhesive, and a longer incubation time was required to form cell clusters. However, maintaining cells at room temperature for a long period of time can be detrimental to cell viability. Increasing the incubation temperature to 37 °C degree showed to considerably accelerate the gelation time, and thereby favors cell to cell attachment. Nevertheless, one should also consider that gelation at physiological temperature might cause changes in fibrils bundling and the collagen structure.[366]

Furthermore, the media used for diluting collagen was also a decisive factor in both the time and quality of the gelation. The addition of 10% FBS, as used in complete media, accelerated the gelation time significantly. Moreover, this addition generated lumps of the cell-collagen network, causing clogging in the inlet of the microfluidic device. To address this issue, methylcellulose was used to avoid lumps. Interestingly, it also prolonged the gelation time, thus providing more time for spheroid formation. For finding the optimized concentration of MC, it should be noted that higher concentration leads to the higher viscosity of the cell-collagen solution, which limits the acoustic microstreaming intensity and domain. The methylcellulose concentration of 0.4% w/v was observed in the experiments to be optimal for increasing the operation window while keeping the acoustic microstreams domain strong enough to cover the channel width at 10 V_{PP}.

The formation of spheroids in continuous flow condition is shown in Figure 6.2.C where the cell trapping and reshaping to spheroids can be accomplished as fast as 10 seconds. The full demonstration of acoustic spheroid assembly processes for MDA-MB-231 and MCF-7 are presented by Video S6.2 and S6.3 respectively, confirming the versatility of the technique and its non-reliance on the tested cell types. Immediately after acoustic

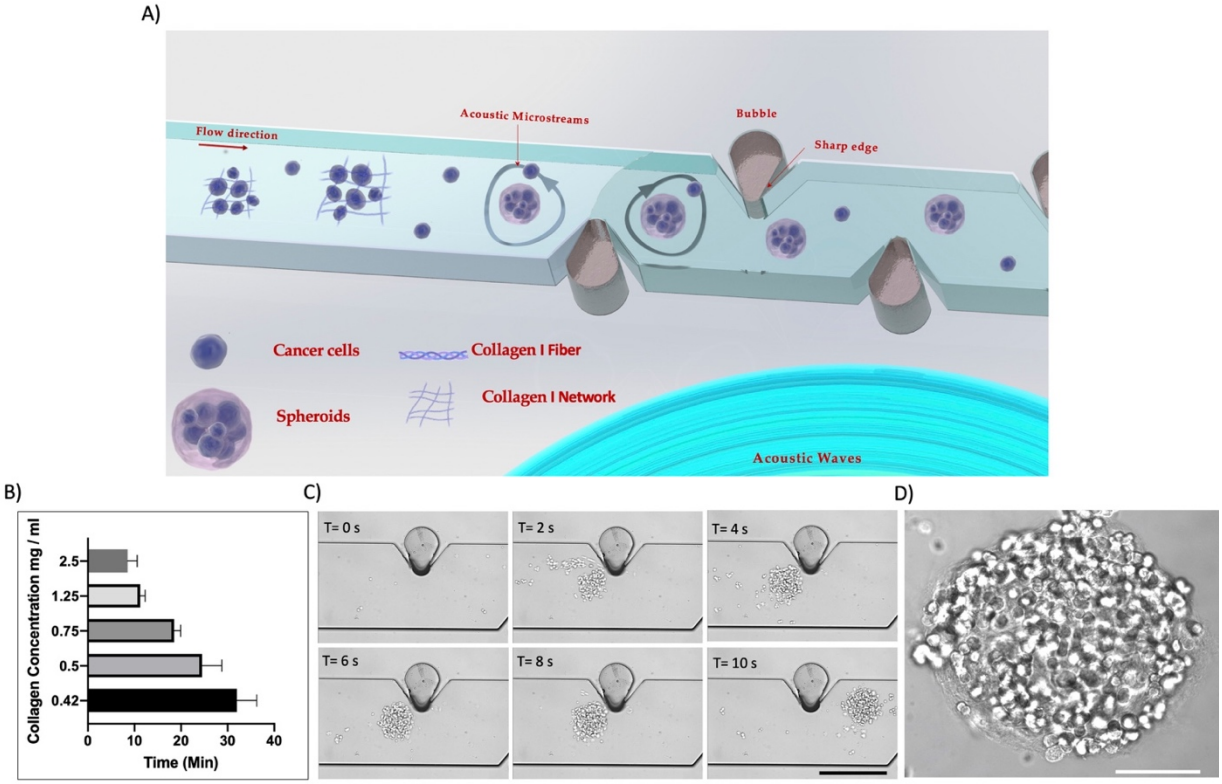

Figure 6.2. **A)** Conceptual illustration of acoustic spheroid formation mechanism by collagen assembly. Cells encompassed by collagen fibrils are infused in the microfluidic channel toward the boundary-driven acoustic streams, whereby they are trapped and reshaped into spheroids. **B)** Window of operation at different collagen concentrations showing the period the cell-collagen solution maintains its homogenous fluidity and adhesivity for acoustic assembly. **C)** Acoustic spheroid formation process in the device over time. Scale bar: 500 μm. **D)** Close up of a spheroid after acoustic assembly, showing the cells are enveloped by collagen, scale bar: 100 μm.

assembly, the collagen embedded in cell aggregate produced the robust cell-Matrix adhesion to protect the unity of the aggregate during retrieval from the microfluidic channel to the Petri dish (Figure 6.2.D).

6.3.4 Retrieving the spheroids

Working with the optimized parameters for the formation of spheroids in the continuous flow condition described above, the retrieval of acoustically formed spheroids was straightforward and did not require any pipetting or any additional steps. Upon removal of acoustic streaming, the collagen network was sturdy enough to hold the cells together, and the formed spheroids followed the flow direction to the outlet (Figure 6.2.A, C) and were collected in a Petri dish for further manipulations. The Petri dish was coated with Poly Hema to avoid spheroids' attachment to the substrate and was covered with parafilm to keep sterility during the acoustic assembly. The spheroids were then resuspended in fresh media and incubated for further compaction and growth. A common challenge faced during the culture of spheroids in a gel-free medium is the amalgamation of spheroids together and the formation of big clumps.[367] In our case, spheroids are more susceptible to clumping, especially in the first 2 days, due to the abundance of collagen in the spheroids. To prevent the undesired clumping of the retrieved spheroids, the Petri dish was filled with 1% MC in complete growth media. This helped to minimize the movement of spheroids due to the high viscosity of the milieu. The beneficial effect of MC addition is presented in Figure S6.3A and S6.3B. The spheroids incubated in regular media fused together and spheroids incubated in media with MC remained as individuals. However, one should note that the high fusion capacity of spheroids could present an interesting option for tissue engineering and for their 3D printing of cells where the creation of more complex biomimetic tissue is required.

6.3.5 Spheroid culture and analysis of cell survival/functionality

Figure 6.3.A depicts the size development and morphological evolution of spheroids formed by acoustic assembly with MDA-MB-231 cell line and MCF-7 cell line separately. During the first hour of cultivation, individual cell boundaries are discernible. After a few hours in culture and until a day of incubation, the aggregates' size shrinks, and their boundaries become less distinguishable. The smooth surface of the cell cluster indicates the formation of monolithic spheroids.

According to the initial cell concentration in aggregates, the expected diameter of spheroids was around 200 micrometers immediately after the assembly. However, a variation in their size was observed over the cultivation period. The mean diameter of spheroids over time is depicted in Figure 6.3.B, showing a similar pattern of decrease in the size of the spheroids of both cell types during the first day. The decrease in the diameter is attributed to the reconfiguration of cells in the spheroids in combination with the compaction phase which in the cells creates tighter junctions by secretion of integrins and/or cadherins.[368,335] The compaction phase is followed by the proliferation of cells that leads to gradual growth in the diameter of the spheroids with slightly higher growth for MDA-MB-231 spheroids compared to MCF-7 spheroids.

The spheroids of both cell-line show almost similar round morphology over 5 days of culture. MDA-MB-231 cells generally compacted faster and showed cells at peripheral of spheroids after 4 days. This tendency of MDA-MB-231 cells to migrate out of the spheroids can be attributed to their higher invasiveness.[369,370] While the well-defined spheroids of MCF-7 cells (Figure 6.3. A, C) is commonly observed in all methods, the compact spherical morphology of acoustically assembled MDA-MB-231 spheroids was interesting, as this cell type usually remains in loose form due to the weak cell-cell adhesion in other methods of spheroid formation.[371,351,359] To further emphasize the quality of cell-cell adhesion with our methodology, the shaking plate was used to form spheroids with MDA-MB-231 and confirm the loose aggregation (Figure S6.4).

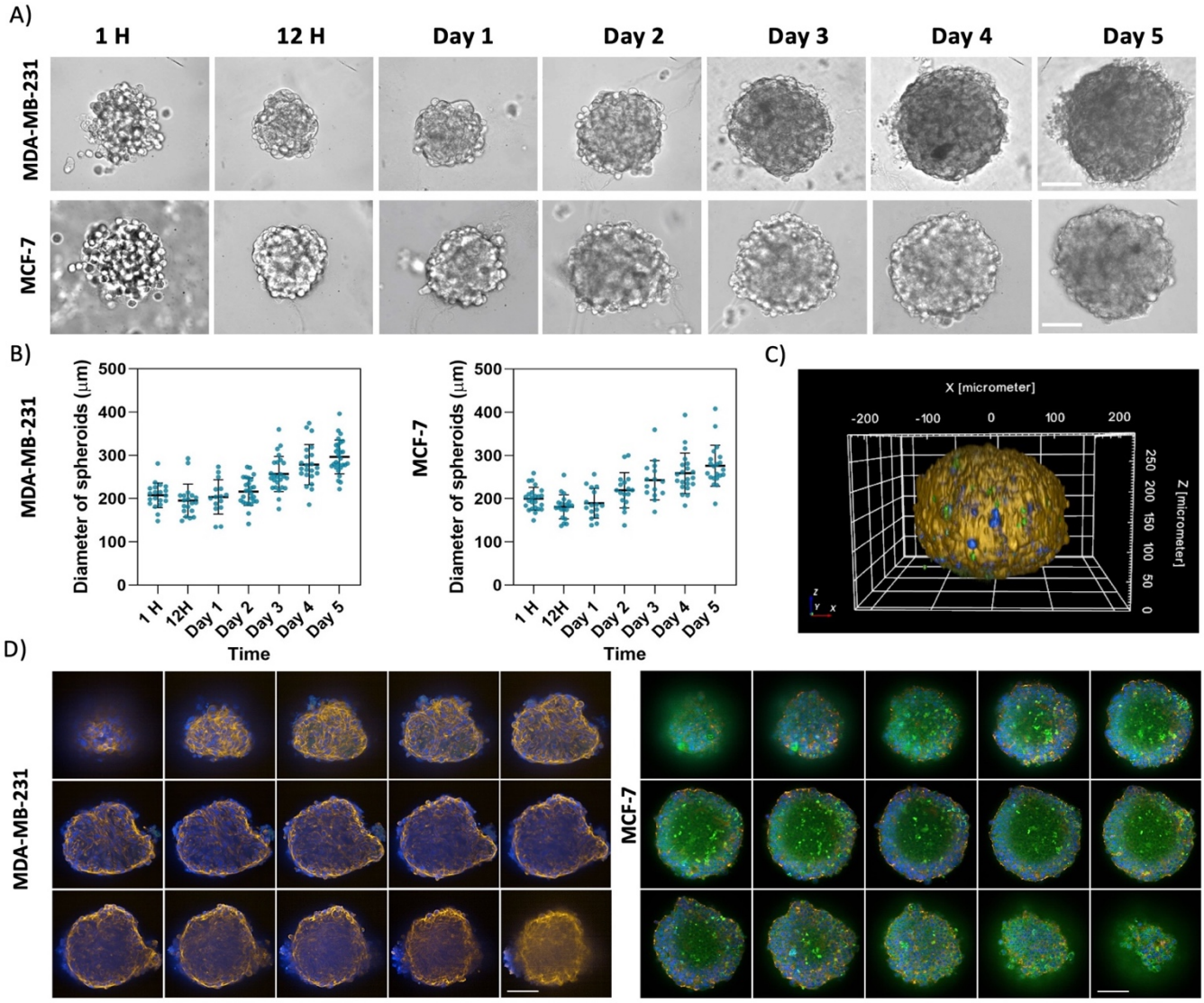

Figure 6.3. Long-term culture of **A)** MDA-MB 231 and MCF-7 cell spheroids. Pictures acquired by bright field microscopy, showing the evolution of the morphology and size of spheroids from 1h after acoustic formation to day 5. The individual cell profiles become less discernible as spheroids develop and secret their ECM proteins. The diameter development of **B)** MDA-MB-231 and MCF-7 over 5 days, showing an initial decrease in size during the first day, followed by gradual growth ($n \geq 15$). **C)** 3D reconstruction of a spheroid. **D)** The cross-sections of spheroids acquired by confocal microscopy and stained with Hoechst 33342 (blue), Alexa Fluor 594 phalloidin (yellow), and E-cadherin (green) for MDA-MB-231 and MCF-7. Scale bar: 100 µm.

The difference in the quality of cell aggregates between MDA-MB-231 and MCF-7 cells stems from the compaction mechanism of these spheroids. MCF-7 cells secret and accumulate E-cadherin on their surface to promote compact junctions through homophylic cadherin–cadherin bindings, in contrast, these binding molecules have no participation in the compaction of MDA-MB-231 spheroids.[331,351,359] As it could be seen in Figure 6.3.D, green-stained E-cadherin molecules are visible at cell junctions in the MCF-7 spheroids, but are absent in MDA-MB-231 spheroid even though they also form compact spheroids in acoustic assembly. Since in the acoustic spheroid formation cells are surrounded by collagen I, we believe that the presence and interaction of collagen I with integrin b proteins has played an essential role in the compaction of MDA-MB-231, which is in agreement with the literature findings.[371,351] From this result, one can conclude that the acoustic assembly is compatible with both cell lines despite their difference in the compaction mechanism.

Figure 6.4.A and B show the MCF-7 and MDA-MB-231 cell viability in spheroids determined by a live/dead assay kit. The result showed that the cell viability was maintained even after 7 days. Some dead cells were distributed through the spheroids, but they did not seem to indicate any necrotic core. This can be due to the relatively small size of spheroids as well as the active assembly of the cells, which was shown to prevent the formation of necrotic cores.[160,326] Interestingly, image analysis of cell viability over 7 days (Figure 6.4C and D) indicated that the cell viability in spheroids formed after acoustic exposure is higher than the cell viability of individual cells at 10 V_{PP} (Figure 6.1.D). This can be attributed to the high tensile strength of collagen network[357] that can act as a shield and protect the cell membrane from shear stress induced by the microstreams. Collagen fibrils surrounding the suspended cells can also support them against cell death due to non-adherence, as reported by Shin *et al* with polymer nanofibers.[372,373]

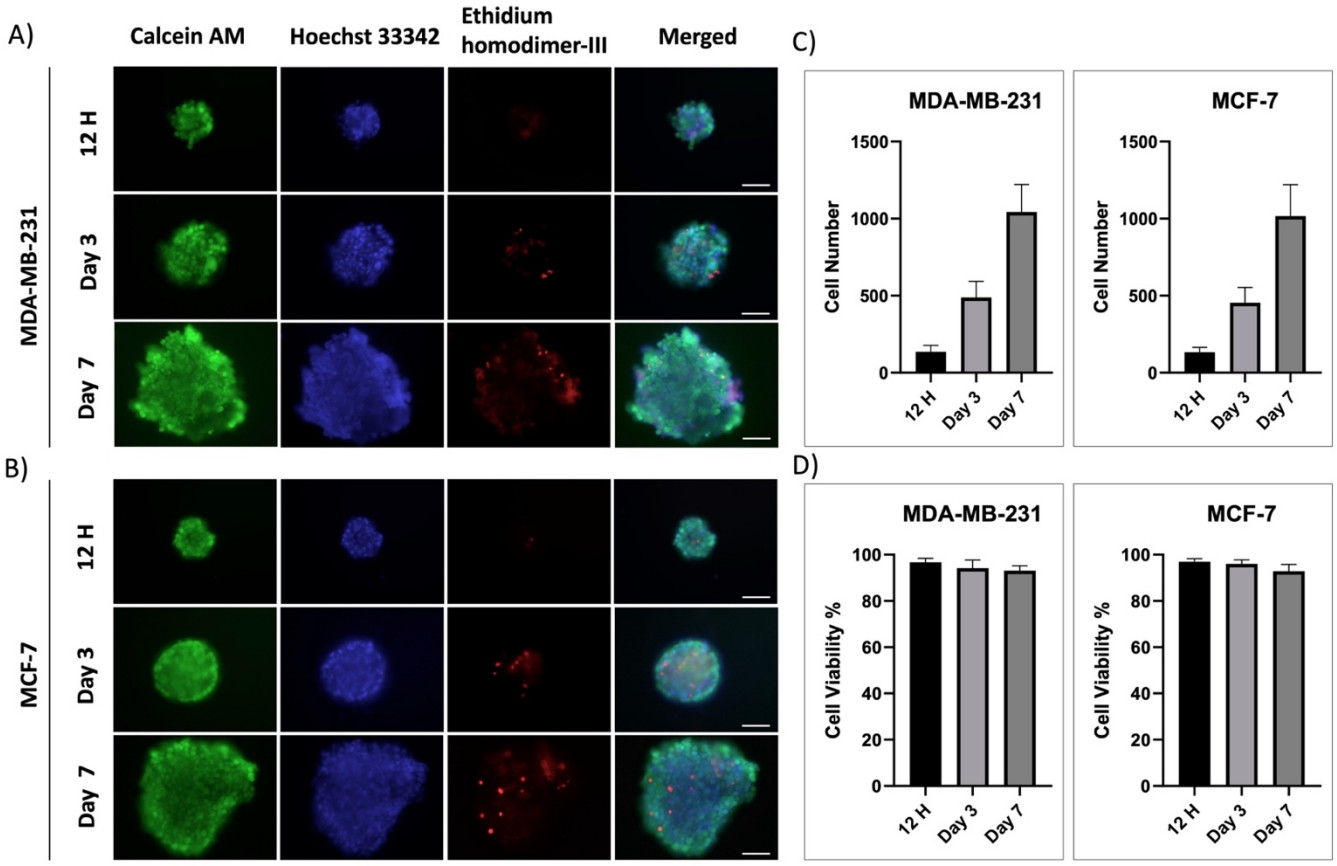

Figure 6.4. Cell Viability in acoustically formed spheroids. **A)** MDA-MB-231 and **B)** MCF-7 spheroids were stained with green Calcein AM for live cells, red ethidium homodimer III for dead cells, and Hoechst 33342 for nuclei. **C)** and **D)** show the cell number and the percentages of viable cells in the spheroids in 12 hrs., Day 3 and Day 7. Scale bar: 100 µm. The bar shows mean+SD.

6.3.6 Features of spheroid formation in acoustic microstreams

Multicellular spheroids formation.

The demonstration of the acoustic formation of coherent spheroids by our platform without relying on homophilic cadherin-cadherin interactions through the use of

collagen I, open the possibility for the formation of multicellular, heterotypic spheroids or cell-particle spheroids, regardless of their biological or inorganic nature. Figure 6.5.A shows the multicellular spheroids of MCF-7 cells which normally form homotypic cell-cell adhesion mediated by E-cadherin and MDA-MB-231, which do not express E-cadherin and their aggregation relies on integrin b-collagen I binding. MCF-7 cells stained with Green CellTracker™ CMFDA demonstrate approximately 118.0± 20.6 cells and MDA-MB-231 stained by Deep Red Cytopainter shows 103.3± 29.9 cells. Blue spots are results of Hoechst 33342 staining nuclei of both cell types with an approximate number of 229.9 ± 64.3. This purely physical assembly strategy allows to juxtapose and co-culture consortia of multi cell lines or multi-species cells for creating synthetic crosstalk between cells. Moreover, one of the challenges in studying multicellular spheroids is the variant extracellular environment which can be mitigated by the controlled incorporation of collagen using our platform.[374]

Composite spheroids formation.

Cell-particle composite spheroids have been used in numerous applications from guiding the spheroids in a magnetic field by incorporating magnetic particles to sensing or regulating mechanical properties, increasing cell viability, and inducing differentiation in stem cells.[338,375–377] Since particles, unlike cells, do not tend to actively self-assemble, many studies use centrifugation or gravity-based methods to incorporate particles. However, in the likely case of disparity between the density of cells and particles, it leads to sedimentation and therefore, uneven distribution of particles and cells. Additional steps and equipments such as *Random Positioning Machine* are required to improve the quality of the composite spheroids.[378] In this work, the acoustic assembly platform is used to alleviate the uneven distribution challenge by homogenizing the multi-cells or cell particle mixtures simultaneously to the spheroid formation. Figure 6.5.B shows the homogenous and densely packed spheroid of 5 μm diameter polystyrene particles (green) with an approximate total of 3666.7±590.2 and MDA-MB-231 cells which are recognizable by their blue nuclei

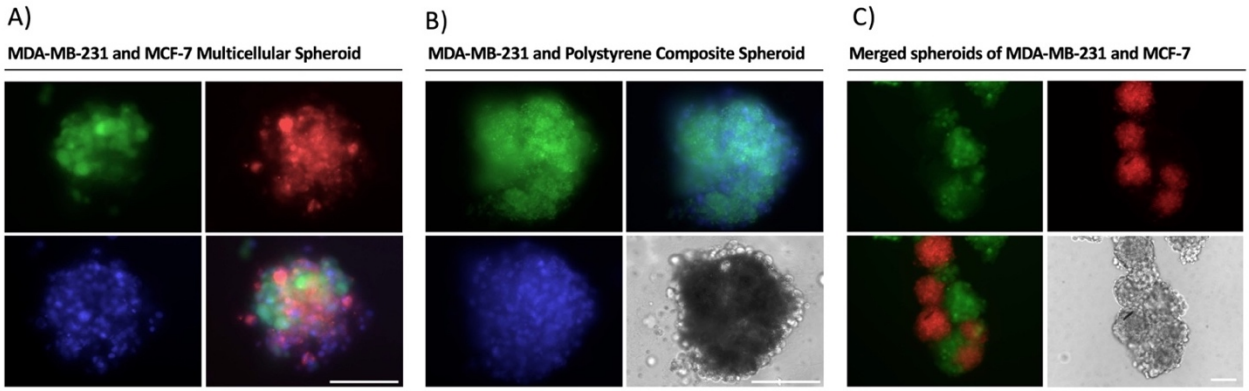

Figure 6.5. **A)** The multicellular spheroids of MCF-7 cells stained with Green CellTracker™ CMFDA and MDA-MB-231 cells stained with Deep Red Fluorescence Cytopainter. Nuclei of both cell types were stained with Hoechst 33342. **B)** Hybrid Cell particle spheroids. MDA-MB-231 (blue) and green fluorescent PS particles (5 µm) were mixed in collagen solution and assembled in acoustic microstreams to form cell-particle spheroids. **C)** Spheroids of MCF-7 cells (Green) and MDA-MB-231 (red) merged after 24 hrs. Scale bar: 150 µm.

stained with Hoechst 33342 and show 346.7± 87.1 cells. Moreover, since the interfaces between cells and microparticles are supported by collagen fibrils in acoustic assembly, it obviates the need to conjugate RGD peptides or collagen fibrils to particles' surface to ensure their attachment to the spheroid.[379,380,381] The forced and random positioning of cells in multicellular spheroids both with or without particles can be specifically helpful for studying the morphological changes and migration behaviors of cell types over time, due to differences in cadherin and integrin expression levels in a spheroid.[376]

Spheroids as tissue building blocks.

The fusion of multiple spheroids as building blocks are increasingly studied for engineering complex tissue structures.[382] Two important prerequisites for the use of spheroids as building blocks in tissue engineering are i) robust ECM to ensure stability and integrity of spheroids during the process and ii) the adhesiveness of spheroids to

initiate fusion.[383] However, during spheroid development, these two parameters progress inversely: as the spheroids mature and ECM deposition surges, adhesiveness among spheroids decreases.[383] Another factor adding to the complexity of using spheroids as building blocks, is the viability of cells since during the time needed to form mechanically stable spheroids, the core cells can be deprived of oxygen and nutrients. The ability of our acoustic device to incorporate collagen in a well-controlled manner can help to simultaneously promote both the mechanical stability and adhesiveness of spheroids.[384,385] Video S6.4 shows the spheroids retained their unity under shear stress immediately after formation. Moreover, the addition of collagen I as the adhesion-promoting factor can be used to study and control the kinetics of spheroid fusion.[385] To demonstrate this capability, the spheroids of MDA-MB-231 stained by Deep Red Cytopainter and MCF-7 stained with Green CellTracker™ CMFDA were cultured together in a 35 mm Petri dish within an hour of their formation. After 24 hours in the culture, both cell types retain their integrity, but the spheroids were starting to merge (Figure 6.5.C). The rapid production of high cell-density spheroids and their ability to immediately be used as building blocks can address some of the challenges of slow-growth spheroid formation such as deprivation of oxygen and nutrients to the cells over time.

6.4 Conclusion

We introduced a rapid and matrix-supported spheroid formation method using an acoustically-driven microfluidic platform. We demonstrated that cells can be aggregated in the eye of the vortex which can be used independently as a cell trapping/enrichment system or as a spheroid formation device. By adding collagen as a bioadhesive, the acoustic platform could shape and support cells into a 3D spheroid in seconds and recapitulate the native growth environment. The device allows for physical assembly and homogenous agglomeration of multi-types of cells or even particles in the vicinity of each other for studying cell behaviors such as migration, crosstalk, or changes in the morphology. The closely packed acoustic assembly holds

the potential to overcome some of the spheroid's formation challenges, especially for bottom-up tissue engineering such as low density, lack of cell-matrix and cell-cell communication after formation or reduced fusion ability after maturation. Moreover, this technique opens the venue for regulating both the mechanical and chemical characteristics of the growth microenvironment by additional steps such as crosslinking or encapsulating chemical cues in the collagen. The platform can also be used for shear stress studies on both spheroids and cells by applying controllable acoustic forces. The stability of rapidly formed spheroids combined with their high fusion tendency along with the ability of our device for making composite spheroid with functional particles such as magnetic particles that can be used for the directed fusion of spheroids, offer the possibility of creating complex tissue structures as models to investigate the underlying mechanisms of various diseases and develop the treatment modalities.

6.5 Material and Method

6.5.1 Materials:

A negative photoresist (SU-8 2050) was obtained from MicroChem Corp., USA. Polydimethylsiloxane (PDMS) was purchased from Dow Corning Corp., Canada. PTFE tubings (RK-06407-41) are from Cole-Parmer Inc., Canada. Trichloro (1H,1H,2H,2H- perfluorooctyl) silane, True gel 3D, and Poly-L-lysine, and Methylcellulose with the viscosity of 400 cP were ordered from Sigma-Aldrich, Canada. Microscope Glass slides were from Fisher Scientific, Canada. PhotoGel®-LAP kit was purchased from Advanced Biomatrix Inc. Piezoelectric transducers: model SMBA4510T05M were purchased from STEINER & MARTINS INC, USA. Parylene-C dimers were obtained from Specialty Coating Systems, USA.

6.5.2 Device fabrication and setup

The master mold was fabricated by spin-coating negative photoresist (SU-8 2050) on a wafer in two layers with the baking time, spin speed and lithography dosage per the manufacturer protocol. The master mold was silanized prior to pouring standard 10:1PDMS solution for replication of the channel patterns through soft lithography. After liftoff, the PDMS was permanently bonded onto a 75 x 50 mm glass slide by plasma surface treatment at 100 W for 1 min. For the experiment of Alginate and PLL and GelMA, the microfluidic channel was coated with Parylene-C while for the collagen assembly no coating was needed. Next, the piezoelectric transducer was mounted on the glass slide next to PDMS microchannels.

The function generator (AFG3011C, Tektronix, USA) was connected to the piezoelectric transducer and was regulated to generate squared radiofrequency (RF) signals at the resonance frequency of the platform for the maximum streaming effect. The piezoelectric STEMiNC (SMBA4510T05M) was used as the acoustic source at the resonance frequency of 16.1 kHz.

6.5.3 Impedance Measurement

Impedance spectroscopy for monitoring the gelation process was conducted with Agilent 4294A high precision impedance analyzer (Agilent, Palo Alto, CA). A constant frequency of 300 KHz and a peak-to-peak AC voltage of 5 mV were applied on a series of 300 μm interdigitated electrodes. The change of impedance for a fixed volume of collagen solution (300 μl) on the electrodes was recorded by GPIB computer data logging for 600 data nodes over the span of 90 minutes.

6.5.4 Cell culture

Malignant breast tumor cells (MDA-MB-231 cell line) and human breast adenocarcinoma cells MCF-7 were obtained from the American Type Culture Collection (ATCC, Rockville, MD). Both cell lines were cultured in Dulbecco's modified Eagle medium (DMEM), supplemented with 10% FBS and

1% penicillin/streptomycin (GIBCO). Cells were kept in T75 cell culture flasks and were split every 2–3 days. Prior to spheroid formation cells were suspended by 0.25% trypsin-EDTA and centrifuged at 200 g for 7 min at room temperature. Cells were then fully dispersed (critical) in DMEM without FBS to be added later in collagen solution.

6.5.5 Collagen-MC mixture preparation

8 parts of chilled Type I bovine atelocollagen solution, 3 mg/ml (PureCole) were gently mixed with 10X culture media. The solution was carefully neutralized by the addition of sterile 0.1 M NaOH, monitored by phenol red in the 10x media. The final volume was adjusted to reach a total of 10 parts per manufacturer protocol with sterile water. The collagen solution was diluted in serum-free media and was mixed in cell suspension via gentle pipetting. Finally, the MC dissolved in media was added to the mixture to reach the final concentration of 0.42 mg/ml collagen+ 0.4w/v MC.

6.5.6 Acoustic spheroid formation

Prior to each experiment, the microfluidic channel was sterilized by infusing 70% ethanol and was subsequently washed 2x with phosphate-buffered saline (PBS). The tubing was contained in ethanol 70% solution or autoclaved at 120^{o} (for 20 min) and washed 2x with PBS before attachment to the chip. The collagen solution was aspirated into 1 ml sterile syringe (Becton Dickinson) without a needle to avoid excessive shear stress on collagen fibrils which can affect the homogeneity of the solution. Needles (preferably larger gauges than 22G) can be used after aspiration as a connector to the tubes since the infusion flow rate is slow. The other inlet of the chip can be either PBS or DMEM to push spheroids into the outlet and subsequently the Petri dish when necessary. After connecting the inlets to the syringes, the outlet tube was guided to the Petri dish which was covered with a sterile parafilm layer. Harvard syringe pumps with two

independent motors were used to infuse the cell-collagen solution and PBS into the microchannel. The harvested spheroids are incubated at 37 °C and 5% CO_2 and after 1h the media is replaced with fresh media + 1%w/v MC to remove the residuals of collagen and stabilize the spheroids.

6.5.7 Low surface adhesion coating

To prevent attachment of the spheroids to the dish, the retrieval Petri dished were coated with 1.2 mg/ml poly (2-hydroxyethyl methacrylate) (poly HEMA) and incubated overnight to dry. Alternatively, the bioinert plates from Ibidi were used for better imaging.

6.5.8 Live/Dead Cell Evaluation

The viability tests were done by a live/dead assay kit (Viability/Cytotoxicity Assay Kit, Biotium). Cells or spheroids were washed with PBS and stained green with 2 μM Calcein AM for live cells and red with 4 μM ethidium homodimer-III for dead cells. The percentages of live and dead cells were quantified by analyzing images with ImageJ software.

6.5.9 Immunostaining

Spheroids were washed twice with PBS and were fixed in 4% (v/v) paraformaldehyde for 30 min. The fixed spheroids were permeabilized in 1% (w/v) Triton X-100 (Sigma-Aldrich) in PBS, were exposed to 1% BSA solution for 2h and washed in PBS before incubation in E-cadherin gap junction marker (Biotium) overnight at 4°. The antibody solution was washed 3 times with PBS and the Alexa Fluor 594 phalloidin (Sigma-Aldrich, Canada) and Nucblue (Sigma-Aldrich, Canada) were added to the spheroids to stain their F-actin and nuclei. Finally, the spheroids were washed after 30 min and clearing solution Scaleview 4 was added to the spheroid prior to the imaging. Pictures were acquired using Opera Phenix™ high-content screening system, Perkin Elmer.

6.5.10 Cell tracking and counting

MCF-7 cells were stained with CellTracker™ Green CMFDA (5-chloromethylfluorescein diacetate) and MDA-MB-231 cells were stained with Deep Red Fluorescence - Cytopainter (ab176736) following the manufacturer instructions for multicellular spheroids. The staining was done in the attached condition, 24 h prior to the experiment and cells were washed multiple times with PBS and media to ensure complete removal of unincorporated dyes which can label the other cell during experiments and cause crossover.

Cells in spheroids were counted with pictures acquired from a confocal microscope (Opera Phenix™ high-content screening system) at Z distance of 5 micrometers. The Hoechst 33342 stained nuclei were identified in the “Find Nuclei” module of Harmony® 4.9 imaging and analysis software.

6.6 Supporting Information

6.6.1 Over crosslinked collagen solution not showing formability

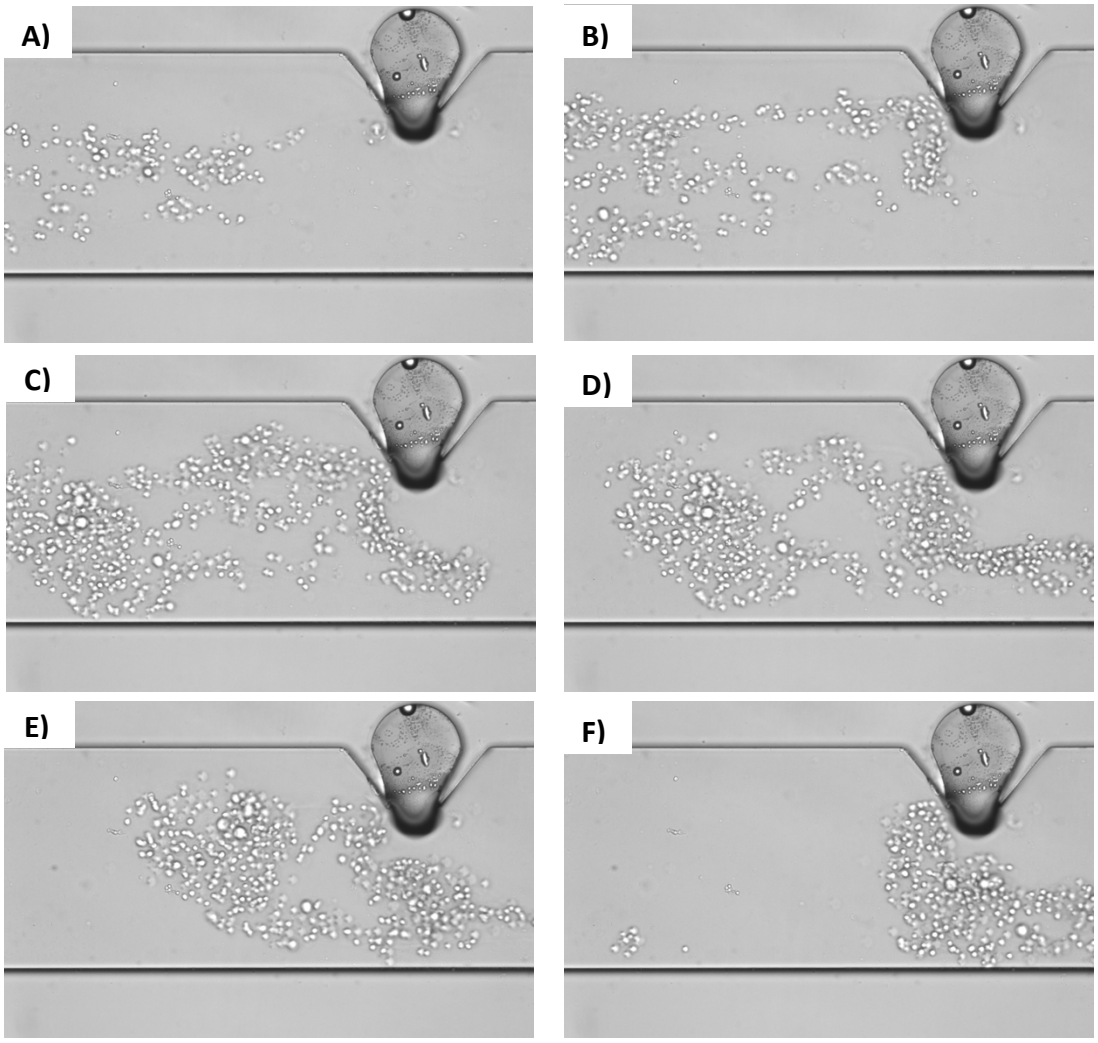

Figure S 6.1. Collagen solution after reaching the time window shows stiffer cell-collagen fiber network that is not formable by acoustic streams.

6.6.2 Impedance analysis of collagen at different concentrations over time

Generally, the impedance diagrams start by plateau or moderate slope region followed by a steeper slope. The phase transition of collagen was approximate to the breakpoint in the diagram. As it can be seen, in the lower concentration of collagen, the breakpoint in the curve becomes less discernible and the transition happens gradually. The

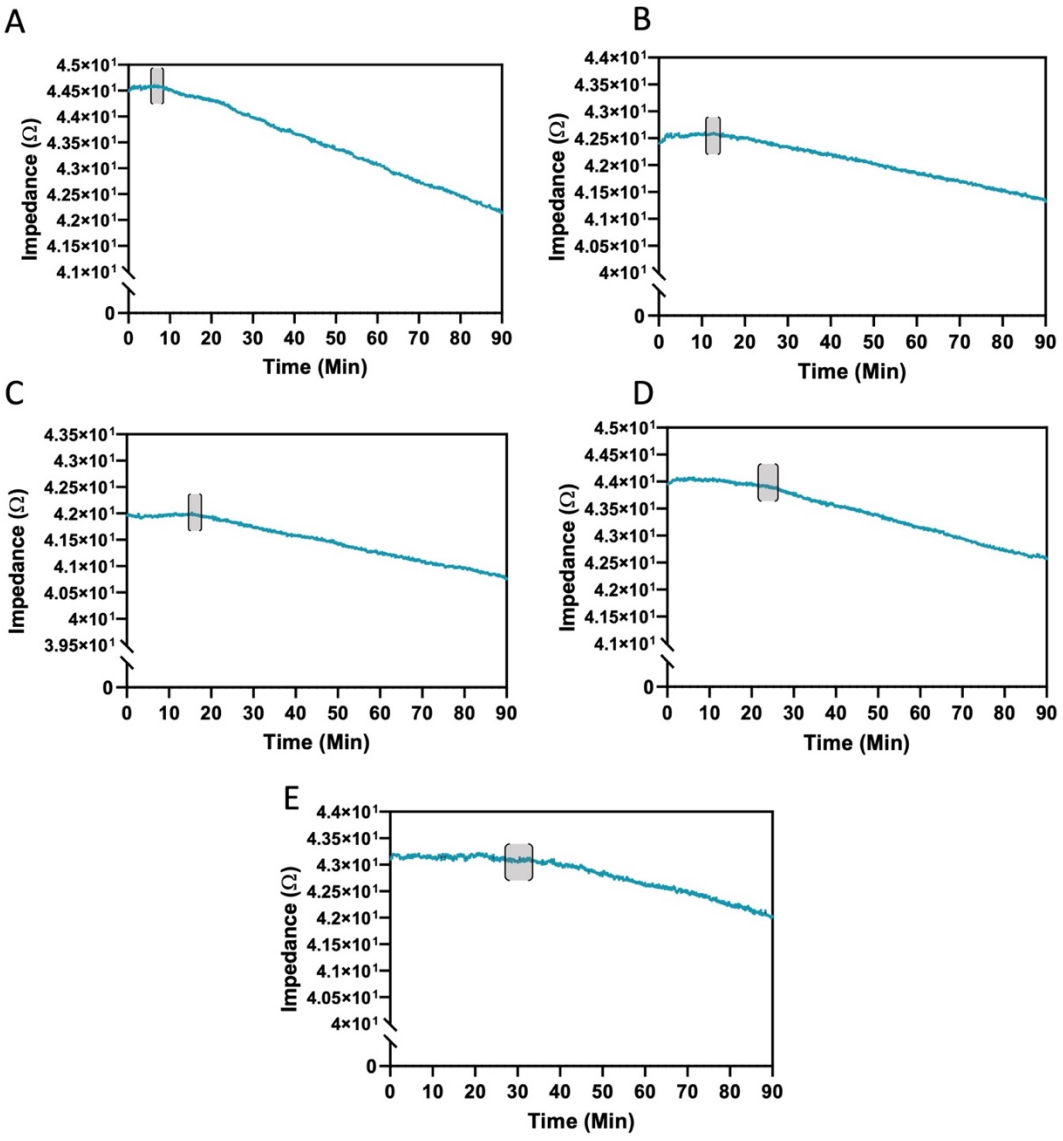

Figure S 6.2. A) Collagen concentration: 2.5mg/ml. **B)** 1.25mg/ml. **C)** 0.75mg/ml. **D)** 0.5mg/ml. **E)** 0.42mg/ml.

gelation process was also empirically monitored by “inverted tube test” to confirm the transition points.

6.6.3 Spheroid culture in Media vs Media+ 1% Methylcellulose

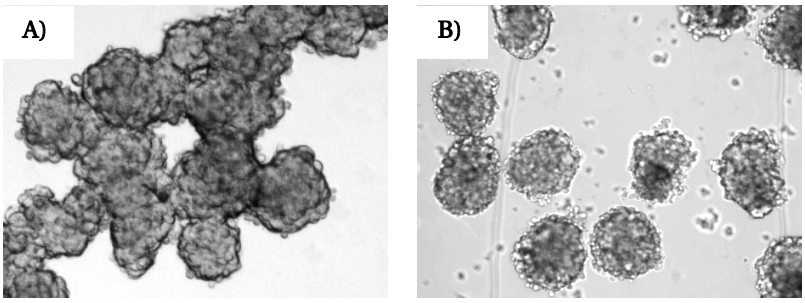

Figure S 6.3. Acoustically formed Spheroids incubated in **A)** Media and **B)** Media +1% MC. The spheroids in media alone tend to merge to each other while addition of MC could help to maintain them as individual spheroids.

6.6.4 MDA-MB-231 spheroids formation in shaking plate

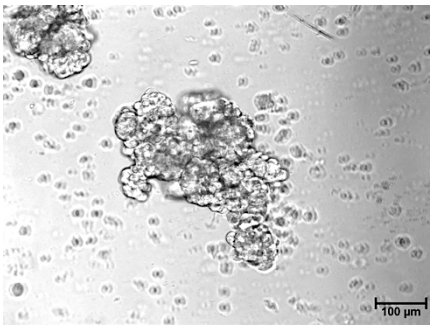

Figure S 6.4. MDA-MB-231 spheroids formed by shaking plate method after 7 days. In this method, in contrast to acoustic methods, the formed aggregates were more fragile and surrounded by numerous floating singles cells.

Video captions.

Video S6.1: Cell trapping in the acoustic microstreams.

Video S6.2: Spheroid formation of MDA-MB-231 cell line (the video is in 2x speed).

Video S6.3: Spheroid formation of MCF-7 cell line (the video is in 2x speed).

Video S6.4: Spheroid maintaining the cohesion under shear stress of different voltages.

7

Sonoprinting Nanoparticles on Cellular Spheroids via Surface Acoustic Waves for Enhanced Nanotherapeutics Delivery

This chapter explores the capacity of surface acoustic waves as means for delivery of nanoparticles and nanotherapeutics to the 3D cellular spheroids. In this study, we developed a high-frequency and low-amplitude acoustic platform, based on the state-of-the-art surface acoustic waves technology to emanate biocompatible acoustic waves. Our aim was to sonoprint nanoparticles on spheroids by inducing Eckart acoustic microstreams and interparticle Bjerknes forces, as a method to increase the delivery efficacy of nanotherapeutics.

Journal Publication:

Reza Rasouli, Radu Alexandru Paun, and Maryam Tabrizian, "Sonoprinting Nanoparticles on Cellular Spheroids via Surface Acoustic Waves for Enhanced Nanotherapeutics Delivery", submitted to "Lab on Chip"

7.1 Abstract

Nanotherapeutics, on their path to the target tissues, face numerous physicochemical hindrances that affect their therapeutic efficacy. The barriers become more pronounced in pathological tissues, such as solid tumors, where the hydrostatic and physical barriers limit the penetration of nanocarriers into deeper regions, thereby preventing the efficient delivery of drug cargo. To address this challenge, we introduce a novel approach that employs surface acoustic wave (SAW) technology to sonoprint and enhance the delivery of nanoparticles onto and into cell spheroids. Our SAW platform is designed to generate focused and unidirectional acoustic waves for creating vigorous acoustic streaming while promoting Bjerknes forces. The effect of SAW excitation on cell viability as well as the accumulation and penetration of nanoparticles on human breast cancer (MCF 7) and mouse melanoma (YUMM 1.7) cell spheroids were investigated. The high frequency, low input voltage, and contact-free nature of the proposed SAW system ensured over 92% cells' viability for both cell lines after SAW exposure. The SAW sonoprinting enhanced the accumulation of 100 nm polystyrene particles on the periphery of the spheroids to near four-fold, while the penetration of nanoparticles into the core regions of the spheroids was improved up to three times. To demonstrate the effectiveness of our SAW platform on the efficacy of nanotherapeutics, the platform was used to deliver nanoliposomes encapsulated with the anti-cancer metal compound copper diethyldithiocarbamate (CuET) to MCF 7 and YUMM 1.7 cell spheroids. Up to a three-fold increase in the cytotoxic activity of the drug was observed in spheroids under the effect of SAW, compared to controls. These promising nanotherapeutic delivery results induced by our SAW platform, coupled with the capacity of SAW-based devices to be manufactured as minuscule wearable patches can offer highly controllable, localized, and continuous acoustic waves to enhance the drug delivery efficiency to target tissues.

7.2 Introduction

Nano-mediated delivery systems are increasingly explored to reduce the off-target toxicity and immune response by protecting the cargo, transporting high payloads of the active agent, and performing controlled release.[6,15] Despite nanomedicines' success in reducing toxicity, their ability in enhancing therapeutic efficacy has been limited in clinical applications.[386,387] One key factor contributing to this limited performance is the poor penetration of nanomedicines into the densely packed tissues, particularly into solid tumors.[388]

The pathological characteristics of tumors, such as high interstitial fluid pressure and the overexpression of extracellular matrix impede the convective flow from the circulation to the tumor interstitium. In the absence of convective flow, the diffusion of nanoparticles (NPs) becomes markedly slower and constrained as the size of the nanocarriers increases.[389] This size dependency creates a dilemma as the larger NPs offer the capacity to carry larger payloads, but their limited penetration prevents them from realizing better efficacy compared to smaller NPs. For instance, Wang *et al.*[390] showed that 100 nm particles did not offer better therapeutic effects compared to that of 30 nm particles despite their larger drug cargo. In another study, the distribution of doxorubicin-loaded nanoliposomes (Doxil®) was shown to be limited to the peripheral cells of tumors.[391] This could be a reason why Doxil® did not show superior efficacy over free doxorubicin in many solid tumors.[387,392]

Given that the majority of the commercially available anticancer nanomedicines are within the 100 to 200 nm range,[386] researchers proposed various methods to improve penetration without shrinking the size and payload of NPs. Generally, there are two main approaches to enhance the tumor penetration of nanoparticles: the first strategy focuses on engineering the characteristics of nanoparticles to overcome the diffusion barriers, while the second method is modulating the tissue or tumor characteristics to facilitate nanoparticle transportation.[16]

Size, surface chemistry, charge, shape, and mechanical properties of NPs are shown to be influential in their penetration depth into spheroids.[16] In optimizing these NP parameters, however, the penetration capacity cannot be the only criterion and other complicated steps of drug delivery, such as circulation time, distribution, clearance, and extravasation should also be considered. Hence, the complex engineering of the nanoparticle is one part of the equation, and the complementary part could be the modulation of the tissue structural barriers and the tumors' physical environment to decompress and reduce physical stresses. One of the methods for stress normalization is to degrade the matrix components, such as collagen.[393] For instance, exposing tumors to extracellular matrix-degrading enzymes, such as collagenase type I, is shown to disrupt the dense interstitial collagen lattices and reduce the intestinal fluid pressure to restore convective flow and enhance the penetration of NPs.[394,395] However, excessive degradation of collagen can make the tumor prone to metastasis and invasion.[16,395,396]

Exogenous forces such as radiation, magnetic, or acoustic forces are commonly explored to modify the tissue or the tumor's physical environment.[16] Mechanical forces have been shown to mitigate the tissue barrier for passive diffusion, while their interaction with NPs can also induce active delivery into the tumors.[397]Among these mechanical forces, acoustic waves have an extended history of applications as means for drug delivery, thanks to their label-free and generally non-invasive nature, as well as their versatility for being used with diverse NPs and tissues.[398,399] Depending on the actuation conditions (*e.g.* frequency, pressure amplitude, pulse duration, wave types, etc.) and the nature of the target tissue (attenuation mechanism and acoustic impedance, state), acoustic waves can create various phenomena such as the hyperthermal effect, cavitation, microstreams, and acoustic radiation forces.[400,401]

One of the conventional acoustic methods for enhancing nanoparticle delivery is through the hyperthermal effect, which occurs by the absorption of sound waves in tissue, usually emitted from a high-intensity focused ultrasound system. The local increase of temperature in tissue can enhance drug delivery by increasing blood circulation, vascular permeability, reducing intratumoral pressure, or the release of

thermosensitive nano-carriers.[400,402] Hyperthermal ultrasound has been used to improve the delivery of magnetic [403] and gold NPs [404] and release thermosensitive nanocarriers such as ThermoDox® into tumors.[405] The other widely explored ultrasound strategy for drug delivery is cavitation-based delivery, which generally requires nano or microbubbles, such as contrast agents in the target tissue. When these bubbles are exposed to an acoustic field, their volume oscillates, which can create microstreams. If the acoustic pressure becomes strong enough, the bubble bursts and releases a shock that induces biophysical effects, such as cell membrane disruption, opening of intercellular junctions, and altering the tumors' perfusion.[405,406] In several preclinical studies, the potential of cavitational ultrasound for overcoming the biological drug delivery barriers for tumors and the brain has been investigated.[406–409] Despite their many advantages, the thermal and cavitation effect of conventional ultrasound systems can cause damage to healthy tissues near the tumor depending on their intensity. Blood vessel dilation and structural damage, oxidative stress by the formation of free radicals, damage to cell membranes and cytoskeleton, and unwanted cavitation can also happen in these ultrasound settings.[402]

In the past few years, Surface Acoustic Wave (SAW) has emerged as a powerful acoustic technology in the biomedical field to address some of the biocompatibility issues of conventional ultrasound systems by offering high frequency, resolution, and controllability. Recently, SAW was shown to increase the uptake of NPs in adherent cells and improve the non-viral transfection of suspended cells by cavitation-free sonoporation. Acoustic microstreams were the dominant effect in this setting.[230,231] Moreover, SAW has shown the capacity for the trapping and enrichment of NPs on microparticles through inducing interparticle Bjerknes forces.[145]

In this study, we developed a SAW platform to sonoprint NPs on spheroids of human breast cancer (MCF 7) and mouse melanoma (YUMM 1.7) cells. These cells were chosen as a model to validate the efficacy of our device using cellular spheroids of epithelial and melanocytic origin due to their different mechanical and biological properties.[410,411] We aimed to employ SAW sonoprinting to enhance the delivery of NPs

to spheroids without inducing cell damage or metastatic phenotypes. The proposed platform was designed to generate focused and unidirectional acoustic waves in high-frequency, non-contact, and low input voltage conditions that are proven to minimize mechanical stress and unwanted cavitation. The operation parameters of the SAW device were optimized to induce two acoustic phenomena called Eckart microstreams and Bjerknes forces for sonoprinting and delivery of NPs onto/into melanoma and breast cancer spheroids. To investigate the effect of SAW sonoprinting on the deposition of NPs on spheroids' surfaces, fluorescent polystyrene NPs with the therapeutically relevant size of 100 nm were first assessed. Deep confocal microscopy was used to monitor the influence of SAW on the penetration of polystyrene NPs in the deeper layers of spheroids and their spatiotemporal distribution in spheroids' mid-cross-section. Subsequently, we employed the SAW platform for the delivery of anticancer CuET-loaded liposomal NPs to our pseudo-tumor models. The efficacy of the acoustic drug delivery was validated by measuring the cytotoxic effect of CuET-loaded liposomal NPs on spheroids. To demonstrate the biosafety of the SAW platform, both cell viability and the metastatic phenotype of cells were assessed by live/dead assay and gene expression in the presence and absence of SAW.

7.3 Results and Discussion

7.3.1 Working mechanism of the acoustic platform

To enhance the delivery of NPs into spheroids by acoustic waves, two steps are required: the first step is to induce the accumulation of NPs on the surface of the spheroids by sonoprinting, and the second step is to increase the penetration of the penetrated NPs into the inner layers. It has been shown that acoustic streaming is the dominant mechanism to deliver vibrational energy to the media and the suspended particles.[231] Acoustic energy has also been reported to permeabilize the cell-cell junctions which could facilitate the penetration of NPs.[215] Bjerknes forces are the other

acoustic phenomena that can boost the accumulation of NPs on tissue or spheroids by creating attractive interparticle forces.

To generate these two acoustic phenomena, we developed a surface acoustic wave platform that consists of interdigital transducers (IDT) on a piezoelectric lithium niobate (LN) substrate with a high electromechanical coupling coefficient. The general working principle of SAW is described as follows: when radio frequency signals reach IDT, each finger vibrates to emanate acoustic waves, which as the name suggests, travel on the surface of the piezoelectric substrate. Positioning the IDT of the same charge on the substrate with a wavelength (λ) distance leads to constructive wave interference between IDTs to create strong surface acoustic waves. The crystal orientation of piezo substrate (127.86° Y-cut, X-propagating) allows generating a wave-type known as leaky Rayleigh waves, which is suitable for transferring acoustic energy into liquids. When Rayleigh waves encounter liquids, the mismatch between the acoustic impedance of the liquid and the piezoelectric substrate leads to leakage of the acoustic energy into fluids and the waves continue their path within the fluid medium. We used this principle to guide the acoustic beam from the piezoelectric surface into the glass-bottom Petri-dish via a coupling layer of deionized water (Figure 7.1.A). Once SAW reaches the spheroids and NPs suspension in the Petri-dish, it creates acoustic streaming flow and acoustic radiation forces, which to our hypothesis, can contribute to the sonoprinting and penetration of NPs in the spheroids (Figure 7.1.B). The main acoustic streaming flow in the system is attributed to Eckart streaming which is the result of viscous attenuation of the acoustic energy during the propagation of waves in the bulk of the fluid.[99] As the acoustic beam travels away from the source, the energy of the waves dissipates at a rate proportional to the square of their frequency, thus generating an acoustic pressure gradient that forms microstreams. These microstreams not only can bring the spheroids and particles to the close vicinity of each other in the eye of the vortex but are also shown to improve the cellular uptake of NPs.[29]

Upon exposure to SAW, particles scatter a portion of the incident acoustic energy in all directions and create a time-averaged inter-particles acoustic force. As such, the

scattered acoustic waves interfere with the acoustic field of the neighbor particles, resulting in the mutual particle-particle force known as secondary Bjerknes force. Depending on the nature of the particles and waves, Bjerknes force can be attractive or repulsive. This force has been recently used to create particles agglomerations, as a method for filtration and enrichment of nanoscale solid particles and vesicles. The intensity of this force is shown to be usually at its peak when the sound wavelength approaches particle diameter ($d/\lambda \approx 0.5 - 1$).[108,109]

7.3.2 Optimization of operating parameters for the SAW platform

To ensure the occurrence of Eckart streams and Bjerknes forces for sonoprinting and delivery of NPs to spheroids, we designed the platform to operate at the frequency of 13.7 MHz. This frequency corresponds to the wavelength of 300 µm and allows to maximize the Bjerknes forces in the spheroids of interest, which have mean diameters within 150-300 µm range ($d/\lambda \approx 0.5 - 1$). For strong Eckart streaming to happen, the chamber dimensions L should be much longer than λ in order to provide enough propagation path for the acoustic beam to attenuate.[93] The attenuation length of SAW in fluids is frequency-dependent and can be calculated by $x_s = \rho_s c_s \lambda_s / \rho_f c_f$, where ρ_s and ρ_f are the densities of the piezoelectric substrate and fluid respectively while c_s and c_f are the propagation speed of acoustic waves in piezoelectric substrate and fluids.[412] Laying these parameters in the above equation, the attenuation length for our SAW platform with the operating wavelength of 300 µm approximates 3.86 mm. Hence, the well diameter of L=1 cm is used in the proposed set-up to provide the sufficient attenuation path for the acoustic waves and the formation of strong Eckart streams.

The next design criterion was the IDT configuration for creating traveling SAW. Straight IDTs are the standard setting for SAW while focused IDTs (FIDT) allow concentrating the acoustic energy in a confined domain. For producing Eckart streams with straight IDT, the chamber should be placed at the edge of IDT to induce heterogeneous exposure of the fluid to acoustic waves. This non-uniformity of acoustic

field becomes very sensitive to the positing of the chamber in each experiment, and also leads to asymmetric vortices.[413]

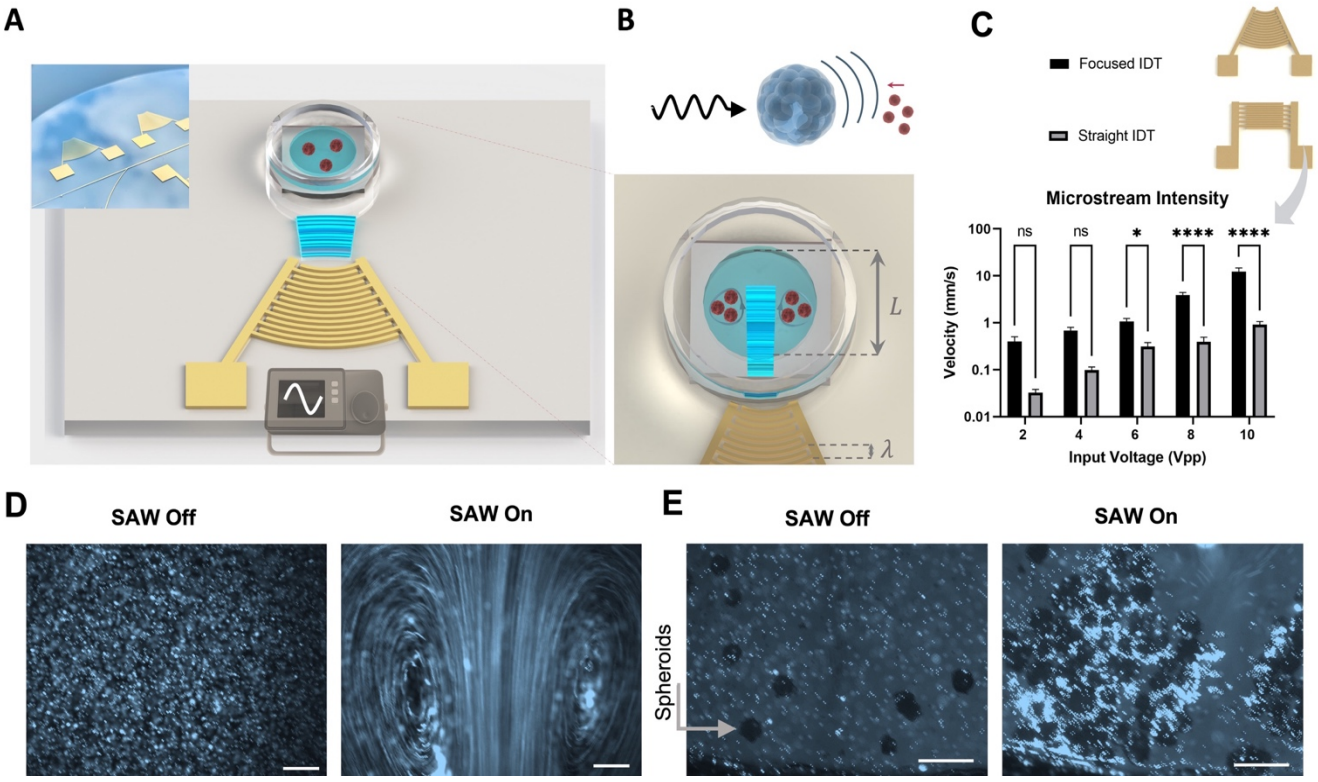

Figure 7.1. A) Rendered image of the SAW platform including a piezoelectric substrate with focused interdigitated transducers (FIDT) and a glass-bottom Petri-dish. Upon activation by the function generator, the surface acoustic waves generated by IDTs travel on the substrate surface and leak into the Petri-dish through the coupling layer (water). **B)** Inside the Petri-dish, acoustic waves propel the media and create acoustic streams which bring the nanoparticles and spheroids to the center of the microstreams to increase the NP uptake. **C)** Comparison of acoustic microstream intensity produced by straight and focused IDTs. **D)** Demonstration of Eckart microstreams' formation in the presence of SAW by using fluorescent polystyrene microparticles. **E)** Suspension of cellular spheroids and microparticles. Upon activation of SAW, spheroids attract the microparticles and increase their concentration in their vicinity. The scale bars are 500 μm. Data are plotted as mean + SD.

In contrast, focused IDTs' design could inherently produce a spatial gradient of acoustic pressure in a highly localized region and create symmetrical acoustic vortices with maximum unidirectional acoustic momentum.[139,414] To quantify the microstream intensity produced by these two designs (straight IDT and focused IDTs), particle streak velocimetry was performed at different input voltages by using fluorescently labeled polystyrene particles of 5 μm for better visualization, as tracking of NP trajectory was barely possible in low magnifications and large domains.[415,416] Figure 7.1.C shows that the microstreaming from the focused IDT design is considerably stronger than that of the straight IDTs. This is in agreement with the literature reporting that the use of focused IDT can minimize reflective standing waves, which tend to suppress acoustic streams.[231,412] Moreover, Zhong *et al.* in a recent study showed that focused IDT can transmit around 4.83 fold more acoustic energy compared to straight IDT, where acoustic waves propagate bi-directionally causing energy loss.[417]

Figure 7.1.D shows the counter-rotating acoustic microstreams from a focused IDT source. In the absence of acoustic energy, particles remained quiescent. As expected, upon the introduction of acoustic waves to the suspension, the acoustic beam propelled the liquid in the propagation direction, creating a time-averaged fluid jet. This jet flow in a confined chamber induces a backflow to develop counter rotational Eckart vortices. The Eckart vortices span throughout the chamber and can be rapidly generated and stopped by controlling the radiofrequency signals (Video S7.1).[93] When the spheroids of YUMM 1.7 cells were introduced to the microparticles suspension and were exposed to the SAW waves from the focused IDT source, the hydrodynamic forces gathered the spheroids in the vortexes while bombarding them with the microparticles. As a result, after only a few seconds of acoustic energy activation, the fluorescent microparticles were surrounding the spheroids, denoting the effectiveness of our acoustic platform in enhancing the exposure of spheroids to the particles (Figure 7.1.E). This accumulation of particles around the spheroids was an indication of the presence of the attractive Bjerknes forces to induce sonoprinting.[145] Moreover, the vigorous acoustic streams that were observable in our SAW platform, suggested the optimal

working parameters for NP penetration for the next sets of experiments. The acoustic streams have been shown to be the main phenomena for delivering acoustic energy to suspended particles and cellular uptake.[230,231] Since the Bjerknes forces decay by the increase of the particle distance, the microstream can also enhance the Bjerknes forces by bringing the spheroids and microparticles into the immediate vicinity of each other. As shown in the Video S7.2, the drag forces from acoustic streams gathered the spheroids and microparticles in the vortex center while the convective mass transfer by the streams ensured the close contact and homogenous exposure of microparticles to spheroids.

7.3.3 Cell spheroids' exposure to SAW does not affect the cell viability

To investigate the impact of acoustic radiation forces and the hydrodynamic forces generated by acoustic streams on cells' viability, coherent and viable spheroids of MCF 7 and YUMM 1.7 were formed with each cell type. Both these cell lines can readily form spheroids in culture and their native occurrence location in the body is rather accessible to acoustic stimulations. Therefore, the bioinert SAW devices can be conceptually employed as skin patches to potentially complement the treatment of skin cancer, such as in-transit or unresectable cutaneous melanoma[418,419] or to locally modulate tumor microenvironment for unresectable breast cancer.[420] The spheroids of both cell-types were cultivated after 3 days and characterized. The size measurement and roundness analysis of the spheroid indicated a slightly larger size for MCF 7 spheroids, but rounder spheroids for YUMM 1.7 (Figure 7.2.A). The size of both spheroids was within the peak Bjerknes forces in the device. Furthermore, as a common indicator of cell-cell compactness in spheroids,[421] the optical density measurement revealed a higher density in YUMM 1.7 (Figure 7.2.A).

Figure 7.2.B, and 2C show the MCF 7 and YUMM 1.7 spheroids for 1, 3, 5, 10, and 15 minutes SAW exposure and control, stained with green Calcein AM as live cell marker, red ethidium homodimer III for dead cells, and blue Hoechst 33342 for nuclei. To

quantify the cell viability in spheroids after SAW exposure, the total number of cells and

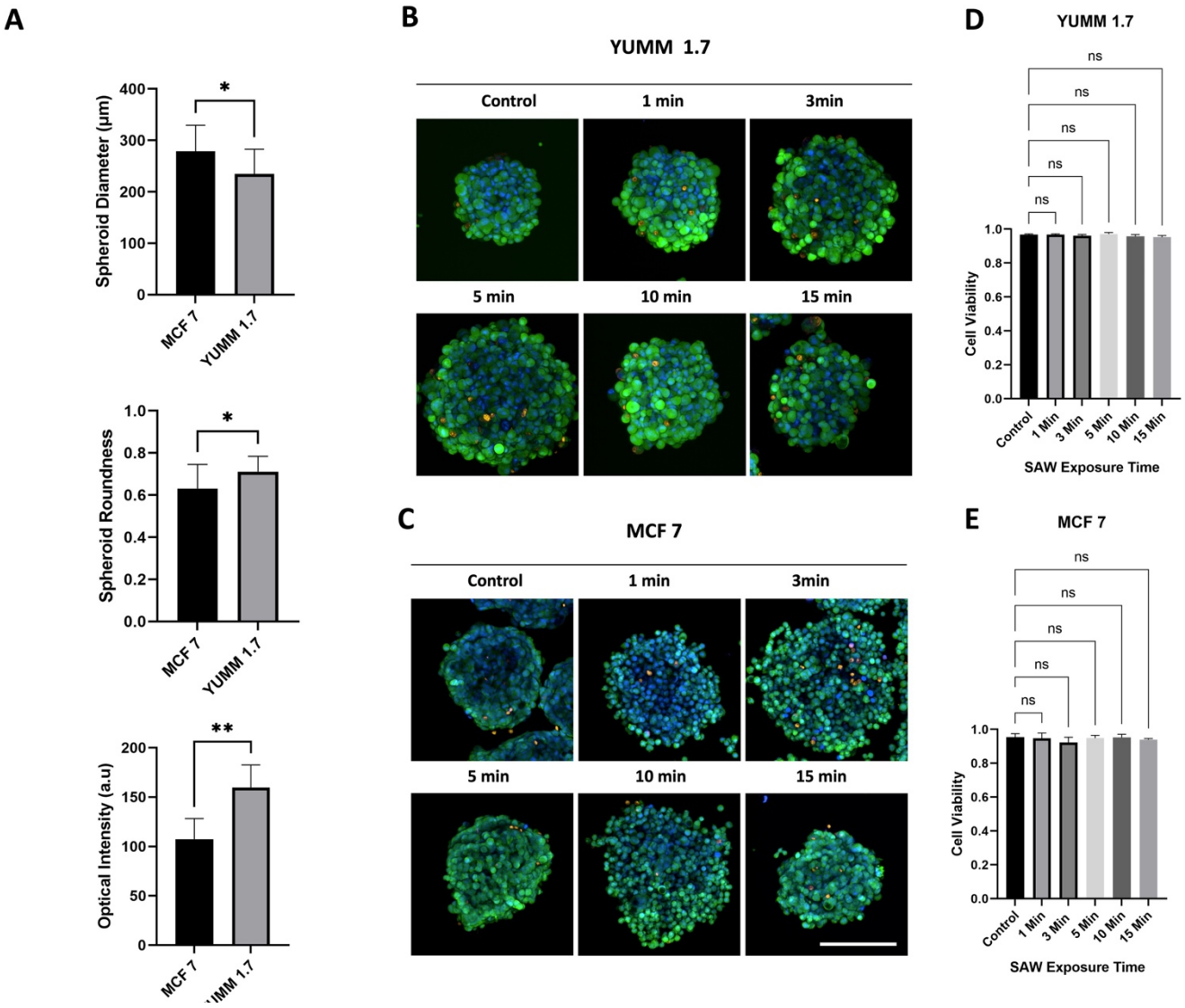

Figure 7.2. A) The morphological characterization of MCF 7 and YUMM 1.7 spheroids, including the diameter, roundness, and optical intensity. The cell viability in the **B)** YUMM 1.7 spheroids and **C)** MCF 7 spheroids after different exposure times to 10 V_{PP} SAW. Spheroids were stained with green Calcein AM for live cells, orange ethidium homodimer III for dead cells, and Hoechst 33342 for nuclei. The figures show the maximum projection of the planes at a Z distance of 10 µm, acquired by high-resolution confocal microscopy. The scale bar is 200 µm. The quantification of cell viability is performed using the Harmony 4.9 software for **D)** YUMM 1.7 and **E)** MCF 7. Data are plotted as mean + SD.

dead cells were counted in 3D and plotted in Figure 7.2D and E. The results indicated no significant effect of the SAW on the cell viability, regardless of the duration of their exposure to SAW. The SAW post-exposure cell viability was over 95% and 92% for YUMM 1.7 cell spheroids and MCF 7 cell spheroids, respectively. These numbers are considerably higher compared to conventional acoustic treatments such as cavitational methods with common cell viability of as low as 60%.[206] The high rates of cell viability in our SAW platform are in agreement with the literature reports, which ascribe the inherent biocompatibility of SAW to the high operation frequency that suppresses the possibility of destructive cavitation and ensures minimal stress on the cells.[230] The high cell viability can also be attributed to the low driving voltage of 10 V_{PP} and the contactless setting of our acoustic platform that reduces heat generation, often harmful to cells.[422]

To fathom and quantify the effect of SAW exposure on the accumulation of NPs on spheroids, fluorescently labeled 100 nm polystyrene NPs with carboxylic acid (COOH) on the surface were employed. The caveats for choosing these NPs were to isolate the effect of SAW on NPs accumulation from other effects, such as nonspecific adsorption or size that might interfere with our measurements.[394] Negatively charged carboxylated NPs were thus purposely chosen to minimize the non-specific adsorption to cell membrane components and to facilitate NPs diffusion into spheroid's core regions.[394] The rationality for choosing 100 nm diameter particles was based on the fact that most anticancer nanomedicines have a diameter in this range. This NP size is reported to allow for an optimal cargo loading capacity while being within the efficient nano delivery size range (between renal clearance and upper EPR fenestration sizes).[386]

Sonoprinting of these polystyrene NPs onto YUMM 1.7 and MCF 7 cells spheroids was then examined using the SAW platform. To better represent the total NP accumulation on the spheroids, the maximum projection of the spheroids treated with 5 μg mL^{-1} polystyrene NPs was acquired by confocal microscopy (Figure 7.3). Predictably, as the spheroid exposure time to NPs increased from 3 min to 15 min, a higher concentration of NPs was attached to the spheroids' surface of both cell types,

regardless of the application of SAW (Figure 7.3.B, 3C). Nevertheless, at each time point, the presence of SAW significantly enhanced both the distribution and the density of NPs on spheroids compared to control spheroids (NSAW). In addition, the application of SAW allowed for a more homogenous distribution of NPs on the spheroids. This can be attributed to the acoustic microstreams shown in Video S5.2, which constantly rotate spheroids and transport NPs, exposing the entire spheroids' interfaces uniformly to NPs. The more noticeable impact of the SAW, however, was the increase in the number of NPs' accumulated onto the spheroids.

In order to quantify the NP concentration, the average fluorescent intensity of the NPs within the spheroid's boundary was measured. As depicted in Figure 7.3.D and E, for all the time points, when SAW was applied, the intensity of NPs was significantly higher. The mean NP accumulation was increased to 2.7-fold for MCF 7 spheroids and approximately 3.7 times for YUMM 1.7 after 15 min exposure to SAW, compared to that of spheroids without the application of SAW. Interestingly, the intensity of accumulated NPs was substantially less in YUMM 1.7 compared to that of MCF 7 cell lines. This can be due to the more compact structure of YUMM 1.7 spheroids as revealed by the measurement of their optical density (Figure 7.2.A).

7.3.4 SAW increases the delivery of NPs into the core of cell spheroids

Although NPs in the range of 100 nm in diameter present the optimal size, their therapeutic effects for the treatment of solid tumors have so far been limited due to their low penetration into the core of the tumor.[390] To analyze the dynamics of polystyrene nanoparticle penetration into our pseudo-tumor model and their spatiotemporal distribution following their exposure to SAW, we conducted a NP transport assay using the pulse-chase procedure[423] followed by 3D deep imaging and zonal analysis of the spheroids.

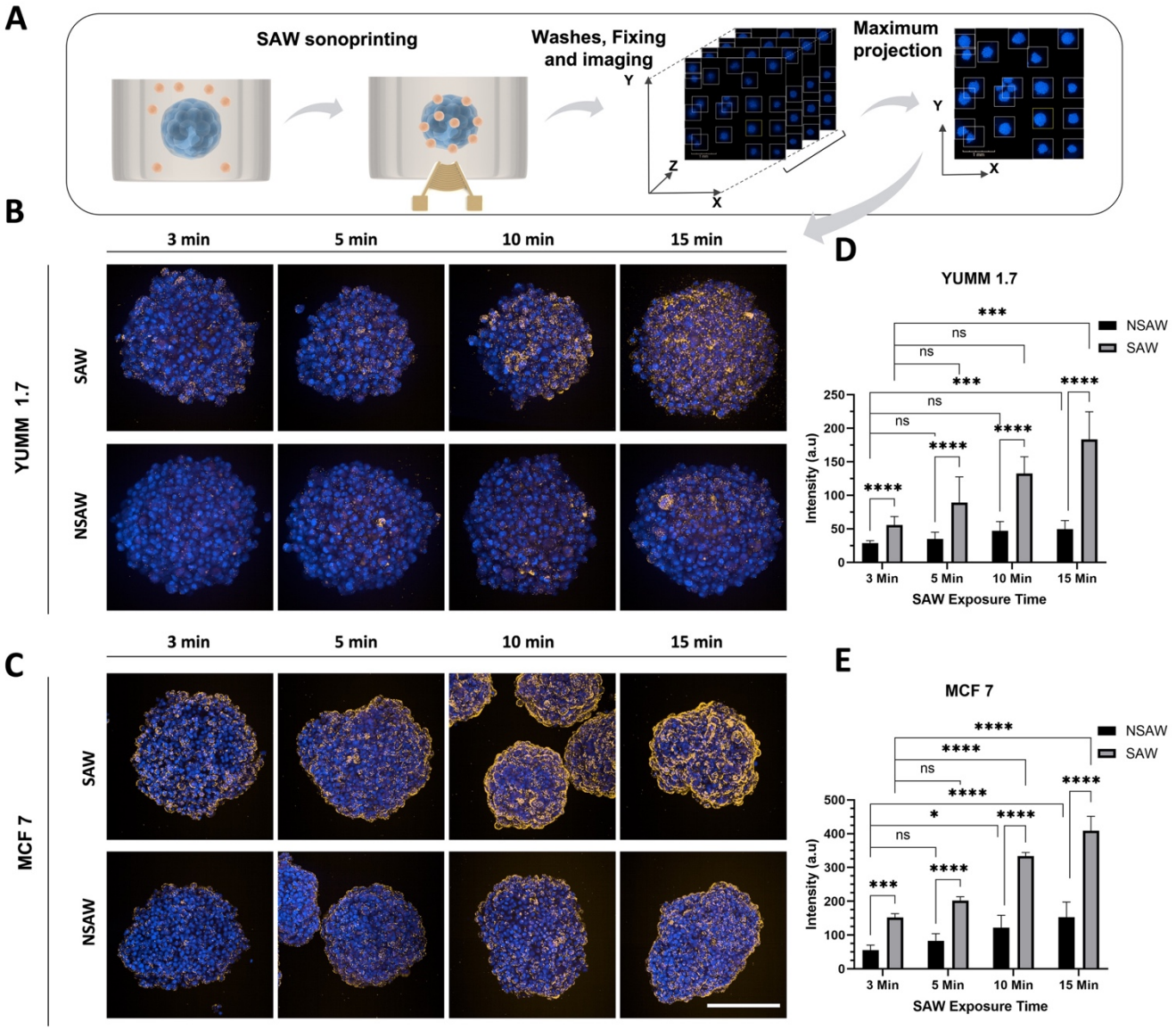

Figure 7.3. A) Overview of the SAW-mediated sonoprinting experiments and analysis. Accumulation of the 100 nm polystyrene nanoparticles (orange) on spheroids of **B)** YUMM 1.7 and **C)** MCF 7 cells in the presence (SAW) and absence (NSAW) of acoustic waves with different exposure times. The cells' nuclei were stained with blue Hoechst 33342. The figures show the maximum projection of the planes acquired by water-immersed, high-resolution confocal microscopy. The scale bar is 200 μm. The fluorescent intensity of the nanoparticles was measured and quantified in graph **D)** for YUMM 1.7 and **E)** for MCF 7. Data are plotted as mean + SD.

The pulse-chase procedure included a 10 min treatment of spheroids with 5 µg mL^{-1} FluoSpheres NPs in serum-free media to enable uptake (pulse time) with and without SAW activation. The spheroids were then washed and translocated to a fresh medium to remove suspended NPs and stop the uptake. After the pulse treatment, the spheroids were incubated for 0, 3, 6 and 24 hours for investigating the NP penetration pattern throughout the spheroid's layers over time (chase time). Analysis of the spatiotemporal distribution of NPs in the spheroids necessitated deep and high-resolution imaging of the spheroids' inner layers (Figure 7.4.A). To enhance the visualization of the spheroids' core, optical clearance was performed which is shown to increase the light transmission depth by reducing the scattering and absorption in the spheroids.[424]

Figure 7.4.B and 4C show the NPs distributions at the middle cross-section of MCF 7 and YUMM 1.7 cell spheroids respectively, acquired by water-immersion confocal microscopy. Immediately after NP treatment (chase time = 0 h), the accumulation of NPs was restricted to the peripheries of the spheroids. However, in the presence of SAW, some NP spots could be detected in the inner layers of MCF 7 spheroids, while compact YUMM 1.7 spheroids do not reveal a significant increase of fluorescence intensity in the core. As the chase time progresses, the NPs gradually migrate from the outermost layers into the inner layers for both cell type spheroids. The rate of this translocation seems to be strongly influenced by their exposure to SAW. In the absence of the SAW, the NPs distribution shows dominant peripheral localization even at 24 hours chase time point. SAW exposure considerably increased the penetration of the NPs into the inner layers and the fluorescence was distributed more uniformly throughout the spheroids. To quantify the SAW impact on the penetration of NPs into the core, we defined two image zones by the Harmony software (Figure 7.4.A, right). The outer boundary line defines the boundary of the spheroids in the Hoechst 33342 channel. To omit the NP stuck on the periphery of the spheroids from the penetration measurements, we defined a core region with a distance of 30 µm from the spheroid's boundary.

The fluorescent intensity of NPs in the core region was measured for different incubation times and subtracted from the control (Figure 7.4D and E). The SAW

activation increased the intensity of NPs in the core region by approximately two times for MCF 7 while the surge was almost threefold for YUMM 1.7 spheroids after 24 hours

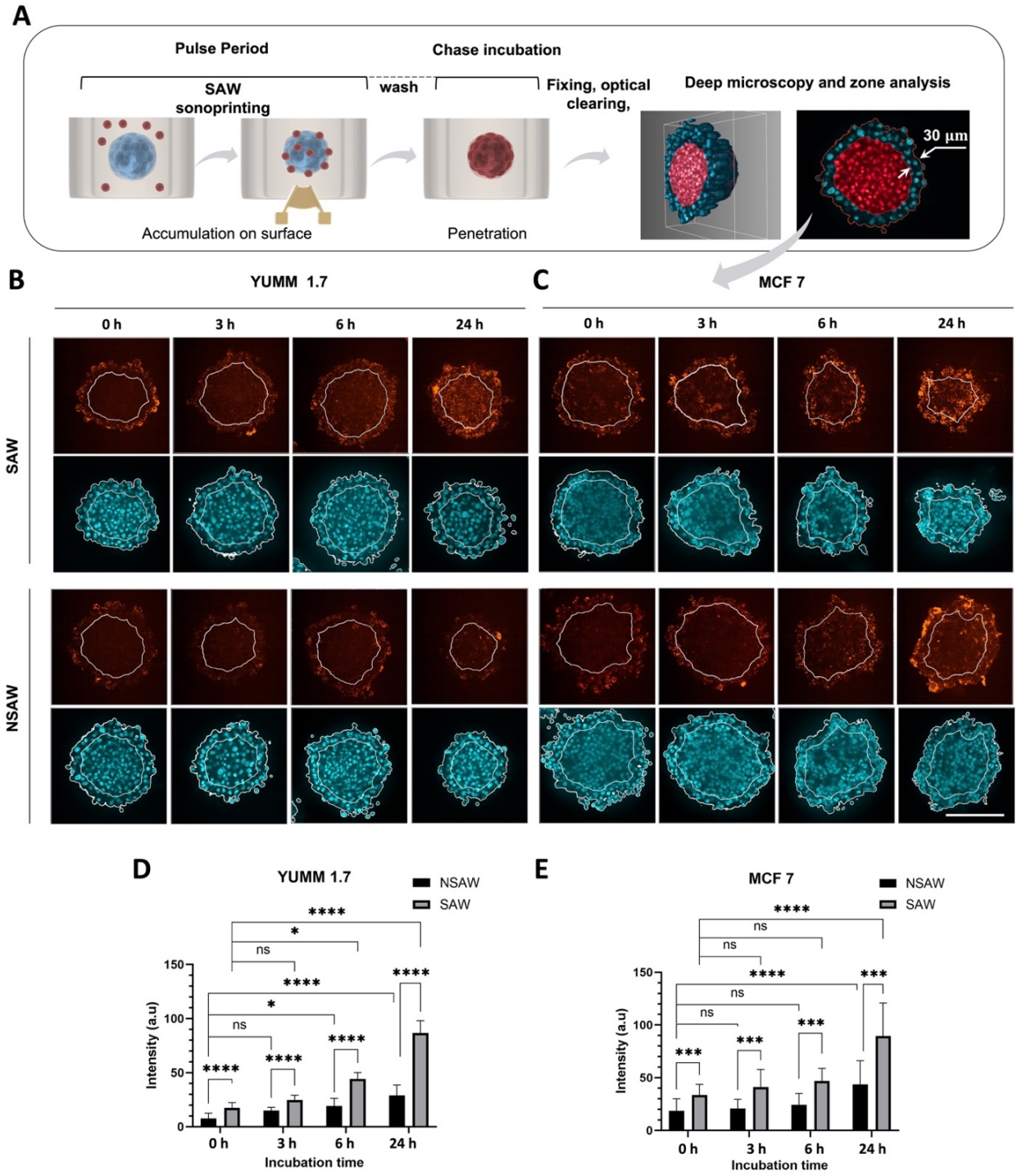

Figure 7.4. A) The experiment sketch for the nanoparticle transport assay, deep confocal microscopy, and zone analysis of spheroids. After the transport assay, the spheroids are fixed and cleared. The mid cross-section of spheroids are imaged and divided into two zones of total and core zones delineated by white boundaries. The distribution of the 100 nm polystyrene nanoparticles (red) after different chase times, in the spheroids of **B)** YUMM 1.7 and **C)** MCF 7 spheroids with (SAW) and without (NSAW) acoustic waves. The figures show the mid cross-section of the spheroids in the red channel for nanoparticles (top) and cyan channel for cells' nuclei stained with Hoechst 33342 (bottom) acquired by water-immersed confocal microscopy. In the Cyan channel, the outer line shows the boundary of the spheroids defined by the nuclei, and the inner line (the same line in red channel) shows the core zone of the spheroids with a 30 μm margin from the spheroid's boundary. Scale bar is 200 μm. **D)** and **E)** show the intensity of the nanoparticles penetrated to the core region for YUMM 1.7 and MCF 7 cells respectively, quantified by image analysis of spheroids' cross-sections. Data plotted as mean + SD.

of incubation. Similar to NPs sonoprinting results, the penetration of NP was considerably higher in MCF 7 cell spheroids compared to YUMM 1.7 cell spheroids. This superior NPs intensity in the MCF 7 cell spheroids' core could be a result of their higher NP uptake as well as their less compact structure compared to that of YUMM 1.7.

7.3.5 SAW increases the efficacy of anticancer drug nanoliposome delivery into spheroids

Demonstrating that the surface acoustic waves actuation leads to nanoparticle sonoprinting onto and higher trafficking into cell spheroids, as a proof-of-concept study, we investigated the capacity of the SAW technique for delivery of nanotherapeutics to MCF 7 and YUMM 1.7 spheroids as pseudo-tumor models. To this end, nanoliposomes encapsulating the CuET metal complex (LP-CuET) were used. CuET is a promising drug candidate for cancer therapy that causes cancer cell death by blocking the p97-NPL4 pathway leading to the accumulation of misfolded proteins and a heat shock response.[425] Since cancer cells tend to be highly mutated, they contain a larger number of defective proteins that can lead to heightened proteotoxic stress,

potentially making them more sensitive to CuET.[425] Nanoliposomes are used to carry CuET, as the drug is not soluble in aqueous media, such as body fluids.[426]

Since the nanoliposomal CuET formulation might prevent the penetration of CuET into deep layers of tumors and potentially limit its efficacy, we used our SAW platform to overcome the physical and cellular barriers of LP-CuET delivery. Both cell spheroids were exposed to 5, 10, and 20 μM LP-CuET with a mean size of 110.7 ±1.0 nm (Figure S7.1) for 10 minutes in the presence or absence of SAW. The spheroids were then washed and immediately moved to fresh media.

Figure 7.5.A shows the viability of spheroids after 6-hour chase incubation. As the concentration of LP-CuET increases, more dead cells can be detected in the spheroids in the NSAW group; however, the percentage of dead cells remained small even at 20 μM, since the spheroids were exposed to LP-CuET for just 10 minutes and moved to the fresh media immediately. In the SAW group, on the other hand, the number of dead cells and their structure was more noticeable, particularly at the periphery of the spheroids. Moreover, the disintegration of the spheroid structure was evident by the number of cells detached from spheroids and dispersed in the wells with increasing concentration of LP-CuET. Both the cell detachment and death were the result of the SAW-mediated delivery, which suggest higher accumulation of the nanoliposomes and deeper penetration, only after 10 minutes of spheroid exposure to SAW. The effect of SAW on cytotoxic efficacy of LP-CuET in YUMM 1.7 and MCF 7 spheroids are shown in Figure 7.5.B and C. For any concentrations of LP-CuET, the anticancer activity was boosted with SAW exposure. A 55 % increase in the number of MCF 7 dead cells and near a threefold increase for YUMM 1.7 spheroids could be noted for 20 μM LP-CuET concentration. This result shows the SAW can increase the sensitivity of YUMM 1.7 spheroids to LP-CuET, which is interesting given that 2D cultured YUMM 1.7 cells are slightly less sensitive to CuET than MCF 7 cells (Figures S7.2).

Higher risks of metastatic behavior are frequently reported in other spheroids modulation methods such as tumor collagenase treatment,[16,395,396] which in fact has

comparable performance to our SAW platform in terms of penetration increase of ≈3-fold for the 100 nm carboxylated polystyrene beads.[394]

To investigate whether SAW has a similar effect on the spheroids' phenotype, we measured the expression of the CD90 gene. CD90 is used in our study as a surrogate marker for metastatic melanoma, as higher CD90 expression is associated with a migratory metastatic phenotype.[427] CD90 is also an active regulator of cell-cell adhesion in various cancer types involved in cell migration.[428–430]. RT-qPCR results showed no change in CD90 expression in the YUMM 1.7 cell spheroids after SAW exposure or upon LP-CuET treatment suggesting there is no significant difference occurring in the mechanics of YUMM 1.7 cell motility in these conditions (Figure 7.5.D). Interestingly, when spheroids were treated with both LP-CuET and SAW, there was an apparent but non-significant decrease in CD90 expression (0.706-fold decrease). This trend seems consistent with previous literature findings considering that endoplasmic reticulum stress, which is caused by LP-CuET, is associated with the downregulation of CD90 expression.[431] A limitation of this assay, however was that affected cells could detach from the spheroid surface upon cytotoxic LP-CuET/SAW treatment (Figure 7.5.A), which could be lost during the process of mRNA isolation and purification, resulting in an experimental bias towards the cells in the core of the spheroid. The expression of HSP70 was also measured (Figure 7.5.E), since HSP70 is known to be upregulated during CuET-induced heat shock, as HSP70 is a protein chaperone that is essential for cellular homeostasis during proteotoxic stress.[425,432] We observed a significant upregulation of HSP70 during treatment with LP-CuET alone (~10-fold increase, p=0.0102) and a similar nonsignificant upregulation of HSP70 (~10-fold increase, p=0.0747) upon exposure of YUMM 1.7 spheroids to SAW. The upregulation of HSP70 during SAW treatment alone could be due to localized vibrational and acoustic energy on the cells. The combinatory effect of LP-CuET and SAW, however, was drastically larger (near 40-fold increase, p=0.0136), suggesting a marked increase in proteotoxic

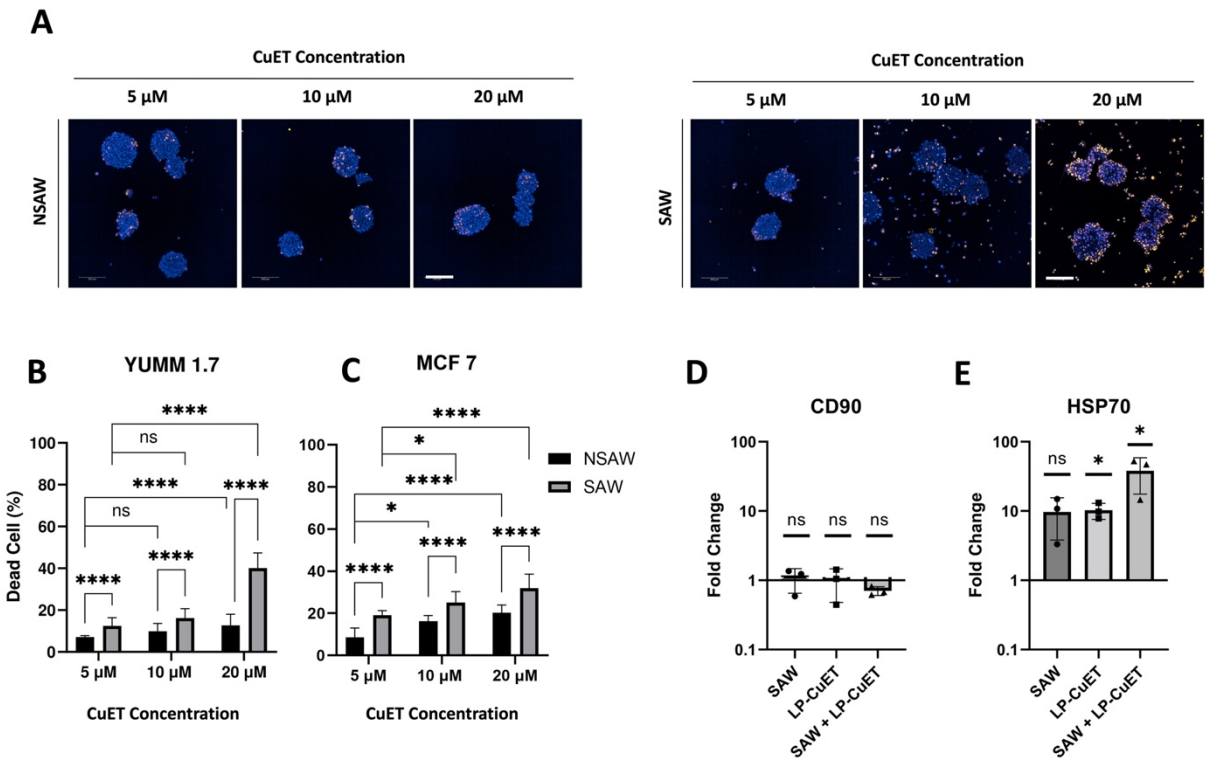

Figure 7.5. A) The anticancer activity of liposomal CuET nanoparticles with different concentrations, with and without acoustic waves. The dead cells are stained by orange ethidium homodimer III, while blue Hoechst 33342 shows the nuclei of total cells. More dissociated cells and less compact structures are observable with the exposure to SAW, especially at higher concentrations. The figures are the maximum projection of confocal planes, and the scale bar is 200 µm. **B)** and **C)** show the percentage of dead cells over the total number of cells for YUMM 1.7 and MCF 7 spheroids, respectively. Data are plotted as mean + SD. **D)** and **E)** RT-qPCR results of CD90 and HSP70 genes with YUMM 1.7 cell spheroids exposed to 10 min SAW alone (SAW), 10 µM of LP-CuET NPs, and the combination of SAW and LP-CuET NPs for 10 min. The results are normalized to NSAW, and the statistical analysis is performed using ΔCt values (Figures S7.3).

stress in the spheroids and thereby the effective delivery of the drug-loaded NPs. While the increase in HSP70 from NSAW control samples was not statistically significant in the SAW group alone, there was a clear trend towards more cellular stress as cells were exposed to acoustic energy but without any significant changes in cytotoxicity when LP-

CuET was absent. Taken together, the data suggest that SAW improves NP sonoprinting, penetration and delivery into cancer cell spheroids leading to more pronounced efficacy in the presence of cytotoxic nanoparticles.

7.4 Conclusion

In this work, we introduced a SAW platform to enhance the delivery of NPs to 3D pseudo-tumors, modeled by breast cancer MCF 7 and melanoma YUMM 1.7 spheroids. The proposed surface acoustic waves-based platform was fabricated on a lithium niobate substrate with focused interdigitated transducers and activated with 10 V_{PP} driving voltage, allowing for the generation of acoustic microstreams and Bjerknes forces that induce the convective transport and aggregation of the nanoparticles in the cell spheroids. The SAW sonoprinting led to a significant increase in the accumulation of NPs onto as well as significantly more trafficking of NPs into inner layers of the cell spheroids. The SAW platform was challenged for delivering anticancer nanotherapeutics using liposomal CuET nanoparticles in spheroids. The presence of SAW caused higher cell death, indicating enhanced drug delivery efficacy. Moreover, while higher concentrations of the drug could be delivered to the pseudo-tumor, the RT-qPCR results for YUMM 1.7 cell spheroids showed no significant increase in the metastatic phenotype of the spheroids. Although the *in vivo* effects of SAW-assisted drug delivery should be thoroughly explored, the efficient nanotherapeutic delivery results shown in this study coupled with the wide range of bioinert and wearable materials compatible with this technology open the venue for the development of exciting biomedical devices, such as skin patches or even as implanted devices to enhance the drug delivery by administering localized, continuous, and controllable acoustic waves.

7.5 Materials and Methods

7.5.1 Materials

127.86° Y-cut, X-Propagating SAW grade Lithium Niobate wafers (4-inch diameter) were acquired from Precision Micro-Optics (Massachusetts, USA). MatTek 35mm glass-bottom Petri dish #1.5 coverslip, Dulbecco's Modified Eagle Medium (DMEM) Fetal Bovine Serum (FBS), Penicillin-Streptomycin (P/S), Formaldehyde solution, Invitrogen NucBlue™ Live ReadyProbes Reagent (Hoechst 33342) and Orange/red fluorescently labeled 100 nm polystyrene carboxylated NPs (FluoSpheres, cat. no. F8800 Molecular Probes, Oregon) were purchased from Thermo Fisher Scientific, Canada. 96 Well glass bottom plate with high-performance #1.5 cover glass was acquired from Cellvis, USA. Tissue optical clearing reagent Scaleview-S4 was acquired from FUJIFILM Wako Pure Chemical Corporation, USA.

7.5.2 Device fabrication and setup

The focused design for IDTs was used to restrict and concentrate the acoustic energy to the confined domain in the well. Each IDT had a thickness of 75 μm with the same gap size between the fingers, corresponding to the wavelength of λ =300 μm.

The SAW substrate was fabricated by standard soft-lithography and E-beam evaporation. A 500 μm, double-sided polished 127.86° lithium niobate piezoelectric wafer was coated by 10 μm-thick photoresist layers (S1813, MicroChem, Texas, USA) with the bake time, spin speed and lithography dosage per the manufacturer protocol. After developing the pattern, a 10 nm titanium adhesion layer and 100 nm gold layer was deposited on the substrate, using an E-beam evaporator (BJD1800, Airco Temescal, California, USA). The sacrificial S1813 was peeled off by sonication in Microposit MF319 developer, at 70° C to develop the interdigitated transducers.

For operating the platform, IDTs were connected to the function generator (AFG3011C, Tektronix, USA) and were activated by squared radiofrequency (RF) signals at their optimum frequency, which is determined by IDT design and their wavelength (λ = 300 μm, correspond to the frequency of f ≈13.7 MHz). The acoustic waves were transported from the piezoelectric substrate to the glass bottom Petri dish (MatTek) using DI water as the coupling layer.

7.5.3 Cell culture

Mouse Melanoma Cell line (YUMM 1.7) and human breast adenocarcinoma cells MCF 7 were purchased from the American Type Culture Collection (ATCC, Rockville, MD). Both cell lines were cultured in Dulbecco's modified Eagle medium (DMEM) with 10% FBS and 1% penicillin/streptomycin (GIBCO). The cells were cultured in T75 cell flasks and were suspended by 0.25% (w/v) Trypsin prior to spheroid formation.

7.5.4 Spheroid formation

For MCF 7 spheroids' formation, the suspended cells were transferred to low attachment Petri-dish. The Petri dish carrying suspended MCF 7 cells was then transferred to a shaker plate in the incubator with a spinning speed of 80-90 rpm. The cells naturally form spheroids and after 3 days they were harvested for the NP delivery tests. To produce YUMM 1.7 spheroids, Trypsinized and suspended cells were transferred to a 96-Well, Non-Treated, U-Shaped-Bottom Microplate. After 24 hours, the multiple spheroids were formed in each well, and to detach them from the plate, each well was pipetted multiple times. The suspended spheroids were then moved to a low adhesion Petri-dish which was placed on a shaker plate in the incubator for 2 additional days prior to the NP delivery tests.

7.5.5 NP transport assay in spheroids

After 3 days in culture, spheroids were washed with PBS, followed by 15-minute serum starvation in DMEM in the incubator at 37 °C. Fluorescently tagged 100 nm polystyrene carboxylated NPs were diluted in a serum-free DMEM medium. After serum starvation,

spheroids were transferred to the glass bottom petri dish and NPs were added to the spheroids to reach the final volume of 160 µL. For nanoparticle accumulation and penetration tests, fluorescently tagged 100 nm polystyrene carboxylated were diluted in serum-free DMEM medium to reach the final concentration of 5 µg mL^{-1}. According to the manufacturer, FluoSpheres nanoparticles were produced by incorporating the fluorescent dye within the bead's polystyrene matrix. Compared to surface conjugation, this method offers better trapping dye molecules and protecting them from leakage into surrounding media. This was critical in the NP penetration experiments to ensure the proper monitoring of NP diffusion into spheroids.

For the anticancer drug delivery test, liposomal CuET was added to reach the final concentration of 5,10, and 20 µM. NP treatment for the NSAW groups involved 10 minutes incubation of spheroids with the abovementioned concentrations for each test, followed by two washing steps with PBS. For the SAW experiments, a drop of water was placed on the piezoelectric substrate as the coupling layer and the Petri-dish was mounted on the drop. The glass well of the Petri-dish, where the spheroid and NPs were present, was carefully aligned on top of IDT. Upon activation with 10 V_{PP} driving voltage and the frequency of 13.7 MHz, the IDT generated visible Eckart streams in the middle of the glass well. After 10 min of SAW exposure, the spheroids were washed two times with PBS followed by either incubation or fixing depending on the follow-up experiments.

7.5.6 Live/Dead Cell evaluation

The viability assays were performed by the live/dead kit (Viability/Cytotoxicity Assay Kit, Biotium, USA). Spheroids were washed with PBS and stained green with 2 µM Calcein AM for live cells and red with 4 µM ethidium homodimer-III for dead cells. Hoechst 33342 was used per manufacturer's protocol to stain the cells' nuclei.

7.5.7 Sample preparations for imaging

After nanoparticle treatments, spheroids were washed twice with PBS before fixing in 4% (v/v) paraformaldehyde for 30 min. Clearing solution Scaleview S4, which is compatible with well plates, was added to the spheroid prior to the imaging to enhance light penetration depth. Incubating spheroids in the clearing agent at 37 °C overnight allowed the clearing agent to homogenize the light refractive indices in the 3D sample and improve signal detection in the inner layers of spheroids.[433,434] Pictures were acquired using confocal mode on Opera Phenix™ high-content screening system (Perkin Elmer) equipped with microlens-enhanced spinning disk. For the penetration and accumulation studies, spheroids were imaged by water immersion objectives in order to acquire higher image quality in z-direction.[433]

7.5.8 Image analysis

The particle streak velocimetry technique was used for quantitative analysis of microstreams. The displacement (Δ) of particles by microstreams was measured at various exposure times (τ) with imageJ to calculate the velocity.

The total number of Cells was counted in 3D from the confocal images (Opera Phenix™ high-content screening system). The Hoechst 33342 stained nuclei were identified in the "Find Nuclei" module of Harmony® 4.9 imaging and analysis software. To detect the dead cells, "Find Cell" in the ethidium homodimer channel was used. For zone analysis of the spheroids, the "Find region" and resized region modules of the software were used.

7.5.9 Liposomal CuET synthesis

CuET encapsulation was performed using the ethanol injection method, as previously described.[426] Briefly, phospholipids, cholesterol, and CuET were dissolved in 100% ethanol and heated to 50°C. The solution was then rapidly injected into ultrapure water to yield liposomal CuET. The ethanol was removed by rotary evaporation and the solution was filtered using a 0.22 µm membrane, suspended in 1x PBS and stored at 4°C.

7.5.10 RNA isolation and RT-qPCR

YUMM 1.7 spheroids were divided into four groups: LP-CuET treated (10 μM, for 10 minutes) with and without SAW, SAW without LP-CuET (10 minutes), and no SAW (NSAW) control group. Spheroids were then washed and incubated for 6 h in serum-free media prior to RNA extraction. Total RNA was extracted using TRIzol™ and the PureLink® RNA mini kit. RNA quality was evaluated by NanoDrop™ One C, and one-step RT-qPCR was performed using the Luna® Universal One-Step RT-qPCR kit according to manufacturer instructions. Fold change in gene expression was calculated using the $2^{-\Delta\Delta Ct}$ method using GAPDH as a housekeeping gene and normalized to NSAW controls. The following primers were used:

Gene	Forward (5'-3')	Reverse (5'-3')
GAPDH	CCCTTAAGAGGGATGCTTTCAAGT	ACTGTGCCGTTGAATTTGCC
CD90	CTAAGTCCGTGCAGGAAGGG	CACACTCCAGAGGCTTGGTT
HSP70	GAAGGTGCTGGACAAGTGC	GCCAGCAGAGGCCTCTAATC

7.5.11 Statistical analysis

All experiments were performed independently with a minimum of 3 replicates. One-way analysis of variance (ANOVA) was applied for comparison of three or more group means using the Tukey test, and student's regular t test was used to assess the statistical significance between two SAW treated and untreated (NSAW) groups. For RT-qPCR results, Dunnett's 3T correction was carried out. The data were then plotted using GraphPad Prism (GraphPad software, San Diego, CA, USA) and were considered significant when $p < 0.05$ (* < 0.05, ** < 0.05, *** < 0.005, **** < 0.0001).

7.6 Supporting Information

7.6.1 Characterization of liposomal CuET nanoparticles:

Size and size distribution of LP-CuET nanoparticles measured with Nanoparticle tracking analysis, showing the mean particle size of 110.7 +/-1.0 nm.

Stats: Mean +/- Standard Error	
Mean:	110.7 +/-1.0 nm
Mode:	94.0 +/-5.0 nm
SD:	40.7 +/- 0.9 nm

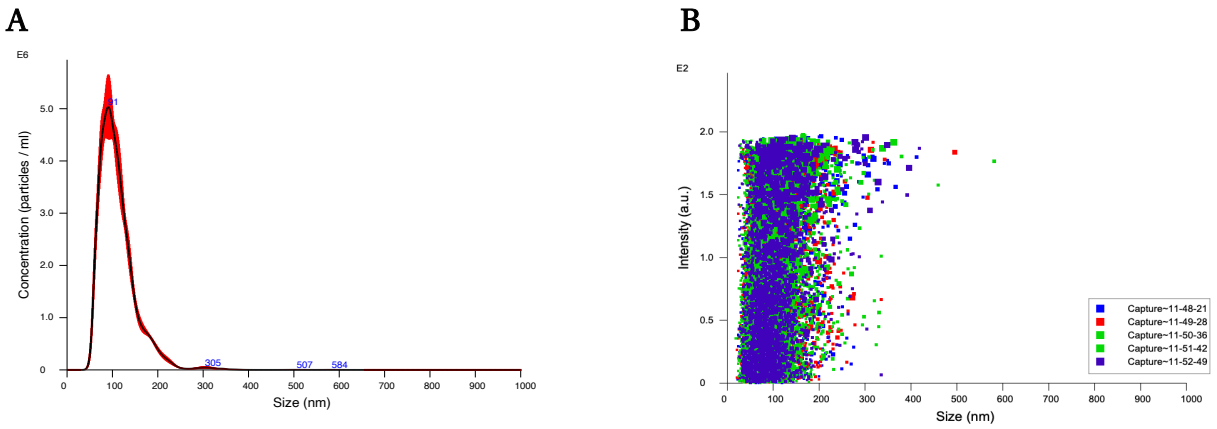

Figure S 7.1. Nanoparticle tracking analysis of LP-CuET, Showing the size and size distribution **A)** averaged concentration / size for experiments, **B)** intensity/size graph.

7.6.2 Delta Ct values of RT-qPCR experiments of different treatment groups in YUMM 1.7 spheroids normalized to GAPDH

NSAW is the control group, SAW is spheroids only exposed to the acoustic waves without liposomal CuET nanoparticles, LP-CuET is the group exposed to the nanoparticles but without SAW and finally SAW+ LP-CuET is the group exposed to LP-CuET nanoparticle in the presence of acoustic stimulation. Welch's one-way ANOVA with Dunnett's 3T correction (n=3) were used to graph the significance of the results from the last figure.

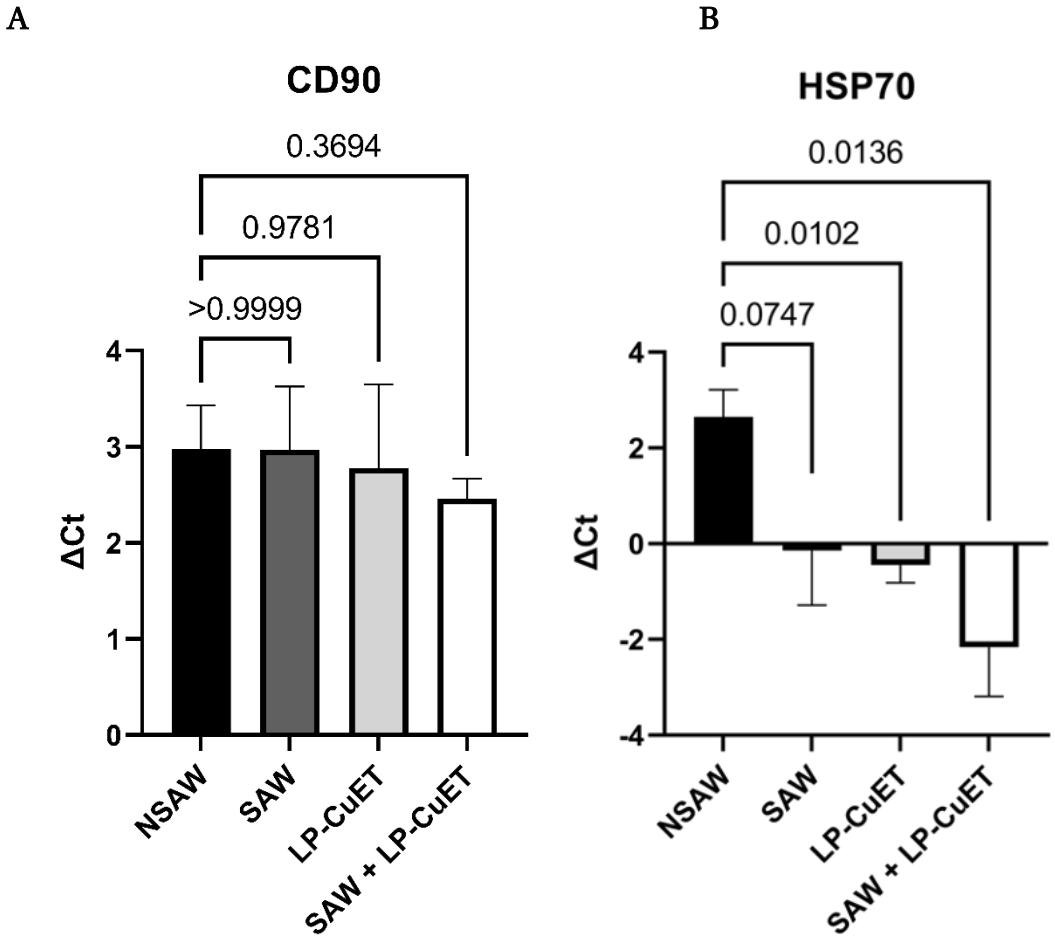

Figure S 7.2. Delta Ct values of RT-qPCR experiments of different treatment groups in YUMM 1.7 spheroids normalized to GAPDH **A)** CD90 **B)** HSP70.

7.6.3 Toxicity analysis of LP-CuET for both cell types

Half maximal inhibitory concentration (IC50) of LP-CuET was measured for both MCF-7 and YUMM-1.7 cells in 2D to analyze the cellular survival and their sensitivity to the drug.

IC50 was calculated by using the Sulforhodamine B assay. 10000 Cells were seeded at each well of 96-well plates and incubated overnight before treating with various concentrations of LP-CuET for 72h. Cells were fixed with 50% TCA, stained with 0.4% suflorhodamine B, and resuspended in TRIS buffer (10 mM) at a final volume of 200 µL per well.

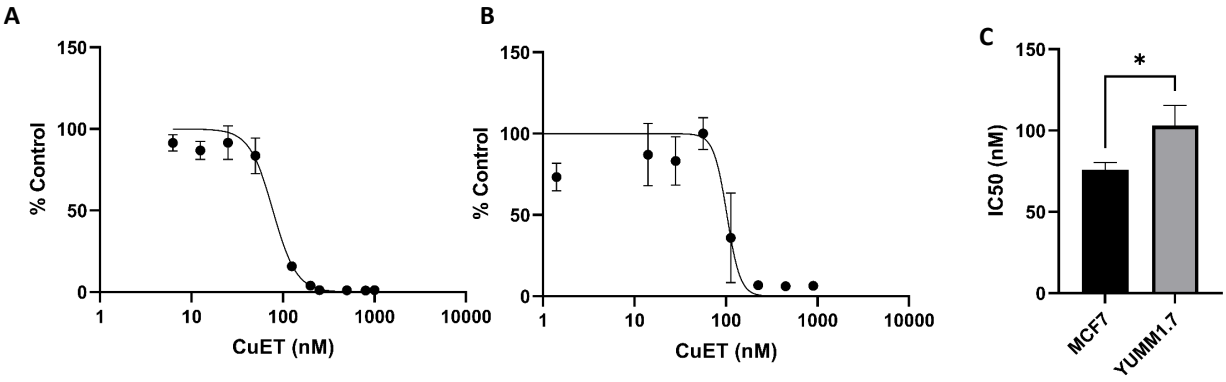

Figure S 7.3. A) Representative IC50 curve of an individual experiment for MCF7 treated with LP-CuET. **B)** Representative IC50 curve of an individual experiment for YUMM 1.7 treated with LP-CuET **C).** IC50 difference between MCF 7 and YUMM 1.7 showing increased sensitivity of MCF 7 cells to LP-CuET. Student's t-test with Welch's correction of 3 individual experiments (n=3) derived from the previous curves in **A)** and **B)**.

Video captions.

Video S7.1: Eckart microstreams formation in the presence of 13.7 MHz focused SAW, demonstrated by streak lines of fluorescent polystyrene microparticles (video is in 2x speed).

Video S7.2: Aggregation of microparticles around cellular spheroids upon activation of SAW, (video is in 2x speed).

8 Contributions to Original Knowledge

The goal of this thesis was to introduce novel on-chip techniques and platforms to harness the acoustofluidics potential for addressing some of the most common challenges in the fields of nanotherapeutics and regenerative medicine. Previous literature had established acoustofluidics capacity for precise, safe, and controllable handling of the bioparticles and biofluids. Here, we expanded the promising applications of acoustofluidic by showcasing rapid and continuous methods for the development of nanotherapeutics, synthesis of 3D cellular spheroids, and as means for delivery of nanotherapeutics to the spheroids. The key original contributions to knowledge are explained in more detail in their respective chapters.

Chapters 3 and **4** of this thesis provide an overview of the most frequently studied acoustofluidic concepts and forces in both SAW and BAW-based devices, their working mechanisms, and the resulting acoustic phenomena for sensing and the manipulation of bioparticles and biofluids. Moreover, this review debates the levels of biocompatibility, throughput, versatility, integration, and sensitivity of each acoustic method which are the pre-requisite knowledge before adopting the best-suited acoustofluidic technology based on the application of interest. After discussing the specifics and features of each acoustic method, the advancement and novel acoustic strategies in bio-applications such as cell separation and sorting, tissue engineering, therapeutic development, and biosensing are reviewed.

Outcome: *Reza Rasouli, Karina Martinez Villegas, and Maryam Tabrizian, "Acoustofluidics – Changing Paradigm in Tissue Engineering, Therapeutics Development, and Biosensing", submitted to Lab on Chip.*

In **Chapter 5**, the rapid acoustic micromixer was developed for the synthesis of organic nanoparticles. The key original contributions of this work are:

- Design and development of a high-throughput boundary-driven microstreaming platform, compatible with nanoparticle synthesis conditions.
- Generation of substantially stronger microstreams by an efficient combination of oscillatory sharp edges and bubbles.
- Investigating and clarifying the Physics behind the optimum operation frequency.
- Achieving ultra-rapid mixing time of 0.8 ms, one of the fastest reported micromixers in the literature by disruption of the laminar flow with the vigorous vortical streams.
- Synthesizing liposomes and PLGA-PEG nanoparticles, as two FDA-approved and frequently used drug nanocarriers and fine-tune their size by controlling the mixing time.
- Mitigating the common complexities in the synthesis of nanoparticles, namely controlling the size of nanoparticles, synthesis throughput, and clogging.

Outcome: *Rasouli, Reza, and Maryam Tabrizian. "An ultra-rapid acoustic micromixer for synthesis of organic nanoparticles." Lab on a Chip 19.19 (2019): 3316-3325.*

Chapter 6 presented a novel continuous-flow and on-chip method for the rapid production of multicellular spheroids. The key original contributions of this work are:

- The first continuous-flow and on-chip method for the rapid production of multicellular spheroids, using locally confined and controllable microstreams.
- Testing a library of materials and their compatibility with the platform, followed by the optimization and characterization of collagen I+ methylcellulose mixture.
- Employing the acoustic platform as spheroids assemble line where cells were trapped, compressed, and adhered together with Collagen I to form compact spheroids in spans of 10 seconds.
- Showcasing the cell independency of the method by forming multicellular spheroid and composite spheroids.
- The production of mechanically stables spheroids with a high tendency to merge which opens the venue for the integration of the rapid and continuous-flow acoustic platform with 3D bioprinters to generate building blocks for tissue engineering.

Outcome: *Rasouli, Reza, and Maryam Tabrizian. "Rapid Formation of Multicellular Spheroids in Boundary-Driven Acoustic Microstreams." Small 17.39 (2021): 2101931.*

The work in **Chapter 7** was the first application and investigation of surface acoustic waves for the delivery of nanoparticles to the spheroids and pseudo tumors. The key original contributions of this work are:

- Design and development of a high-frequency acoustic platform using the state-of-the-art surface acoustic waves technology to induce Bjerknes forces and Eckart streaming.
- Optimization of the design and operation parameters to generate biocompatible, focused, and unidirectional acoustic waves.
- The first demonstration of the feasibility and applicability of surface acoustic waves for the delivery of nanoparticles to the spheroids and pseudo tumors by SAW sonoprinting.

- Enhancing the nanoparticle accumulation on spheroids and increasing the penetration of polystyrene nanoparticles into inner layers of spheroids.
- Validating the effectiveness of the SAW nanoparticle delivery method by showing the enhanced cytotoxic performance of anti-cancer liposomal CuET nanotherapeutics in pseudo tumors.

Outcome: *Reza Rasouli, Radu Alexandru Paun, and Maryam Tabrizian, "Sonoprinting Nanoparticles on Cellular Spheroids via Surface Acoustic Waves for Enhanced Nanotherapeutics Delivery", submitted to "Lab on Chip"*

9

General Discussion & Conclusion

In this thesis, we sought to design and develop novel acoustofluidic platforms and methodologies as powerful tools for controlled on-chip manipulation of biospecimens, in light of their biomedical applications. Through our results, subject to the original contribution, we were able to validate the versatility and the enormous potential of acoustofluidics to take a gamut of roles in developing means for the multifaceted field of nanotherapeutics and regenerative medicine.

This work encompassed three interrelated and complementary studies which involved developing efficient, cost-effective, and easy-to-use acoustofluidic platforms for i) on-chip synthesis of organic nanoparticles as therapeutic carriers, ii) rapid formation of multicellular spheroids as building blocks for tissue engineering and 3D biomimetic constructs, and finally, iii) for investigating the effect of high-frequency acoustic waves on delivery of nanoparticles to the 3D spheroids. To this end, we explored various acoustic phenomena such as boundary-driven acoustic streams, Eckart streams, and acoustic radiation forces.

The journey started with designing a rapid and efficient micromixer to control the synthesis of organics nanoparticles. The quality and duration of mixing govern the self-assembly and nanoprecipitation of nanoparticles, by determining the supersaturation and nucleation rate. [318,319] Hence, rapid and homogenous mixing of the solvent and the anti-solvent allows to control and fine-tune the ultimate size and polydispersity of the nanoparticles which are two of the most influential characteristics in their therapeutic

performance.[8] To achieve this rapid and homogenous mixing for tunable nanoparticle synthesis, we developed a boundary-driven acoustic device that could generate strong counter-rotating microstreams to disrupt the laminar streamlines. We proposed a platform that could efficiently integrate oscillatory sharp edges and bubbles as two methods of generating microstreams. In doing so, we showed the combination of bubbles and sharp edges at their immediate proximity can have a synergetic effect and induce substantially stronger vortical fluid motion than the superposition of their effects. This combinatory mechanism allowed to achieve vigorous microstreams with higher throughput at lower driving voltages, which can lead to more stability and less power consumption.

During the characterization of the device, we noticed the optimum frequency that produced the strongest acoustic streams deviated from the literature suggestions. Previous works attributed the optimum frequency to the resonance frequency of the bubbles which is calculatable by Rayleigh–Plesset equation.[312] To investigate the root cause of this deviation from theory, we used the same bubble design with three different piezo transducers and conducted the impedance analysis of each system. Interestingly, the optimum frequency matched the resonance frequency of the acoustic settings rather than the bubble, suggesting the dominance of the setting's geometry and acoustic transducer resonance effect in the optimum frequency.

We further used the device to generate PLGA-PEG nanoparticles and liposomes, as two of the FDA-approved and most extensively employed nanocarriers for drug delivery. The size of the nanoparticles, which is one of the most influential characteristics in deciding their fate in circulation, could be easily tuned in the acoustic mixer by controlling the mixing time. As we increased the total flow rate, the time of mixing decreased and smaller nanoparticles could be produced, which was in line with the literature.[320] Moreover, the rapid and homogenous acoustic mixing led to better NP size distribution and the production of higher nanoparticle concentration compared to the standard microfluidic method, by obviating the aggregation and clogging.

The boundary-driven platform developed in the first study showed locally controllable microstreams, which lend themselves to the precise manipulation of bioparticles. Considering this important feature of our platform, we used the device for the continuous production of multicellular spheroids. Spheroids are 3D cell constructs with tremendous potential to be used as building blocks of tissue engineering and faithful models of native tissue for drug screening and discovery. However, most current spheroid formation methods focus primarily on the first phase of the spheroids formation which is the physical aggregation of the cells to promote direct cell-cell contact. They then rely on cells' capacity to secrete extracellular matrix to form coherent and mechanically stable spheroids. This dependency on cell capacity of producing binding proteins is not only time-consuming, but is also cell-type dependent, while many cell types do not tend to form spheroids by nature.[435] Therefore, we adapted our initial boundary-driven acoustic device into a spheroid assembly line and used the hydrodynamic forces from the acoustic microstreams to trap and aggregate cells into compact 3D cell clusters. To achieve coherent and mechanically stable spheroids, we tested a library of biomaterials to hold the cells together. The performance of the materials was assessed with respect to criteria of adhesiveness, formability, and retrievability of spheroids. The optimization process led to establishing a mixture of type I collagen (0.42 mg mL^{-1}) and methylcellulose (0.4% w/v) as the biomaterial of choice for accelerating the formation of stable spheroids to as fast as 10s. As such, our method allowed to bypass the delay of ECM secretion phase which could take hours to days, even when using the 'state-of-the-art' methodologies for spheroid formation such as magnetic forces,[12] surface acoustic waves,[13,190] and dielectrophoeresis.[339]

To showcase the ability of the acoustic spheroid assembly for reducing cell-type dependency, we made spheroids from two cell types of MDA-MB-231 and MCF-7 which differ in the nature of their compaction.[351] Both cell types could form coherent and compact spheroids in our acoustic method. This is particularly interesting for MDA-MB-231 cells, which usually form loose aggregates in other spheroid formation

methods due to the lack of E-cadherin secretion. [331,351,359] According to the literature reports, we believe that the compaction of MDA-MB-231 spheroids in our acoustic methods could be due to the beneficial interaction of collagen I, used as the bioadhesive, with integrin b proteins.[371,351] The cell/particle independency of acoustic spheroids formation methods was further challenged by forming multi-cellular spheroids and particle-cell composite spheroids. During the acoustic assembly, the cell viability remained over 90 % to show the high biocompatibility of the process.

For the first time, we could show in this study that the acoustofluidic device can be used as a continuous and on-chip spheroid assembly method and to produce mechanically stable spheroids, either with one cell type or with multiple cell lines. Hence, the acoustofluidic spheroids formation methodology proposed in this thesis could address some of the fundamental challenges in tissue engineering by offering means for rapid and continuous production of spheroids with high cellular density, high viability, and simultaneous ECM incorporation to ensure easy retrieval and structural integrity of spheroids for further manipulations.

The connecting link between the nanotherapeutic aspect of the thesis and the 3D spheroids formation is explored in the third part of the thesis, where we developed a high-frequency SAW platform and investigated the role of surface acoustic waves in enhancing nanoparticle delivery to spheroids and pseudo tumors. Although the literature has shown the effectiveness of conventional acoustic systems in permeabilizing tumor structure and nanoparticle delivery through cavitation, the harsh and uncontrollable nature of the inertial cavitation could be damaging to the neighboring tissues.[402]

The SAW device was designed to generate focused and unidirectional acoustic waves in high-frequency, non-contact, and low input voltage conditions in order to minimize mechanical stresses and unwanted cavitation. This resulted in a biocompatible SAW setting that showed no significant adverse effect on the viability of the cells. We further optimized the operation parameters of the SAW device to induce Eckart streaming and Bjerknes forces, as the main mechanisms to sonoprint

nanoparticles on spheroids and enhance their penetration into the deeper layers of spheroids. Acoustic streaming is the dominant mechanism to deliver the vibrational energy to the media and the suspended particles[231] while Bjerknes forces could boost the accumulation of nanoparticles on spheroids by creating attractive forces between them.[108,109,145]

The platform showed the ability to sonoprint polystyrene NPs with a therapeutically relevant mean size of 100 nm onto the spheroids, increasing their accumulation onto the spheroids by up to four-fold. The influence of SAW on the spatial distribution of polystyrene NPs into spheroids was monitored through a NP transport assay [423] followed by 3D deep imaging and zonal analysis of the spheroids. The results showed that SAW activation could increase the NPs concentration in the core regions of the spheroids by up to three times.

To potentiate this finding toward a real nanotherapeutic delivery application and its clinical translation, the SAW platform was used to deliver anticancer CuET-loaded liposomal nanoparticles to YUMM 1.7 pseudo-tumors. The efficacy of the acoustic delivery approach was validated by measuring the cytotoxic activity of anti-cancer liposomal CuET, showing up to a three-fold increase in the number of dead cells in the spheroids after the application of high-frequency surface acoustic waves. One important implication of this study is that since SAW technology is compatible with bioinert and flexible materials, the technique holds tremendous promise to be manufactured as either implant or skin patches. Although the technology is still novice and extensive experiments are required to well-characterize the in-vivo effects of SAW, our results demonstrated the applicability of SAW to increase the efficiency of nanotherapeutics to tumors with continuous, low amplitude, and localized acoustic waves, through implementing a minuscule chip in the site of interest.

Overall, in this thesis, we presented the motivation, strategies, designs and developments, and analysis of multiple acoustic-based devices for precise manipulation of bioparticles and biofluids. Through three original research articles, we showcased the acoustofluidic potential for addressing some of the most common

challenges in the fields of nanotherapeutics and regenerative medicine. The implementation of novel on-chip operations further proved the versatility and unique capacity of the acoustics systems in taking various roles, from therapeutic development to tissue engineering and nanotherapeutic delivery systems.

10

Limitations & Future Perspective

10.1 Limitations and Proposed Mitigations

In this section, we discuss the challenges faced in fulfilling each of the objectives as well as the strategies to address the limitations of our studies for further development of our platforms for the research applications or their clinical translation.

For the acoustofluidic synthesis of nanoparticles, one of the initial challenges was the leakage of uncross-linked PDMS oligomers into the solvents used for the NP synthesis. These free oligomers could self-assemble and create nanoparticles which were detectable by NTA and DLS. To eliminate the PDMS oligomers' leakage and formation of artifact NPs, the literature proposes multiple extraction and washing steps using harsh solvents, which could damage the sharp edges embedded in our acoustofluidic platform.[436] Instead, we found that coating the channel with Parylene C by a chemical vapor deposition process could block the PDMS oligomers' leakage into the liquid phase running in the microfluidic channel. Interestingly, the coating did not affect the intensity of the microstreams and also could sustain over time and after multiple utilization of the platform. However, the Parylene C coating slightly decreased the optical transparency of the microchip. While this was not a limitation in our experiments, the decrease in optical properties of the platform should be considered if one needs to use it with a light excitation method such as UV for performing light-initiated reactions in the microfluidic channels. The other limitation of the platform resides in the choice of the solvents for the formation of NPs. Generally, liquids with

high surface energy could better trap the bubbles, as the trapping of the bubbles is initiated by surface tension. Therefore, solvents such as ethanol with low surface energy can destabilize the bubbles. Hence, if working with very low surface energy media is required, some modifications, such as minimizing the interface length between the sharp edges should be implemented in the design of the acoustofluidic platforms.

In the spheroid's formation study, the challenges were primarily material-oriented rather than those related to the device. As mentioned earlier, there were multiple criteria for choosing the compatible material. There is a trade-off in choosing the material, in that it should be adhesive to glue the cells together but does not adhere to the channel walls. The use collagen fibers under shear stress was one of the solutions, but as mentioned in the article, extra care should be given to optimizing the concentration and level of crosslinking of collagen fibers. Moreover, there should naturally be a limit to the viscosity of the bioinks that could be used with our platform to maintain the boundary-driven acoustic microstreams, although we did not reach the limit even at the highest concentrations used.

The third study on acoustically-mediated nanoparticle delivery to the spheroids showed the feasibility and preliminary applicability of high frequency SAW to increase the drug delivery efficiency of nanotherapeutics. However, this is an emerging technology, which still requires an extensive body of experiments. Indeed, although the high-frequency acoustic waves have shown to be one of the most biocompatible forces for the manipulation of biospecies, they induce unique biophysical phenomena such as sonoporation, mechanotransduction, and cytoskeletal vibration. These phenomena can be instrumental for many *in vivo* and *in vitro* applications of the device, albeit it can also add another layer of operational complexity which should be fully scrutinized and characterized prior to its use with sensitive biospecies.

10.2 Future Research Trends

This section presents the author's perspective on the complementary studies for the advancement of the research conducted in this thesis and a general reflection on the

knowledge gained through the literature review on the odyssey of acoustofluidics toward its clinical success.

As a future work in the nanoparticle synthesis study, one complementary experiment that can highlight the capacity of the platform in nanotherapeutic development is testing its encapsulation efficiency. It has already been established that rapid mixing can lead to higher encapsulation efficiency, both for hydrophobic and hydrophilic drugs.[437] During the nanoparticle self-assembly, the cargo tends to escape the nanoparticle into low concentration regions. Rapid mixing can alleviate the situation by homogenizing the concentration prior to nanoparticle self-assembly. Since the device offers ultra-rapid mixing, it is plausible that higher encapsulation efficiency can be achieved with this platform.

Another appealing feature of the platform for translation to the industry is its parallelization capacity. In this platform, one acoustic source is enough to activate multiple oscillatory structures in both series and parallel channels, rendering it suitable for high-throughput and energy-efficient nanoparticle synthesis. To this end, further studies are required for optimizing the position of the acoustic source and the resonance frequency of the system to ensure the uniform acoustic waves exposure and generation of homogenous acoustic streams.

The near future advancement for the acoustic spheroid formation study should include extending the library of the materials compatible with the acoustic mechanism, such as bioinks that can be crosslinked during the acoustic trapping with external stimuli such as UV or heat. Similar to the nanoparticle synthesis study, in this platform a single acoustic source can activate hundreds of oscillatory structures both in series and parallel for the scaled and energy-efficient production of spheroids.

The integration of the platform with a 3D bioprinter is the overarching goal that can realize the full potential of the platform. Ideally, the cells-bioink suspensions could be infused in such a 3D printer where the acoustic platform acts as an on-chip and continuous spheroids assembly line, and finally, the 3D spheroids will be printed as tissue building blocks. This proposed printer can exploit the merging capacity of

spheroids', easier handling, prolonged cell survival, and high cell density to recreate complex native tissue architectures. In fact, a world-renowned industrial partner has already initiated the collaboration with our group for possible integration and commercialization of the platform with their 3D bioprinter.

As for the third study, one plausible future application of the device can be *in vitro* nanotherapeutic delivery to spheroids such as gene delivery, or immunoengineering. For instance, the platform allows to coat the spheroids with nanoparticle for enhanced gene transfection or with immune-protective polymers. Moreover, the compatibility of the SAW technology to be manufactured with flexible and bio-inert material offers the exciting biomedical applications, such as making efficient skin patches to enhance the delivery of nanotherapeutics to unresectable melanoma tumors or even as implanted devices to administer localized, continuous, and controllable acoustic waves to the target sites.

Apart from the technology developments realized during this Ph.D. project, we believe that the biomedical applications of acoustofluidics are endless, particularly for the development of point of care and biosensing devices. New trends advocate for the integration of low-cost, accessible and portable systems such as smartphones with acoustic platforms to revolutionize the field of PoC devices through removing the need for the use of tedious benchtop analytical tools.[438,439] The digital input and output of acoustic biosensors facilitate both activation and electronic readout in smartphones. Moreover, the integration of acoustic biosensing and biofouling reduction mechanisms is one of the unique and promising potentials of acoustofluidics for developing rapid and precise biosensing strategies.

Undoubtedly, by a perceptive selection of the acoustic strategy, wave mode, chamber geometry, and materials, researchers can exploit the opportunities in the field for both manipulation and sensing of bio-species using acoustofluidics. Furthermore, the versatility of these platforms for single-cell analysis, enrichment of particles, assembly of tissue constructs, and the detection and quantification of biomolecules are among numerous applications of acoustofluidic-based devices that can significantly

contribute to fundamental biological studies, tissue engineering, clinical sample handling, and drug development, to name a few.

Bibliography

1. Wu, M. *et al.* Acoustofluidic separation of cells and particles. *Microsystems Nanoeng.* **5**, 32 (2019).
2. Ding, X. *et al.* Surface acoustic wave microfluidics. *Lab Chip* **13**, 3626 (2013).
3. Meng, L. *et al.* Acoustic tweezers. *J. Phys. D. Appl. Phys.* **52**, 273001 (2019).
4. Lenshof, A., Johannesson, C., Evander, M., Nilsson, J. & Laurell, T. Acoustic Cell Manipulation. in 129–173 (Microsystems and Nanosystems, 2017). doi:10.1007/978-3-319-44139-9_5
5. Xie, Y., Bachman, H. & Huang, T. J. Acoustofluidic methods in cell analysis. *TrAC Trends Anal. Chem.* **117**, 280–290 (2019).
6. Blanco, E., Shen, H. & Ferrari, M. Principles of nanoparticle design for overcoming biological barriers to drug delivery. *Nat. Biotechnol.* **33**, 941–951 (2015).
7. Jahn, A. *et al.* Microfluidic mixing and the formation of nanoscale lipid vesicles. *ACS Nano* **4**, 2077–2087 (2010).
8. Feng, Q., Sun, J. & Jiang, X. Microfluidics-mediated assembly of functional nanoparticles for cancer-related pharmaceutical applications. *Nanoscale* **8**, 12430–12443 (2016).
9. Ding, S., Anton, N., Vandamme, T. F. & Serra, C. A. Microfluidic nanoprecipitation systems for preparing pure drug or polymeric drug loaded nanoparticles: an overview. *Expert Opinion on Drug Delivery* **13**, 1447–1460 (2016).
10. Belliveau, N. M. *et al.* Microfluidic synthesis of highly potent limit-size lipid nanoparticles for in vivo delivery of siRNA. *Mol. Ther. Acids* **1**, e37 (2012).
11. Laschke, M. W. & Menger, M. D. Life is 3D: Boosting Spheroid Function for Tissue Engineering. *Trends in Biotechnology* **35**, 133–144 (2017).
12. Yaman, S., Anil-Inevi, M., Ozcivici, E. & Tekin, H. C. Magnetic Force-Based Microfluidic Techniques for Cellular and Tissue Bioengineering. *Front. Bioeng. Biotechnol.* **6**, (2018).
13. Chen, K. *et al.* Rapid formation of size-controllable multicellular spheroids via 3D acoustic tweezers. *Lab Chip* **16**, 2636–2643 (2016).
14. Moshksayan, K. *et al.* Spheroids-on-a-chip: Recent advances and design considerations in microfluidic platforms for spheroid formation and culture. *Sensors and Actuators, B: Chemical* **263**, 151–176 (2018).
15. Chen, X. *et al.* Nitric oxide-induced stromal depletion for improved nanoparticle penetration in pancreatic cancer treatment. *Biomaterials* **246**, 119999 (2020).
16. Ding, J. *et al.* Engineered nanomedicines with enhanced tumor penetration. *Nano Today* **29**, 100800 (2019).
17. Tóth, E. L., Holczer, E. G., Iván, K. & Fürjes, P. Optimized Simulation and Validation of Particle Advection in Asymmetric Staggered Herringbone Type Micromixers. *Micromachines 2015, Vol. 6, Pages 136-150* **6**, 136–150 (2014).

18. Stroock, A. D. *et al.* Chaotic mixer for microchannels. *Science (80-.).* **295**, 647–651 (2002).
19. Rasouli, M., Abouei Mehrizi, A., Goharimanesh, M., Lashkaripour, A. & Razavi Bazaz, S. Multi-criteria optimization of curved and baffle-embedded micromixers for bio-applications. *Chem. Eng. Process. - Process Intensif.* **132**, 175–186 (2018).
20. Bazaz, S. R. *et al.* A hybrid micromixer with planar mixing units. *RSC Adv.* **8**, 33103–33120 (2018).
21. Cheung, C. C. L. & Al-Jamal, W. T. Sterically stabilized liposomes production using staggered herringbone micromixer: Effect of lipid composition and PEG-lipid content. *Int. J. Pharm.* **566**, 687–696 (2019).
22. Gdowski, A. *et al.* Optimization and scale up of microfluidic nanolipomer production method for preclinical and potential clinical trials. *J. Nanobiotechnology* **16**, 1–10 (2018).
23. Stott, S. L. *et al.* Isolation of circulating tumor cells using a microvortex-generating herringbone-chip. *Proc. Natl. Acad. Sci. U. S. A.* **107**, 18392–18397 (2010).
24. Dang, B. Van *et al.* Can 3D-printed spacers improve filtration at the microscale? *Sep. Purif. Technol.* **256**, 117776 (2021).
25. Gomez-Aranzadi, M., Arana, S., Mujika, M. & Hansford, D. Integrated microstructures to improve surface-sample interaction in planar biosensors. *IEEE Sens. J.* **15**, 1216–1223 (2015).
26. Yu, X. *et al.* A Nanostructured Microfluidic Immunoassay Platform for Highly Sensitive Infectious Pathogen Detection. *Small* **13**, 1700425 (2017).
27. Pariset, E. *et al.* Anticipating Cutoff Diameters in Deterministic Lateral Displacement (DLD) Microfluidic Devices for an Optimized Particle Separation. *Small* **13**, (2017).
28. Yamada, M., Seko, W., Yanai, T., Ninomiya, K. & Seki, M. Slanted, asymmetric microfluidic lattices as size-selective sieves for continuous particle/cell sorting. *Lab Chip* **17**, 304–314 (2017).
29. Zeming, K. K., Salafi, T., Chen, C. H. & Zhang, Y. Asymmetrical Deterministic Lateral Displacement Gaps for Dual Functions of Enhanced Separation and Throughput of Red Blood Cells. *Sci. Reports 2016 61* **6**, 1–10 (2016).
30. Okano, H. *et al.* Enrichment of circulating tumor cells in tumor-bearing mouse blood by a deterministic lateral displacement microfluidic device. *Biomed. Microdevices* **17**, 1–11 (2015).
31. Holm, S. H., Beech, J. P., Barrett, M. P. & Tegenfeldt, J. O. Separation of parasites from human blood using deterministic lateral displacement. *Lab Chip* **11**, 1326–1332 (2011).
32. Wunsch, B. H. *et al.* Nanoscale lateral displacement arrays for the separation of exosomes and colloids down to 20 nm. *Nat. Nanotechnol. 2016 1111* **11**, 936–940 (2016).
33. Henry, E. *et al.* Sorting cells by their dynamical properties. *Sci. Reports 2016 61* **6**, 1–11 (2016).
34. Huang, D., Man, J., Jiang, D., Zhao, J. & Xiang, N. Inertial microfluidics: Recent advances. *Electrophoresis* **41**, 2166–2187 (2020).
35. Zhang, J. *et al.* Fundamentals and applications of inertial microfluidics: a review. *Lab Chip* **16**, 10–

34 (2015).

36. Wang, L. *et al.* Sickle-like Inertial Microfluidic System for Online Rare Cell Separation and Tandem Label-Free Quantitative Proteomics (Orcs-Proteomics). *Anal. Chem.* **94**, 6026–6035 (2022).
37. Shen, S. *et al.* Spiral microchannel with ordered micro-obstacles for continuous and highly-efficient particle separation. *Lab Chip* **17**, 3578–3591 (2017).
38. Warkiani, M. E. *et al.* Slanted spiral microfluidics for the ultra-fast, label-free isolation of circulating tumor cells. *Lab Chip* **14**, 128–137 (2013).
39. Condina, M. R. *et al.* Rapid separation and identification of beer spoilage bacteria by inertial microfluidics and MALDI-TOF mass spectrometry. *Lab Chip* **19**, 1961–1970 (2019).
40. Zhao, Z., Yang, Y., Zeng, Y. & He, M. A microfluidic ExoSearch chip for multiplexed exosome detection towards blood-based ovarian cancer diagnosis. *Lab Chip* **16**, 489–496 (2016).
41. Gossett, D. R. *et al.* Hydrodynamic stretching of single cells for large population mechanical phenotyping. *Proc. Natl. Acad. Sci. U. S. A.* **109**, 7630–7635 (2012).
42. Huang, H. *et al.* Generation and manipulation of hydrogel microcapsules by droplet-based microfluidics for mammalian cell culture. *Lab Chip* **17**, 1913–1932 (2017).
43. Chu, L. Y., Utada, A. S., Shah, R. K., Kim, J. W. & Weitz, D. A. Controllable Monodisperse Multiple Emulsions. *Angew. Chemie Int. Ed.* **46**, 8970–8974 (2007).
44. Lashkaripour, A. *et al.* Machine learning enables design automation of microfluidic flow-focusing droplet generation. *Nat. Commun.* **12**, 25 (2021).
45. Lashkaripour, A., Rodriguez, C., Ortiz, L. & Densmore, D. Performance tuning of microfluidic flow-focusing droplet generators. *Lab Chip* **19**, 1041–1053 (2019).
46. Markey, A. L., Mohr, S. & Day, P. J. R. High-throughput droplet PCR. *Methods* **50**, 277–281 (2010).
47. Sjostrom, S. L. *et al.* High-throughput screening for industrial enzyme production hosts by droplet microfluidics. *Lab Chip* **14**, 806–813 (2014).
48. Kang, D. K., Monsur Ali, M., Zhang, K., Pone, E. J. & Zhao, W. Droplet microfluidics for single-molecule and single-cell analysis in cancer research, diagnosis and therapy. *TrAC Trends Anal. Chem.* **58**, 145–153 (2014).
49. Sart, S., Tomasi, R. F. X., Amselem, G. & Baroud, C. N. Multiscale cytometry and regulation of 3D cell cultures on a chip. *Nat. Commun.* **8**, (2017).
50. Wang, J. *et al.* Droplet Microfluidics for the Production of Microparticles and Nanoparticles. *Micromachines 2017, Vol. 8, Page 22* **8**, 22 (2017).
51. Sabhachandani, P. *et al.* Generation and functional assessment of 3D multicellular spheroids in droplet based microfluidics platform. *Lab Chip* **16**, 497–505 (2016).
52. Yaman, S., Anil-Inevi, M., Ozcivici, E. & Tekin, H. C. Magnetic force-based microfluidic techniques for cellular and tissue bioengineering. *Front. Bioeng. Biotechnol.* **6**, 192 (2018).

53. Robert, D. *et al.* Cell sorting by endocytotic capacity in a microfluidic magnetophoresis device. *Lab Chip* **11**, 1902–1910 (2011).
54. Zhao, W., Cheng, R., Miller, J. R. & Mao, L. Label-Free Microfluidic Manipulation of Particles and Cells in Magnetic Liquids. *Adv. Funct. Mater.* **26**, 3916–3932 (2016).
55. Mensing, G. A., Pearce, T. M., Graham, M. D. & Beebe, D. J. An externally driven magnetic microstirrer. *Philos. Trans. R. Soc. A Math. Phys. Eng. Sci.* **362**, 1059–1068 (2004).
56. Tsai, T. H., Liou, D. S., Kuo, L. S. & Chen, P. H. Rapid mixing between ferro-nanofluid and water in a semi-active Y-type micromixer. *Sensors Actuators A Phys.* **153**, 267–273 (2009).
57. Furlani, E. P. Magnetophoretic separation of blood cells at the microscale. *J. Phys. D. Appl. Phys.* **40**, 1313 (2007).
58. Tan, S. H., Nguyen, N. T., Yobas, L. & Kang, T. G. Formation and manipulation of ferrofluid droplets at a microfluidic T-junction. *J. Micromechanics Microengineering* **20**, (2010).
59. Modarres, P. & Tabrizian, M. Alternating current dielectrophoresis of biomacromolecules: The interplay of electrokinetic effects. *Sensors Actuators B Chem.* **252**, 391–408 (2017).
60. Modarres, P. & Tabrizian, M. Frequency hopping dielectrophoresis as a new approach for microscale particle and cell enrichment. *Sensors Actuators B Chem.* **286**, 493–500 (2019).
61. Archer, G. P., Betts, W. B. & Haigh, T. Rapid differentiation of untreated, autoclaved and ozone-treated Cryptosporidium parvum oocysts using dielectrophoresis. *Microbios* **73**, 165–172 (1993).
62. Salari, A., Navi, M., Lijnse, T. & Dalton, C. AC Electrothermal Effect in Microfluidics: A Review. *Micromachines* **10**, (2019).
63. Modarres, P. & Tabrizian, M. Phase-controlled field-effect micromixing using AC electroosmosis. *Microsystems Nanoeng.* **6**, (2020).
64. Hossan, M. R., Dutta, D., Islam, N. & Dutta, P. Review: Electric field driven pumping in microfluidic device. *Electrophoresis* **39**, 702–731 (2018).
65. Modarres, P. & Tabrizian, M. Electrohydrodynamic-Driven Micromixing for the Synthesis of Highly Monodisperse Nanoscale Liposomes. *ACS Appl. Nano Mater.* **3**, 4000–4013 (2020).
66. Wu, J. Biased AC electro-osmosis for on-chip bioparticle processing. *IEEE Trans. Nanotechnol.* **5**, 84–88 (2006).
67. Ashkin, A., Dziedzic, J. M., Bjorkholm, J. E. & Chu, S. Observation of a single-beam gradient force optical trap for dielectric particles. *Opt. Lett. Vol. 11, Issue 5, pp. 288-290* **11**, 288–290 (1986).
68. Grier, D. G. A revolution in optical manipulation. *Nat. 2003 4246950* **424**, 810–816 (2003).
69. Jähnke, T. & Rauch, P. Optical tweezers for single-cell, multicellular investigations in the life sciences. *Am. Lab.* **47**, (2015).
70. Dai, X. *et al.* Optical tweezers-controlled hotspot for sensitive and reproducible surface-enhanced Raman spectroscopy characterization of native protein structures. *Nat. Commun. 2021 121* **12**, 1–

9 (2021).

71. Mohanty, S., Khalil, I. S. M. & Misra, S. Contactless acoustic micro/nano manipulation: a paradigm for next generation applications in life sciences. *Proc. R. Soc. A Math. Phys. Eng. Sci.* **476**, 20200621 (2020).
72. Fakhfouri, A. *et al.* Surface acoustic wave diffraction driven mechanisms in microfluidic systems. *Lab Chip* **18**, 2214–2224 (2018).
73. Destgeer, G. & Sung, H. J. Recent advances in microfluidic actuation and micro-object manipulation via surface acoustic waves. *Lab Chip* **15**, 2722–2738 (2015).
74. Pethig, R. Dielectrophoresis: Using Inhomogeneous AC Electrical Fields to Separate and Manipulate Cells. *Crit. Rev. Biotechnol.* **16**, 331–348 (1996).
75. MacDonald, M. P., Spalding, G. C. & Dholakia, K. Microfluidic sorting in an optical lattice. **426**, 421–424 (2003).
76. Ozcelik, A. *et al.* Acoustic tweezers for the life sciences. *Nat. Methods* **15**, 1021–1028 (2018).
77. Gao, Y., Fajrial, A. K., Yang, T. & Ding, X. Emerging on-chip surface acoustic wave technology for small biomaterials manipulation and characterization. *Biomaterials Science* **9**, 1574–1582 (2021).
78. Jiang, Y. *et al.* SAW sensor for Influenza A virus detection enabled with efficient surface functionalization. *Sensors Actuators B* **209**, 78–84 (2015).
79. Turbé, V. *et al.* Towards an ultra-rapid smartphone- connected test for infectious diseases. *Sci. Rep.* **7**, 11971 (2017).
80. Zida, S. I., Lin, Y. & Khung, Y. L. Current Trends on Surface Acoustic Wave Biosensors. *Adv. Mater. Technol.* **6**, 2001018 (2021).
81. Stamp, M. E. M. E. M., Brugger, M. S. S., Wixforth, A. & Westerhausen, C. Acoustotaxis – in vitro stimulation in a wound healing assay employing surface acoustic waves. *Biomater. Sci.* **4**, (2016).
82. Rosenblum, J. I., Gazes, M. I. & Greenberg, N. Surface acoustic wave patch therapy affects tissue oxygenation in ischemic feet. *Wounds* **26**, 301–305 (2014).
83. Miansari, M. *et al.* Inducing Mild Traumatic Brain Injury in C. elegans via Cavitation-Free Surface Acoustic Wave-Driven Ultrasonic Irradiation. *Sci. Rep.* **9**, 12775 (2019).
84. Pons, J. *Emerging Actuator Technologies*. *Emerging Actuator Technologies: A Micromechatronic Approach* (John Wiley & Sons, Ltd, 2005). doi:10.1002/0470091991
85. Yeo, L. Y. & review of fluid mechanics, F.-J. R. Surface acoustic wave microfluidics. *Annu. Rev. Fluid Mech.* (2014).
86. Ahmed, H., Ramesan, S., Lee, L., Rezk, A. R. & Yeo, L. Y. On-Chip Generation of Vortical Flows for Microfluidic Centrifugation. *Small* **16**, 1903605 (2020).
87. Rezk, A. R., Tan, J. K. & Yeo, L. Y. HYbriD Resonant Acoustics (HYDRA). *Adv. Mater.* **28**, 1970–1975 (2016).

88. Zhang, J., Wu, Q., Zhang, X., Wan, H. & Wang, P. Acoustic Transducer and Its Applications in Biosensors. in *Handbook of Cell Biosensors* 1–19 (Springer International Publishing, 2021). doi:10.1007/978-3-319-47405-2_65-1
89. Go, D. B. B., Atashbar, M. Z. Z., Ramshani, Z., Chang, H.-C. & Degree, P. D. Surface acoustic wave devices for chemical sensing and microfluidics: a review and perspective. *Anal. Methods* **9**, 4112–4134 (2017).
90. Friend, J. & Yeo, L. Y. Microscale acoustofluidics: Microfluidics driven via acoustics and ultrasonics. *Rev. Mod. Phys.* **83**, 647–704 (2011).
91. Bruus, H. Acoustofluidics 10: Scaling laws in acoustophoresis. *Lab Chip* **12**, 1578–1586 (2012).
92. Manasseh, R. Acoustic Bubbles, Acoustic Streaming, and Cavitation Microstreaming. in *Handbook of Ultrasonics and Sonochemistry* 33–68 (Springer Singapore, 2016). doi:10.1007/978-981-287-278-4_5
93. Wiklund, M., Green, R. & Ohlin, M. Acoustofluidics 14: Applications of acoustic streaming in microfluidic devices. *Lab Chip* **12**, (2012).
94. Nyborg, W. L. Acoustic Streaming near a Boundary. *J. Acoust. Soc. Am.* **30**, 329–339 (1958).
95. Lei, J., Glynne-Jones, P. & Hill, M. Comparing methods for the modelling of boundary-driven streaming in acoustofluidic devices. *Microfluid. Nanofluidics* **21**, 23 (2017).
96. Leibacher, I., Hahn, P. & Dual, J. Acoustophoretic cell and particle trapping on microfluidic sharp edges. *Microfluid. Nanofluidics* **19**, 923–933 (2015).
97. Hashmi, A., Yu, G., Reilly-Collette, M., Heiman, G. & Xu, J. Oscillating bubbles: a versatile tool for lab on a chip applications. *Lab Chip* **12**, 4216 (2012).
98. Rasouli, M. R. & Tabrizian, M. An ultra-rapid acoustic micromixer for synthesis of organic nanoparticles. *Lab Chip* **19**, 3316–3325 (2019).
99. Eckart, C. Vortices and Streams Caused by Sound Waves. *Phys. Rev.* **73**, 68–76 (1948).
100. Hertz, G. & Mende, H. Der Schallstrahlungsdruck in Flüssigkeiten. *Zeitschrift für Phys.* **114**, 354–367 (1939).
101. Deshmukh, S., Brzozka, Z., Laurell, T. & Augustsson, P. Acoustic radiation forces at liquid interfaces impact the performance of acoustophoresis. *Lab Chip* **14**, 3394–400 (2014).
102. Augustsson, P., Karlsen, J. T., Su, H.-W., Bruus, H. & Voldman, J. Iso-acoustic focusing of cells for size-insensitive acousto-mechanical phenotyping. *Nat. Commun.* **7**, 11556 (2016).
103. Karlsen, J. T., Qiu, W., Augustsson, P. & Bruus, H. Acoustic Streaming and Its Suppression in Inhomogeneous Fluids. *Phys. Rev. Lett.* **120**, 054501 (2018).
104. Drinkwater, B. W. From chip-in-a-lab to lab-on-a-chip: towards a single handheld electronic system for multiple application-specific lab-on-a-chip (ASLOC). **16**, 2360 (2014).
105. Baresch, D., Thomas, J.-L. & Marchiano, R. Observation of a Single-Beam Gradient Force

Acoustical Trap for Elastic Particles: Acoustical Tweezers. *Phys. Rev. Lett.* **116**, 024301 (2016).

106. Samandari, M., Abrinia, K. & Sanati-Nezhad, A. Acoustic manipulation of bio-particles at high frequencies: An analytical and simulation approach. *Micromachines* **8**, (2017).
107. Destgeer, G., Lee, K. H., Jung, J. H., Alazzam, A. & Sung, H. J. Continuous separation of particles in a PDMS microfluidic channel via travelling surface acoustic waves (TSAW). *Lab Chip* **13**, 4210 (2013).
108. Mettin, R., Akhatov, I., Parlitz, U., Ohl, C. & Lauterborn, W. Bjerknes forces between small cavitation bubbles in a strong acoustic field. *Phys. Rev. E* **56**, 2924–2931 (1997).
109. Habibi, R. *et al.* Lab on a Chip Exosome trapping and enrichment using a sound wave activated nano-sieve (SWANS) †. **20**, 3633 (2020).
110. Qiu, W., Karlsen, J. T., Bruus, H. & Augustsson, P. Experimental Characterization of Acoustic Streaming in Gradients of Density and Compressibility. *Phys. Rev. Appl.* **11**, 024018 (2019).
111. Van Assche, D. *et al.* Gradient acoustic focusing of sub-micron particles for separation of bacteria from blood lysate. *Sci. Rep.* **10**, 1–13 (2020).
112. Antfolk, M., Magnusson, C., Augustsson, P., Lilja, H. & Laurell, T. Acoustofluidic, Label-Free Separation and Simultaneous Concentration of Rare Tumor Cells from White Blood Cells. *Anal. Chem.* **87**, 9322–9328 (2015).
113. Antfolk, M., Antfolk, C., Lilja, H., Laurell, T. & Augustsson, P. A single inlet two-stage acoustophoresis chip enabling tumor cell enrichment from white blood cells. *Lab Chip* **15**, 2102–2109 (2015).
114. Chen, Y. *et al.* High-throughput acoustic separation of platelets from whole blood. *Lab Chip* **16**, 3466–3472 (2016).
115. Petersson, F., Åberg, L., Swärd-Nilsson, A.-M. & Laurell, T. Free Flow Acoustophoresis: Microfluidic-Based Mode of Particle and Cell Separation. *Anal. Chem.* **79**, 5117–5123 (2007).
116. Shi, J., Huang, H., Stratton, Z., Huang, Y. & Huang, T. J. Continuous particle separation in a microfluidic channel via standing surface acoustic waves (SSAW). *Lab Chip* **9**, 3354 (2009).
117. Nam, J., Lim, H., Kim, D. & Shin, S. Separation of platelets from whole blood using standing surface acoustic waves in a microchannel. *Lab Chip* **11**, 3361 (2011).
118. Li, S. *et al.* An On-Chip, Multichannel Droplet Sorter Using Standing Surface Acoustic Waves. *Anal. Chem.* **85**, 5468–5474 (2013).
119. Lee, K. *et al.* Acoustic Purification of Extracellular Microvesicles. *ACS Nano* **9**, 2321–2327 (2015).
120. Wu, M. *et al.* Acoustic Separation of Nanoparticles in Continuous Flow. *Adv. Funct. Mater.* **27**, 1606039 (2017).
121. Wu, M. *et al.* Isolation of exosomes from whole blood by integrating acoustics and microfluidics. *Proc. Natl. Acad. Sci.* **114**, 10584–10589 (2017).

122. Li, P. & Huang, T. J. Applications of Acoustofluidics in Bioanalytical Chemistry. *Anal. Chem.* **91**, 757–767 (2019).

123. Ding, X. *et al.* Cell separation using tilted-angle standing surface acoustic waves. *Proc. Natl. Acad. Sci.* **111**, 12992–12997 (2014).

124. Li, P. *et al.* Acoustic separation of circulating tumor cells. *Proc. Natl. Acad. Sci.* **112**, 4970–4975 (2015).

125. Bruus, H. Acoustofluidics 7: The acoustic radiation force on small particles. *Lab Chip* **12**, 1014 (2012).

126. Petersson, F., Nilsson, A., Holm, C., Jönsson, H. & Laurell, T. Continuous separation of lipid particles from erythrocytes by means of laminar flow and acoustic standing wave forces. *Lab Chip* **5**, 20–22 (2005).

127. Franke, T., Abate, A. R., Weitz, D. A. & Wixforth, A. Surface acoustic wave (SAW) directed droplet flow in microfluidics for PDMS devices. *Lab Chip* **9**, 2625 (2009).

128. Franke, T., Braunmüller, S., Schmid, L., Wixforth, A. & Weitz, D. A. Surface acoustic wave actuated cell sorting (SAWACS). *Lab Chip* **10**, 789 (2010).

129. Ahmad, R. *et al.* Acoustic Wave-Driven Functionalized Particles for Aptamer-Based Target Biomolecule Separation. *Anal. Chem.* **89**, 13313–13319 (2017).

130. Destgeer, G., Ha, B. H., Jung, J. H. & Sung, H. J. Submicron separation of microspheres via travelling surface acoustic waves. *Lab Chip* **14**, 4665–4672 (2014).

131. Wang, K. *et al.* Sorting of tumour cells in a microfluidic device by multi-stage surface acoustic waves. *Sensors Actuators B Chem.* **258**, 1174–1183 (2018).

132. Collins, D. J. J. *et al.* Selective particle and cell capture in a continuous flow using micro-vortex acoustic streaming. *Lab Chip* **17**, 1769–1777 (2017).

133. Wang, C., Jalikop, S. V & Hilgenfeldt, S. Efficient manipulation of microparticles in bubble streaming flows. *Biomicrofluidics* **6**, 012801 (2012).

134. Thameem, R., Rallabandi, B. & Hilgenfeldt, S. Particle migration and sorting in microbubble streaming flows. *Biomicrofluidics* **10**, 014124 (2016).

135. Patel, M. V., Tovar, A. R. & Lee, A. P. Lateral cavity acoustic transducer as an on-chip cell/particle microfluidic switch. *Lab Chip* **12**, 139–45 (2012).

136. Garg, N. *et al.* Whole-blood sorting, enrichment and in situ immunolabeling of cellular subsets using acoustic microstreaming. *Microsystems Nanoeng.* **4**, 17085 (2018).

137. Patel, M. V., Nanayakkara, I. A., Simon, M. G. & Lee, A. P. Cavity-induced microstreaming for simultaneous on-chip pumping and size-based separation of cells and particles. *Lab Chip* **14**, 3860 (2014).

138. Nivedita, N., Garg, N., Lee, A. P. P. & Papautsky, I. A high throughput microfluidic platform for

size-selective enrichment of cell populations in tissue and blood samples. **142**, 2558–2569 (2017).

139. Fakhfouri, A., Devendran, C., Collins, D. J. J., Ai, Y. & Neild, A. Virtual membrane for filtration of particles using surface acoustic waves (SAW). *Lab Chip* **16**, 3515–3523 (2016).
140. Collins, D. J., Ma, Z., Han, J. & Ai, Y. Continuous micro-vortex-based nanoparticle manipulation via focused surface acoustic waves. *Lab Chip* **17**, 91–103 (2017).
141. Cui, W., Mu, L., Duan, X., Pang, W. & Reed, M. A. A polarized nonlinear optical response in a topological insulator Bi 2 Se 3-Au nanoantenna hybrid-structure for all-optical switching Trapping of sub-100 nm nanoparticles using gigahertz acoustofluidic tweezers for biosensing applications †. *Nanoscale* **11**, 14625 (2019).
142. Mao, Z. *et al.* Enriching Nanoparticles via Acoustofluidics. *ACS Nano* **11**, 603–612 (2017).
143. Hammarström, B., Laurell, T. & Nilsson, J. Seed particle-enabled acoustic trapping of bacteria and nanoparticles in continuous flow systems. *Lab Chip* **12**, 4296 (2012).
144. Ku, A. *et al.* Acoustic Enrichment of Extracellular Vesicles from Biological Fluids. *Anal. Chem.* **90**, 8011–8019 (2018).
145. Habibi, R. & Neild, A. Sound wave activated nano-sieve (SWANS) for enrichment of nanoparticles. *Lab Chip* **19**, 3032–3044 (2019).
146. Karthick, S., Pradeep, P. N., Kanchana, P. & Sen, A. K. Acoustic impedance-based size-independent isolation of circulating tumour cells from blood using acoustophoresis. *Lab Chip* **18**, 3802–3813 (2018).
147. Shields, C. W., Johnson, L. M., Gao, L. & López, G. P. Elastomeric Negative Acoustic Contrast Particles for Capture, Acoustophoretic Transport, and Confinement of Cells in Microfluidic Systems. *Langmuir* **30**, 3923–3927 (2014).
148. Ai, Y., Sanders, C. K. & Marrone, B. L. Separation of Escherichia coli Bacteria from Peripheral Blood Mononuclear Cells Using Standing Surface Acoustic Waves. *Anal. Chem.* **85**, 9126–9134 (2013).
149. Wang, C., Jalikop, S. V. & Hilgenfeldt, S. Size-sensitive sorting of microparticles through control of flow geometry. *Appl. Phys. Lett.* **99**, 034101 (2011).
150. Sehgal, P. & Kirby, B. J. Separation of 300 and 100 nm Particles in Fabry–Perot Acoustofluidic Resonators. *Anal. Chem.* **89**, 12192–12200 (2017).
151. Ku, A. *et al.* Acoustic Enrichment of Extracellular Vesicles from Biological Fluids. *Anal. Chem.* **90**, 8011–8019 (2018).
152. Collins, D. J. *et al.* Self-Aligned Acoustofluidic Particle Focusing and Patterning in Microfluidic Channels from Channel-Based Acoustic Waveguides. *Phys. Rev. Lett.* **120**, 074502 (2018).
153. Guex, A. G., Di Marzio, N., Eglin, D., Alini, M. & Serra, T. The waves that make the pattern: a review on acoustic manipulation in biomedical research. *Materials Today Bio* **10**, 100110 (2021).
154. Armstrong, J. P. K. & Stevens, M. M. Using Remote Fields for Complex Tissue Engineering. *Trends*

in Biotechnology **38**, 254–263 (2020).

155. Dalecki, D. & Hocking, D. C. Advancing Ultrasound Technologies for Tissue Engineering. in *Handbook of Ultrasonics and Sonochemistry* 1–26 (Springer Singapore, 2015). doi:10.1007/978-981-287-470-2_28-1
156. Wang, Z. *et al.* Single-cell patterning technology for biological applications. *Biomicrofluidics* **13**, 061502 (2019).
157. Armstrong, J. P. K. *et al.* Engineering Anisotropic Muscle Tissue using Acoustic Cell Patterning. *Adv. Mater.* **30**, 1802649 (2018).
158. Kang, B. *et al.* High-resolution acoustophoretic 3D cell patterning to construct functional collateral cylindroids for ischemia therapy. *Nat. Commun.* **9**, 5402 (2018).
159. Naseer, S. M. *et al.* Surface acoustic waves induced micropatterning of cells in gelatin methacryloyl (GelMA) hydrogels. *Biofabrication* **9**, 015020 (2017).
160. Olofsson, K., Hammarström, B. & Wiklund, M. Ultrasonic Based Tissue Modelling and Engineering. *Micromachines* **9**, 594 (2018).
161. Olofsson, K. *et al.* Acoustic formation of multicellular tumor spheroids enabling on-chip functional and structural imaging. *Lab Chip* **18**, 2466–2476 (2018).
162. Buikema, J. W., Van Der Meer, P., Sluijter, J. P. G. & Domian, I. J. Engineering Myocardial Tissue: The Convergence of Stem Cells Biology and Tissue Engineering Technology. *Stem Cells* **31**, 2587 (2013).
163. Mauck, R. L. *et al.* Engineering on the Straight and Narrow: The Mechanics of Nanofibrous Assemblies for Fiber-Reinforced Tissue Regeneration. *Tissue Eng. Part B. Rev.* **15**, 171 (2009).
164. Shi, J. *et al.* Acoustic tweezers: patterning cells and microparticles using standing surface acoustic waves (SSAW). *Lab Chip* **9**, 2890 (2009).
165. Guo, F. *et al.* Controlling cell–cell interactions using surface acoustic waves. *Proc. Natl. Acad. Sci.* **112**, 43–48 (2015).
166. Li, S. *et al.* Standing Surface Acoustic Wave Based Cell Coculture. *Anal. Chem.* **86**, 9853–9859 (2014).
167. Lata, J. P. *et al.* Surface Acoustic Waves Grant Superior Spatial Control of Cells Embedded in Hydrogel Fibers. *Adv. Mater.* **28**, 8632–8638 (2016).
168. Garvin, K. A., Dalecki, D. & Hocking, D. C. Vascularization of Three-Dimensional Collagen Hydrogels Using Ultrasound Standing Wave Fields. *Ultrasound Med. Biol.* **37**, 1853–1864 (2011).
169. Comeau, E. S., Hocking, D. C. & Dalecki, D. Ultrasound patterning technologies for studying vascular morphogenesis in 3D. *J. Cell Sci.* **130**, 232–242 (2017).
170. Sriphutkiat, Y., Kasetsirikul, S., Ketpun, D. & Zhou, Y. Cell alignment and accumulation using acoustic nozzle for bioprinting. *Sci. Rep.* **9**, 1–12 (2019).

171. Chansoria, P., Narayanan, L. K., Schuchard, K. & Shirwaiker, R. Ultrasound-assisted biofabrication and bioprinting of preferentially aligned three-dimensional cellular constructs. *Biofabrication* **11**, 035015 (2019).

172. Bernassau, A. L., MacPherson, P. G. A., Beeley, J., Drinkwater, B. W. & Cumming, D. R. S. Patterning of microspheres and microbubbles in an acoustic tweezers. *Biomed. Microdevices* **15**, 289–297 (2013).

173. Bernassau, A. L., Gesellchen, F., MacPherson, P. G. A., Riehle, M. & Cumming, D. R. S. Direct patterning of mammalian cells in an ultrasonic heptagon stencil. *Biomed. Microdevices* **14**, 559–564 (2012).

174. Gladkov, A. *et al.* Design of Cultured Neuron Networks in vitro with Predefined Connectivity Using Asymmetric Microfluidic Channels. *Sci. Rep.* **7**, 1–14 (2017).

175. Gesellchen, F., Bernassau, A. L., Déjardin, T., Cumming, D. R. S. & Riehle, M. O. Cell patterning with a heptagon acoustic tweezer-application in neurite guidance. *Lab Chip* **14**, 2266–2275 (2014).

176. Bazou, D., Foster, G. A., Ralphs, J. R. & Coakley, W. T. Molecular adhesion development in a neural cell monolayer forming in an ultrasound trap. *Mol. Membr. Biol.* **22**, 229–240 (2005).

177. Tian, Z. *et al.* Generating multifunctional acoustic tweezers in Petri dishes for contactless, precise manipulation of bioparticles. *Sci. Adv.* **6**, (2020).

178. Bouyer, C. *et al.* A Bio-Acoustic Levitational (BAL) Assembly Method for Engineering of Multilayered, 3D Brain-Like Constructs, Using Human Embryonic Stem Cell Derived Neuro-Progenitors. *Adv. Mater.* **28**, 161–167 (2016).

179. Tait, A. *et al.* Engineering multi-layered tissue constructs using acoustic levitation. *Sci. Rep.* **9**, 9789 (2019).

180. Ding, X. *et al.* Tunable patterning of microparticles and cells using standing surface acoustic waves. *Lab Chip* **12**, 2491–2497 (2012).

181. Kang, P. *et al.* Acoustic tweezers based on circular, slanted-finger interdigital transducers for dynamic manipulation of micro-objects. *Lab Chip* **20**, 987–994 (2020).

182. Bian, Y. *et al.* Acoustofluidic waveguides for localized control of acoustic wavefront in microfluidics. *Microfluid. Nanofluidics* **21**, 132 (2017).

183. cohen, S. *et al.* Large-scale acoustic-driven neuronal patterning and directed outgrowth. *Sci. Rep.* **10**, 1–11 (2020).

184. Cai, H. *et al.* Acoustofluidic assembly of 3D neurospheroids to model Alzheimer's disease. *Analyst* **145**, 6243–6253 (2020).

185. Bazou, D., Coakley, W. T., Hayes, A. J. & Jackson, S. K. Long-term viability and proliferation of alginate-encapsulated 3-D HepG2 aggregates formed in an ultrasound trap. *Toxicol. Vitr.* **22**, 1321–1331 (2008).

186. Liu, J. *et al.* Functional three-dimensional HepG2 aggregate cultures generated from an ultrasound trap: Comparison with HepG2 spheroids. *J. Cell. Biochem.* **102**, 1180–1189 (2007).
187. Kuznetsova, L. A., Bazou, D., Edwards, G. O. & Coakley, W. T. Multiple three-dimensional mammalian cell aggregates formed away from solid substrata in ultrasound standing waves. *Biotechnol. Prog.* **25**, 834–841 (2009).
188. Olofsson, K., Carannante, V., Takai, M., Önfelt, B. & Wiklund, M. Ultrasound-Based Scaffold-Free Core-Shell Multicellular Tumor Spheroid Formation. *Micromachines* **12**, 329 (2021).
189. Hu, X. *et al.* Lab on a Chip On-chip hydrogel arrays individually encapsulating acoustic formed multicellular aggregates for high throughput drug testing †. **20**, 2228 (2020).
190. Chen, B. *et al.* High-throughput acoustofluidic fabrication of tumor spheroids. *Lab Chip* **19**, 1755–1763 (2019).
191. Wu, Y. *et al.* Acoustic assembly of cell spheroids in disposable capillaries. *Nanotechnology* **29**, 504006 (2018).
192. Guo, F. *et al.* Precise Manipulation and Patterning of Protein Crystals for Macromolecular Crystallography Using Surface Acoustic Waves. *Small* **11**, 2733–2737 (2015).
193. Kurashina, Y., Takemura, K. & Friend, J. Cell agglomeration in the wells of a 24-well plate using acoustic streaming. *Lab Chip* **17**, 876–886 (2017).
194. Alhasan, L. *et al.* Rapid Enhancement of Cellular Spheroid Assembly by Acoustically Driven Microcentrifugation. *ACS Biomater. Sci. Eng.* **2**, 1013–1022 (2016).
195. Huang, P. *et al.* Acoustofluidic Synthesis of Particulate Nanomaterials. *Adv. Sci.* **6**, 1900913 (2019).
196. Le, N. H. A. *et al.* Acoustically enhanced microfluidic mixer to synthesize highly uniform nanodrugs without the addition of stabilizers. *Int. J. Nanomedicine* **Volume 13**, 1353–1359 (2018).
197. An Le, N. H. H. *et al.* Ultrafast star-shaped acoustic micromixer for high throughput nanoparticle synthesis. *Lab Chip* **20**, 582–591 (2020).
198. Pourabed, A. *et al.* High throughput acoustic microfluidic mixer controls self-assembly of protein nanoparticles with tuneable sizes. *J. Colloid Interface Sci.* **585**, 229–236 (2021).
199. Kurosawa, M., Watanabe, T., Futami, A. & Higuchi, T. Surface acoustic wave atomizer. *Sensors Actuators A Phys.* **50**, 69–74 (1995).
200. Qi, A. *et al.* Template-free Synthesis and Encapsulation Technique for Layer-by-Layer Polymer Nanocarrier Fabrication. *ACS Nano* **5**, 9583–9591 (2011).
201. Alvarez, M., Friend, J. & Yeo, L. Y. Rapid generation of protein aerosols and nanoparticles via surface acoustic wave atomization. *Nanotechnology* **19**, (2008).
202. Qi, A., Friend, J. R. & Yeo, L. Y. Investigation of SAW atomization. in *Proceedings - IEEE Ultrasonics Symposium* 787–790 (IEEE, 2009). doi:10.1109/ULTSYM.2009.5441556
203. Winkler, A., Harazim, S. M. M., Menzel, S. B. B. & Schmidt, H. SAW-based fluid atomization using

mass-producible chip devices. *Lab Chip* **15**, 3793–3799 (2015).

204. Rajapaksa, A. E. *et al.* Effective pulmonary delivery of an aerosolized plasmid DNA vaccine via surface acoustic wave nebulization. *Respir. Res.* **15**, 60 (2014).
205. Qi, A. *et al.* Miniature inhalation therapy platform using surface acoustic wave microfluidic atomization. *Lab Chip* **9**, 2184 (2009).
206. Rezk, A. R., Ahmed, H., Ramesan, S. & Yeo, L. Y. High Frequency Sonoprocessing: A New Field of Cavitation-Free Acoustic Materials Synthesis, Processing, and Manipulation. *Adv. Sci.* **8**, 2001983 (2021).
207. Go, D. B., Atashbar, M. Z., Ramshani, Z., Chang, H.-C. & Degree, P. D. Surface acoustic wave devices for chemical sensing and microfluidics: a review and perspective Analytical Methods CRITICAL REVIEW. **9**, 4112 (2017).
208. Rajapaksa, A., Qi, A., Yeo, L. Y., Coppel, R. & Friend, J. R. Enabling practical surface acoustic wave nebulizer drug delivery via amplitude modulation. *Lab Chip* **14**, 1858–1865 (2014).
209. Steinacher, M., Du, H., Gilbert, D. & Amstad, E. Production of Additive-Free Amorphous Nanoparticles with a SAW-Based Microfluidic Spray-Dryer. *Adv. Mater. Technol.* **4**, 1800665 (2019).
210. Barnes, P. New treatments for chronic obstructive pulmonary disease. *Curr. Opin. Pharmacol.* **1**, 217–222 (2001).
211. Wang, Y., Rezk, A. R., Khara, J. S., Yeo, L. Y. & Ee, P. L. R. Stability and efficacy of synthetic cationic antimicrobial peptides nebulized using high frequency acoustic waves. *Biomicrofluidics* **10**, 034115 (2016).
212. Marqus, S. *et al.* High frequency acoustic nebulization for pulmonary delivery of antibiotic alternatives against Staphylococcus aureus. *Eur. J. Pharm. Biopharm.* **151**, 181–188 (2020).
213. Alhasan, L., Qi, A., Rezk, A. R., Yeo, L. Y. & Chan, P. P. Y. Integrative Biology Assessment of the potential of a high frequency acoustomicrofluidic nebulisation platform for inhaled stem cell therapy †. *This J. is Cite this Integr. Biol* **8**, 12 (2016).
214. Ramesan, S., Rezk, A. R. & Yeo, L. Y. High frequency acoustic permeabilisation of drugs through tissue for localised mucosal delivery. *Lab Chip* **18**, 3272–3284 (2018).
215. Li, Y., Chen, Z. & Ge, S. Sonoporation: Underlying Mechanisms and Applications in Cellular Regulation. *BIO Integr.* **2**, 29–36 (2021).
216. Stewart, M. P., Langer, R. & Jensen, K. F. Intracellular delivery by membrane disruption: Mechanisms, strategies, and concepts. *Chem. Rev.* **118**, 7409–7531 (2018).
217. Tomizawa, M. *et al.* Sonoporation: Gene transfer using ultrasound. *World J. Methodol.* **3**, 39–44 (2013).
218. Qiu, Y., Zhang, C., Tu, J. & Zhang, D. Microbubble-induced sonoporation involved in ultrasound-

mediated DNA transfection in vitro at low acoustic pressures. *J. Biomech.* **45**, 1339–1345 (2012).

219. Hassan, M. A. *et al.* Modulation control over ultrasound-mediated gene delivery: Evaluating the importance of standing waves. *J. Control. Release* **141**, 70–76 (2010).
220. Morshedi Rad, D. *et al. A Comprehensive Review on Intracellular Delivery*. *Advanced Materials* **33**, 2005363 (2021).
221. van Wamel, A. *et al.* Vibrating microbubbles poking individual cells: Drug transfer into cells via sonoporation. *J. Control. Release* **112**, 149–155 (2006).
222. Fan, Z., Kumon, R. E. & Deng, C. X. Mechanisms of microbubble-facilitated sonoporation for drug and gene delivery. *Ther. Deliv.* **5**, 467–486 (2014).
223. Meng, L. *et al.* Sonoporation of Cells by a Parallel Stable Cavitation Microbubble Array. *Adv Sci* **6**, 1900557 (2019).
224. Aghaamoo, M. *et al.* High-Throughput and Dosage-Controlled Intracellular Delivery of Large Cargos by an Acoustic-Electric Micro-Vortices Platform. *Adv. Sci.* **9**, 2102021 (2022).
225. Carugo, D. *et al.* Contrast agent-free sonoporation: The use of an ultrasonic standing wave microfluidic system for the delivery of pharmaceutical agents. *Biomicrofluidics* **5**, 044108 (2011).
226. Belling, J. N. *et al.* Acoustofluidic sonoporation for gene delivery to human hematopoietic stem and progenitor cells. *Proc. Natl. Acad. Sci. U. S. A.* **117**, 10976–10982 (2020).
227. Krasovitski, B., Frenkel, V., Shoham, S. & Kimmel, E. Intramembrane cavitation as a unifying mechanism for ultrasound-induced bioeffects. *Proc. Natl. Acad. Sci.* **108**, 3258–3263 (2011).
228. Zhang, Z. *et al.* Hypersonic Poration: A New Versatile Cell Poration Method to Enhance Cellular Uptake Using a Piezoelectric Nano-Electromechanical Device. *Small* **13**, 1602962 (2017).
229. Reusch, T. *et al.* Collective lipid bilayer dynamics excited by surface acoustic waves. *Phys. Rev. Lett.* **113**, 118102 (2014).
230. Ramesan, S., Rezk, A. R., Dekiwadia, C., Cortez-Jugo, C. & Yeo, L. Y. Acoustically-mediated intracellular delivery †. *Nanoscale* **10**, 13165 (2018).
231. Ramesan, S. *et al.* Acoustofection: High-Frequency Vibrational Membrane Permeabilization for Intracellular siRNA Delivery into Nonadherent Cells. *ACS Appl. Bio Mater.* **4**, 2781–2789 (2021).
232. Meng, L. *et al.* On-chip targeted single cell sonoporation with microbubble destruction excited by surface acoustic waves. *Appl. Phys. Lett.* **104**, 073701 (2014).
233. Song, B. *et al.* A novel portable cell sonoporation device based on open-source acoustofluidics. in *2020 IEEE/RSJ International Conference on Intelligent Robots and Systems (IROS)* 2786–2791 (IEEE, 2020). doi:10.1109/IROS45743.2020.9341603
234. Peng, D. *et al.* Mechanisms and Applications of Neuromodulation Using Surface Acoustic Waves—A Mini-Review. *Front. Neurosci.* **15**, 27 (2021).
235. Devendran, C., Carthew, J., Frith, J. E. & Neild, A. Cell Adhesion, Morphology, and Metabolism

Variation via Acoustic Exposure within Microfluidic Cell Handling Systems. *Adv. Sci.* **6**, 1902326 (2019).

236. Greco, G. *et al.* Surface-Acoustic-Wave (SAW)-Driven Device for Dynamic Cell Cultures. *Anal. Chem.* **90**, 7450–7457 (2018).
237. Brugger, M. S. *et al.* Orchestrating cells on a chip: Employing surface acoustic waves towards the formation of neural networks. *Phys. Rev. E* **98**, 012411 (2018).
238. Doan, N., Reher, P., Meghji, S. & Harris, M. In vitro effects of therapeutic ultrasound on cell proliferation, protein synthesis, and cytokine production by human fibroblasts, osteoblasts, and monocytes. *J. Oral Maxillofac. Surg.* **57**, 409–419 (1999).
239. Brugger, M. S. *et al.* Vibration enhanced cell growth induced by surface acoustic waves as in vitro wound-healing model. *Proc. Natl. Acad. Sci.* **117**, 31603–31613 (2020).
240. Lee, I.-C., Wu, H.-J. & Liu, H.-L. Dual-Frequency Ultrasound Induces Neural Stem/Progenitor Cell Differentiation and Growth Factor Utilization by Enhancing Stable Cavitation. *ACS Chem. Neurosci.* **10**, 1452–1461 (2019).
241. Lee, Y. S. *et al.* An ultra-effective method of generating extramultipotent cells from human fibroblasts by ultrasound. *Biomaterials* **143**, 65–78 (2017).
242. Ambattu, L. A. *et al.* High frequency acoustic cell stimulation promotes exosome generation regulated by a calcium-dependent mechanism. *Commun. Biol.* **3**, 1–9 (2020).
243. Ranade, S. S., Syeda, R. & Patapoutian, A. Mechanically Activated Ion Channels. *Neuron* **87**, 1162–1179 (2015).
244. Kumar, P., Kumar, D., Jha, S. K., Jha, N. K. & Ambasta, R. K. Ion Channels in Neurological Disorders. in *Advances in Protein Chemistry and Structural Biology* **103**, 97–136 (Academic Press Inc., 2016).
245. Ye, J. *et al.* Ultrasonic Control of Neural Activity through Activation of the Mechanosensitive Channel MscL. *Nano Lett.* **18**, 4148–4155 (2018).
246. Lin, Z. *et al.* On-Chip Ultrasound Modulation of Pyramidal Neuronal Activity in Hippocampal Slices. *Adv. Biosyst.* **2**, 1800041 (2018).
247. Lin, Z. *et al.* Ultrasound stimulation modulates voltage-gated potassium currents associated with action potential shape in hippocampal CA1 pyramidal neurons. *Front. Pharmacol.* **10**, (2019).
248. Pan, Y. *et al.* Mechanogenetics for the remote and noninvasive control of cancer immunotherapy. *Proc. Natl. Acad. Sci.* **115**, 992–997 (2018).
249. Zhou, W. *et al.* Ultrasound neuro-modulation chip: activation of sensory neurons in Caenorhabditis elegans by surface acoustic waves. *Lab Chip* **17**, 1725–1731 (2017).
250. Hilliard, M. A. *et al.* In vivo imaging of C. elegans ASH neurons: Cellular response and adaptation to chemical repellents. *EMBO J.* **24**, 63–72 (2005).

251. Gourgou, E. & Chronis, N. Chemically induced oxidative stress affects ASH neuronal function and behavior in C. elegans. *Sci. Rep.* **6**, 38147 (2016).
252. Lin, Z. *et al.* Non-invasive ultrasonic neuromodulation of neuronal excitability for treatment of epilepsy. *Theranostics* **10**, 5514–5526 (2020).
253. Luo, J., Fu, Y. Q. & Milne, W. Acoustic wave based microfluidic and lab-on-chip. (2013).
254. Rocha-Gaso, M.-I., March-Iborra, C., Montoya-Baides, Á. & Arnau-Vives, A. Surface Generated Acoustic Wave Biosensors for the Detection of Pathogens: A Review. *Sensors* **9**, 5740–5769 (2009).
255. Chang, K. *et al.* Label-free and high-sensitive detection of human breast cancer cells by aptamer-based leaky surface acoustic wave biosensor array. *Biosens. Bioelectron.* **60**, 318–324 (2014).
256. Wang, T. *et al.* Surface Acoustic Waves (SAW)-Based Biosensing for Quantification of Cell Growth in 2D and 3D Cultures. *Sensors* **15**, 32045–32055 (2015).
257. Cai, H. L. H.-L. *et al.* A third-order mode high frequency biosensor with atomic resolution. *Biosens. Bioelectron.* **71**, 261–268 (2015).
258. Zhang, J. *et al.* Recent advances in acoustic wave biosensors for the detection of disease-related biomarkers: A review. *Anal. Chim. Acta* **1164**, 338321 (2021).
259. Wei, X., Zhang, J., Zhuang, L., Wan, H. & Wang, P. A Novel Surface Acoustic Wave Biosensor for Real-Time Monitoring of Cell Contractile Properties. *ECS Meet. Abstr.* **MA2020-01**, 1970–1970 (2020).
260. Senveli, S. U. *et al.* A surface acoustic wave biosensor for interrogation of single tumour cells in microcavities. *Lab Chip* **16**, 163–171 (2016).
261. Lamanna, L., Rizzi, F., Bhethanabotla, V. R. & De Vittorio, M. Conformable surface acoustic wave biosensor for E-coli fabricated on PEN plastic film. *Biosens. Bioelectron.* **163**, (2020).
262. Ten, S. T. *et al.* Highly sensitive Escherichia coli shear horizontal surface acoustic wave biosensor with silicon dioxide nanostructures. *Biosens. Bioelectron.* **93**, 146–154 (2017).
263. Kordas, A. *et al.* Rapid Salmonella detection using an acoustic wave device combined with the RCA isothermal DNA amplification method. *Sens. Bio-Sensing Res.* **11**, 121–127 (2016).
264. Tsougeni, K. *et al.* Lab-on-Chip platform and protocol for rapid foodborne pathogen detection comprising on-chip cell capture, lysis, DNA amplification and surface-acoustic-wave detection. *Sensors Actuators B Chem.* **320**, 128345 (2020).
265. Matatagui, D. *et al.* Comparison of two types of acoustic biosensors to detect immunoreactions: Love-wave sensor working in dynamic mode and QCM working in static mode. *Sensors Actuators B Chem.* **189**, 123–129 (2013).
266. Choi, Y.-S., Lee, J., Lee, Y., Kwak, J. & Suk Lee, S. Increase in detection sensitivity of surface acoustic wave biosensor using triple transit echo wave. *Appl. Phys. Lett.* **113**, 083702 (2018).
267. Tretjakov, A., Syritski, V., Reut, J., Boroznjak, R. & Öpik, A. Molecularly imprinted polymer film

interfaced with Surface Acoustic Wave technology as a sensing platform for label-free protein detection. *Anal. Chim. Acta* **902**, 182–188 (2016).

268. Wang, C. C. *et al.* AuNP-Amplified Surface Acoustic Wave Sensor for the Quantification of Exosomes. *ACS Sensors* **5**, 362–369 (2020).
269. Baca, J., Severns, V., Lovato, D., Branch, D. & Larson, R. Rapid Detection of Ebola Virus with a Reagent-Free, Point-of-Care Biosensor. *Sensors* **15**, 8605–8614 (2015).
270. Gray, E. R. *et al.* Ultra-rapid, sensitive and specific digital diagnosis of HIV with a dual-channel SAW biosensor in a pilot clinical study. *npj Digit. Med.* **1**, 35 (2018).
271. Turbé, V. *et al.* Towards an ultra-rapid smartphone- connected test for infectious diseases. *Sci. Rep.* **7**, 11971 (2017).
272. Liu, X., Wang, J.-Y., Mao, X.-B., Ning, Y. & Zhang, G.-J. Single-Shot Analytical Assay Based on Graphene-Oxide-Modified Surface Acoustic Wave Biosensor for Detection of Single-Nucleotide Polymorphisms. *Anal. Chem.* **87**, 9352–9359 (2015).
273. Zhang, Y., Yang, F., Sun, Z., Li, Y. T. & Zhang, G. J. A surface acoustic wave biosensor synergizing DNA-mediated: In situ silver nanoparticle growth for a highly specific and signal-amplified nucleic acid assay. *Analyst* **142**, 3468–3476 (2017).
274. Huang, Y., Das, P. K. & Bhethanabotla, V. R. Surface acoustic waves in biosensing applications. *Sensors and Actuators Reports* **3**, 100041 (2021).
275. Renaudin, A., Chabot, V., Grondin, E., Aimez, V. & Charette, P. G. Integrated active mixing and biosensing using surface acoustic waves (SAW) and surface plasmon resonance (SPR) on a common substrate. *Lab Chip* **10**, 111–115 (2010).
276. Sonato, A. *et al.* Lab on a Chip A surface acoustic wave (SAW)-enhanced grating-coupling phase-interrogation surface plasmon resonance (SPR) microfluidic biosensor †. **16**, 1224 (2014).
277. Meyer, G. D. G. D. *et al.* Nonspecific binding removal from protein microarrays using thickness shear mode resonators. *IEEE Sens. J.* **6**, 254–261 (2006).
278. Pan, S. *et al.* Biofouling Removal and Protein Detection Using a Hypersonic Resonator. *ACS Sensors* **2**, 1175–1183 (2017).
279. Liu, J., Li, S. & Bhethanabotla, V. R. Integrating Metal-Enhanced Fluorescence and Surface Acoustic Waves for Sensitive and Rapid Quantification of Cancer Biomarkers from Real Matrices. *ACS Sensors* **3**, 222–229 (2018).
280. Cular, S., Bhethanabotla, V. R. & Branch, D. W. Simultaneous surface manipulation and sensing in a biosensor using a hexagonal saw device. in *AIChE Annual Meeting, Conference Proceedings* (2006).
281. Singh, R., Sankaranarayanan, S. K. R. S. & Bhethanabotla, V. R. Cite as. *Appl. Phys. Lett* **94**, 263503 (2009).

282. Vauthier, C. & Ponchel, G. *Polymer Nanoparticles for Nanomedicines*. (Springer, 2017).
283. Kim, Y. *et al.* Mass production and size control of lipid–polymer hybrid nanoparticles through controlled microvortices. *Nano Lett.* **12**, 3587–3591 (2012).
284. Valencia, P. M., Farokhzad, O. C., Karnik, R. & Langer, R. Microfluidic technologies for accelerating the clinical translation of nanoparticles. *Nat. Nanotechnol.* **7**, 623 (2012).
285. Mahmoodi, Z. *et al.* A simple coating method of PDMS microchip with PTFE for synthesis of dexamethasone-encapsulated PLGA nanoparticles. *Drug Deliv. Transl. Res.* **9**, 707–720 (2019).
286. Zhang, L. *et al.* Microfluidic synthesis of hybrid nanoparticles with controlled lipid layers: understanding flexibility-regulated cell–nanoparticle interaction. *ACS Nano* **9**, 9912–9921 (2015).
287. Rivas, C. J. M. *et al.* Nanoprecipitation process: From encapsulation to drug delivery. *Int. J. Pharm.* **532**, 66–81 (2017).
288. Tanaka, R. *et al.* Verification of the mixing processes of the active pharmaceutical ingredient, excipient and lubricant in a pharmaceutical formulation using a resonant acoustic mixing technology. *RSC Adv.* **6**, 87049–87057 (2016).
289. Cai, G., Xue, L., Zhang, H. & Lin, J. A Review on Micromixers. *Micromachines 2017, Vol. 8, Page 274* **8**, 274 (2017).
290. Knight, J. B., Vishwanath, A., Brody, J. P. & Austin, R. H. Hydrodynamic Focusing on a Silicon Chip: Mixing Nanoliters in Microseconds. *Phys. Rev. Lett.* **80**, 3863 (1998).
291. Lee, C. Y., Wang, W. T., Liu, C. C. & Fu, L. M. Passive mixers in microfluidic systems: A review. *Chem. Eng. J.* **288**, 146–160 (2016).
292. Carugo, D., Bottaro, E., Owen, J., Stride, E. & Nastruzzi, C. Liposome production by microfluidics: potential and limiting factors. *Sci. Rep.* **6**, 25876 (2016).
293. Amrani, S. & Tabrizian, M. Characterization of Nanoscale Loaded Liposomes Produced by 2D Hydrodynamic Flow Focusing. *ACS Biomater. Sci. Eng.* **4**, 502–513 (2018).
294. Wang, S., Huang, X. & Yang, C. Mixing enhancement for high viscous fluids in a microfluidic chamber. *Lab Chip* **11**, 2081–2087 (2011).
295. Bernassau, A. L. *et al.* Controlling acoustic streaming in an ultrasonic heptagonal tweezers with application to cell manipulation. *Ultrasonics* **54**, 268–274 (2014).
296. Collins, D. J., Ma, Z. & Ai, Y. Highly localized acoustic streaming and size-selective submicrometer particle concentration using high frequency microscale focused acoustic fields. *Anal. Chem.* **88**, 5513–5522 (2016).
297. Wang, C., Rallabandi, B. & Hilgenfeldt, S. Frequency dependence and frequency control of microbubble streaming flows. *Phys. Fluids* **25**, 22002 (2013).
298. Capretto, L., Cheng, W., Hill, M. & Zhang, X. Micromixing within microfluidic devices. in *Microfluidics* 27–68 (Springer, 2011).

299. Liu, R. H., Yang, J., Pindera, M. Z., Athavale, M. & Grodzinski, P. Bubble-induced acoustic micromixing. *Lab Chip* **2**, 151–157 (2002).
300. Ahmed, D., Mao, X., Shi, J., Juluri, B. K. & Huang, T. J. A millisecond micromixer via single-bubble-based acoustic streaming. *Lab Chip* **9**, 2738–2741 (2009).
301. Liu, R. H., Lenigk, R., Druyor-Sanchez, R. L., Yang, J. & Grodzinski, P. Hybridization enhancement using cavitation microstreaming. *Anal. Chem.* **75**, 1911–1917 (2003).
302. Xie, Y. *et al.* Single-shot characterization of enzymatic reaction constants K m and k cat by an acoustic-driven, bubble-based fast micromixer. *Anal. Chem.* **84**, 7495–7501 (2012).
303. Yazdi, S. & Ardekani, A. M. Bacterial aggregation and biofilm formation in a vortical flow. *Biomicrofluidics* **6**, 44114 (2012).
304. Nama, N., Huang, P. H., Huang, T. J. & Costanzo, F. Investigation of acoustic streaming patterns around oscillating sharp edges. *Lab Chip* **14**, 2824–2836 (2014).
305. Huang, P.-H. *et al.* An acoustofluidic micromixer based on oscillating sidewall sharp-edges. *Lab Chip* **13**, 3847 (2013).
306. Green, R., Ohlin, M. & Wiklund, M. Applications of acoustic streaming. *R. Soc. Chem. London* 312–336 (2014).
307. Rayleigh, J. W. S. B. *Scientific papers*. **1**, (University Press, 1899).
308. Rayleigh, Lord. On the Circulation of Air Observed in Kundt's Tubes, and on Some Allied Acoustical Problems. *Proc. R. Soc. London Ser. I* **36**, 10–11 (1883).
309. Stuart, J. T. Laminar boundary layers. *Clarendon, Oxford* (1963).
310. Zarembo, L. K. Acoustic streaming. in *High-intensity ultrasonic fields* 135–199 (Springer, 1971).
311. Elder, S. A. Cavitation microstreaming. *J. Acoust. Soc. Am.* **31**, 54–64 (1959).
312. Leighton, T. G. Bubble population phenomena in acoustic cavitation. *Ultrason. Sonochem.* **2**, S123–S136 (1995).
313. Ovchinnikov, M., Zhou, J. & Yalamanchili, S. Acoustic streaming of a sharp edge. *J. Acoust. Soc. Am.* **136**, 22–29 (2014).
314. Lenshof, A., Magnusson, C. & Laurell, T. Acoustofluidics 8: Applications of acoustophoresis in continuous flow microsystems. *Lab Chip* **12**, 1210 (2012).
315. Pons, J. L. *Emerging actuator technologies: a micromechatronic approach*. (John Wiley & Sons, 2005).
316. Rao, S. S. & Yap, F. F. *Mechanical vibrations*. **4**, (Prentice Hall Upper Saddle River, 2011).
317. Capretto, L., Carugo, D., Mazzitelli, S., Nastruzzi, C. & Zhang, X. Microfluidic and lab-on-a-chip preparation routes for organic nanoparticles and vesicular systems for nanomedicine applications. *Adv. Drug Deliv. Rev.* **65**, 1496–1532 (2013).
318. Liu, D., Zhang, H., Fontana, F., Hirvonen, J. T. & Santos, H. A. Microfluidic-assisted fabrication of

carriers for controlled drug delivery. *Lab Chip* **17**, 1856–1883 (2017).

319. Chopra, S. *et al.* Design of insulin-loaded nanoparticles enabled by multistep control of nanoprecipitation and zinc chelation. *ACS Appl. Mater. Interfaces* **9**, 11440–11450 (2017).
320. Johnson, B. K. & Prud'homme, R. K. Mechanism for rapid self-assembly of block copolymer nanoparticles. *Phys. Rev. Lett.* **91**, 118302 (2003).
321. Bachman, H. *et al.* Acoustofluidic devices controlled by cell phones. *Lab Chip* **18**, 433–441 (2018).
322. Blondel, D. & Lutolf, M. P. NCCR Bio-iNspiRed MateRials Bioinspired Hydrogels for 3D Organoid Culture. *Chimia (Aarau).* **73**, 81–85 (2019).
323. Zhang, H., Zhu, Y. & Shen, Y. Microfluidics for Cancer Nanomedicine: From Fabrication to Evaluation. *Small* **14**, 1800360 (2018).
324. Wu, J., Chen, Q., Liu, W., He, Z. & Lin, J.-M. Recent advances in microfluidic 3D cellular scaffolds for drug assays. *TrAC Trends Anal. Chem.* **87**, 19–31 (2017).
325. Keller, F., Rudolf, R. & Hafner, M. Towards optimized breast cancer 3D spheroid mono-and co-culture models for pharmacological research and screening. *J. Cell. Biotechnol.* **5**, 89–101 (2019).
326. Egger, D., Tripisciano, C., Weber, V., Dominici, M. & Kasper, C. Dynamic cultivation of mesenchymal stem cell aggregates. *Bioengineering* **5**, 1–15 (2018).
327. Wang, A., Madden, L. A. & Paunov, V. N. Advanced biomedical applications based on emerging 3D cell culturing platforms. *J. Mater. Chem. B* **8**, 10487 (2020).
328. Laschke, M. W. & Menger, M. D. Spheroids as vascularization units: From angiogenesis research to tissue engineering applications. *Biotechnol. Adv.* **35**, 782–791 (2017).
329. Bulanova, E. A. *et al.* Bioprinting of a functional vascularized mouse thyroid gland construct. *Biofabrication* **9**, (2017).
330. Ayan, B. *et al. Aspiration-assisted bioprinting for precise positioning of biologics*. *Sci. Adv* **6**, (2020).
331. Cui, X., Hartanto, Y. & Zhang, H. Advances in multicellular spheroids formation. *J. R. Soc. Interface* **14**, 20160877 (2017).
332. Velasco, V., Shariati, S. A. & Esfandyarpour, R. Microtechnology-based methods for organoid models. *Microsystems and Nanoengineering* **6**, (2020).
333. Tsai, H. F., Trubelja, A. & of the Royal~…, S.-A. Q. Tumour-on-a-chip: microfluidic models of tumour morphology, growth and microenvironment. *J. R.* (2017).
334. Nunes, A. S., Barros, A. S., Costa, E. C., Moreira, A. F. & Correia, I. J. 3D tumor spheroids as in vitro models to mimic in vivo human solid tumors resistance to therapeutic drugs. *Biotechnol. Bioeng.* **116**, 206–226 (2019).
335. Huang, Y. L. *et al.* Tumor spheroids under perfusion within a 3D microfluidic platform reveal critical roles of cell-cell adhesion in tumor invasion. *Sci. Rep.* **10**, 9648 (2020).

336. Khot, M., Levenstein, M., Kapur, N. & Jayne, D. A Review on the Recent Advancement in "Tumour Spheroids-on-a-Chip". *J. Cancer Res. Pract.* **6**, 55–62 (2019).
337. Trujillo-De Santiago, G. *et al.* materials The Tumor-on-Chip: Recent Advances in the Development of Microfluidic Systems to Recapitulate the Physiology of Solid Tumors. (2019). doi:10.3390/ma12182945
338. Ryu, N.-E., Lee, S.-H. & Park, H. Spheroid Culture System Methods and Applications for Mesenchymal Stem Cells. *Cells* **8**, 1620 (2019).
339. Agarwal, T. & Maiti, T. K. Dielectrophoresis-based devices for cell patterning. in *Bioelectronics and Medical Devices* 493–511 (Elsevier, 2019). doi:10.1016/B978-0-08-102420-1.00026-1
340. Murrow, L. M., Weber, R. J. & Gartner, Z. J. Dissecting the stem cell niche with organoid models: an engineering-based approach. *Development* **144**, 998–1007 (2017).
341. Liu, Y. *et al.* Microfluidic generation of egg-derived protein microcarriers for 3D cell culture and drug delivery. *Sci. Bull.* **62**, 1283–1290 (2017).
342. Shao, C. *et al.* Responsive Inverse Opal Scaffolds with Biomimetic Enrichment Capability for Cell Culture. *Research* **2019**, 1–10 (2019).
343. Sun, Q. *et al.* Microfluidic Formation of Coculture Tumor Spheroids with Stromal Cells As a Novel 3D Tumor Model for Drug Testing. *ACS Biomater. Sci. Eng.* **4**, 4425–4433 (2018).
344. Sabhachandani, P. *et al.* From chip-in-a-lab to lab-on-a-chip: towards a single handheld electronic system for multiple application-specific lab-on-a-chip (ASLOC). **16**, 497 (2014).
345. Kamperman, T., Karperien, M., Le Gac, S. & Leijten, J. Single-Cell Microgels: Technology, Challenges, and Applications. *Trends Biotechnol.* **36**, 850–865 (2018).
346. Lee, A. *et al.* 3D bioprinting of collagen to rebuild components of the human heart. *Science (80-.).* **365**, 482–487 (2019).
347. Wang, H. *et al.* Biomimetic enzyme cascade reaction system in microfluidic electrospray microcapsules. *Sci. Adv.* **4**, (2018).
348. Matos, M. A. & Cicerone, M. T. Alternating current electric field effects on neural stem cell viability and differentiation. *Biotechnol. Prog.* **26**, 664–670 (2010).
349. Jang, M., Yang, S. & Kim, P. Microdroplet-based cell culture models and their application. *Biochip J.* **10**, 310–317 (2016).
350. Jiang, W., Li, M., Chen, Z. & Leong, K. W. Cell-laden microfluidic microgels for tissue regeneration. *Lab on a Chip* **16**, 4482–4506 (2016).
351. Froehlich, K. *et al. Generation of Multicellular Breast Cancer Tumor Spheroids: Comparison of Different Protocols*. *Journal of Mammary Gland Biology and Neoplasia* **21**, 89–98 (Springer New York LLC, 2016).
352. Zhao, S. *et al.* Fabrication of tunable, high-molecular-weight polymeric nanoparticles via ultrafast

acoustofluidic micromixing. *pubs.rsc.org*

353. Wang, Z. *et al.* Cell lysis via acoustically oscillating sharp edges. *Lab Chip* **19**, 4021–4032 (2019).
354. Meng, L. *et al.* Sonoporation of Cells by a Parallel Stable Cavitation Microbubble Array. *Adv. Sci.* **6**, 1900557 (2019).
355. Paredes-Juarez, G. A., Barnett, B. P. & Bulte, J. W. M. Noninvasive Tracking of Alginate-Microencapsulated Cells. in *Methods in Molecular Biology* **1479**, 143–155 (2017).
356. Peela, N. *et al.* Advanced biomaterials and microengineering technologies to recapitulate the stepwise process of cancer metastasis. *Biomaterials* **133**, 176–207 (2017).
357. Alberts, B. *Molecular Biology of the Cell*. (2018).
358. Yoon, J. *et al.* Fabrication of type I collagen microcarrier using a microfluidic 3D T-junction device and its application for the quantitative analysis of cell-ECM interactions. *Biofabrication* **8**, 35014 (2016).
359. Ivascu, A. & Kubbies, M. Diversity of cell-mediated adhesions in breast cancer spheroids. *Int. J. Oncol.* **31**, 1403–1413 (2007).
360. Lin, N., Tang, J., Dufresne, A. & Tam, M. K. C. *Functional Hydrogels as Biomaterials*. **12**, (Springer Berlin Heidelberg, 2018).
361. Kadler, K. E., Hill, A. & Canty-Laird, E. G. Collagen fibrillogenesis: fibronectin, integrins, and minor collagens as organizers and nucleators. *Curr. Opin. Cell Biol.* **20**, 495–501 (2008).
362. Wenstrup, R. J. *et al.* Regulation of Collagen Fibril Nucleation and Initial Fibril Assembly Involves Coordinate Interactions with Collagens V and XI in Developing Tendon. *J. Biol. Chem.* **286**, 20455–20465 (2011).
363. Franke, K., Sapudom, J., Kalbitzer, L., Anderegg, U. & Pompe, T. Topologically defined composites of collagen types i and v as in vitro cell culture scaffolds. *Acta Biomater.* **10**, 2693–2702 (2014).
364. Olegovich Osidak, E., Igorevich Kozhukhov, V., Sergeevna Osidak, M. & Petrovich Domogatskiy, S. Collagen as Bioink for Bioprinting: A Comprehensive Review. *Int. J. Bioprinting* **6**, 1–10 (2020).
365. Mekhail, M., Daoud, J., Almazan, G. & Tabrizian, M. Rapid, guanosine 5'-diphosphate-induced, gelation of chitosan sponges as novel injectable scaffolds for soft tissue engineering and drug delivery applications. *Adv. Healthc. Mater.* **2**, 1126–1130 (2013).
366. Holder, A. J. *et al.* Control of collagen gel mechanical properties through manipulation of gelation conditions near the sol-gel transition. *This J. is Cite this Soft Matter* **14**, 574 (2018).
367. Abe-Fukasawa, N., Otsuka, K., Aihara, A., Itasaki, N. & Nishino, T. Novel 3D Liquid Cell Culture Method for Anchorage-independent Cell Growth, Cell Imaging and Automated Drug Screening. *Sci. Rep.* **8**, 1–12 (2018).
368. Gong, X. *et al.* Generation of Multicellular Tumor Spheroids with Microwell-Based Agarose Scaffolds for Drug Testing. *PLoS One* **10**, e0130348 (2015).

369. Kuo, C.-T. *et al.* Three-dimensional spheroid culture targeting versatile tissue bioassays using a PDMS-based hanging drop array. *Sci. Rep.* **7**, 4363 (2017).
370. Sapudom, J. *et al.* The phenotype of cancer cell invasion controlled by fibril diameter and pore size of 3D collagen networks. *Biomaterials* **52**, 367–375 (2015).
371. Ivascu, A. & Kubbies, M. Rapid Generation of Single-Tumor Spheroids for High-Throughput Cell Function and Toxicity Analysis. *J. Biomol. Screen.* **11**, 922–932 (2006).
372. Shin, J. Y. *et al.* Efficient formation of cell spheroids using polymer nanofibers. *Biotechnol. Lett.* **34**, 795–803 (2012).
373. Białkowska, K., Komorowski, P., Bryszewska, M. & Miłowska, K. Spheroids as a type of three-dimensional cell cultures—examples of methods of preparation and the most important application. *Int. J. Mol. Sci.* **21**, 1–17 (2020).
374. Goers, L., Freemont, P. & Polizzi, K. M. Co-culture systems and technologies: taking synthetic biology to the next level. *J. R. Soc. Interface* **11**, 20140065 (2014).
375. Abbasi, F., Ghanian, M. H., Baharvand, H., Vahidi, B. & Eslaminejad, M. B. Engineering mesenchymal stem cell spheroids by incorporation of mechanoregulator microparticles. *J. Mech. Behav. Biomed. Mater.* **84**, 74–87 (2018).
376. Kim, S., Kim, E. M., Yamamoto, M., Park, H. & Shin, H. Engineering Multi-Cellular Spheroids for Tissue Engineering and Regenerative Medicine. *Adv. Healthc. Mater.* **9**, 2000608 (2020).
377. Gaspar, V. M., Lavrador, P., Borges, J., Oliveira, M. B. & Mano, J. F. Advanced Bottom-Up Engineering of Living Architectures. *Adv. Mater.* **32**, 1903975 (2019).
378. Sahana, J. *et al.* Decreased E-Cadherin in MCF7 Human Breast Cancer Cells Forming Multicellular Spheroids Exposed to Simulated Microgravity. *Proteomics* **18**, 1800015 (2018).
379. Levato, R., Planell, J. A., Mateos-Timoneda, M. A. & Engel, E. Role of ECM/peptide coatings on SDF-1α triggered mesenchymal stromal cell migration from microcarriers for cell therapy. *Acta Biomater.* **18**, 59–67 (2015).
380. Neto, M. D., Oliveira, M. B. & Mano, J. F. Microparticles in Contact with Cells: From Carriers to Multifunctional Tissue Modulators. *Trends in Biotechnology* **37**, 1011–1028 (2019).
381. Lee, W. *et al.* Dispersible hydrogel force sensors reveal patterns of solid mechanical stress in multicellular spheroid cultures. *Nat. Commun.* **10**, 144 (2019).
382. Zhao, L., Mok, S. & Moraes, C. Micropocket hydrogel devices for all-in-one formation, assembly, and analysis of aggregate-based tissues. *Biofabrication* **11**, (2019).
383. Moldovan, N. I., Hibino, N. & Nakayama, K. Principles of the kenzan method for robotic cell spheroid-based three-dimensional bioprinting. *Tissue Eng. - Part B Rev.* **23**, 237–244 (2017).
384. Gao, B. *et al.* 4D Bioprinting for Biomedical Applications. *Trends Biotechnol.* **34**, 746–756 (2016).
385. Mironov, V. *et al.* Organ printing: Tissue spheroids as building blocks. *Biomaterials* **30**, 2164–2174

(2009).

386. Zhu, Y. *et al.* Magnetically Actuated Active Deep Tumor Penetration of Deformable Large Nanocarriers for Enhanced Cancer Therapy. *Adv. Funct. Mater.* **31**, (2021).

387. O'Brien, M. E. R. *et al.* Reduced cardiotoxicity and comparable efficacy in a phase IIItrial of pegylated liposomal doxorubicin HCl(CAELYX™/Doxil®) versus conventional doxorubicin forfirst-line treatment of metastatic breast cancer. *Ann. Oncol.* **15**, 440–449 (2004).

388. Cooper, G. M. The Development and Causes of Cancer. (2000).

389. Nichols, J. W. & Bae, Y. H. Odyssey of a cancer nanoparticle: From injection site to site of action. *Nano Today* **7**, 606–618 (2012).

390. Wang, J. *et al.* The Role of Micelle Size in Tumor Accumulation, Penetration, and Treatment. *ACS Nano* **9**, 7195–7206 (2015).

391. Yuan, F. *et al.* Microvascular Permeability and Interstitial Penetration of Sterically Stabilized (Stealth) Liposomes in a Human Tumor Xenograft'. (1994).

392. Youn, Y. S. & Bae, Y. H. Perspectives on the past, present, and future of cancer nanomedicine. *Adv. Drug Deliv. Rev.* **130**, 3–11 (2018).

393. Chauhan, V. P. & Jain, R. K. Strategies for advancing cancer nanomedicine. *Nat. Mater.* **12**, 958 (2013).

394. Goodman, T. T., Olive, P. L. & Pun, S. H. Increased nanoparticle penetration in collagenase-treated multicellular spheroids. *Int. J. Nanomedicine* **2**, 265–74 (2007).

395. Magzoub, M., Jin, S. & Verkman, A. S. Enhanced macromolecule diffusion deep in tumors after enzymatic digestion of extracellular matrix collagen and its associated proteoglycan decorin. *FASEB J.* **22**, 276–284 (2008).

396. L, Z. *et al.* High Tumor Penetration of Paclitaxel Loaded pH Sensitive Cleavable Liposomes by Depletion of Tumor Collagen I in Breast Cancer. *ACS Appl. Mater. Interfaces* **7**, 9691–9701 (2015).

397. Barua, S. & Mitragotri, S. ScienceDirect Challenges associated with penetration of nanoparticles across cell and tissue barriers: A review of current status and future prospects. *Nano Today* **9**, 223–243 (2014).

398. Mitragotri, S. Devices for overcoming biological barriers: The use of physical forces to disrupt the barriers. *Advanced Drug Delivery Reviews* **65**, 100–103 (2013).

399. Barua, S. & Mitragotri, S. Challenges associated with penetration of nanoparticles across cell and tissue barriers: A review of current status and future prospects. *Nano Today* **9**, 223–243 (2014).

400. Watson, K. D. *et al.* Ultrasound Increases Nanoparticle Delivery by Reducing Intratumoral Pressure and Increasing Transport in Epithelial and Epithelial–Mesenchymal Transition Tumors. *Cancer Res.* **72**, 1485–1493 (2012).

401. Dalecki, D. Mechanical bioeffects of ultrasound. *Annual Review of Biomedical Engineering* **6**, 229–

248 (2004).

402. Entzian, K. & Aigner, A. Drug delivery by ultrasound-responsive nanocarriers for cancer treatment. *Pharmaceutics* **13**, 1–31 (2021).

403. Liu, H. L. *et al.* Magnetic resonance monitoring of focused ultrasound/magnetic nanoparticle targeting delivery of therapeutic agents to the brain. *Proc. Natl. Acad. Sci. U. S. A.* **107**, 15205–15210 (2010).

404. AB, E. *et al.* Focused ultrasound disruption of the blood-brain barrier: a new frontier for therapeutic delivery in molecular neurooncology. *Neurosurg. Focus* **32**, (2012).

405. Jain, A., Tiwari, A., Verma, A. & Jain, S. K. Ultrasound-based triggered drug delivery to tumors. *Drug Delivery and Translational Research* **8**, 150–164 (2018).

406. De Cock, I., Lajoinie, G., Versluis, M., De Smedt, S. C. & Lentacker, I. Sonoprinting and the importance of microbubble loading for the ultrasound mediated cellular delivery of nanoparticles. *Biomaterials* **83**, 294–307 (2016).

407. Snipstad, S., Hanstad, S., Bjørkøy, A., Mørch, Ý. & De Lange Davies, C. Sonoporation using nanoparticle-loaded microbubbles increases cellular uptake of nanoparticles compared to co-incubation of nanoparticles and microbubbles. *Pharmaceutics* **13**, (2021).

408. Bourn, M. D. *et al.* High-throughput microfluidics for evaluating microbubble enhanced delivery of cancer therapeutics in spheroid cultures. *J. Control. Release* **326**, 13–24 (2020).

409. Bing, C. *et al.* Characterization of different bubble formulations for blood-brain barrier opening using a focused ultrasound system with acoustic feedback control. *Sci. Rep.* **8**, 1–12 (2018).

410. Yubero, M. L. *et al.* Effects of energy metabolism on the mechanical properties of breast cancer cells. *Commun. Biol.* **3**, 590 (2020).

411. Brás, M. M., Radmacher, M., Sousa, S. R. & Granja, P. L. Melanoma in the Eyes of Mechanobiology. *Front. Cell Dev. Biol.* **8**, 54 (2020).

412. Destgeer, G. *et al.* Lab on a Chip Lab on a Chip Acoustofluidic particle manipulation inside a sessile droplet: four distinct regimes of particle concentration †. *Lab Chip* **16**, 660 (2014).

413. Destgeer, G. *et al.* Microchannel Anechoic Corner for Size-Selective Separation and Medium Exchange via Traveling Surface Acoustic Waves. *Anal. Chem* **87**, 37 (2015).

414. Destgeer, G. *et al.* Travelling Surface Acoustic Waves Microfluidics. *Phys. Procedia* **70**, 34–37 (2015).

415. Grayver, A. V. & Noir, J. Particle streak velocimetry using ensemble convolutional neural networks. *Exp. Fluids* **61**, 1–12 (2020).

416. Qureshi, M. H., Tien, W. H. & Lin, Y. J. P. Performance comparison of particle tracking velocimetry (PTV) and particle image velocimetry (PIV) with long-exposure particle streaks. *Meas. Sci. Technol.* **32**, (2020).

417. Zhong, R. *et al.* Acoustofluidic Droplet Sorter Based on Single Phase Focused Transducers. *Small* **17**, 2103848 (2021).

418. Moreira, R. B. *et al.* Regression of multifocoal in transit melanoma metastases after palliative resection of dominant masses and 2 years after treatment with ipilimumab. *J. Immunother. Cancer* **5**, 1–4 (2017).

419. Gimbel, M. I., Delman, K. A. & Zager, J. S. Therapy for unresectable recurrent and in-transit extremity melanoma. *Cancer Control* **15**, 225–232 (2008).

420. Joiner, J. B., Pylayeva-Gupta, Y. & Dayton, P. A. Focused Ultrasound for Immunomodulation of the Tumor Microenvironment. *J. Immunol.* **205**, 2327–2341 (2020).

421. Sargenti, A. *et al.* A new method for the study of biophysical and morphological parameters in 3D cell cultures: Evaluation in LoVo spheroids treated with crizotinib. *PLoS One* **16**, e0252907 (2021).

422. Rossmanna, C. & Haemmerich, D. Review of temperature dependence of thermal properties, dielectric properties, and perfusion of biological tissues at hyperthermic and ablation temperatures. *Crit. Rev. Biomed. Eng.* **42**, 467–492 (2014).

423. Cutrona, M. B. & Simpson, J. C. A High-Throughput Automated Confocal Microscopy Platform for Quantitative Phenotyping of Nanoparticle Uptake and Transport in Spheroids. *Small* **15**, 1902033 (2019).

424. Barton, J. K. Dynamic Changes in Optical Properties. in *Optical-Thermal Response of Laser-Irradiated Tissue* 321–349 (Springer Netherlands, 2010). doi:10.1007/978-90-481-8831-4_9

425. Skrott, Z. *et al.* Alcohol-abuse drug disulfiram targets cancer via p97 segregase adaptor NPL4. *Nat. 2017 5527684* **552**, 194–199 (2017).

426. Paun, R. A. *et al.* One-Step Synthesis of Nanoliposomal Copper Diethyldithiocarbamate and Its Assessment for Cancer Therapy. *Pharmaceutics* **14**, 640 (2022).

427. Saalbach, A., Hildebrandt, G., Haustein, U. F. & Anderegg, U. The Thy-1/Thy-1 Ligand Interaction Is Involved in Binding of Melanoma Cells to Activated Thy-1- Positive Microvascular Endothelial Cells. *Microvasc. Res.* **64**, 86–93 (2002).

428. Brenet, M. *et al.* Thy-1 (CD90)-Induced Metastatic Cancer Cell Migration and Invasion Are β3 Integrin-Dependent and Involve a Ca2+/P2X7 Receptor Signaling Axis. *Front. Cell Dev. Biol.* **8**, (2021).

429. Rege, T. A. & Hagood, J. S. Thy-1 as a regulator of cell-cell and cell-matrix interactions in axon regeneration, apoptosis, adhesion, migration, cancer, and fibrosis. *FASEB J.* **20**, 1045–1054 (2006).

430. Hu, P. & Barker, T. H. Thy-1 in Integrin Mediated Mechanotransduction. *Front. Cell Dev. Biol.* **7**, 22 (2019).

431. Sauzay, C., Voutetakis, K., Chatziioannou, A. A., Chevet, E. & Avril, T. CD90/Thy-1, a cancer-associated cell surface signaling molecule. *Front. Cell Dev. Biol.* **7**, 66 (2019).

432. Meriin, A. B. *et al.* Hsp70–Bag3 complex is a hub for proteotoxicity-induced signaling that controls protein aggregation. *Proc. Natl. Acad. Sci.* **115**, E7043–E7052 (2018).
433. Letzsch, S., Boettcher, K. & Schreiner, A. Cellular Imaging and Analysis T E C H N I C A L N O T E Clearing Strategies for 3D Spheroids.
434. Hama, H. *et al.* ScaleS: an optical clearing palette for biological imaging. *Nat. Neurosci. 2015 1810* **18**, 1518–1529 (2015).
435. Han, S. J., Kwon, S. & Kim, K. S. Challenges of applying multicellular tumor spheroids in preclinical phase. *Cancer Cell Int.* **21**, (2021).
436. Lee, J. N., Park, C. & Whitesides, G. M. Solvent Compatibility of Poly(dimethylsiloxane)-Based Microfluidic Devices. *Anal. Chem.* **75**, 6544–6554 (2003).
437. Zhang, L., Chen, Q., Ma, Y. & Sun, J. Microfluidic Methods for Fabrication and Engineering of Nanoparticle Drug Delivery Systems. *ACS Appl. Bio Mater.* **3**, 107–120 (2020).
438. Ozcan, A. Mobile phones democratize and cultivate next-generation imaging, diagnostics and measurement tools. *Lab Chip* **14**, 3187–3194 (2014).
439. Zhang, L., Tian, Z., Bachman, H., Zhang, P. & Huang, T. J. A Cell-Phone-Based Acoustofluidic Platform for Quantitative Point-of-Care Testing. *ACS Nano* **14**, 3159–3169 (2020).